Université catholique de Louvain
Institute of Condensed Matter and Nanosciences
Bio- and Soft Matter

Nanopatterned surfaces to control the development of bacteria and mammalian cells

Catherine Philippart

Thesis submitted in partial fulfillment of the requirements for the Ph.D. Degree in Engineering Sciences

Thesis Committee

Prof. Karine Glinel (Supervisor)	*Université catholique de Louvain*
Prof. Anne des Rieux	*Université catholique de Louvain*
Prof. Sylvain Gabriele	*Université de Mons*
Prof. Jacques Mahillon	*Université catholique de Louvain*
Prof. Madeleine Ramstedt	*Umeå University, Sweden*
Prof. Jean-François Gohy (Chair)	*Université catholique de Louvain*

Louvain-la-Neuve, 2018.

Acknowledgments

I began my PhD thesis in September 2013. Little did I know at that time the valuable lessons I would learn and the great people I would meet and share time with.

First of all, I would like to express my gratitude to my supervisor Prof. Karine Glinel for the time she devoted to me during the last four years. I would especially like to express my special thanks for always keeping her door open to answer my 5 minute questions. She always made herself available to discuss and give suggestions about the work that needed to be done. She provided me with a lot autonomy which I appreciated a lot. Apart from the technical aspects related to this project, she also helped me to improve my soft skills such as the way to write a scientific report and the organization of a presentation.

Thanks to the members of my jury: Professors Anne des Rieux, Sylvain Gabriele, Jean-François Gohy, Jacques Mahillon and Madeleine Ramstedt. I appreciate the time they took to read and to criticize this work in order to improve it. I also value the discussion we had during the private defense which allowed me to examine my work from another angle and helped me to adjust more finely some discussions and conclusions.

Many thanks to all the people who taught me how to use different equipments or gave me useful tips to perform my experiments or analyses: Camille Marie and Cédric Burhin (Ellipsometry, nanoimprint, epifluorescence microscopy), Colette Douchamps (SEM), Sabine Bebelman (FTIR), Sylvie Derclaye and Cécile D'Haese (AFM), Ali Dirani (polymer brush), Antony Fernandes (silane synthesis). Cécile D'Haese additionally performed XPS on my samples and advised me on the analyses to perform on my data. On his side, Pierre Eloy taught me how to analyze my data. Moreover, Prof. Alain Jonas helped me to perform my FTIR and my bacterial analyses by programming the IGOR PRO routines that I used.

I would like to thank the people who helped me in the cleanroom. André Crahay, among other things, performed the descum and etching processes required for my experiments. Christian Renaux, Ester Tooten and Miloud Zitout helped me with my experiments and/or with the technical problems encountered in the cleanroom. Thanks also to all the people who helped me with the practical questions I had throughout these four years.

For my bacterial assays, I would like to thank Yves Dufrêne who allowed

me to work in his lab. Over there, I received help from Sylvie Derclaye whom I could always ask about handling procedures. I always felt I was welcome over there.

For my cell experiments, I worked with Prof. Anne des Rieux and her team. I would like to express my gratitude for the training she gave me, the PCR experiments she performed and the discussion that helped me to improve my analyses and the display of my results. I would also like to thank Natalija, Pauline, Dario, Audrey, John, Bernard and Loïc for their help while facing the daily issues I had regarding the organization of my experiments. I must also say that I felt really welcomed in this team as well.

Thanks to Aurore Becquevort and Anne Bouchat who helped me throughout the administrative procedures. Thanks to Pascal Van Velthem who is always willing to help in case of technical problems including informatics.

I also had the chance to supervise and work with Marion Marin and Eléana Somville whom I could rely upon to carry out properly the project that was given to them. To me it was an enriching experience and I can only hope they felt the same way about it.

I would also like to thank all former and current BSMA members with whom I was always able to talk. Thanks to Tilia, Colette, Diana, Jérémy and Amir that always made sure I was laughing even though my experiments were not going well. Thanks also to Damien, Claire, Eléana, Guillaume, Florian, Sabrina and Saghi to always make me feel welcome in their office. Thanks to Moira, Marion, Pedro, Quentin, Ronggang, Walter, Diana, Bruno and Wael for their friendly discussion.

Merci à Colette Douchamps pour son aide logistique, pour la commande de petit matériel depuis que je suis arrivée dans le laboratoire et aussi pour avoir été une super co-équipière pour la gestion du stock chimique.

Je souhaite aussi remercier mes amis de "eplol" qui m'ont aidée à surmonter certains moments difficiles de cette thèse et sans qui ma vie ne serait pas aussi joyeuse. Merci également à mes amis des études qui sont toujours là en cas de besoin. J'aimerais également remercier les collègues de Matthew qui m'ont toujours bien accueillie dans leur labo même si je ne comprends pas grand chose de leur travail.

J'aimerais aussi remercier ma famille pour son soutien tout au long de cette thèse.

Merci de tout coeur à Matthew qui a vu passer mes meilleurs et plus mauvais

moments lors de cette thèse. Merci de ta patience et de ton soutien dans notre vie de tous les jours.

And thanks to those I forgot to mention but were there for me.

Abstract

The development of surfaces controlling both bacterial and mammalian cell behaviors is of a great interest for applications in tissue engineering. The challenge is to produce surfaces promoting the development of mammalian cells, such as stem cells, while preventing the bacterial colonization. Besides the conventional approaches using antibiotics and bioactive compounds, recent studies showed that surface properties such as topography, stiffness, biochemistry and their patterning can be used to control mammalian or bacterial cells.

In this context, this thesis explores the fabrication of chemical and topographical patterns composed of nanometer lines of hydrophilic polymer brush grafted with peptides, to control both cell types. Three peptides were used: a cell-adhesive peptide (RGD-C) and two bactericidal peptides, *i.e.* cathelicidin (C-LL37) and magainin I (MAG-C). The behaviors of *Escherichia coli* (*E. coli*) and stem cells from the apical papilla (SCAPs) were investigated on these surfaces.

It was evidenced that C-LL37 and RGD-C patterns showed bactericidal and bioadhesive properties towards *E. coli* and SCAPs, respectively, while the antibacterial activity of MAG-C-modified surfaces was limited. Moreover, the comparison of SCAP behavior on homogeneous and patterned surfaces, revealed that nanopatterns grafted with RGD-C or a C-LL37/RGD-C mixture induced a clear variation of SCAP morphology. Thus, the neuronal, osteogenic and adipogenic expression of differentiation markers by SCAPs on patterned surfaces was investigated.

The results obtained during this PhD evidence the potential utility of the peptide-modified nanopatterns for applications in biomedical applications.

Contents

List of Acronyms

AFM : Atomic force microscopy
AMP : Antimicrobial peptide
ANOVA : Analysis of variance
Ag43 : Antigen 43
AR : Aspect ratio
Ar : Argon
(Si-)ATRP : (Surface-initiated) Atom transfer radical polymerization
(rh)BMP-2 : (recombinant human) Bone morphogenetic protein
bipy : 2,2'-Bipyridyl
BSA : Bovin serum albumin
B. subtilis : *Bacillus subtilis*
CFU : Colony forming unit
(Biotin-)LL37-C :
(Biotin-)LLGDFFRKSKEKIGKEFKRIVQRIKDFLRNLVPRTESC
C-LL37 : CLLGDFFRKSKEKIGKEFKRIVQRIKDFLRNLVPRTES
μCP : Micro-contact printing
CRP : Controlled radical polymerization
CTF : Corrected total fluorescence
DAPI : 4',6-diamidino-2-phenylindole
(x)DLVO : (extended) Derjaguin, Landau, Verwey and Overbick
DPN : Dip-pen nanolithography
EBL : Electron beam lithography
ECM : Extracellular matrix
E. coli : *Escherichia coli*
EDC : 1-ethyl-3-(3-dimethylaminopropyl) carbodiimide
FA : Focal adhesion
FBS : Fetal bovine serum
FITC : Fluorescein isothiocyanate
FN : Fibronectin
FTIR : Fourier transform infrared spectroscopy
GTP : Group transfer polymerization
P(HEMA) : Poly(2-hydroxylethyl methacrylate)
P(HEMA-*co*-MAA) : Poly(2-hydroxylethyl methacrylate-*co*-methacrylic acid)

P(HOEGMA) : Poly(hydroxyl-terminated oligo(ethylene glycol) ether methacrylate)
P(HOEGMA-*co*-MAA) : Poly(hydroxyl-terminated oligo(ethylene glycol) ether methacrylate-*co*-methacrylic acid)
LB agar : Luria Bertani Broth with agar
LB broth : Luria Bertani Broth
LbL : Layer-by-layer
L. ivanovii : *Listeria ivanovii*
L. lactis : *Lactococcus latis*
LPS : Lipopolysaccharide
LSC : Limbal stem cell
P(MAA) : Poly(methacrylic acid)
(Biotin-)MAG-C : (Biotin-)Magainin I-C
MEM eagle : Minimum essential medium eagle
MEO_2MA : Di(ethylene glycol) methyl ether methacrylate
P(MEO_2MA-*co*-HOEGMA) : Poly(di(ethylene glycol) methyl ether methacrylate-*co*-hydroxyl-terminated oligo(ethylene glycol) ether methacrylate)
P(MEO_2MA-*co*-MAA) : Poly(di(ethylene glycol) methyl ether methacrylate-*co*-methacrylic acid)
MIC : Minimal Inhibitory Concentration
PMMA : Poly(methyl methacrylate)
MSC : Mesenchymal stem cell
P(MOXA) : Poly(2-methyl-2-oxaline)
N_2 : Nitrogen gas
NaOH : Sodium hydroxide
NIL : Nanoimprint lithography
NHS : N-hydroxysuccinimide
NMP : Nitroxide mediated polymerization
NSC : Neuronal stem cell
OD : Optical density
OEG : Oligo(ethylene glycol)
P(OEGMA) : Poly(oligo(ethylene glycol) methacrylate)
PBS : Phosphate buffered saline
(qRT-)PCR : (quantitative reverse transcription) Polymerase chain reaction
PPEGMA : Poly(poly(ethylene glycol) methacrylate)
P. aeruginosa : *Pseudomonas aeruginosa*

PDMS : Poly(dimethylsiloxane)
PEG : Polyethylene glycol
PEST : Penicillin/streptomycin
PEM : Polyelectrolyte multilayer
PET : Polyethylene terephthalate
PFA : Paraformaldehyde
P. fluorescens : *Pseudomonas fluorescens*
PLL : Poly(L-lysine)
PMPI : 4-Maleimidophenyl isocyanate
PNIPAAm : Poly(N-isopropylacrylamide)
RAFT : Reversible fragmentation chain transfer process
R_a : Roughness average
(FITC-)RGD-C : (Fluorescein isothiocyanate-)KRGDSPC
RNA : Ribonucleic acid
ROMP : Ring-opening metathesis polymerization
R_q : Root mean square roughness
SAM : Self-assembled monolayer
SCAP : Stem cell from the apical papilla
SD : Standard deviation
SEM : Scanning electron microscopy
sem : Standard error of the mean
S. aureus : *Staphylococcus aureus*
S. epidermidis : *Staphylococcus epidermidis*
Blue-strep : Dylight 405 conjugated streptavidin
FITC-strep : Dylight 488 conjugated streptavidin
P(tBMA) : Poly(tert-butyl methacrylate)
THF : Tetrahydrofuran
USSC : Unrestricted somatic stem cell
UV : Ultraviolet
XPS : X-ray photoelectron spectroscopy

Chapter 1

Introduction

The integration of implanted materials in the body is a more and more common approach in the field of tissue engineering. However, up to now, this integration presents two great challenges.

On one hand, the implantation of material into the body unveils the challenge to trigger appropriate cell behaviors without harming the cells. First, the biomaterial must be non-toxic and non-immunogenic. Second, it must get colonized by the host cells and sustain cell functions such as adhesion, proliferation or differentiation. This is why the ideal scaffold for tissue engineering needs to show properties as close as possible to the ones of the natural tissue where the implant is placed [1, 2]. Moreover, some studies focus on the implantation of biomaterials already containing cells able to re-form certain tissues, some of which are difficult to regenerate. Some materials using already specialized cells are frequently used such as the ones for the regeneration of burned skin for badly burned persons [3]. Some others, using stem cells, are still the subject of many researches. For example, biomaterials using mesenchymal stem cells (MSCs) are studied with the aim to produce cardiac tissue patches [4].

On the other hand, implant associated infections are a huge problem for tissue engineering. Actually, implanted materials are responsible for 60-70 % of nosocomial infections [5]. Indeed, three types of implant-associated infections can occur: superficial immediate infection (via infected sutures), deep immediate infection (via non-sterile implantation) and deep late infection (delayed display of infection or relocation of bacteria from another site) [6]. It is also known that bacteria involved in biofilm-associated infections often comprise *Staphylococcus*

epidermidis (*S. epidermidis*), *Staphylococcus aureus* (*S. aureus*), Streptococcus species, *Pseudomonas aeruginosa* (*P. aeruginosa*) and *Escherichia coli* (*E. coli*) [7]. When a biofilm forms on the surface of a prothesis, the only way to stop the infection is often the removal of the implanted material [8]. This is due to the biofilm resistance towards antibiotic treatment or immune system which renders it complicated to eradicate [7, 9, 10]. In fact, so far, the eradication of a biofilm is considered after its establishment on a surface, mainly by the use of antibiotics. However, this leads to the emergence of antibiotic-resistant bacteria due to overuse of antibiotics [11].

In order to meet both challenges described above, recent studies focus on the design of new surfaces improving the colonization by stem cells while preventing the bacterial adhesion thus hindering the formation of a biofilm.

To control the behavior of stem cells, *in vitro* studies use a specific medium allowing to direct them into a targeted differentiation lineage. Another possibility consists in adding specific growth factors in the medium [12, 13]. However, the use of such media is not possible *in vivo*. Therefore, some materials releasing bioactive molecules at the liquid-solid interface have been developed to direct the fate of stem cells. The major challenge with these release-based systems is to finely control the release of the compound in the proper concentration and at the right time to induce the desired effect [12, 14]. Another new approach to control cell behavior is based on a specific design of the material surface. The effect of surface topography, stiffness, biochemistry and micro- and nano-patterning were explored according to this aim [15]. These studies attempt to distinguish the factors affecting the cellular attachment on a surface and the forces exerted at a site of contact. These parameters are the first steps towards the control of other desired cell behaviors such as the differentiation in the case of stem cells.

To circumvent the problem of biofilm formation on a material surface, the continuous release of antimicrobial compounds such as antibiotics or metal derivatives from the material is currently used. However, the resistance of bacteria, the potential cytotoxic effects of the released compounds or the lack of long term effect are frequently encountered issues for these systems [16]. For these reasons, new studies are developed nowadays to explore the influence of micro- and nano-topography on the bacterial adhesion and growth [17, 18]. It was notably shown that the lateral size, the depth and the regularity of the topographical features can modify the colonization of the surface by bacteria as well as the genomic expression of adhered microorganisms. Studies also look

at chemical modifications of the surface to prevent fouling of bacteria [19], to disorganize the development of the biofilm or to kill bacteria upon contact [20]. Finally, a few studies investigate the influence of the lateral variation of the surface stiffness to control the bacterial development [21].

In this context, the objective of this thesis was to prepare chemically nanopatterned surfaces displaying bioactive molecules towards bacterial and mammalian cells to control their development. Indeed, using nanopatterned surfaces is interesting since the extracellular matrix (ECM) is structured at the nanometer scale and consequently the presentation of the ligands reflects this pattern [1]. Moreover, chemical nanopatterns were rarely exposed to bacterial cells. On top of that, although ligands spaced at a distance under 70 nm showed an influence on mammalian cell adhesion and spreading [22], they were rarely gathered in a pattern at the nanometer scale. Then, as our surfaces need to influence both bacterial and mammalian cell development, we grafted both antimicrobial and bioadhesive peptides. This allows to meet the dual goal of providing antimicrobial surfaces while keeping cell friendly properties. The reason to use antimicrobial peptide is to avoid the side-effects related to antibiotics such as the emergence of multi-resistant bacteria [23]. The use of adhesive ligand, on its side, is required to control the adhesion and the development of stem cells. Our goal was thus to display nanometer-sized areas of bioactive molecules to bacteria and mammalian stem cells. Consequently, we developed nanopatterned lines of hydrophilic polymer brush grafted with different antimicrobial peptides and/or one adhesive ligand and that were distributed in a non-adhesive background. Then, we tested these surfaces towards *E. coli* used as a model of pathogen and stem cells from the apical papilla (SCAPs). In the view of these choices, the issues addressed in this thesis were:

- The fabrication of nanopatterned surfaces which display moieties active towards both bacterial and mammalian cells.
- The study of bacterial colonization and the bactericidal efficiency of the surfaces considering the nature of bioactive moieties grafted on the nanopatterns and the small topography produced by the patterning process.
- The influence of the geometry and the nature of the nanopatterns on the SCAP morphology, proliferation and differentiation.

The structure of this manuscript is organized as follows:

- Chapter 2 provides a state of the art of the concepts used in this PhD thesis. A first section is dedicated to the description, the synthesis, the modification and the patterning of polymer brushes. Then, the characterization techniques used during this project are described. Next, bioactive agents to control bacterial and cell behavior are examined. After that, the effect of surface topography, (bio)chemistry and rigidity on bacterial and mammalian cells are reviewed. Finally, some studies looking at discriminating the behaviors of bacterial and mammalian cells on modified surfaces, are presented.

- Chapter 3 explores the surface-initiated atom transfer radical polymerization (Si-ATRP) of four types of hydrophilic polymer brushes bearing functional groups allowing for a subsequent post-modification. The compositions of these brushes are systematically characterized. We finally explain the selection of the appropriate polymer brush to produce bioactive nanopatterns.

- Chapter 4 focuses on the fabrication of nanopatterned polymer brushes and their biofunctionalization. First, we optimized the grafting of bioactive molecules on the selected polymer brush. Then, we combined nanoimprint lithography (NIL) technique, Si-ATRP and post-modification of polymer brush to produce nanopatterned surfaces grafted with different bioactive peptides.

- Chapter 5 analyzes the bacterial behavior on the nanopatterned surfaces grafted with the different peptides. First, the antimicrobial activities in solution of the antibacterial peptides (selected to be grafted onto the brushes) were tested towards *E. coli*. Then, the bacterial colonization and bactericidal efficiency of the nanopatterned surfaces were explored. Finally, we exposed our arguments to select the most relevant nanopatterned surfaces to perform the subsequent assays with stem cells.

- Chapter 6 evaluates the effect of the selected nanopatterned surfaces on SCAP behaviors. More specifically, the cellular adhesion, morphology, proliferation and differentiation were investigated. This chapter highlights the effect of the patterns and the bioactive molecules on cell behaviors.

- Chapter 7 summarizes the main results obtained during this thesis and points out some further researches for the design of biomaterials sustaining

specific cell behaviors while preventing the first step of colonization by bacterial cells.

Chapter 2

State of the art

2.1 Polymer brushes as functional platforms

2.1.1 Definition of polymer brushes

A polymer brush is composed of an ensemble of polymer chains grafted by one end on a surface [24–28]. The spacing between the chains influences their overall conformation. When the distance between them is small, they adopt an extended conformation; however, when the distance is large enough, they tend to fold on themselves and show a mushroom conformation (Figure 2.1) [24, 26, 28].

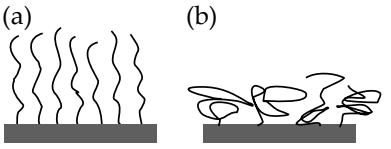

Figure 2.1: Schematic representation of polymer brushes immobilized onto a surface. (a) An extended conformation occurs when the distance between the chains is small (*i.e.* high grafting density) and (b) a mushroom conformation occurs when the distance is large (*i.e.* low grafting density).

2.1.2 Synthesis of polymer brushes on surfaces

Polymer brushes can be attached to solid surfaces by different means: they can either be physisorpted [25] or either grafted on surfaces [25, 26]. In this PhD thesis, we focused on covalently grafted polymer brushes as they offer the

advantage to be permanently attached to the surface [27]. Polymer brushes can be grafted on surfaces via two different approaches named "grafting to" and "grafting from" [25, 26].

The "grafting to" technique consists in the grafting of already polymerized chains bearing a functionalized end by which they are anchored to the surface (Figure 2.2 a) [25,26,28]. One main advantage of this technique is the opportunity to synthesize the polymer chains prior to their grafting and to give them a specific functionality or macromolecular characteristics such as the molar mass [25]. However, a lower grafting density of polymer chains is usually achieved since the chains tend to adopt a mushroom-like conformation during the grafting step [25, 26, 28].

The "grafting from" technique consists in the polymerization of polymer chains directly from the surface thanks to an initiator previously attached onto the surface (Figure 2.2 b) [26]. Grafting from approach allows a higher grafting density with polymer chains adopting an extended conformation [25, 26, 28]. Furthermore, a vast variety of monomers can be used. This allows for the synthesis of polymers with various functional groups on lateral chains that can further undergo post-polymerization modifications [29]. However, unlike grafting to, the grafting from technique only allows for the formation of synthetic polymer brushes.

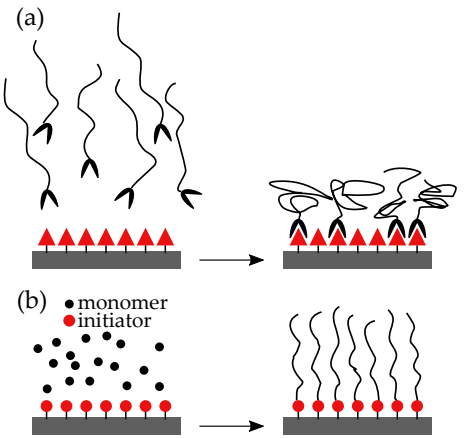

Figure 2.2: Schematic representation of polymer brushes immobilization onto a surface. (a) The "grafting to" technique consists in the grafting of already polymerized chains (black) on a functionalized (red) surface and (b) the "grafting from" technique consists in the polymerization of chains (black) via an initiator already grafted onto a surface (red).

Grafting from the surface can be performed via various polymerization reactions such as controlled radical polymerization (CRP), carbocationic polymerization, anionic polymerization, ring-opening metathesis polymerization (ROMP) or group transfer polymerization (GTP) [25]. CRP is very popular since it allows a better control over molar mass and polydispersity of the brushes [25]. This control is due to the way CRP works since an equilibrium is established between dormant and reactive species [30, 31]. Different CRP use different dormant chains: atom transfer radical polymerization (ATRP) relies on alkyl halides, reversible fragmentation chain transfer process (RAFT) uses thioesters and nitroxide mediated polymerization (NMP) exploits alkoxyamines [30].

Among CRP, ATRP is often used to produce surfaces interacting with biological systems due to its robust nature [32]. It is also advantageous to use ATRP polymerization because mild reaction conditions are required [29]. As mentioned previously, its principle relies on an equilibrium between active and dormant species which allows the control over the molar mass and polydispersity of the chains forming the brush [30, 32]. As shown in Figure 2.3, the dormant specie (R-X) reacts with the transition metal complex having a lower oxidation state (M_t^n-Y), with a rate of activation (k_{act}) to form the reactive product ($R^{\bullet}$) and the transition metal complex having a higher oxidation state (X-M_t^{n+1}-Y). The reactive product then polymerizes before being deactivated. The deactivation reaction consists in the reaction of the radical derivative with the transition metal complex having a higher oxidation state at a rate of k_{deact} (Figure 2.3) [32]. The overall rate of growth of the polymer chain depends on the balance between the rates of activation and deactivation and is called the propagation rate.

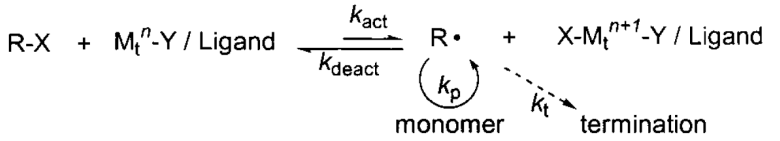

Figure 2.3: ATRP polymerization mechanism extracted from reference [30]. R-X is a dormant species, M_t^n-Y and X-M_t^{n+1}-Y is a transition metal complex at lower and higher oxidation states, respectively and $R^{\bullet}$ is a reactive species. The k_{act}, k_{deact}, k_p and k_t are the rates of activation, deactivation, propagation and termination, respectively.

The kinetics of ATRP polymerization depends on the nature of chemicals

used (*i.e.* the monomer, the initiator and the catalyst) and the environmental conditions (*i.e* the nature of the solvent as well as the temperature used) [29,33].

First, the monomers (*i.e.* the polymerizable units composing the polymer chains) (*e.g.* styrenes, (meth)acrylates, (meth)acrylamides, and acrylonitriles) stabilize the propagating radical [30,33]. Some monomers such as acrylic and methacrylic acids may also be used but the polymerization is much more difficult to control since these monomers can potentially poison the catalyst [34].

Second, the initiator (*i.e.* the molecule allowing the initiation of the polymerization reaction) choice affects the number of growing chains. Indeed, to obtain a large number of growing chains, the initiation needs to be fast and the termination negligible [30]. Moreover, to polymerize a brush with well-defined molar mass and polydispersity, the initiation rate must be much higher than the propagation rate [34]. For instance, Karanam *et al.* tested the polymerization of tert-butyl methacrylate (tBMA) with CuX/N,N,N,N",N"-pentamethyldiethylenetriamine catalytic system with various initiators. The use of ethyl 2-bromoisobutyrate initiator resulted in uncontrolled polymerization because of the slow initiation compared to the high propagation rate constant. However, they were able to control the polymerization of tBMA with p-toluenesulfonyl chloride or 2,2,2-trichloroethanol initiators. They thus evidenced that a judicious selection of the ATRP initiator allowed to synthesize a polymer brush with well-defined molar mass and polydispersity [35].

Third, the catalyst (*i.e.* the metal complex allowing the control over the propagation rate and that is complexed with a ligand helping for its solubilization), a critical compound to control the reaction equilibrium, needs to fulfill specific characteristics [30,33,34]. It has to show: at least two oxidation states separated by one electron, a good affinity towards the halogen used before and after oxidation [30,34] and a low affinity for alkyl radicals. Moreover it must not be a strong lewis acid to prevent the production of carbocations [34] and it has to form a stable complex with the ligand [30]. Apart from these intrinsic characteristics, the amount or specific affinity of the catalyst towards other compounds involved in the ATRP reaction might influence the growth rate of the polymer brush. For instance, Cheng *et al.* evidenced that the ratio of the metal complex at a lower oxidation state to the metal complex at a higher oxidation state influences the rate of ATRP polymerization of poly([2-(Methacryloyloxy)ethyl]trimethylammonium chloride). Indeed, the use of a higher ratio of Cu(I)/Cu(II) induces a rapid growth of the brush but with a

lower surface density and a higher polydipersity [36]. Moreover, the halogen bonded to the catalyst also influences the rate of ATRP polymerization as explained by Karanam *et al.* who synthesized block copolymer brushes of methyl methacrylate (MMA) and tBMA. The PMMA block was first grown in the presence of CuCl because the bond formed between the reactive specie and the chloride atom is more stable than the one formed with the bromide atom which may minimize terminaison reaction and allowed the formation of chlorinated PMMA macroinitiators. The P(tBMA) block was then synthesized with CuBr catalyst on this macroinitiator [37]. The amount of ligand to catalyst ratio is also important for the activation rate. Indeed, Nanda *et al.* measured the k_{act} of different alkyl bromides in presence of different ratio of CuBr to bipyridine with polar (acetonitrile) and less polar (acetonitrile/chlorobenzene (41.5/58.5) (w:w)) solvents. They observed maximal values of k_{act} for ratio of bipyridine/CuBr of 2/1 and 1/1 for polar and less polar solvents, respectively; regardless of the alkyl bromide used. Thus the proportion of ligand to copper ratio influenced the rate of activation of the dormant species [38].

Fourth, the solvent used to perform the ATRP polymerization needs to be carefully chosen in order to avoid side reactions such as chain transfer and interactions with the catalyst. Moreover, some solvents can accelerate the kinetics of polymerization [30,31,33,34]. For instance, Huang *et al.* showed that water accelerated the ATRP polymerization of poly(2-hydroxylethyl methacrylate) (P(HEMA)) [39]. Indeed the brush synthesized in presence of a (1:1 v:v) water/monomer mixture reached a thickness of 700 nm in 12 hours compared to its polymerization without water (*i.e.* only the pure monomer), which reached a thickness of 6 nm for the same polymerization time, at room temperature. On their side, Nanda *et al.* , which study was mentioned above, also explored the influence of solvent polarity on the k_{act} of ATRP polymerization. They measured the k_{act} of different ethyl 2-bromoisobutyrate in presence of different ratios of CuBr to bipyridine and compared the effect of three solvents: acetonitrile, acetonitrile/chlorobenzene (41.5/58.5) (w:w) and acetonitrile/water (44/56) (w:w). At the optimal bipyridine/copper ratio of 2/1, the k_{act} is the largest for the acetonitrile/water solvent and the smallest for the acetonitrile/chlorobenzene solvent. The polarity of the solvent thus influenced the polymerization rate [38].

Finally, the ATRP rate increases with the temperature but one must be careful to side reactions which also occur faster in such conditions [34].

2.1.3 Modification of polymer brushes

A wide variety of functions can be present on the polymer chains and allow the grafting of compounds by post-polymerization modifications. Consequently, an abundance of coupling reactions can be applied to the polymer chains bearing functional groups [40, 41]. Gunay *et al.* summarized eight types of reactions commonly used for the modification of polymers (Figure 2.4) [42].

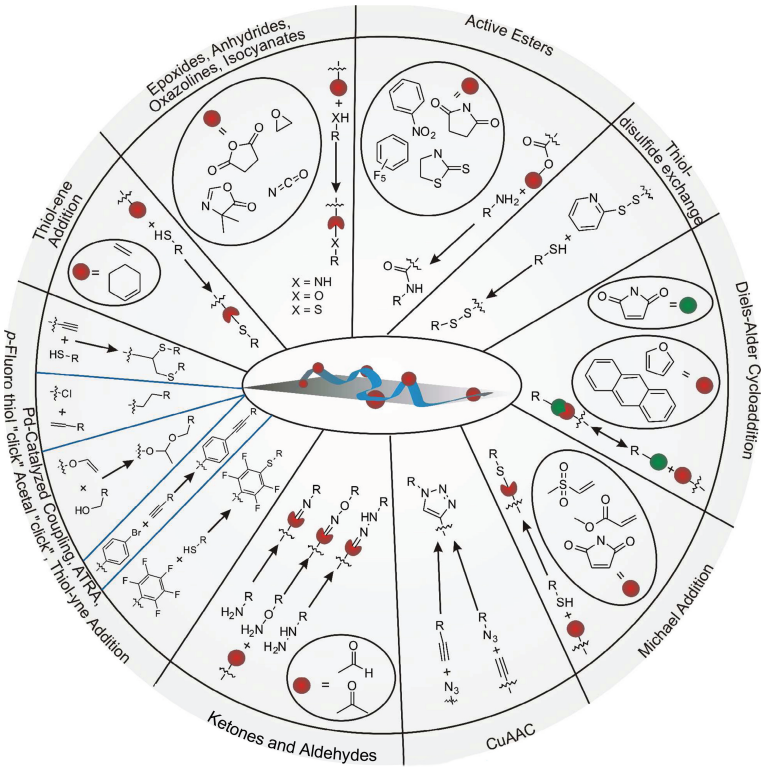

Figure 2.4: Post-polymerization modifications commonly used and classified by reaction type; image extracted from reference [42]. The red and green dots represent the chemical functions reacting in a specific reaction type.

- The thiol-ene addition reaction is the reaction between an alkene present on the polymer chain and a thiolated molecule. It is mediated by an alkyl radical formed thanks to thermal or photochemical initiation [42, 43] or can follow a Michael addition (explained later in this section) [43, 44]. Using a radical source for the modification can lead to side reactions such as intramolecular cyclization (*e.g.* vinyl groups present on polybutadiene

[42]) [42–44].

- Epoxide, anhydride, oxazoline, and isocyanate functions are tolerant to radical polymerization [42]. When they are available on the polymer chain, they can react with molecules bearing amine, alcohol or thiol [42]. However, polymer functionalized by epoxides are proned to crosslink with other unreacted epoxide groups [42]. Isocyanate groups can be modified with amines, alcohols and thiols but whereas the modification with amines and thiols is quick, the modification with alcohols needs a catalyst [42] or a large excess of alcohols [43].

- Active ester functional groups present on the polymer chain are usually modified with amines and can react in the presence of weaker nucleophiles such as alcohols [41–43, 45]. The most common active ester used is N-hydroxysuccinimide (NHS) which shows a good hydrolytic stability [42, 43]. The reaction of NHS ester with amine is widely used for tethering proteins [28]. Two monomers, N-acryloxysuccinimide and N-methacryloxysuccinimide, are commonly used to prepare polymers showing side-chains ended with NHS esters [42, 43]. Despite many advantages, active ester side-chains present on polymer chains can undergo side-reactions such as ring opening of the succinimide group [43].

- Thiol-disulfide exchange implies the exchange of a compound bearing a thiol group with a disulfide bond present in the polymer chain. This reaction is pH dependent [42,43]. The disulfide bond can be cleaved under redox stimulation if the grafted molecule needs to be released [42].

- Diels-Alder reaction is the cycloaddition of a diene on the grafted compound and a substituted alkene on the polymer chain [42]. It can be done in quantitative yield, is tolerant to many functional groups and is reversible at a temperature higher than the one of the bond formation [28, 42].

- Micheal type addition is the reaction of a polymer chain bearing acrylates, maleimides or vinyl sulfones with thiolated molecules [42]. Michael addition can thus be used to couple maleimides and thiols [41–43] but can also be performed with amines. However, Michael addition of thiols is one order of magnitude faster than amines at neutral pH [43]. Cysteine residue which contains a thiol functional group is widely used in Michael

addition which requires a pH range of 6.5-7.5 for the coupling with a maleimide derivative [41].

- The Huisgen 1,3-dipolar cycloaddition is the reaction between azides and alkynes, present either on the polymer chain or the molecule to be grafted. It can be carried out at mild conditions and in a regioselective fashion when Cu(I) salts are used as catalyst and form a triazole [41, 42]. This reaction is tolerant to many functional groups and can accept a wide range of conditions such as aqueous solvents and ambient temperature [43, 44]. However, removing the copper residues can be challenging [42].

- Ketones and aldehydes (present on the polymer chain) "can be modified by primary amines, alkoxyamines, and hydrazines to form imines, oximes, and hydrazones, respectively" [41–43].

- Other reactions such as Pd-catalyzed coupling, atom transfer radical addition, p-fluoro thiol "click", acetal "click", thiol-yne addition can be used to couple compounds on the polymer brushes [28, 41–43].

- A lot of crosslinking reagents can be used to modify the initial chemistry of brushes and thus allow for the grafting of a greater range of components [40, 46].

- Non-covalent post-polymerization modifications can also be used to modify polymer brushes. Among these modifications, we can mention hydrogen bonding, metal coordination, orthogonal side-chain-functionalized block copolymers, ionic interactions and hydrophobic interactions [44].

2.1.4 Patterning of polymer brushes

The patterning of polymer brushes on a solid surface is used to spatially display the functional compounds grafted on their side-chains. This type of patterning is called chemical patterning because only the chemical nature of the surface changes laterally depending on the nature of the polymers and compounds displayed. In the techniques described here, the desired patterns can be obtained by two approaches: either the initiator of polymerization is patterned allowing further polymerization from the surface or the polymer brush is selectively removed from selected parts of the surface using ultraviolet (UV) or electron exposure [24].

The first techniques described here are based on the sequential grafting of selected areas of the surface with different molecules among which lies the initiator required for the polymerization of the macromolecular chains from the surface. These techniques can be based on the use of a mold (Figure 2.5) or light/electron beams (Figure 2.6) or based on atomic force microscopy (Figure 2.7).

Micro-contact printing (μCP) uses a mold (Figure 2.5a) to produce micrometer size patterns [47]. A poly(dimethylsiloxane) (PDMS) stamp is dipped in "ink" and then brought into contact with the surface to transfer the ink molecules in a pre-determined pattern [22, 48–50]. This technique allows for the quick patterning of a large surface at low-cost [24, 48] but is subject to the transfer of potential defects of the mold and to distortion of the mold [24, 49]. A recent process allows the nano-contact printing with features reaching the nanometer scale [50].

NIL (Figure 2.5b) also uses a mold to create a pattern in a polymer film heated above its glass transition temperature [48, 49]. The nanopatterned polymer film can then be used to selectively mask a part of the surface which allows for the sequence grafting of different molecules [47]. This technique allows for the quick patterning of a large surface at low-cost [48].

The techniques explained hereafter are based on the emission of a beam of light or electrons, allowing the removal of parts of the polymer film masking the surface. Photolithography (Figure 2.6) is used to produce a pattern into a photoresist allowing the sequence grafting of different molecules [22,47]. Portions of a photosensitive polymer film spin-coated on a substrate are exposed through a mask to UV light. The exposed or non-exposed regions, depending on the nature of the resin, are then discarded in a developing solution, for positive and negative resins, respectively. This uncovers the underlying surface and permits the grafting of molecules on these open regions [22]. In this technique, the size of the patterned features is limited by the wavelength of the light [24].

Electron beam lithography (EBL) is based on the emission of an electron beam applied on selected regions of the surface; the exposed or non-exposed regions are then discarded in a developing solution, for positive and negative resins, respectively. This uncovers the underlying surface [22, 50]. Again, the uncovered regions are subsequently grafted by selected molecules. The polymer mask is then removed to functionalize the rest of the surface. EBL allows for a high resolution but is slower and shows lower throughput compared to stamping

techniques [24, 48].

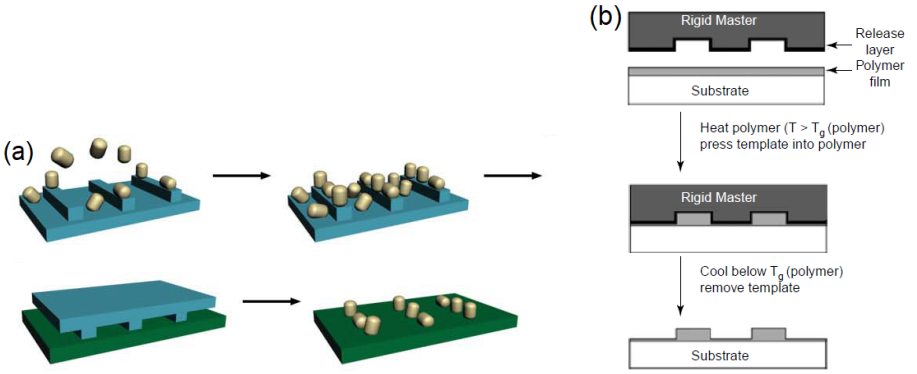

Figure 2.5: Fabrication of chemical patterns (*e.g.* patterning of a polymerization initiator) by (a) contact printing and (b) NIL. For the contact printing technique (a), the stamp is first inked with the molecules that need to be grafted. Then, the inked mold is applied on a surface. Finally, the molecules are transferred to the surface at the place of the contact between the protuberances of the inked stamp and the surface, to form the desired pattern. Image extracted from reference [48]. For the NIL technique (b), the rigid mold is first put into contact with the polymer film and the system is heated above the glass transition temperature of the polymer. Then, the system is cooled down below the glass transition temperature of the film and the mold is removed. Image extracted from reference [49].

Some patterning techniques use atomic force microscopy (AFM) (Figure 2.7). Dip-pen nanolithography (DPN) (Figure 2.7a) requires the use of an AFM probe loaded with molecules to deposit the "ink" on pre-determined regions of a surface [22, 24, 47, 48, 50, 51]. This technique is quite slow since each molecule has to be inked separately [47]. This technique can be used with small molecules or directly with polymers [50, 51]. Nanografting (Figure 2.7b) is also based on the use of an AFM probe. It involves the mechanical removal of a pregrafted self-assembled monolayer (SAM) or polymer layer followed by immediate grafting of molecules present in solution, at the tip of the probe [24, 48, 50, 51].

Chemical patterns can also be prepared by ablation or denaturation of a polymer brush already grafted on a given surface. The ablation of the polymer layer is performed by using a beam of light or electrons. For instance, photolithography allows the deactivation of grafted initiator molecules in selected areas. The remaining initiators are then subsequently used to growth polymer

chains through radical polymerization [24].

EBL can be used to remove a polymer brush grafted on a surface by direct exposure to the electron beam [51].

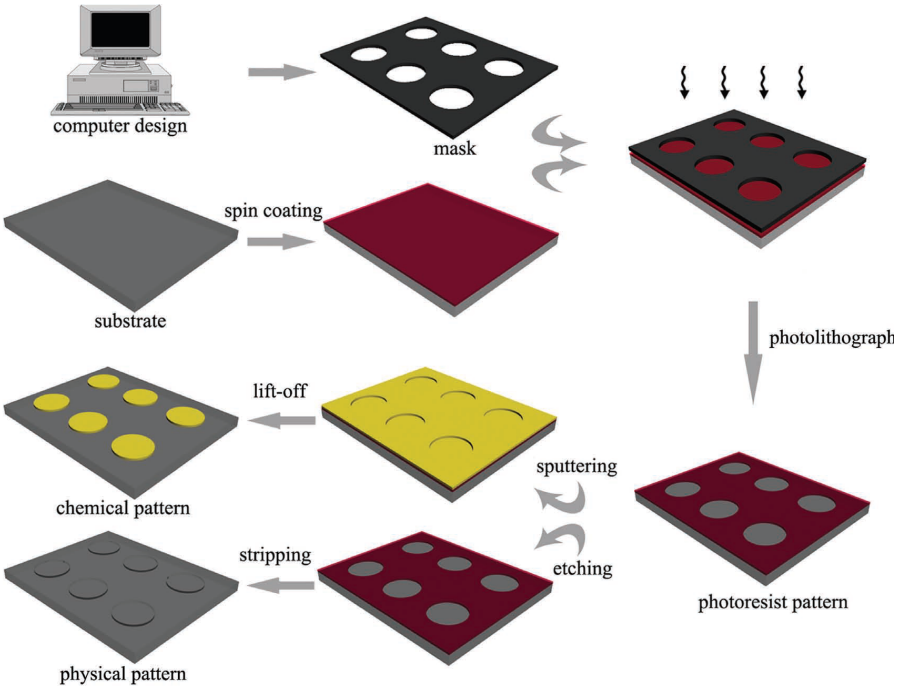

Figure 2.6: Photolithography technique. First, a spin-coated film is exposed to the UV light through a mask. The positive resin is developed and the exposed regions are removed. Then the patterned photoresist is used as a removable mask to induce chemical or topographical patterning. Image extracted from reference [22].

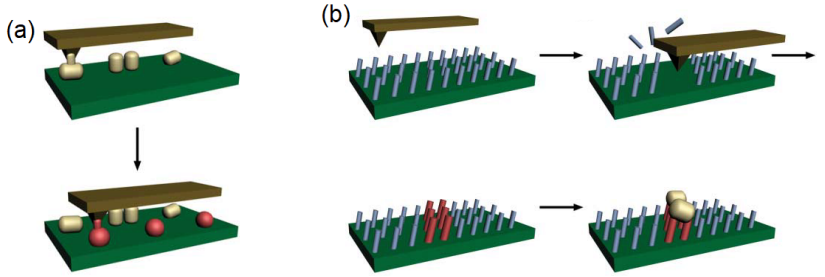

Figure 2.7: Fabrication of patterned surfaces based on SAMs or grafted polymer chains, using AFM-based technique. In the DPN technique (a), the selected molecules are deposited on a solid surface with an inked AFM probe used as a fountain pen. In the nanografting technique (b), an AFM probe is used as a stylus to scratch away grafted molecules and the open surface is immediately filled with another molecule. Finally, the patterned layer can be used as an anchoring layer to immobilize other molecules of interest. Images extracted from reference [48].

2.2 Surface characterization techniques

2.2.1 Ellipsometry

This technique is used to determine the thickness and optical constants of a thin film deposited on a given substrate. Its principle relies on the measurement of the change of light polarization after reflection on the analyzed surface. The polarized incident beam can be expressed by two components, one parallel (E_i^p) and one perpendicular (E_i^s) to the plane of incidence. The polarized reflected and transmitted beams can also be expressed in parallel (E_r^p and E_t^p) and perpendicular components (E_r^s and E_t^s). The complex reflection coefficients (r_{int}^p and r_{int}^s) define the polarization change between the incident beam light and the reflected beam light for the parallel and perpendicular components, respectively, at each interface and are defined by the equations:

$$r_{int}^p = \frac{E_r^p}{E_i^p} \tag{2.1}$$

$$r_{int}^s = \frac{E_r^s}{E_i^s} \tag{2.2}$$

The total reflection coefficients for parallel (r_{tot}^p) and perpendicular (r_{tot}^s) components, considering all interfaces present on the measured surface, are related

to the relative phase shift parameter Δ (with δ^p and δ^s being the phase shift in the parallel and the perpendicular components, respectively) and the relative amplitude attenuation parameter ψ by the equation:

$$\rho = \frac{r^p_{tot}}{r^s_{tot}} = \tan\psi \exp(i\Delta) \tag{2.3}$$

with

$$\Delta = \delta^p - \delta^s \tag{2.4}$$

and

$$\tan\psi = \frac{E^p_r}{E^s_r} \tag{2.5}$$

The ellipsometric data are represented as a Δ and ψ curve which is linked to the physical parameters of the system studied. These can be deduced from the curves obtained with the help of a computer algorithm [52].

2.2.2 Fourier transform infrared spectroscopy (FTIR)

This technique allows to determine the chemical functionalities present into a polymer brush. Indeed each functional group absorbs a given energy when exposed to a given wavelength. This energy corresponds to a vibrational transition but also to rotational energy states. To be detectable the vibration must induce a change in the dipole moment of the molecule. The measured absorption spectrum displays the variation of the absorbed light as a function of the wavelength used [46, 53].

2.2.3 Scanning electron microscopy (SEM)

SEM technique is based on the use of a focused electron beam which is bombarded on the sample surface and leads to elastic and inelastic interactions with the exposed matter. Elastic interactions comprise the production of backscattered electrons, while inelastic interactions produce the emission of secondary electrons, x-rays and Auger electrons. The emission of secondary electrons is used to produce an image of the sample morphology [46, 54].

2.2.4 AFM

The principle of the AFM technique relies on a probe scanning a surface while a laser is reflected on the cantilever bearing the probe. This laser is directed on a photodiode in order to detect the movements of the probe (Figure 2.8). Three modes of scanning are mainly used: the contact mode, the tapping mode and the non-contact mode [46, 55].

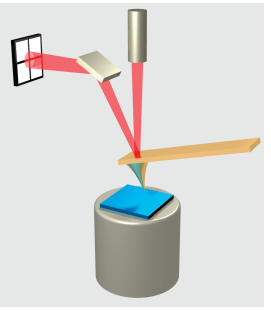

Figure 2.8: Principle of the AFM technique. The AFM probe scans the surface and the movement of the probe is monitored by a laser beam reflected on a cantilever and ending its path in a dielectric diode. Image extracted from reference [55].

Modified probes can also be used to image or detect particular features on the surface. For instance, Alsteen *et al.* reviewed the use of AFM probes grafted with molecules specifically selected to interact with given surfaces. Such experiment allows to measure specific interactions between the probe and the surface and consequently to map the chemistry of the surface. For example, they pointed out that AFM probes, functionalized with antibody recognizing membrane cytochrome of *Shewanella oneidensis*, allowed to establish that these adhesins were grouped in nanodomains in the bacterial membrane [56]. The probe can also be modified with a bacterial or fungal cell which interacts with coated surfaces. For example, Herman *et al.* immobilized a *S. epidermidis* bacterium on an AFM probe and scanned a fibrinogen coated surface to measure the force driving the adhesion of the bacterium [57]. Similarly, Beaussart *et al.* immobilized *Lactococcus plantarum* on the probe and scanned hydrophobic and lectin-coated surfaces to measure the different forces driving the adhesion of the bacterium [58]. On their side, Alsteens *et al.* immobilized a *Saccharomyces cerevisae* cell, expressing Als5p adhesion protein from *Candida albicans*, on

the probe. They measured the forces between the adhesion peptide present on the cell and surfaces coated with hydrophobic, hydrophilic and fibronectin coatings. They quantified the forces present in the adhesion of Als5p protein to the surfaces [59]. Finally, the probe can be modified with a bacterium to investigate the interaction with another bacterium immobilized on a surface. For instance, Beaussart *et al.* immobilized *S. epidermidis* on the probe and measured the interaction forces occuring with *Candida albicans* immobilized on a hydrophobic surface [60].

2.2.5 X-ray photoelectron spectroscopy (XPS)

This technique is used to determine the chemical composition of the top several nanometers of a surface. The X-ray beam that passes through the analyzed sample excites electrons which are ejected with a kinetic energy (E_k) equals to:

$$E_k = h\nu - E_B - \phi. \tag{2.6}$$

with hν the energy of incident photons, E_B the binding energy and ϕ the work function of the analyzer. The electrons are then sorted by kinetic energy and counted. Finally, the results are displayed as the count per second versus the binding energy. Each binding energy position thus corresponds to an atom in a particular chemical state [46, 61].

2.2.6 Epifluorescence microscopy

Fluorescence emission occurs when an electron in an excited state returns to its initial state by emitting a photon. An epifluorescence microscope consists in four elements: a lamp to excite the fluorescent compound, a filter to separate excitation and emission lights, an objective and a fluorescent light detector (Figure 2.9). This technique allows the imaging of fluorescent compounds grafted on the sample surface [62].

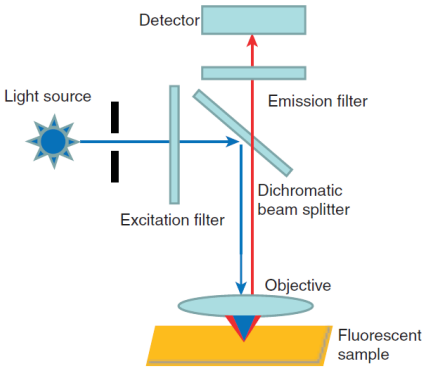

Figure 2.9: Principle of epifluorescence microscopy. The excitation light is emitted by a light source and its interaction with the sample results in an emitted light ending its path in a detector. The excitation and emission lights are separated by a dichroic beam splitter. Image extracted from reference [62].

2.3 Bioactive agents to control cell behaviors

2.3.1 Active agents towards bacterial and mammalian cells

2.3.1.1 Different types of bioactive agents

Bioactive agents have a specific action towards bacteria or mammalian cells depending on their nature and mode of action. First, we describe different types of antimicrobial agents then we focus on bioactive agents relevant for mammalian cells.

Antimicrobial agents

Antimicrobial agents can be synthetic such as quaternary ammonium molecules or polymers, polyamines [63], synthetic peptides [46, 63, 64] and antibiotics [65] or metal ions [66] or even derived from natural components such as for polysaccharides, enzymes, peptides [46, 63, 64], quorum quenching molecules and essential oils [64].

- Polymers bearing quaternary ammonium groups can interact with the negatively charged membrane of bacteria [32, 63, 67, 68]. However, the charge density of the polymer chains needs to be sufficient to disrupt

the membrane which then releases intracellular components [32, 63]. For example, Schofield *et al.* prepared surfaces covered with poly(4-vinyl pyridine) quaterized with bromobutane, to get antimicrobial activity [69]. Polyelectrolytes bearing a sufficient density of positive charges are also able to kill bacteria upon contact [70, 71]. Huang *et al.* synthesized brushes of poly((trimethylamino)ethyl methacrylate chloride) by ATRP on gold surfaces and investigated the bactericidal properties of the resulting surfaces. They evidenced the killing efficiency of these polymer layers against *E. coli*, *S. epidermidis* and *Stenotrophomonas maltophilia*. Moreover, the surfaces were successfully regenerated by washing with an electrolyte solution allowing the detachment of bacterial debris from the surface [70].

- Metals and metal oxide derivatives such as silver, gold, zinc oxide, silica, titanium dioxide, alumina, iron oxide and copper are known to show antibacterial properties [66,68]. For instance, Pollini *et al.* have deposited silver nanoparticles onto a catheter surface using a photodeposition process. They showed that this coating induced long-lasting antimicrobial properties against *E. coli* [72]. Cheng *et al.* also introduced silver nanoparticles into titanium oxide nanotubes, immobilized on the surface, by soaking them in a $AgNO_3$ solution. They tested the nanotubes against methicillin-resistant *S. aureus* for its antibacterial activity and bio-integration. The realease of Ag nanoparticles helped to prevent the colonization for 30 days while maintaining osseointegration properties [73].

- Some cationic polysaccharides such as chitosan are antimicrobial [46,63,68]. Cationic polysaccharides might act via different modes of action: they can act as surfactants, which modify physical characteristics of abiotic and biotic surfaces, or as signaling molecules, which modify the bacterial response, or they can block receptors of the bacterial cell [74]. For example, Shi *et al.* used titanium surfaces grafted with chitosan chains modified with (Arg-Gly-Asp) RGD peptides to decrease the adhesion of pathogenic *S. aureus* and *S. epidermidis* while promoting osteoblast attachment [75].

- Enzymes such as proteinase K, trypsin, subtilisin, lysozyme and so on are antimicrobial enzymes commonly used to prevent bacterial adhesion onto surfaces [63, 68]. They are non-toxic, anti-fouling and show different modes of action [64]. Indeed, they can prevent adhesion of bacteria by

damaging glycoproteins used by bacteria to attach to the surface or by killing bacteria; they can also catalyze the production of biocidal products using precursors present into the environment [76] or impair communication between bacterial cells [77]. For instance, Yu *et al.* produced nanopatterned surfaces bearing both lysozyme molecules to kill bacteria upon contact and poly(N-isopropylacrylamide) (PNIPAAm) brush to prevent bacterial colonization. To elaborate these surfaces, they first grafted an ATRP initiator on a substrate, removed selectively ATRP initiator via interferometric lithography and finally grew the PNIPAAm brush. The lysosyme molecules are adsorbed onto the remaining surface. The thermoresponsive properties of PNIPAAm allowed to switch from bactericidal at 37°C, by exposing the enzyme molecules, to repellent at 25°C (Figure 2.10). This method limits the accumulation of debris on the surface [78].

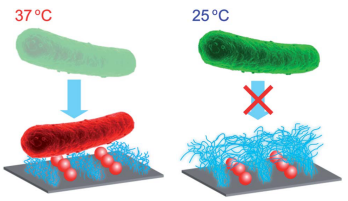

Figure 2.10: The surface switched from bactericidal at 37°C by exposing the adsorbed lysozyme molecules to anti-fouling when the PNIPAAm brush adopted an extended conformation at 25°C. Image extracted from reference [78].

- Antimicrobial peptides (AMPs) such as magainin I, polymyxin B, defensins, apoprotinin, nisin [63] are interesting candidates to produce antimicrobial coatings. Their efficiency is related to their mode of action. We will provide a detailed description of the activity of AMPs later in this section.

- Antibiotics are widely used as antimicrobial compounds but bacteria tend to develop resistance mechanisms in their presence. As can be seen in Figure 2.11, the antibiotic resistance outbreak is happening shortly after the commercialization of a new drug. Now, some resistant strains can be found for nearly all antibiotics [11]. At least four resistance mechanisms are known: alteration of the antibiotic via the use of enzymes, alteration of the target by bacteria by reprogramming or camouflaging,

drug efflux or reduced permeability of the cell wall [65, 79]. In spite of this drawback, antibiotics are often used to fabricate antibacterial surfaces. Some experiments showed the efficacy of antibiotics when resistance does not occur. For example, Kohnen *et al.* immersed a catheter in a solution containing a combination of antibiotics (rifampin and sparfloxacin). They showed that the slow release of antibiotics from the catheter surface reduced the colonization by *S. epidermidis* for at least one year [80].

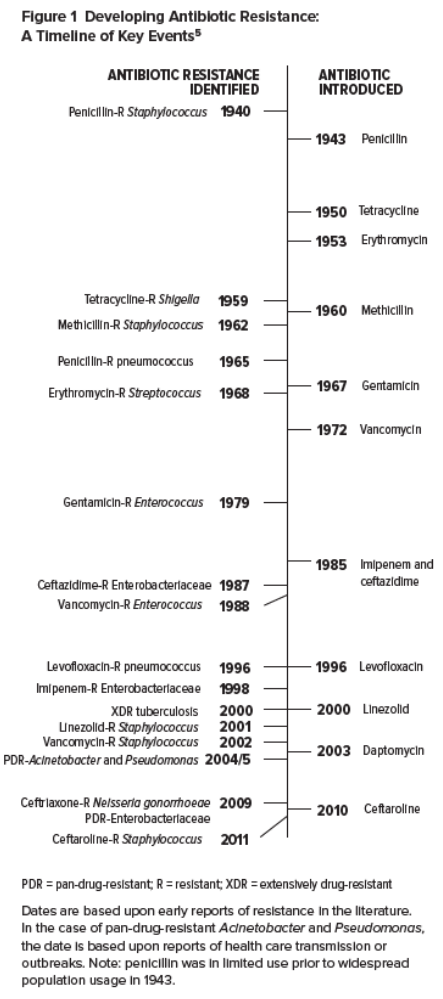

Figure 2.11: The outbreak of resistance to antibiotics with time (left) after their introduction for the treatment of infections (right). Image extracted from reference [11].

- Quorum quenching sensing molecules are molecules capable of competing with autoinducers produced by bacteria in order to interfere with their communication mechanism [64, 68]. These competing molecules are classified in three main groups: N-acyl homoserine lactone analogs, 2 (5H)-furanones and other compounds not structurally related to N-acyl homoserine lactones [64].

- Essential oils are produced by plants. Their mode of action is unclear but it seems that their antibactericidal properties are based on their hydrophobicity. They show a broad antimicrobial spectrum. However, they have a limited stability with temperature or with UV exposure; some can be toxic. Moreover, upon exposure one can show allergic reaction nausea, dizziness, headache or lightheadedness [64].

Agents active towards mammalian cells

Various derivatives such as polysaccharides, proteins present in the ECM or peptides extracted from these ECM proteins, growth factors [46] or synthetic factors develop specific interactions with mammalian cells through specific receptors.

- Polysaccharides such as heparin were immobilized on surfaces to develop hemocompatible devices [46].

- Proteins from the extracellular matrix such as collagen, gelatin, elastin, fibrin, fibronectin and so on were grafted on surfaces to enhance cell adhesion and proliferation [46, 81]. Small sequences can be extracted from these ECM proteins. Among those sequences, the most known peptides used to trigger cellular behavior are the ones containing the RGD sequence. RGD is indeed the most known integrin binding motif [82]. For example, Lei *et al.* hydrolyzed and oxidized polyethylene terephthalate (PET) surfaces to produce carboxylic groups. They then immobilized RGDS and SVVYGLR or YIGSR moieties on PET via 1-ethyl-3-(3-dimethylaminopropyl) carbodiimide (EDC)/N-hydroxysuccinimide (NHS) coupling reaction. The presentation of RGDS allowed the enhancement of adhesion while SVVYGLR or YIGSR enhanced the spreading and migration. The co-presentation of the RGDS and SVVYGLR peptides induced endothelial cell adhesion, spreading and migration. This surface biofunctionalization thus has potential application to develop endothelialization

of vascular prostheses [83]. On their side, Rowley *et al.* used alginate hydrogels modified with RGD via carbodiimide chemistry and regulated myoblast proliferation and differentiation by varying the amount of RGD grafted [84]. The other peptide sequences available to trigger specific cellular behavior includes KGD, NGR, KQAGDV and LDV [81, 85, 86].

- Other approaches such as the ones enhancing the phagocytosis by macrophages or the response of dendritic cells thanks to leaching compounds are also used to induce cellular responses towards bacteria [5].

- Growth factors are used to trigger differentiation in specific lineages. For example, vascular endothelial growth factors can be used to initiate endothelialization [46]. On their side, Ren *et al.* grafted fibronectin (FN) and recombinant human bone morphogenetic proteins (rhBMP-2) on poly(oligo(ethylene glycol)methacrylate) P(OEGMA) brush. It was shown that these surfaces promoted the differentiation of osteoblast cells [87]. Zouani *et al.* also used PET grafted with BMP-2 to boost the differentiation of osteoblast precursors [88].

- Synthetic compounds are also used to induce specific cell responses. For example, Wang *et al.* loaded nanoparticles composed of poly(ethylene glycol)-poly(lactic acid) with TNP-470, an analog of fumagillin which displays inhibitory effect on angiogenesis, to target blood vessels forming nearby tumorous sites with the aim of hindering tumor expansion [89].

2.3.1.2 RGD peptide

The use of recognition motifs instead of a whole protein is advantageous for the handling process. Indeed, proteins need to be isolated and purified, they are subject to proteolytic degradation, it is difficult to control their orientation on a surface and their adsorption might denature them [85].

However, the use of short analog peptides avoids such drawbacks. Indeed, they present a higher stability towards heat treatment and pH-variation and they can be packed with a higher density [85]. Among those peptides lie the derivatives of the RGD sequence (Figure 2.12) [85]. This sequence is often used to help cell adhesion via cell integrin receptors and was identified from numerous ECM proteins such as vitronectin, fibronectin and collagen [81, 85].

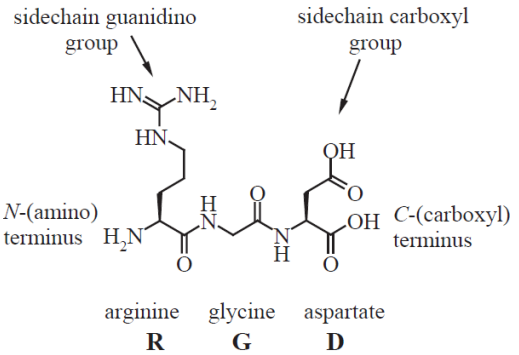

Figure 2.12: RGD sequence and molecular formula. Image extracted from reference [85].

The RGD sequence, taken out of the context of the protein, loses its affinity and specificity [85]. To retain the activity of this RGD sequence, derivatives must be produced. These derivatives either imply blocking the C-terminal end locked or adding other amino acids surrounding the RGD sequence to copy the natural sequences found in the natural proteins [81, 85]; some surrounding amino acids might however silence the activity of the RGD sequence [81]. The amino acids added at the C-terminal end are more significant for integrin binding than the one added at the N-terminal end [81]. Apart from the activity, the selectivity of the RGD derivatives also depends on the added amino acids [85]. Furthermore, the spatial organization of the peptide (*i.e.* linear or cyclic) controls its binding affinity towards a particular integrin. This incites the researchers to carefully select cyclic or linear RGD peptide derivatives [1, 81, 85].

2.3.1.3 AMPs

AMPs are produced by living organisms to protect themselves against micro-organisms [6, 64, 77]. The specificity of AMPs towards bacteria is due to the difference in composition and topology of bacterial membranes compared to mammalian cell ones, even thought cytotoxic effects can sometimes occur [6, 77]. AMPs are generally short cationic peptides (*i.e.* 10-25 amino acids) [6] which adopt an amphipathic structure [6, 23, 64, 77, 90]. Apart from their common characteristics, they can be classified into four classes: linear helical peptides, peptides enriched with a given amino acid, peptides with one disulfide bridge

and peptides with two or more disulfide bridges [64].

AMPs act mainly by disrupting the phospholipid membrane of bacteria [23, 64, 90]. Indeed cationic AMPs are first adsorbed on the bacterial membrane by electrostatic interactions; their clustering then induces the damaging of the membrane [6, 23, 77]. Depending on the AMP, the membrane disruption occurs according to different mechanisms (Figure 2.13) named barrel-stave, carpet-like [20, 64, 77] or toroidal-pore [20, 77]. The barrel-stave mechanism is based on the formation of a transmembrane pore resulting from the embedding of a few peptide molecules which strongly interact with each other [64]. The hydrophobic region of the peptide molecules is oriented towards the lipid bilayer whereas the hydrophilic region is oriented towards the interior of the pore [20, 77, 91]. This type of mechanism is found for alamethicin, for instance, [91] and leads to the leakage of intracellular components in the surrounding medium [77, 91]. The carpet-like model needs a larger amount of peptide molecules [64]. It induces the solubilization of the membrane by a detergent-like action [20, 64, 91, 92] which may lead to micellization of the bacterial membrane [77, 91]. In the toroidal-pore model, the peptides insert into the membrane to form clusters [6, 77] and induce the bending of the membrane so that the hydrophilic end of the lipids as well as the hydrophilic part of the peptides are turned towards the inner part of the formed pore [20, 91]. This leads to a leakage of intracellular ions [6, 77]. The peptides may then cross the membrane to reach their intracellular target [6]. Indeed, not all AMPs use the membrane disruption mechanism to exert their antimicrobial potential [23, 64, 77, 90]. Some might act on intracellular targets preventing the correct activity of the bacterium [23, 64, 90]. Consequently, they might alter cytoplasm membrane septum formation or inhibit the synthesis of proteins, cell wall components or nucleic acids [23, 77, 90].

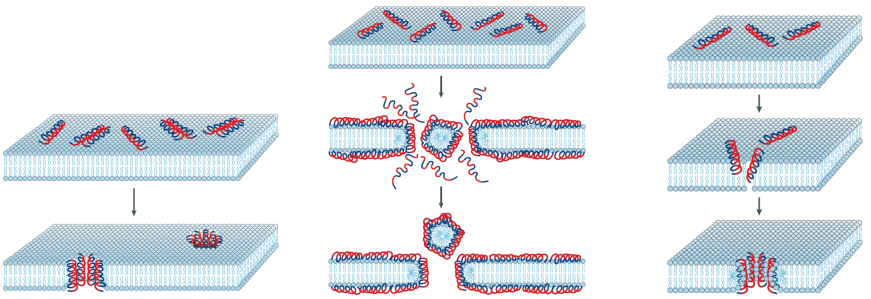

(a) Barrel-stave model. **(b)** Carpet-like model. **(c)** Toroidal-pore model.

Figure 2.13: Mechanisms of membrane permeabilization by AMPs. In the barrel-stave model (a), the hydrophobic region (blue) of the peptide molecules is oriented towards the lipid bilayer while the hydrophilic region (red) is oriented towards the inner part of the formed pore. In the carpet-like model (b), the peptide molecules induce the micellization of the membrane. In the toroïdal-pore model (c), the peptide molecules induce the bending of the lipid membrane. The hydrophilic part (red) of the peptides and the hydrophylic end of the lipid molecules (circles) are turned towards the inner part of the formed pore. Image extracted from reference [91].

The advantages of AMPs compared to other antimicrobial compounds are numerous. Many of them have a broad-spectrum activity and rapid killing kinetics and they are not known to induce microorganism resistance [6,64,77,90]; moreover, they act at low concentration [6] and, in some cases, show anti-inflammatory activity [64]. However, AMPs also show disadvantages. They might induce local toxicity, hemolytic activity, be sensitive to proteolysis, pH and high salt concentration. Moreover, they can induce allergy after a repeated exposure and their production cost is quite high [23, 64, 77]. Some *de novo* AMPs (*i.e.* engineered AMPs) have been considered to avoid the disadvantages of natural AMPs [6, 23, 77]. For example, Lim *et al.* immobilized arginine-tryptophan-rich peptides on PDMS surfaces pre-modified with polyethylene glycol (PEG). They evidenced the bactericidal properties of these surfaces towards *E. coli*, *S. aureus* and *P. aeruginosa* bacteria without cytotoxic effects against erythrocyte cells [93]. The development of a potential resistance of bacteria towards AMPs is rare compared to antibiotics [23]. Indeed, the resistance to antibiotics is due to their mechanism of action [94] which differs from the one of AMPs. The resistance to AMPs by genetic mutations is thus less likely [23,90]. As a consequence, bacteria have to coordinate different countermeasures

to defend themselves against AMPs [23]. These defense mechanisms depend on the bacterial strain, are energy demanding for bacteria and are activated only when required [77]. For example, some bacteria modify their membrane composition leading to weaker interactions with AMPs [94]. Others can also entrap AMP molecules by secreting proteins [23,77,94], degrade AMP molecules with the help of peptidases and proteases or actively extrude them [94]. This leads, for some gram-positive bacteria (*e.g. S. aureus* and *S. epidermidis*), to the production of AMP sensors able to regulate gene expression when bacteria come into contact with AMPs [6].

In this PhD thesis, we focused on two antimicrobial peptides: magainin I and LL37. Magainin I is a 23-amino acid peptide secreted on the skin of the African frog *Xenopus laevis* [95]. Magainin I peptide has a net charge of +4 at physiological pH and adopts an α-helix conformation [95]. Magainin I peptide has multiple modes of action [90,95]. However, it interacts mainly with membranes by the toroidal-pore model [91,95,96].

The LL37 peptide is the only human peptide in the family of the cathelicidin-derived AMPs [97]. Cathelicidins form a distinct class of proteins which act as precursor molecules for the release of antimicrobial peptides and are present in the innate immune system of mammals [97]. This peptide is located in the C-terminal region of the cathelicidin protein hCAP18 (Figure 2.14) and can be released by proteolytic cleavage to exert its antimicrobial effect. It is a 37-amino acid peptide which does not contain any cysteine residue. LL37 is a multifunctional peptide playing different roles in the living organism. It shows antimicrobial properties against various pathogens such as bacteria, fungi and virus [97,98]. LL37 peptide also acts as an alarmin agent. Indeed, it is secreted by leukocytes, epithelial cells and neutrophils (its precursor is located in the granules) and released in inflamed or infection sites. It also has a chemotaxis function and chemoattracts T-cell leukocytes, mononuclear cells, neutrophils and dendritic cells; it promotes wound healing as a growth factor for epithelial cells [97,98]. Once the cells are recruited to the site of infection, LL37 is capable of modulating their secretions [98]. LL37 peptide intervenes in apoptosis and promotes angiogenesis during and after the infection [97,98].

LL37 peptide has a net charge of +6 at physiological pH and adopts an α-helix conformation. As can be seen in the Figure 2.15a, this peptide has an amphipathic structure [97–99]. The α-helix of LL37 peptide is divided in three parts (Figure 2.15b): the N-terminal helix, the C-terminal helix and the

C-terminal tail [98]. The helixes are separated by a bend. The N-terminal helix is involved in chemotaxis, peptide oligomerization, proteolytic resistance and hemolytic activity. The C-terminal helix is involved in the antimicrobial, anticancer and antiviral properties [98]. LL37 peptide acts on the bacterial membrane according to the toroidal-pore model to exert their antimicrobial activity [91, 98, 100].

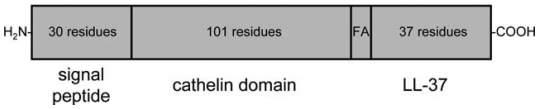

Figure 2.14: Cathelicidin hCAP18 representation. Image extracted from reference [97].

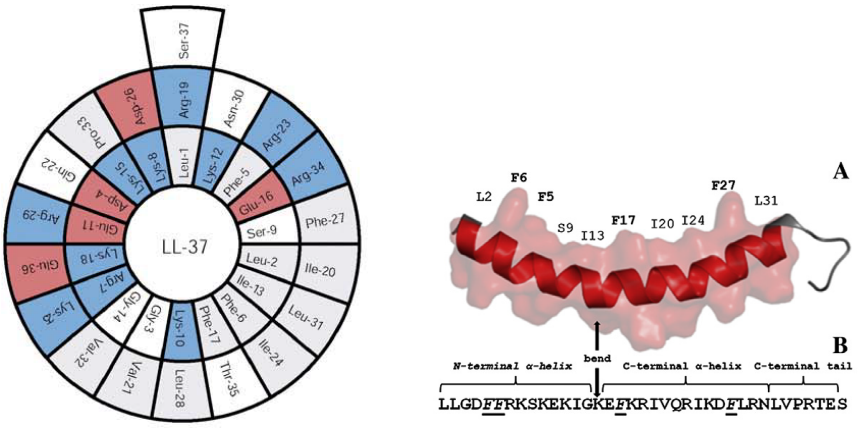

(a) Helical wheel projection. **(b)** LL37 α-helix structure.

Figure 2.15: Representations of the structure of LL37 peptide. Helical wheel projection (a) of LL37 peptide (image extracted from reference [97]). The blue residues are positively charged, the red ones negatively charged, the white ones are polar and the gray ones are hydrophobic. LL37 α-helix structure (b) (image extracted from reference [98]). This structure is divided in three parts: the N-terminal helix, the C-terminal helix and the C-terminal tail.

2.3.2 Grafted vs. non-grafted agents: advantages and limitations of both techniques

There are two methods to obtain antimicrobial killing surfaces: incorporation or adsorption of antimicrobial agents in the material from which they are

progressively released [16, 46, 67, 77, 101] and covalent linking of antimicrobial agents [16, 46, 67, 101, 102].

Different architectures are available to produce surface either releasing or covalently linking antimicrobial agents. Salwiczek *et al.* interestingly reviewed the different architectures of non-fouling polymer coatings incorporating AMPs [20]. The design of low-fouling polymeric films bearing antimicrobial agents can be based on multilayer, icing, bottle brush and castle architectures (Figure 2.16) [20]. The multilayer architecture involves the layer-by-layer (LbL) deposition of both polymers and AMPs (or another antimicrobial compound) which are later released in the environment. This method is versatile but not adapted for long term applications since such coatings are not stable [20]. Moreover, it can only be used for charged molecules (*e.g.* highly charged and water-soluble AMPs) [76, 77]. The icing architecture is obtained by grafting the AMPs on the terminal functional groups of a polymer brush. This architecture allows to interfere with the early stage of biofilm formation [20]. The bottle brush architecture is obtained by grafting AMPs throughout the whole polymer brush thickness, via the functional groups located on the side-chains available. The amount of AMPs grafted can be controlled and does not shield the low-fouling background [20]. Finally, the castle architecture is obtained by first grafting the AMP molecules onto the surface then the non-fouling polymer chains onto this AMP layer [20].

Now, we focus on released-based system characteristics. The first systems based on the release of antimicrobial agents were impregnated with antibiotics or silver but a lot of compounds can be used. Clouthier *et al.* summarized the antimicrobial agents used in released-based systems [16]. These released-based surfaces show disadvantages such as a limited reservoir which leads to a short term use, cytotoxicity and inflammatory responses and resistance of bacterial strains. These disadvantages are due to the progressive decrease in the amount of active molecules released in the environment [16, 77]. Moreover, the electrostatic interactions between peptides and the material may denature the peptides and consequently affect their activity [64]. To limit these disadvantages, some parameters of released-based systems need to be modified. The control of release kinetics, for example, could be based on stimuli-responsive coatings. In fact, the best responsive surfaces would be surfaces releasing agents only when they are surrounded by bacteria [16]. The long-term stability needs to be addressed more systematically to improve the durability of these antibacterial

coatings [16]. Finally, the use of multifunctional surfaces could help face some of the problems encountered with release-based systems [16].

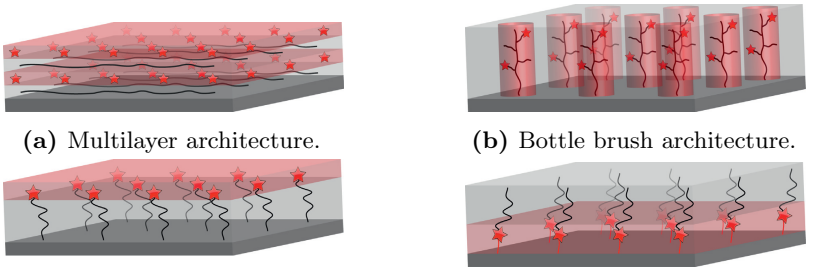

(a) Multilayer architecture. **(b)** Bottle brush architecture.

(c) Icing architecture. **(d)** Castle architecture.

Figure 2.16: Different structures of non-fouling polymer coatings incorporating AMPs (or another antimicrobial agent). The red stars represent the AMP molecules and the black lines represent the non-fouling polymer chains. The multilayer architecture (a) is the LbL deposition of polymers and antimicrobial compounds. The bottle brush architecture (b) consists in the grafting of the antimicrobial compounds on the polymer side-chains throughout the whole thickness of the polymer brush. The icing architecture (c) consists in grafting the compounds on the terminal functional groups of the polymer brush. The castle architecture (d) consists in grafting first the compounds and then the polymer chains. Image extracted from reference [20].

Surface multifunctionality can be addressed in three different ways: multi-release, multi-approach or multi-property. Multi-release is based on the co-release of multiple antibacterial compounds. It allows a reduced bacterial resistance and possibly a synergistic antibacterial action [16]. Multi-approach consists in combining release of an antimicrobial agent with a surface showing contact killing and/or anti-adhesive properties [16]. For example, Wang *et al.* prepared coatings showing both anti-fouling and release properties by electrostatically depositing on poly(L-lysine) primed silicon substrate microgels of anti-fouling poly(ethylene glyol-*co*-acrylic acid) incorporating L5 antimicrobial peptide molecules. They evidenced that these layers reduce significantly the colonization of the surface by *S. epidermidis*, for 10 hours [103]. Multi-property consists in adding supplementary properties to the release-based system of antimicrobial. For example, the biocompatibility is an important factor needed for the *in vivo* implantation of materials [16].

Antimicrobial agents can be covalently grafted by different techniques: grafting to, grafting from or can be formed during the fabrication of the

substrate [63]. Here, we focus on the grafting of antimicrobial agents on polymer chains. The chemical reactions used to perform chemical grafting on the polymer chains are described in the section 2.1.3. The covalent immobilization of AMPs is recommended for medical applications [101] to avoid any potential cytotoxicity or hemolytic activity [64]. The grafting of AMPs on a surface such as an implant allows to use a lower amount of AMPs compared to systemic administration and to spatially regulate the activity of the surface [20]; moreover, according to this approach, AMP molecules are linked by a more stable bond, have an extended half-life, are less prone to metabolization and show long-term activity [6, 46, 77]. However, the resulting contact killing surfaces are rapidly contaminated by bacterial debris [16]. Moreover, because of their contact-based antimicrobial properties, they require to be defect-free [16]. Besides, the immobilization of AMP molecules must be carefully thought as highlighted by Bagheri *et al.* who demonstrated that the mode of action of the AMPs must be taken into account before the immobilization of the molecules onto the surface. They notably immobilized cationic peptides acting on the membrane (*i.e.* pore forming peptides) or on internal components (*i.e.* peptides targeting the nucleic acids) of bacteria. When immobilized, the peptide targeting intracellular components was inactive [104]. Additionaly, the bioactivity of the molecules might change after immobilization [6, 46, 77]. There are several factors influencing the activity of covalently grafted molecules such as the nature of the polymer brush to be grafted, the number of functional groups available for grafting [46], the spacer length and flexibility [6, 46, 77], the surface concentration of active compounds and the peptide orientation [6, 77]. However, the spacer length is more critical than the concentration to influence the activity of immobilized AMPs [77, 101]. The orientation of the immobilized molecules is also important to get active coatings [20]. Indeed, in the study from Bagheri *et al.* mentioned above, they showed that the melittin peptide was less active when grafted by its N-terminal end compared to its C-terminal end [104]. On their side, Gabriel *et al.* grafted LL37 onto a SAM in a random or oriented manner with ou without linker. They concluded that the use of a PEG spacer and a N-terminal immobilization are both necessary to keep the antimicrobial properties of the peptide [105]. Cao *et al.* who grafted pilus antibody on silicon wafer surfaces via PEG and jeffamine spacers (polyether diamines based predominantly on a poly(ethylene oxide) backbone) of different lengths, pointed out that the length of the spacer has a strong influence on the spacer coil conformation, and thus the unbinding

force. Moreover the conformaton of the spacer can hide some active binding sites [106].

2.4 Bacterial behavior on surfaces

2.4.1 Principles of surface colonization by bacteria

2.4.1.1 The role of biofilm

The biofilm is a high density population of bacteria surrounded by a three-dimensional highly hydrated matrix sticking on a surface [6, 107]. This matrix is produced by bacteria, represents 50-90 % of the biofilm organic matter and adopts a sponge-like structure allowing the diffusion of small molecules through it [6, 107, 108]. Its composition may vary depending on the species and growth conditions [109] and usually includes exopolysaccharides, deoxyribonucleic acid, proteins [6, 107–110], lipids [107], glycolipids, membrane vesicles and ions such as Ca^{2+} [108]. Following their embedding in the biofilm matrix, bacteria may adopt another phenotype than the one in the planktonic state [111].

The biofilm is advantageous for bacteria since it helps them to resist to stressful conditions [6, 77]. The environmental parameters that may affect bacteria viability include UV radiation, pH variation, osmotic shock, desiccation, flow conditions and biocidal substances [6, 66, 107, 111, 112]. The biofilm also helps to resist to physical or mechanical stimuli [110] or immunological defenses [66, 112] and prevents the wash out of enzymes, nutrients and signaling molecules which are essential for bacterial cell development [112]. The restricted access of biocidal substances to bacteria inside the biofilm results from their limited diffusion through the matrix due to electrostatic and hydrophobic interactions [107, 111].

The biofilm heterogeneity in time and space [110] induces an heterogeneity in the metabolic states of bacteria. Indeed, bacteria embedded in the biofilm matrix enter a stationary phase which also contributes to the resistance to biocidal substances compared to bacteria in the growth phase [107, 111]. Due to the nutrient gradient inside the biofilm, a subpopulation of bacteria (0.1-10 %) showing different phenotypes, called persister cells, arises. The gradient may even lead to the outbreak of bacteria with a different genotype [113]. In addition, due to the proximity of bacteria, the horizontal gene transfer between resistant and non-resistant strains is favored [6].

2.4.1.2 The formation of biofilm

A biofilm forms with a specific sequence of events (Figure 2.17) [6]. First, bacteria adhere to the material surface through reversible then irreversible adhesion and finally produce a conditioning layer. This conditioning layer is composed of proteins and polysaccharides adsorbed on the colonized surface. In a second step, following microcolonies formation, the biofilm matures and a three-dimensional structure is formed, composed of bacteria and polymeric matrix. Finally, some bacteria detach from the mature biofilm to colonize other available surfaces [5, 6, 8, 20, 47, 66, 77, 107].

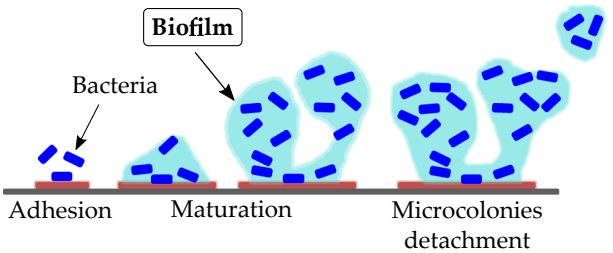

Figure 2.17: Colonization of the surface by bacteria and formation of the biofilm. First, the bacteria adhere on the surface. Then, during the maturation of the biofilm, bacteria multiply and the biofilm matrix is produced. Finally, microcolonies detach from the biofilm to colonize other surfaces.

The initial adhesion of bacteria is a two-step process. First, bacteria adhere in a reversible manner on the surface via non-specific interactions (Figure 2.18a) [47, 77, 112, 114]. This reversible adhesion depends on van der Waals interactions, dominant near the surface, and electrostatic interactions, dominant at a larger distance from the surface, which in turn vary according to the ionic strength of the medium [107, 114]. Indeed, the material surfaces and bacteria are typically negatively charged in aqueous medium [114]. However, in presence of counterions in the medium, these negative charges are screened and the bacteria can come close to the material surface [114]. As described in Figure 2.19, the free energy decreases greatly in presence of a high ionic strength while it increases in presence of a low ionic strength which prevents the adhesion of bacteria onto the surface [114]. With an intermediate ionic strength, a local free energy minimum occurs [114]. Bacteria can thus come close to the surface thanks to brownian motion, mobile appendices, gravitational forces or hydrophobic/hydrophilic interactions [8, 66, 107]. Apart from the ionic strength,

the pH, the temperature and the composition of the conditioning film influence the reversible attachment on the surface [107, 112].

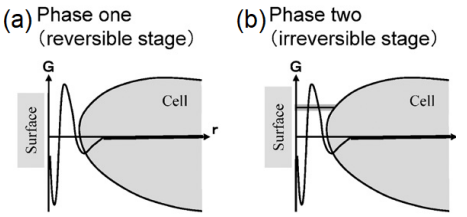

Figure 2.18: Two-step adhesion process of bacterium (image extracted from reference [114]). (a) The bacterium approaches the surface until the local minimum in free energy is reached. (b) The irreversible attachment results from the interaction between a bacterial appendage and the surface.

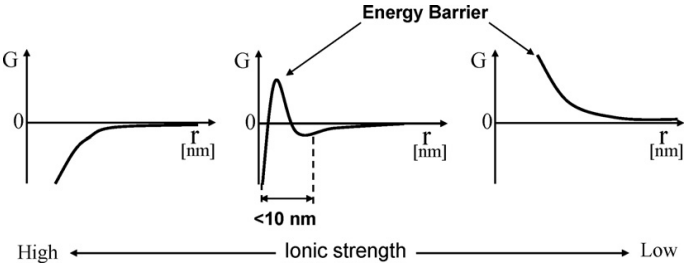

Figure 2.19: The total free energy of the interaction between the bacterium and the material surface is influenced by the ionic strength. For high ionic strength, there is no energy barrier. For intermediate ionic strength, there exists a local minimum of energy being immediately followed by an energy barrier. For low ionic strength, only an energy barrier is present. Image extracted from reference [114].

Second, bacteria attach irreversibly on the surface via specific interactions mediated by their appendices which pass the energy barrier (Figure 2.18b) [8, 47, 66, 77, 114]. These specific interactions are mediated by adhesins [108] such as flagella, pili and curli. A flagellum confers motility to the bacterium which enables the bacterium to come closer to the surface [8, 108]. Pili (also called fimbrae) are long appendages (10 nm diameter and a few micrometers long [8]) found at the extremity of the bacterium which can attach to the material surface and retract. Thus these appendages contribute to pull the bacterial cell close to the material surface [108]. Some bacteria secrete factors improving the attachment of pili onto the surface [108]. Type I pili are implicated in

the surface sensing mechanism [8] and can also attach to the eukaryotic cells in a mannose dependent manner [108, 112] via lectins [8]. Type IV pili can move the bacterial cell towards the surface without the help of a flagellum and can specifically bind to target molecules of the host [114]. Curli can attach to ECM proteins such as fibronectin, laminin and plasminogen [112] but can also promote bacterium-surface or bacterium-bacterium interactions [108, 112].

Once this first monolayer of bacteria is formed, the biofilm is remodeled to form a multilayer biofilm composed of bacterial cell clusters [108]. The biofilm maturation is mostly due to bacterium-bacterium interactions [112]. Some surface adhesins such as antigen 43 (Ag43), AidA and TibA are autotransporter adhesins which contribute to the maturation of the biofilm [112]. More specifically, Ag43 promotes bacterium-bacterium adhesion [8, 112] while AidA and TibA are glycosylated surface proteins that promote adhesion to eukaryotic cells [112]. The secretion of quorum sensing factors is also necessary for bacterial communication [113].

The formation of a three-dimensional matrix is a key event in the maturation of the biofilm which allows for the irreversible attachment of the colonies to the material surface [107, 112]. For *E. coli*, three exopolysaccharides were detected in the biofilm matrix: poly-β-1,6-N-acetyl-glucosamine, cellulose and colanic acid [112]. Some bacterial cell surface polysaccharides can also contribute to the biofilm matrix such as lipopolysaccharides, which are glycolipidic polymers attached to the outer membrane of gram-negative bacteria; or capsule, which comprises capsular polysaccharides firmly attached to the bacterial cell [112].

Finally, the microcolony detachment is triggered by different factors such as the nutritional cues, oxygen depletion and the presence of nitric oxide, cyclic diguanylate monophosphate or quorum sensing signals [108]. This dispersion is essential for the renewal of bacterial colonies [109].

Apart from the surface properties and the bacterial membrane composition, the environment might influence the biofilm formation and maintenance. The formation of biofilm depends indeed on the environmental signals (*e.g.* mechanical, nutritional and metabolic signals), the presence of inorganic molecules, host-derived signals, antimicrobials, quorum sensing molecules, the osmolarity, temperature, pH and the ionic strength [107, 108]. In particular, the mechanical forces exerted on the biofilm influence its shape [115]. Moreover, nutrient-rich media (notably with NaCl, glucose and Ca^{2+}) enhance the formation of the biofilm [107].

2.4.1.3 Adhesion theory

Various models have been proposed to model bacterial adhesion. They are based on the thermodynamic, the Derjaguin, Landau, Verwey, and Overbick (DLVO) and the extended DLVO (xDLVO) theories [8, 107, 114].

The thermodynamic theory states that the free energy of adhesion (ΔG_{adh}) is related to the interfacial energies of the surface-bacterium γ_{sb}, surface-medium γ_{sm}, and bacterium-medium γ_{bm} according to the following equation [107, 116]:

$$\Delta G_{adh} = \gamma_{sb} - \gamma_{sm} - \gamma_{bm} \tag{2.7}$$

Adhesion is favored if the free energy is negative as a result of the first interactions of the bacteria with the surface and surrounding medium [114]. However, this model does not take into account the distance between the bacteria and the material surface [107] and the interaction is considered reversible [114, 116]. Despite these shortcomings, the thermodynamic theory can help us to understand general mechanisms such as the influence of hydrophilic/hydrophobic interactions between the bacterium and the surface on the adhesion process [114].

On its side, the DLVO model takes into account the cell-surface distance [107, 114, 116]. In the xDLVO model, the hydrophobic/hydrophilic interactions and the osmotic interaction are included [107, 114, 116]. The total free energy of adhesion ΔG_{adh} is related to the Lifshitz-van der Waals interactions ΔG_{VdW}, the electric double layer interactions ΔG_{dl} and the acid–base interactions ΔG_{AB} by the equation:

$$\Delta G_{adh} = \Delta G_{VdW} + \Delta G_{dl} + \Delta G_{AB} \tag{2.8}$$

These theories consider the bacterium as a colloidal particle which does not take into account the adaptation of the bacterium to the environment by the active modification of its surface [8, 107, 114, 117]. As explained before, the appendages present at the surface of the bacterium help to counteract repulsive forces due to physical interactions [8, 107, 114]. Moreover, the material surfaces considered do not vary in roughness which is another source of problem for the prediction of bacterial adhesion [107].

2.4.2 Surface properties and nanopattern designs influencing bacterial adhesion and biofilm formation

The surface properties able to influence the bacterial adhesion and biofilm formation on the surface are the topography, the chemistry, the stiffness and possibly a combination of these previous properties through the use of smart-responsive surfaces. Here, we purposely focus only on systems which affect bacterial behavior by contact and do not detail released-based systems. On the contrary to what is usually done in the literature (*i.e.* classification based on the surface property studied), we define three categories (*i.e.* promoting, killing and controlling of bacterial behavior) based on the measurement of the viability of bacteria exposed to different material cues. Figure 2.20 summarizes the surface features promoting or controlling bacterial adhesion and therefore the biofilm formation, or even killing bacteria upon contact.

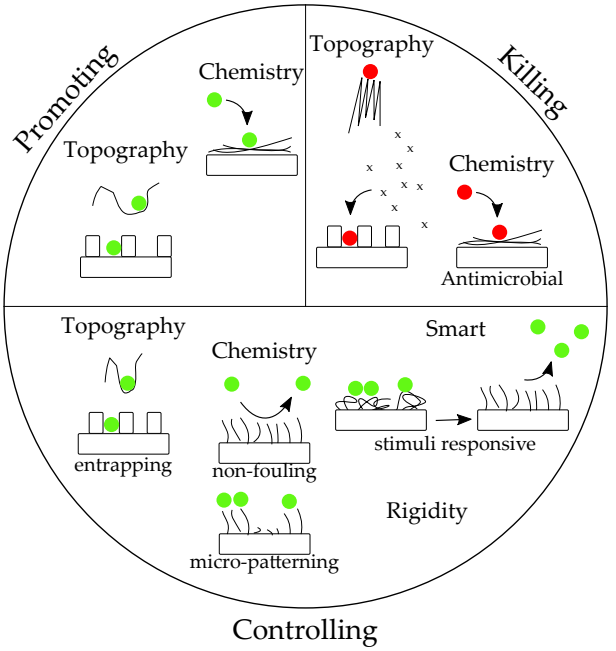

Figure 2.20: The surface properties can be used to promote the adhesion, to control or to kill bacteria. The surface properties available to influence bacterial behaviors are the topography, the chemistry and the rigidity. The stimuli responsive surfaces can also be used.

2.4.2.1 Surface properties and designs to promote bacterial adhesion

The surfaces favoring the formation of a biofilm allow bacteria to adhere without hindering the bacterium-bacterium interactions. To favor bacterial adhesion on a surface, two main properties of the surface can be used: the topography and the chemistry.

Topography

Surface topography can promote bacterial adhesion when the topographical features displayed are larger than the bacterium size. Either random topography (Figure 2.21c) or well-defined topography (Figure 2.22) can meet this criterion. These topographical structures allow bacteria to attach at the bottom of pits of the topography to prevent their removal via shear forces [8, 17, 110] while still being able to make bacterium-bacterium interactions. To illustrate this behavior, Hou *et al.* tested the adhesion of *E. coli* on PDMS surfaces composed of protruding squares with lateral dimensions varying from 2 to 100 μm, spaced from 5 to 20 μm with a height of 10 μm. They evidenced that bacteria preferred to adhere in the valleys offered by the surface regardless of the lateral dimensions of squares and valleys [118].

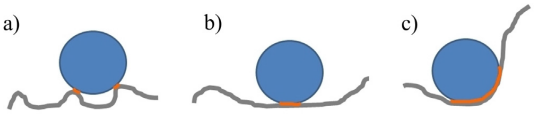

Figure 2.21: The effect of surface micro- and nano-roughness on the adhesion of bacteria. (a) Smaller nanotopographical features hinder the contact between the bacterium and the surface; (b) a flat surface leads to a larger contact area between with the surface compared to (a); (c) the contact area is higher for larger topographical features compared to a flat surface. Image extracted from reference [18].

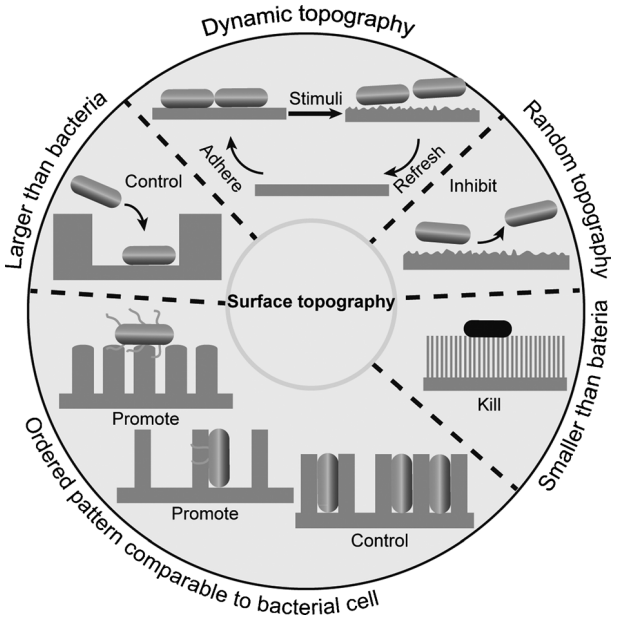

Figure 2.22: The influence of the surface topography on the bacterial adhesion depends on the topographical pattern dimensions compared to the size of bacteria. Image extracted from reference [17].

Chemistry

The chemical composition of the surface can also favor bacterial adhesion. To do so, the surface must promote the adhesion of bacteria without harming them. For example, some bacteria attach more easily on positively charged surfaces but this may render them non-viable. Moreover, the growth of some bacteria is higher on negatively charged surfaces [8]. In particular, surfaces bearing cationic quaternary amine groups show killing properties [63, 68]. The patterning of bioadhesive area on a material surface can also be done to control the spatial development of the biofilm. For instance, Hou *et al.* tested the adhesion of *E. coli* on patterned surfaces showing squares of SAM terminated with methyl functionality and side dimension of 125 μm distributed in a triethylene glycol SAM non-adhesive background. They could localized the bacterial adhesion specifically on the squares [119].

2.4.2.2 Surface properties to control bacterial adhesion

The surfaces controlling the biofilm formation prevent the adhesion of bacteria or disorganize the first steps of the biofilm formation. Different approaches are used to control the bacterial colonization of the surface. They involve a specific topography, the development of non-fouling or smart surfaces or even modify the surface rigidity.

Topography

A first approach consists in using random or ordered topography. Random surface topography needs to be smaller than the bacterium size to form point-like adhesion hindering fouling (Figure 2.21a) or to entrap the bacteria in order to prevent bacterium-bacterium interactions. In the case of ordered topography, the bacteria must be entrapped in the topographical features (Figure 2.22). Having surfaces presenting patterns with a comparable size to the one of bacteria allows for the entrapping of bacteria into the structured array. Such a distribution of bacteria onto the surface affects the natural organization required for the biofilm formation [17]. Another study, however, states that a topographical pattern showing stripes of comparable size to the one of bacteria might enhance bacterial communication via flagella interconnections and thus biofilm formation [110].

Here, we explored the effect of topographical roughness on the bacterial response. Taylor *et al.* tested the adhesion of *P. aeruginosa* and *S. epidermidis* on smooth and rough PMMA. Among the roughness tested (with R_a roughness average varying from 0.04 to 7.89 μm), the R_a roughnesses comprised between 1.12 and 1.29 μm allowed for a higher number of adhered bacteria while a R_a roughness higher than 1.86 μm decreased the adhesion of bacteria. The authors thus confirmed that the adhesion of bacteria depends on the value of the roughness [120]. Seddiki *et al.* observed the same phenomenon. Indeed, they tested the adhesion of *E. coli* on rough titanium surfaces. When the surface roughness produced cavities which were big enough to accept bacteria, the adhesion was increased while a limited adhesion was observed on rough surfaces showing a small number of cavities able to welcome bacteria. Indeed the remaining surface provided point-like adhesions [18]. On their side, Singh *et al.* studied the formation of *E. coli* and *S. aureus* biofilms as well as the amount of proteins adhered on nanostructured titanium surfaces. They showed that the increase of the nanometer scale roughness, with root mean square roughness (R_q)

ranging from 16 to 32 nm, reduced the attachment of bacteria and the formation of biofilm. They also evidenced that the proteins adhered in much higher amount on rougher surfaces. This phenomenon might prevent the formation of biofilm on surfaces due to the inaccessibility of the underlying surface to bacteria (*i.e.* passivation effect) and the smoothing of the nanoroughness (*i.e.* flattening effect) [121]. Indeed, surfaces having a roughness $R_a \leq 0.8$ nm can be considered like "hygienic" due to their low propensity to bacterial colonization [122]. Meng *et al.* also pointed out that the results obtained on random topography do not only depend on the surface roughness but also on the shape of bacteria [17]. Indeed, round shaped bacteria are able to obtain more contact area on a rougher surface while the result is reversed for rod-shaped bacteria [17].

Moreover, Rizzelo *et al.* studied the modifications occuring in the genome and proteome of the gram-negative bacteria *E. coli* adhered on nanostructured gold surfaces compared to flat glass surfaces and smooth gold surfaces. They concluded that the nanostructuration of the surface induced a change of the bacterial surface composition and prevented the expression of surface appendices playing an important role in the bacteria colonization process [123]. Theoritical model can also be implemented in an attempt to predict bacterial behavior. Decuzzi *et al.* developed an interesting mathematical model to characterize the adhesion strength on rough surfaces. This model takes into account the specific and non-specific interactions taking place at the substrate/membrane interface as well as its elasticity. They distinguished three regimes based on the surface energy (γ) of the substrate: for small γ, an increase in roughness is detrimental; for large γ, an optimal roughness exists; for intermediate γ; roughness has a minor effect on adhesion [124].

Now, we focus on ordered topography. In the case of an ordered surface topography, the dimensions of the features are important for bacterial retention [110]. Indeed, when the appropriate topography is designed, bacteria tend to attach to the bottom of the valleys [8, 47, 125]. For instance, Hochbaum *et al.* were able to entrap bacteria between nanopillars of 300 nm diameter and 2 μm high. To do so, the nanopillars needed to be spaced with an interdistance similar to the size of bacteria. When the interdistance was larger, the bacteria were observed to be randomly distributed on the surface (Figure 2.23). However, in each of these cases, bacteria tended to maximize their contact with the pillars. Such a behavior was observed for bacteria presenting or not bacterial appendages [126]. Another example is the study of Kappell *et al.* who tested different

geometries (*i.e.* bars, squares and circles) of topographical microstructures formed in silicon elastomer against *S. aureus*, *S. epidermidis* and *P. aeruginosa*. These structures had a width of 1.78 to 22.25 μm spaced by 0.26 to 17.35 μm, with a height of 0.51 μm. They showed that the bacteria generally grew between the bars and squares when the spacing was superior to 0.92 μm. For the circle features, even thought the spacing was smaller (*i.e.* 0.26 μm), the bacteria grew between the features. Among the geometries tested, the pattern showing squared protrusions of 4 μm-width, separated by a distance of 2.52 μm reduced the formation of biofilm for the three bacteria tested [125].

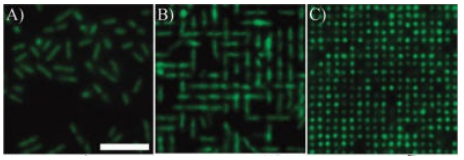

Figure 2.23: *P. aeruginosa* adhered on nanopost arrays showed different distributions as the function of the pattern size. The spacing between the post are (A) 2.2, (B) 0.9 and (C) 0.7 μm. When the spacing was larger than the bacterial size (A), bacteria adhered randomly. As the spacing decreases, the bacteria align perpendicular to (B) or along (C) the nanoposts. Image extracted from reference [126].

To detect the difference between micro- and nanotopography influences on the adhesion of bacteria, Diaz *et al.* tested the adhesion of *Pseudomonas fluorescens* (*P. fluorescens*) on microstructured (550 nm-width rows separated by 750 nm-width and 120 nm-deep channels) and nanostructured gold surfaces (*i.e.* randomly oriented grains of 50-100 nm). They observed that microstructured surfaces induced a decrease of the bacterial adhesion because the bacteria were entrapped into the channels. In contrast, dense bacterial aggregates were observed on nanostructured surfaces (Figure 2.24). The authors thus demonstrated that the dimension of the topography is essential to control the arrangement of bacteria adhered onto the surface and consequently, the subsequent formation of the biofilm. Moreover, they showed that bacteria adhered on microstructured surfaces were more sensitive to antibiotic (streptomicin) compared to bacteria adhered on nanostructured surfaces. Therefore the authors concluded that these non-aggregated bacteria were not protected by a cluster of bacterial cell and matrix which allowed the antibiotic molecules to reach more easily the bacteria [127]. Then, Diaz *et al.* compared ordered nanostructured gold

surface (250 nm-period pattern with 20 nm-height) with the two previously described surfaces. Interestingly, the ordered nanotopography also hindered the formation of bacterial aggregates. The ordering of the surface might thus have an influence on bacterial aggregates compared to random topography [128]. Another study by Xu *et al.* compared the adhesion of *S.epidermidis* and *S. aureus* on nanostructured poly(urethane urea) showing pillars of either 400 or 500 nm-diameter spaced by 400 or 500 nm, respectively, and a smooth surface used as control. They confirmed that nanostructured surfaces reduced bacterial adhesion because of the limited possibility to form anchoring points with the surface [129].

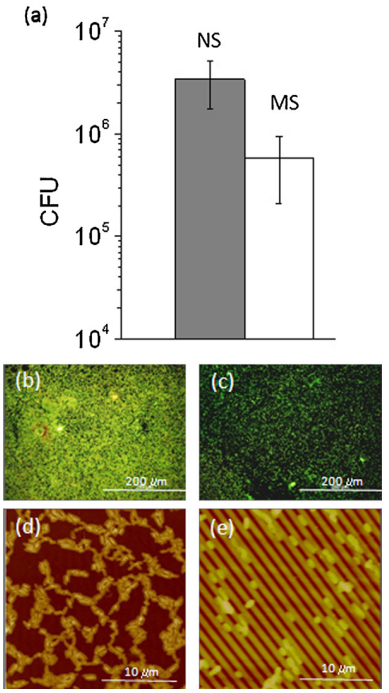

Figure 2.24: Adhesion of *P. fluorescens* on nanostructured (NS) and microstructured (MS) surfaces. (a) The number of adhered bacteria was larger on NS surface compared to MS surface; epifluorescence microscopy images recorded for bacteria adhered on (b) NS and (c) MS showed that the number of bacteria was higher on the NS surface compared to the MS surface, AFM on (d) NS showed that bacteria form ramified patterns while on (e) MS a large number of bacteria is isolated. Image extracted from reference [127].

Finally, the production of extracellular polymeric material and bacterial

appendages are influenced by the dimensions of the surface topography. Diaz *et al.* explored the production of polymeric material and studied the adhesion of *P. fluorescens* on different surfaces including nanostructured gold surfaces (900 nm-width channel with a height of 90 nm) and smooth and microrough silicon surfaces (small boxes of 2 μm-height and 8 μm-long). On nanostructured surfaces, the bacteria were entrapped in the channels, the length of bacteria was smaller, a smaller number of bacteria adhered and a smaller production of polymeric material appeared than on smooth gold surfaces. On the contrary for microrough surfaces, the amount of bacteria was smaller and the production of polymeric material was higher than on smooth silicon surfaces. They concluded that when the dimensions of the nanostructures or roughness were similar to the ones of bacteria, the bacteria adhered easily and less polymeric substances were produced [130]. On their side, Hsu *et al.* designed topographical patterns in silica with different geometries: circular wells with a diameter of 500 nm and spaced by 200 nm and rectangle wells having a width of 1 μm, a length of 1.5 or 2 μm and spaced by 2 μm or 500 nm. All wells had a depth of 27-32 nm. They tested the adhesion of *E. coli*, *Listeria innocua* and *P. fluorescens*. They found that bacteria tended to maximize their contact area with the surfaces and that the topography influenced the production of different appendages by bacteria (SEM observation suggests that the type of appendages varies with the topography) [122].

These different researches presented above show the relevance of topographically modified surfaces on bacterial behavior. It is thus worth considering to control the bacterial behavior with this parameter and to finely control the spatial arrangement of topographical features.

Chemistry

A second approach to control bacterial colonization is to use non-adhesive coatings based on PEG [19, 131–133], polyacrylamide, dextran, zwitterionic polymers, enzymes [17, 20, 67, 68, 107] or superhydrophobic surfaces [107, 109, 132, 133]. These surfaces are called passive or anti-adhesive [77].

To produce polymeric chains resisting fouling, some essential macromolecular characteristics are required: hydrophilicity, presence of moieties leading to the formation of hydrogen bonds with water, non-charged [67, 68, 71, 134] and conformational flexibility [67]. PEG-based layers have been extensively used to prevent the adsorption of proteins and thus hinder the bacterium

attachment [17, 77]. For instance, Ista *et al.* who used gold surfaces grafted with a dense layer of oligo(ethylene glycol), proved that the surface colonization by *S. epidermidis* and *Deleya marina* was efficiently prevented [135]. The non-adhesive characteristics of PEG layers are due to their strong hydrophilic nature [17, 71, 77]. Two phenomenons explain the non-fouling behavior of PEG: the proteins approaching the surface compress the PEG chains and are subsequently elastically rejected from the surface; the water removal resulting from the compression of PEG chains is not thermodynamically favorable (Figure 2.25) [67,132,134]. Many studies state that resistance to fouling is increased with the chain length and the grafting density of the macromolecules immobilized onto the surface [17, 67, 132]. However, others state that having a long chain is not required to prevent fouling but that a layer thickness of 10 nm of P(OEGMA) chain is necessary to prevent fouling [19]. Others claim that SAMs of only two units of oligo(ethylene glycol) (OEG) are necessary to prevent fouling by proteins [134]. The water intake of the hydrophilic chains is important to prevent fouling [19] but also the hydrophilicity of the head group of the anchored molecule [19, 134] as well as the overall conformation which needs to be helical or amorphous in case of longer OEG chains [134]. The main disadvantage of PEG is its sensitiveness to oxygen [17, 67, 132]. However, other problems can arise from the compaction of the polymer chains composed of OEG units. Tugulu *et al.* used ATRP to synthesize poly(poly(ethylene glycol) methacrylate) (PPEGMA) brushes from the surface and tested different chain densities to study the stability of the polymer brushes in cell culture medium. They pointed out that for highly packed polymer chains of PPEGMA, some chains were detached from the surface probably due to the osmotic stress produced by the complexation of the polymer chains with salts. This problem could be circumvented by the use of less densely packed chains, without compromising the non-fouling properties of the brushes [136].

Apart from a homogeneous layer of SAMs or polymer brushes, nanogels of PEG have also been used to produce anti-fouling surfaces. The patterning of these nanohydrogels were proved to be efficient against bacterial fouling. Indeed, Krsko *et al.* studied the effect of the spacing between PEG nanohydrogels of 150 nm diameter, deposited onto vinyl methoxysiloxane silanized glass, on the adhesion of *S. epidermidis*. They concluded that a spacing equal to the bacterial size allowed the bacteria to adhere but also showed that bacteria did not form clusters. When the spacing was reduced to a size inferior to the size of the

bacterium, the adhesion of bacteria was not detected. They also pointed out that the swelling of the nanogels was necessary to impart non-fouling properties to the surface: indeed, the water intake needs to be sufficient [137].

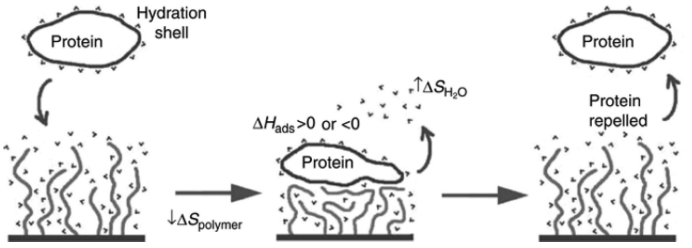

Figure 2.25: PEG anti-fouling mechanism. Before the contact between the hydrated polymer chains and the protein, the water content of the chains is high. While the protein enters in contact with the surface, the water content decreases due to the compression of the polymer layer by the protein. This is not thermodynamically favorable so that the protein is repelled. Image extracted from reference [132].

Other polymers than PEG derivatives were used to produce non-fouling layers. For example, propylene sulfoxide oligomers resist the fibrinogen adsorption [67]. Pidhatika *et al.* produced another non-fouling polymer based on poly(2-methyl-2-oxazoline) polymer (P(MOXA)) grafted on poly(L-lysine) (PLL). This copolymer was adsorbed on various substrates and they optimized the grafting density of P(MOXA) on PLL in order to avoid bacterial adhesion. So, they found that the ratio of P(MOXA) to PLL should be around 0.33 to prevent fouling. In fact, an optimal grafting density of polymer brush needs to be reached to shield substrate charges, prevent the adsorption of proteins on the brush and repel bacteria [138]. Moreover, they compared the stability of P(MOXA) and PEG in different media. They evidenced that degradation occured via side chain degradation for both polymers and that P(MOXA) was more stable than PEG even though the non-fouling properties were kept over the all study [139].

Zwitterionic polymers such as poly(caboxybetaine) [17, 132], phosphorylcholine derivatives [67, 132], poly(N-hydroxypropyl methacrylamide), poly(N-sulfobetaine methacrylamide) [20] or sulfobetaine [132] are also alternative to PEG to produce non-fouling layers. Some enzymes such as DNase I which are non-adhesive can also be used [17].

The disadvantages of all these low-fouling systems are their potential degra-

dation, inhomogeneity and handling difficulty which allow for the adhesion of bacteria after a long term [19, 20, 131].

Another approach to control the arrangement of bacteria on a surface is to chemically pattern the surface at the micrometer scale. For instance, Choi *et al.* designed polyelectrolyte multilayers (PEMs) of polyallylamine hydrochloride and polystyrene sulfonate with the upmost layer being the cationic polyallylamine hydrochloride layer. Selected regions of these PEMs were then covered by non-fouling poly(ethylene glycol)-poly(D,L-lactide) diblock copolymer by micromolding in the capillaries technique. With these surfaces, they were able to pattern *P. aeruginosa*, *E. coli* bacteria and *Saccharomyces cerevisiae* at the micrometer scale on adhesive area of different shapes (Figure 2.26). They were able to create microarrays [140]. Similarly, Wong *et al.* patterned at the micrometer scale (diameter of 2 μm and height of 100-200 nm) cationic polymers (poly-L-lysine or polyethyleneimine) distributed in a non-fouling background of hexamethyldisilazane. They found that they could localize *E. coli* adhesion on the adhesive patches while keeping their viability for at least 1 hour [141]. The immobilization of bacteria is interesting to identify specific biological activities such as expression of gene and proteins, viability and toxicity [140].

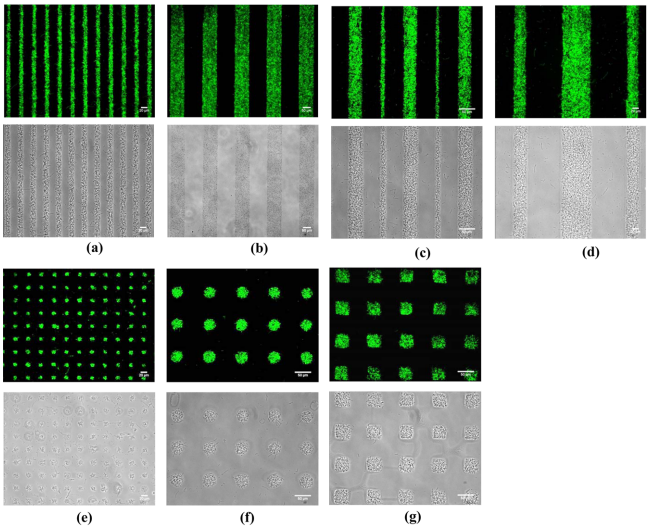

Figure 2.26: *P. aeruginosa* labelled in green adhered on micropatterned PEM films with different dimensions and shapes. Image extracted from reference [140].

Smart surfaces

A third approach to control bacterial colonization consists in using smart-responsive surfaces. These surfaces respond to the environmental changes. They can be enzyme responsive, mechanoresponsive, pH-responsive, humidity-responsive, temperature-responsive, electro-responsive [17, 67, 132], salt ionic strength-responsive or light-responsive [109]. For example thermo- and pH-responsive polymers can be used to prepare surfaces which sequentially switch between fouling and non-fouling properties [109]. This is the case for the study of Yu *et al.*, explained above in section 2.3.1.1, who patterned PNIPAAm and lysozyme molecules [78]. On the same principle, they also patterned lines of PNIPAAm alternating with bactericidal quaternary ammonium salt [142].

Rigidity

A fourth approach to control bacterial colonization is to use mechanical cues to regulate mechanical properties of the surface. Indeed, when the softness of a coating is increased beyond a threshold value, the growth of bacteria is inhibited [17, 71]. Lichter *et al.* confirmed this observation by studying the behavior of *S. epidermidis* and *E. coli* on PEMs of poly(allylamine) hydrochloride and poly(acrylic acid), assembled over a range of conditions. They showed that the number of adhered colonies increased with the stiffness of the surfaces comprised between 1 and 100 MPa [143]. However, Saha *et al.* obtained different results by studying the behavior of *Lactococcus lactis* (*L. lactis*) and *E. coli* on surfaces coated with PEMs, composed of PLL and a hyaluronan derivative modified with photoreactive vinylbenzyl groups, showing a lateral variation of stiffness. This variation of stiffness did not influence the growth of *L. lactis*. However, the growth of *E. coli* was more rapid on softer regions (E = 30 kPa) than on stiffer regions (E = 150 kPa) [21]. Since these researchers used different ranges of stiffness and ways to analyze the bacterial coverage, the influence of the surface stiffness on the bacterial adhesion and growth remains an open question. Even though the response of bacterial cells to rigidity is not clear, the rigidity at which the bacteria react should be linked to the rigidity of the *in vivo* environment of mammalian cells (see section 2.5.1). Indeed, they need to adapt to the environmental conditions to adhere and subsequently form a biofilm.

2.4.2.3 Surface properties killing bacteria

The surfaces killing bacteria considered here are surfaces showing bactericidal effect upon contact or allowing the antimicrobial agent to access with ease the immobilized bacteria. Indeed, if the access to the bacterial membrane is made easier by the immobilization of the bacterium, the use of antimicrobial agent is more efficient.

Topography

Topographical patterns displaying high aspect ratio such as the ones found on cicada wings which consist in high aspect ratio nanopillars (200 nm-height and 60 nm-diameter cap), induce a disruption of the bacterial membrane [17, 144]. Surfaces mimicking the cicada wing structure were synthetically reproduced using black silicon. It was evidenced that these surfaces successfully killed *P. aeruginosa*, *S. aureus* and *Bacillus subtilis* (*B. subtilis*) bacterial cells [145]. Moreover, it was shown that isolated bacteria adhered on topographical patterns are more sensitive to antibiotics than the aggregated ones adhered on flat surfaces. The reason for this was explained above for the study performed by Diaz *et al.* [127].

(Bio)chemistry

Bioactive compounds killing bacteria upon contact can also be grafted on the surfaces using different approaches explained in Figure 2.16. For example, Blin *et al.* who immobilized magainin I on paramagnetic silica particles coated with a poly(2-(2-methoxyethoxy)ethyl methacrylate-*co*-hydroxyl-terminated oligo(ethylene glycol) methacrylate) brush, showed the antimicrobial activity of the immobilized peptide towards *Listeria ivanovii* (*L. ivanovii*) [146]. Cassin *et al.* also proved the antimicrobial activity of PEMs grafted with LL37 towards *E. coli* [147]. On their side, Humblot *et al.* demonstrated the antibacterial effect of magainin I immobilized on SAMs against *L. ivanovii*, *Enterococcus faecalis* and *S. aureus*. However, they raised the concern of the accumulation of inactive bacteria on the surface which resulted in attractive centers for active ones [148]. Peyre *et al.* produced patterned squares of magainin I peptide immobilized on mercapto hexadecanoic acid (200 μm-width with an interdistance of 420 μm between squares) and distributed in a non-adhesive background. They tested these surfaces against *L. ivanovii* and showed a reduction of bacterial adhesion

due to the PEG background and a decrease in bacterial growth around 28 % due to the presence of the bactericidal magainin I peptide [149].

Synthetic polycations are also used to produce killing layers. For instance, quaternized groups disrupt the bacterial membrane [32, 71, 133]. For example, Cheng *et al.* used poly(N,N-dimethyl-N-(ethoxycarbonylmethyl)-N-[2'-(methacryloyloxy)ethyl]-ammonium bromide) to kill bacteria upon contact and then hydrolyzed the polymer to switch to a non-fouling zwitterionic polymer which released dead bacterial cells from the surface [150].

2.4.3 Description of *E. coli*

E. coli is a predominant species of gram-negative bacteria in the gastrointestinal tract [112]. The cell wall structure of gram negative bacteria is complex. A plasma membrane surrounded by a peptidoglycan layer of 10 nm is further separated from an outer membrane by the periplasmic space [151]. This outer membrane consists in proteins, lipopolysaccharides (LPS) and phospholipids [151]. The different structures decorating the cell wall determine the way bacteria interact with their environment [151]. Indeed, several cell wall structures are responsible for the adhesion of bacteria on abiotic surfaces as well as for the bacterium-bacterium interactions (Figure 2.27). The expression of these structures by the bacterial cell depends on the bacterial strain as well as the planktonic or sessile state of the strain. Flagellum is a well-known cell wall structure of bacteria which helps the bacterium to make contact with a surface [108, 115, 152, 153] while pili and fimbrae are appendices helping to overcome repulsive forces and anchor bacteria to a surface [108, 115, 152]. In many cases, the outer membrane of gram-negative bacteria are decorated with LPS and pili which play an essential role in the pathogenicity of the bacterial strain [151].

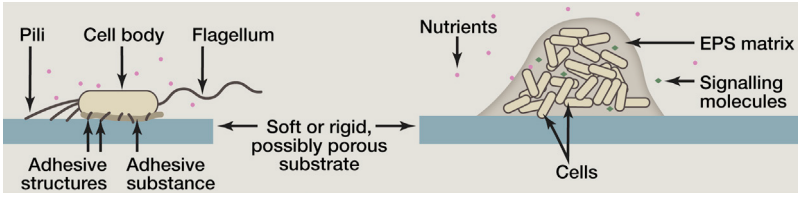

Figure 2.27: Surface appendices, adhesive substance and molecules available to bacteria to attach and form a biofilm on solid surfaces. Image extracted from reference [115].

We now focus on the cell wall structures showing up on *E. coli* and playing a role in the adhesion to surfaces and in the formation of a biofilm (Figure 2.27 left). First, the flagella available on the side of the bacteria allow to counteract hydrodynamic and electrostatic forces preventing the adhesion [8, 108, 112].

Once the bacterium is loosely attached to the surface, type 1 pili, curli and conjugative pili help to strengthen the adhesion of bacteria to the surface [112].

- Type 1 pili are composed of pilin subunits and have a tubular structure with a diameter of 5-7 nm and a length of about 0.2 to 2 μm [8, 112, 153]. Even though these structures are involved in the binding to abiotic surfaces [152], they can also adhere to eukaryotic cells via a mannose-dependent manner thanks to lectins located at their tip [8, 108, 112, 115, 152, 154]. The pili can also bind on the fibronectin [154]. Moreover, they can be expressed in an ON and OFF manner at the surface of the bacterium [112, 153].

- Curli self-aggregate at the bacterial surface to form 6-12 nm diameter structures with a length of about 0.5 to 1 μm [112]. Apart from their role in the attachment to extracellular matrix [8, 112], they also facilitate bacterium-bacterium interactions [112].

- Conjugative pili, on their side, help the adhesion on abiotic surfaces and the communication with other bacteria [112]. However, their main function is to be related to the horizontal gene transfer [153]. This pilus could also functionally substitutes for structures such as type 1 pilus, Ag43 or curli [112].

After the adhesion step, the maturation of the biofilm is facilitated by autotransporter adhesins and cell surface polysaccharides [112].

- Antigen 43 is an outer membrane protein that promotes bacterium-bacterium adhesion allowing for the development of biofilm [8, 112, 153]. It can be expressed in an ON and OFF manner at the surface of the bacterium [112]. The cell self-aggregation phenomenon mediated by this molecule is blocked in the presence of type 1 pili which prevent it by increasing the spacing between bacterial cells [153].

- AidA and TibA are glycosylated surface proteins allowing the adhesion of bacterium onto eukaryotic cells. As a consequence, they are involved in virulence of pathogenic *E. coli*. They also promote biofilm formation on abiotic surfaces [112].

- LPS are glycolipidic polymers helping for the adhesion to abiotic surfaces and formation of the biofilm. They also contribute to the biofilm phenotype. *E. coli* produces mainly LPS O antigen and capsular K antigen [112].
- Capsules are polysaccharides firmly attached to the bacterium surface [112].

The expression of genes in *E. coli* modulates the appendices present on the cell wall for a given time. As the bacterium adapts to its environment, this expression varies with time and leads to the differential expression of surface appendices through time [112].

2.5 Mammalian cell behavior on surfaces

2.5.1 *In vivo* environment of cells

The environment in which cells evolve has a huge impact on their fate. This reason pushed us to take a brief look at the ECM composition as well as the soluble factors available to cells in their *in vivo* environment. Many states and behaviors of cells such as stemness, viability, self-renewal and differentiation are controlled with the combination of three components which are soluble factors (such as growth and signaling factors), cell-cell interactions and cell-matrix adhesions [12, 13, 22, 155]. Dingal *et al.* provided a noteworthy overview of these multiple factors affecting stem cell fate [13].

The ECM is composed of collagens, fibrous proteins, proteoglycans and glycoproteins which concentrations depend on the nature of the tissue [1]. For example, for skin, tendon, bone and cartilage, crossbands of fibril-forming collagens decorated with FACIT collagens and interwoven with type VI collagen constitute the backbone of these tissues while elastic tissues such as ligaments, vascular walls and skin also include fibrillar components such as elastin and fibrillin [1]. Moreover, glycoproteins such as fibronectin, laminin and thrombospondins are also included in the ECM [1]. The mechanical properties of the ECM are defined by its composition. Indeed, the collagen and elastin interwoven fibers with diameters ranging from 10 to 300 nm [156] provide tensile strength to the tissue [156, 157]. On their side, proteoglycans define the elasticity of many tissues [1], regulate matrix assembly, carry growth factors and determine the resilience of tissues [1]. They form a hydrogel resisting compressive

forces [156, 157]. When taking a closer look to the tissues, one can see that each tissue corresponds to a range of elasticity as displayed in Figure 2.28 [12]. As a consequence, when stem cells are seeded on a material with a stiffness corresponding to the one of the natural tissue matrix, they tend to commit to the corresponding lineage. In the case of neurogenesis, the elastic modulus has to be lower than 1 kPa, for myogenesis it is around 10 kPa and for osteogenesis it is larger than 30 kPa [158]. It is worth noting that fibrotic tissue resulting from an injury can be a homing signal for cells which usually tend to colonize stiffer tissues [12].

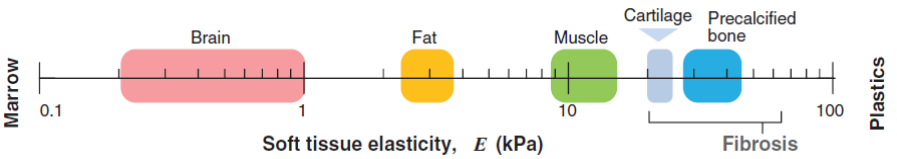

Figure 2.28: The elasticity of tissues varies depending on their function. Image extracted from reference [12].

The 3D architecture of ECM molecules, which varies amongst tissues, provides mechanical properties but also topographical and adhesive features to the matrix which allow for the regulation of stem cell behaviors [1,155,157]. The 3D architecture of ECM is a function of the size of the fibrils and the pores which are directly related to the nature and the arrangement of the macromolecules forming the ECM [157]. For example, collagen type I forms fibril patterns with a width of 68 nm, a depth of 3-5 nm and an interfibrillar spacing depth of 35nm [159]. This example illustrates that the ECM is also organized at the nanometer scale. Interestingly, the nanoscale features in the ECM are similar to the size of cell receptors [160]. Many cell structures range at the nanoscale such as the cytoskeleton elements, the transmembrane proteins, the saccharide chains and filopodia [157]. Due to the nanoscale dimensions of the fibers, adhesive epitopes are also displayed at the nanometer scale [1]. A lot of proteins (*e.g.* fibronectin, vitronectin, fibrinogen, laminin) embedded in ECM contain the RGD recognition motif for cell adhesion [81, 85, 157]. It is worth noting that other cell adhesion sequences can be recognized by cells [81, 85].

The ECM architecture influences all types of cells. Stem cell behavior, however, can also be influenced by soluble factors or cell-cell contacts. Undoubtedly, growth factors influence strongly stem cell fate [12]. They are notably well

regulated in space and time for the embryonic development [12]. For example, BMP-2 influences the differentiation of osteoblast precursors into mature osteoblasts [88, 92]. However, some cell types need to come into contact between each other before the growth factors affect their fate [12]. It is worth noting that ECM can also retain growth factors, cytokines and other molecules to limit their diffusion [1, 12].

2.5.2 Dynamics of adhesion, proliferation and differentiation of cells

The adhesion of cells on the surface is a key phenomenon which directs the other behaviors of cells such as migration, proliferation and differentiation.

The adhesion of cells to the surface is mediated by adhesion receptors present on the cell surface. The most know adhesion receptor is called the integrin which is 10-100 times more common than the other receptors [156, 161]. The other receptors contributing to the cellular adhesion are receptors of the immunoglobulin superfamily, non-integrin collagen or laminin receptors, glycolipids, glycosaminoglycans and glycosylphosphatidylinositol-linked receptors [161]. The integrin receptor is composed of two non-covalently associated glycoprotein subunits α and β [47, 81, 82, 160–162] and is 10 nm wide [47, 156]. Mammalian cells can express 18 α and 8 β subunits which can form 24 different integrins [82, 86, 162]. Due to these different subunits, integrins are expressed differently by cells coming from different tissues [81, 82] and have different binding specificity [81, 82, 163]. They also fill different adhesive roles (*e.g.* adhesion strenghtening, mechanotransduction) [81, 85, 161]. They can be classified as laminin-binding, collagen-binding, leukocyte and RGD-recognizing integrins [82]. For example, $\alpha_5\beta_1$ integrin helps strengthen the adhesion with fibronectin while $\alpha_v\beta_3$ controls the mechanotransduction [161].

The formation of "focal adhesions" (FAs) by cells is initiated by the binding of integrin receptors to extracellular components present in the environment, on the external side of the cell membrane, and to the binding of intracellular components present in the cytoplasm, on the internal side of the cell membrane [156, 161]. The cell first forms nascent adhesions (with a size inferior to 0.25 μm) composed of 3-4 gathered integrins. Then, the further recruitment of integrins allows the formation of focal complexes which are dot-like contacts (with a diameter around 0.5-1 μm) with the surface [47, 161, 164]. The formation of these focal complexes

implies the sensing of nanoscale properties of the surface [161]. This probing is realized by filopodia [47] and/or lamellipodia [161,164] at the end of which the complexes are formed [47,161]. It is worth noting that the dynamic probing of the surface by cells causes the remodeling of the ECM [156]. The maturation of these focal complexes is then done by recruiting more integrins [2,160,162] or merging with other complexes [161] which results in the formation of elongated structures (around 0.25-0.5 μm wide and 2-10 μm long [156]) called FAs [161]. Some authors even classify FAs of length higher than 5 μm as super mature adhesions [47,164]; these fibrillar adhesions are involved in the remodeling of the ECM [164]. In the cell, the lamellae sustain the formation of more stable adhesions [161].

So far, we focused on the gathering of integrins to form FAs. However, the FAs are also characterized by the recruitment of molecules coming from the cytoplasm at the internal part of the membrane, forming the adhesome [161,162]. As described in Figure 2.29, the structure of a FA consists in integrin extracellular domains bounded to the ECM and intracellular domains covered by an integrin signaling layer composed of adapter proteins followed by a force transduction layer of short fibers connected to the actin stress fibers [161].

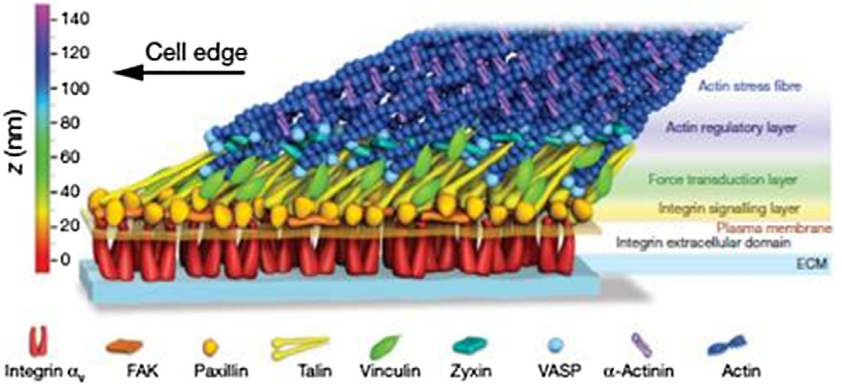

Figure 2.29: Architecture of a FA. The integrin extracellular domain is linked to the ECM. The integrin intracellular domain is covered by adapter proteins and a force transduction layer of short fibers connected to the actin stress fibers. Image extracted from reference [161].

The binding of integrins triggers the recruitment of proteins located inside the cell which results in the formation of a link with the cytoskeleton [2, 86, 156,161,162]. The proteins directly involved in the linkage with integrins are

talin, α-actinin and filamin [161]. Other molecules such as vinculin and focal adhesion kinase bind indirectly to the internal part of the integrin receptor and sustain the formation of actin stress fibers [86, 161]. One important molecule, talin, allows to stabilize the ligand and induces clustering by mediating the crosslinking of integrins with actin and other proteins such as vinculin [162]. Moreover, the mechanical forces generated by the binding of the integrins with the surface activate the binding of vinculin molecules with talin. It is interesting to know that the FAs are stabilized when vinculin are under tension [161, 164]. Apart from the clustering of integrins, the binding of FAs also triggers the recruitment of molecules regulating intracellular pathways [156].

One important factor to be also taken into account when discussing adhesion of cells is the fact that the FA structure is dynamic [161]. In fact, the dynamical assembly and disassembly of FAs play a key role in adhesion, migration, proliferation and differentiation [156]. If the disassembly is faster than the assembly, the cell becomes non-adherent; in contrast, if the disassembly is slower than the formation of FAs, the adhesion is stable. Moreover, if the formation at the leading edge and the disassembly at the rear end of the cell are rapid, the cell is migrating [85, 162]. The disassembly of FAs happens at the rear of a migrating cell or when the actin fibers disassemble [161]. Moreover, the formation of nascent adhesions in the protrusion construction and retraction are less stable [161]; the stabilization of the FAs, and thus the assembly or dissassembly of the FAs, depends on the mechanical forces exerted on them [164, 165].

Cell adhesion is the first step before the occurence of other cell behaviors such as proliferation and differentiation. Actually, the cell interactions with the environment via surface sensing or soluble factors induce mechanotransduction signals which influence cell behaviors [2, 82, 155] such as adhesion, proliferation, survival or apoptosis, shape, polarity, motility, haptotaxis, gene expression and differentiation [82]. It is interesting to note that the number of proliferating and differentiating cells follow an inverse relation [12, 160].

Among the surface properties, the rigidity is important for cell fate. As the cytoskeleton is linked to the FAs, the mechanical cues of the surface is transmitted via these FAs to the cytoskeleton which then organizes according to these cues [166]. The receptors are submitted to a tension which, in response, leads to different transcriptions of the genes and thus phenotypes [160]. As a consequence, the characteristics of FAs and thus the cytoskeleton are different on soft and stiff substrates [156].

In conclusion, the mechanical environment influences specific behaviors of cells such as differentiation [1,155]. The differentiation of MSCs in the myogenic lineage happens on firm gels coated with collagen I while osteogenic differentiation is preferred by cells adhering on still gels and neuron differentiation is preferred on soft matrix [12]. Other factors affecting cell fate are topographical and chemical cues displayed to the cells [167,168]. It is worthy to note that cell responses not only depend on material cues but also on the cell type [168].

2.5.3 Surface properties and nanopattern designs influencing mammalian cell behavior

In this section, we review the relationship between the cell morphology and the cell fate as well as the influence of various surface cues such as topography, chemistry and stiffness on cell behavior. We focus our review on stem cells which can follow different pathways of differentiation. The most studied stem cells are MSCs, neuronal stem cells (NSCs), unrestricted somatic stem cells (USSCs), skeletal stem cells and limbal stem cells (LSCs) [2].

2.5.3.1 Characteristics of the cell morphology

Cell morphology is directly related to the behavior and the fate of a cell [156]. First, the cell spreading needs to be over a critical value to prevent apoptosis. It was shown that the cell spreading is more important than the contact area with the ECM to prevent apoptosis. The fact that the spreading is critical for cells has been verified for different cell lines even though the spreading is cell line dependent [22]. While the spreading area is important for the cellular viability, it is also crucial to determine the differentiation lineage in which the cell commits (of course, the commitment also depends on the cell type) [156]. For example, a restricted cell spreading promotes adipogenesis while a large spreading favors osteogenesis [22]. Even more, the perimeter of the MSCs can be linked to the degree of adipogenic or osteogenic differentiation [22].

The cell shape also plays an important role in the cell fate. As a matter of fact, cells optimize their shape to fulfill specific functions in *in vivo* conditions [155]. Moreover the cell anisotropy is critical for directing the commitment of stem cells [22]. Indeed, the cytoskeletal tension implied in the differentiation is linked to the aspect ratio (AR) of the cell. So, a given tension is required for the commitment of a cell in a particular lineage which results in a specific

AR value [22]. For example, Lee *et al.* showed that MSCs forced to adopt a round shape on chemical micropatterned surfaces expressed more adipogenesis markers compared to neurogenesis markers [158]. On their side, Kilian *et al.* also compared the differentiation potential of MSCs on FN patterns with different geometries distributed in a non-adhesive background. They observed that a smaller area promoted the differentiation in the adipocyte lineage while a larger area promoted the osteoblast lineage. Overall, the geometrical features promoting contractility promoted osteogenesis [169].

It is worth noting that, even though cell morphology is important in determining the fate of cells, cell-cell contacts also have a great impact on the osteogenic, adipogenic [22] or neuronal differentiation [170].

2.5.3.2 Topographical cues

Contact guidance

The most famous phenomenon observed on topographical patterns is the contact guidance. It results from the sensing of the anisotropic topographical features by the cell [22] and is guided by both biological and physical factors [22]. Generally, a contact guidance leads to the elongation of the cell along grooves or ridges [22, 47, 167, 171, 172]. However, some cells do not align along the groove axis such as the neurites of hippocampus neurons [22]. Contact guidance can also be experienced by surface sensing appendices [2, 167], *i.e.* filopodia, with features with a height comprised between 10 and approximately 35 nm [160]. Following this first step, the cytoskeleton and finally the cell body align along the nanoscale guidance cue [160]. In addition to this pinpointed phenomenon, cells could change their guidance mechanism via the use of nanometer membrane projections called "nanopodia" [160]. In that case, the clustering of integrins might be reduced [47].

Broad phenomenons on topographical structures

More generally, surface microstructures influence the cell morphology and cytoskeletal organization while nanostructures affect the proliferation, differentiation and alignment [172]. This is because nanotopographical features modulate molecular arrangement, dynamic organization and signaling of the cellular adhesion machinery [155]. Thus the cellular functions are affected by the thickness, shape and spacing of patterns [172]. Badique *et al.* who produced surface structures made of poly-L-lactic acid micropillars (with a lateral size of

2-20 μm, spaced by 2-20 μm and with a height of 6 μm) studied the nucleus deformation for different lines of osteosarcoma cells. They showed that the nucleus deformation was a function of the geometry of the topography, the cell phenotype and the cytoskeletal organization [173]. Actually, the changes in cell shape and in cytoskeleton organization result in the remodeling of the chromatin which regulates the gene expression [160].

In the next paragraphs, we also explored the influence of the topographical parameters on adhesion, cell spreading, migration, proliferation and differentiation.

Cell Adhesion and spreading

The topographical features are often used for *in vitro* studies in order to trigger the cell adhesion [22, 161]. For instance, surface microwells are used to confine cells and control their aggregation [22], nanopits and nanoposts to reduce or promote cell adhesion depending on the height of the feature [160, 167, 171] and nanogratings to enhance it [171]. To sum up, nanoscale patterns tend to improve cell adhesion and growth [172] because "nanostructures enhance the topographical interactions and provide more contact points for stronger cell adhesion" [168]. On the other side, this might "restrict cell spreading therefore reducing the contacting area between cell and substrate" [168]. Not all studies agree with this conclusion as pillar shaped patterns induce large degree of extension [172] or shallow nanopits induce cell spreading [167]. Cell spreading is mediated (at least in fibroblasts) by the formation of filopodia then by the lamellipodia nucleation from the filopodia near the cell body [174]. These observations on adhesion and spreading were reported by several researchers. For example, Dalby *et al.* produced 95 nm-height islands of polystyrene with various diameters (and with an average width of 0.99 +/- 0.69 μm) and an interspacing from centre-to-centre of 1.67 +/- 0.66 μm to study the initial adhesion of fibroblasts. They showed that this nanotopography induced a faster response of fibroblasts compared to flat surfaces. They showed that the cells quickly formed filopodia that sensed the islands and seemed to use nanotopography as "stepping stones" (Figure 2.30) [175].

On their side, Zhou *et al.* showed that HeLa cells aligned along the grooves of bare PDMS micropatterns (with a width varying from 1.5 to 3 μm, an interspacing from 2 to 30 μm and a depth from 0.2 to 1.1μm); however this alignment was reduced when the surfaces were coated with FN and when the spacing between the features was increased. Moreover, the cell alignment was

proportional to the groove depth and the spreading area decreased with a groove interspacing increasing [176].

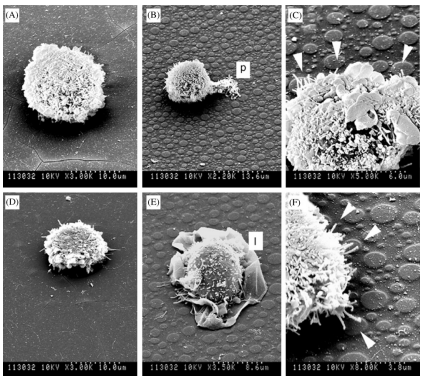

Figure 2.30: SEM images of fibroblasts on a flat control surface (left) and 95 nm islands (middle and right) after 5 (A-C) and 30 minutes (D-F) incubation. The cells on the nanopatterned surface reacted faster than the ones on the control surface. The arrows show filopodia interacting with the islands at both times (C and F). Image extracted from reference [175].

Migration

Topography can also induce migration of cells which is called "topotaxis" [22]. Indeed, one effect of the topography on a cell is to induce cell polarity [171] which is required for migration since cell produces a protruding end and a rear end. Microtopography can be used to induce migration. For instance, multidirectional migration of cells is observed on microgrid patterns [172]. But migration can also be regulated on surfaces displaying nanocues [22]. For example, migration velocities are increased in the direction of the nanograting axis [171]. It also seems that optimal topography dimensions for adhesion and migration can be found. For instance, Lamers *et al.* studied the adhesion and migration of osteoblasts on different nanopatterns (72-536 nm-ridges, 77-453 nm-grooves and 33-158 nm-depth) made of silicon. They evidenced that the pattern showing grooves of 305 nm and ridges of 320 nm with a depth of 143 nm allowed for the best cellular adhesion and migration [159].

Proliferation and differentiation

Proliferation and differentiation are also topography dependent [22]. Indeed, the size and order of nanopattern topography can influence the fate of stem

cells [166, 172]. The time period at which the cell is exposed to a particular topography also influences their fate [166]. For example, nanoroughness increases protein adsorption and thus cell viability [2] allowing for a further proliferation [22, 156] or differentiation [2, 171].

Proliferation is influenced by the lateral size and the height of the nanotopography: a larger proliferation occurs at lower height (50-100 nm) compared to higher height (500-600 nm) [2, 172]. As explained above, Dalby *et al.* produced 95 nm-height islands of polystyrene with various diameters and studied the initial adhesion and proliferation of fibroblasts on these surfaces. They found that, even though the adhesion reaction of fibroblasts was faster on nanotographical patterns, the proliferation of these fibroblasts was impaired by topography probably due to the change in cell shape resulting from the adhesion on the islands [175].

The topography can be used to preserve stemness or to induce differentiation in a particular lineage. First, nanopatterns may be used to maintain the stemness state of embryonic stem cells [177]. For example, an "enhancement of self-renewal and proliferation was observed in mouse embryonic stem cells cultured on a nanofibrillar scaffold in comparison with a tissue culture plastic surface in the presence of leukemia inhibitory factor" [171]. Bae *et al.* explored the use of nanotopographical structures for the conservation of the stemness of human embryonic stem cells. For this, they produced surfaces decorated with nanopillars of increasing diameter (from 120 to 360 nm and a center-to-center interspacing of 440 nm). Nanopillars allowed the formation of compact cellular colonies. The expression of undifferentiated markers increased with the decrease of the nanopillar diameter and the formation of FAs was unstable on nanopillars having dimensions ranging from 120 to 170 nm [178].

Differentiation in a particular lineage is also influenced by topographical patterns. For instance, it was shown that microgrooves can be used to control the differentiation. Indeed, the epigenetic state of cells can be changed by confining them in microgrooves which induces an elongation of nuclei. The effect of the microgrooves is thus similar to the effect of epigenetic molecules. This effect also occurs on nanofibers suggesting that the change in morphology is responsible for the epigenetic state [179]. For example, Charest *et al.* explored the reaction of myoblasts to topographical patterns composed of grooves and ridges or holes with a width or diameter, respectively, ranging from 5 to 75μm. The myoblasts aligned along the grooves compared to the surfaces with holes

or the flat control for which no particular alignement was observed. While influencing alignment, the topographically patterned surfaces did not influence the density or differentiation of myoblasts [180]. On their side, Zouani *et al.* seeded human MSCs on patterned wells showing lateral micro-dimensions of 8.5 μm and a depth varying from 10 to 100 nm. Small topography promoted the adhesion while 100 nm depth allowed for a collective cell organization leading to differentiation in the osteoblast lineage (Figure 2.31) [181].

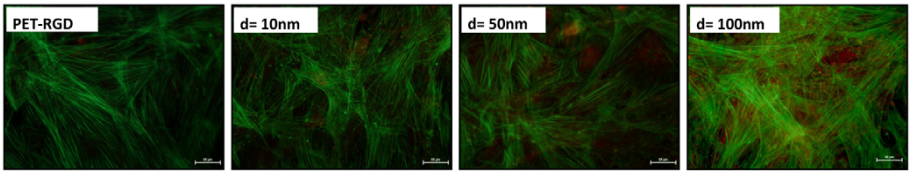

Figure 2.31: Differentiation of human MSCs after three weeks on surfaces showing wells with depth (d) varying from 10 to 100 nm. The more osteopontin, the more the cells are led to the differentiation in the osteoblast lineage. Actin, green; osteopontin, red. Scale bars: 50 mm. Image extracted from reference [181].

Finally, hierarchical structures are interesting because they combine the micro- and nanotopography. They can notably increase cell contact with the surface providing cues for proliferation and differentiation [172].

2.5.3.3 (Bio)chemical cues

In this section, we focus on chemical and biochemical cues influencing the adhesion, cell spreading, viability or apoptosis, migration, proliferation and differentiation.

Cell adhesion and spreading

The adhesion of cells on surfaces depends on the nature of the material and the chemical functions displayed, the distance between adhesive moieties such as RGD, their density, their patterning, their accessibility or specificity and their co-presentation.

When we focus on the functional groups displayed to cell, we can distinguish difference in the reaction of different cell lines. For example, it was shown that fibroblasts as well as keratinocytes adhere more strongly on amine and

carboxylic acid terminated surfaces [171]. On the contrary, surfaces bearing CH3, PEG and OH terminated groups showed less attachment [171].

When looking at biochemical factors, we first think of RGD peptides. It is well-known that the distance between the RGD moieties plays an important role in the formation of FAs. Indeed, a critical distance of 60-70 nm for the display of ligands must not be exceeded for the clustering of integrins [1,22,47,167,182]. At the nanoscale, RGD ligands separated by 70 nm are not able to induce mature adhesion [160,161]. However, surface tension development can happen if the distance between the ligands is smaller than 70 nm [161]. This tension depends rather on the number of integrins than on an increase of tension per molecule [161]. For example, Cavalcanti-Adam *et al.* showed that embryonic fibroblasts spread on surfaces displaying c(RGDfK) spaced by 58 nm while their spreading was limited on surfaces with 110 nm spaced RGD (Figure 2.32) [183]. Moreover, Cavalcanti-Adam *et al.* also showed that when cells were seeded on 108 nm spaced RGD peptides, the spreading was delayed compared to cells on 58 nm spaced peptides [184].

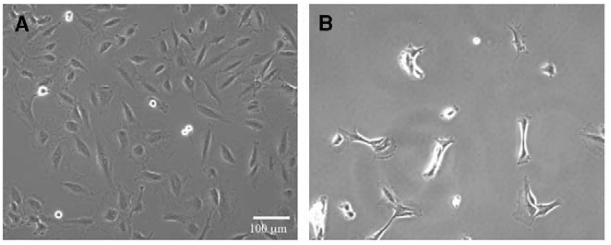

Figure 2.32: Phase-contrast images of fibroblasts after 24 hours on surfaces with immobilized RGD peptides placed at (A) 58 nm and (B) 110 nm interdistance. Cells on (A) show a spread morphology while cells on (B) have a limited cell spreading. Image extracted from reference [183].

The decrease of the distance between the RGD moieties is obtained by increasing their density on the surface [1,85]. However, the distribution of these moieties is also important for the cellular response [1]. As a consequence, RGD density is related to cell spreading, cell viability, focal contact formation and cell proliferation [85]. Indeed, clusters containing 4-5 ligands are necessary to get stable adhesion [161]. It is worth noting cell spreading is increased on more adhesive surfaces [156]. Gallant *et al.* used a gradient of immobilized RGD peptides to evaluate the effect of their density on smooth muscle cells. They

first pointed out that, with increasing RGD density, the number of adherent cells increased. Then they evidenced that the cell spreading was smaller on high density surfaces and the aspect ratio was lower on low density surfaces (Figure 2.33) [185].

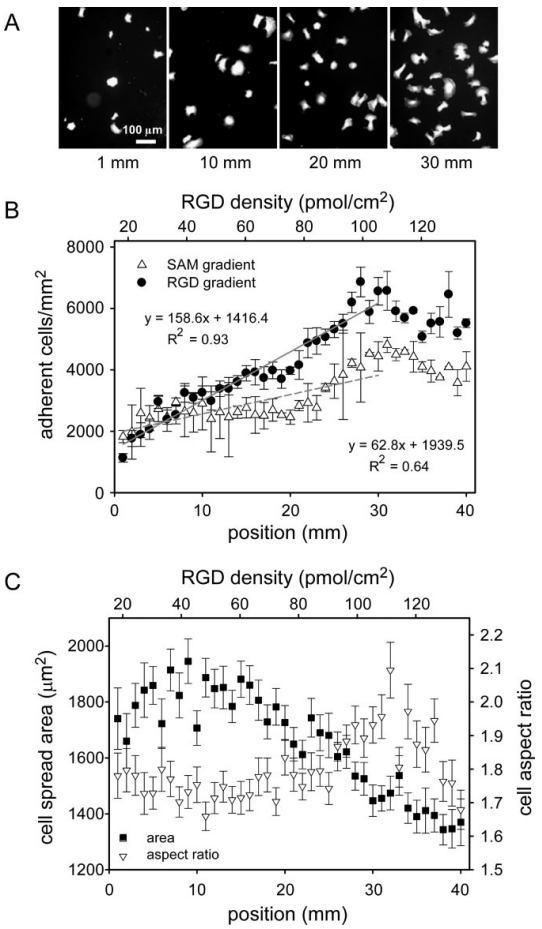

Figure 2.33: Characteristics of smooth muscle cells adhered on surfaces showing a gradient of RGD peptide density. (A) microscopy images showing morphology of cells adhered at different distances (from 1 to 30 mm) from the starting point of the surface gradient. The RGD density varies from 20 pmol/cm^2 at 1 mm to 100 pmol/cm^2 at 30 mm. Density (B) and spread area (C) of adherent cells as a function of the position on the peptide gradient. Image extracted from reference [185].

The RGD ligand can also be patterned to influence the adhesion of cells.

Actually, the size of the RGD adhesive patches is essential to control cell spreading [161]. Many examples of RGD patterning can be found in the litterature. For example, Lehnert *et al.* produced different patterns of ECM coated regions separated by a SAM of hydrophilic protein-resistant thiol. They showed that melanoma cells spread on ECM coated regions as small as 0.1 μm^2 when the interdistance between the patches was less than 5 μm. The spreading behavior of cells did not occur when the dots of at least 1 μm^2 size were separated by more than 30 μm. They thus proved that the spacing of adhesive regions influenced cell behaviors [186]. On their side, Kalinina *et al.* also tested the adhesion of murine fibroblasts on micropatterned surfaces showing 42.2 μm-width peptide lines spaced by 19.4 μm 1-octadecanethiol passivated gold stripes of 63 nm-height. Cells spread on these peptide lines after one hour but not on the non-functionalized parts and also produced FAs (Figure 2.34) [187]. Hoesli *et al.* tested the endothelial cell adhesion and proliferation on surfaces showing micropatterns of GRGDS and WQPPRARI peptides. They found that micropatterns of RGD allowed for the control of cell shape and orientation. Surfaces micropatterned with both peptides led to directional spreading of cells [188]. Gallant *et al.* studied the fibroblast adhesion strengthening on different circular islands covered with FN, with dimensions ranging from 2 to 20 μm in diameter and distributed in a non-adhesive background. An increase of the adhesive area increased the adhesion strength which attained a threshold for 10 μm diameter islands. They also confirmed that a critical number of bound integrins are necessary for adhesion [189]. Interestingly, they evidenced that the binding of integrins was related to the adhesion strength but that FA assembly provided only 30% of the strengthening response [189].

Ligands can be patterned or spaced ideally to induce cell adhesion but if the accessibility of the peptides is not optimized, the cell reaction does not occur as expected. In fact, a minimal spacer length (*i.e.* the distance between the anchoring point and the surface) might be necessary for cell attachment; however cell attachment might be impaired when the spacer is too long [85]. For instance, Tugulu *et al.* used P(HEMA) and PPEGMA brushes to immobilize GGG**RGD**S. The study of the reaction of human umbilical vascular endothelial cells on the grafted brushes allowed to conclude that more hydrophilic and longer spacer length might increase ligand motility thus rendering more difficult for the cell integrins to interact with the RGD peptides. This confirmed that the polymer on which the RGD peptide is grafted might influence the adhesion

of cells [190]. On their side, Pallarola *et al.* used different spacers to display the c(-**RGD**fX-) peptide specific to integrin $\alpha_v\beta_3$ from rat embryo fibroblasts. They showed that polyproline spacer was better for cell adhesion than aminohexanoic acid and PEG spacers [191]. Navarro *et al.* studied the effect of the grafting position of RGD peptide in poly(methacrylic acid) (P(MAA)) brushes on cell behavior. They showed that burying the RGD peptide into the brush had an influence on the osteoblast cell spreading and on FA formation: the spreading area was smaller and the FAs were located at the internal part of the cell instead of the periphery [192]. The specificity of RGD peptide to a specific integrin meaningfully influences sustainability of the surface and thus cell behavior. For example, cyclo(**RGD**fk) is more resistant to enzymatic degradation and has a matching conformation to conjugate with integrins [22].

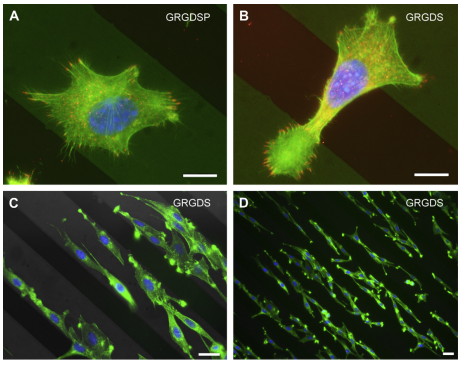

Figure 2.34: Morphology of cells adhered on micropatterned surfaces. (A,B) adhesion of murine fibroblasts on stripes modified by RGD derivatives; cells cultured for (C) 4 hours and (D) 48 hours on surfaces modified by RGD derivatives. The cells spread on the functionalized lines. Vinculin staining for focal contacts in red, actin filament labeling with phalloidin in green, staining of nuclei with 4',6-diamidino-2-phenylindole (DAPI) in blue. Scale bars are (A,B) 10 mm and (C,D) 20 mm. Image extracted from reference [187].

Finally, the co-presentation of the RGD peptide with another ligand can improve cell function. For example, Zhang *et al.* compared the effect of RGD sequence and the binding domain of fibronectin $III_{9,10}$, containing RGD and a synergistic site of RGD, on adhesion of fibroblasts. They compared the effect of surfaces bearing the same concentration of RGD or III fibronectin domain. They were able to show that fibroblasts adhesion and spreading were higher on surfaces with immobilized fibronectin domains [193]. Desseaux *et al.* used a

P(HEMA) brush to co-present RGD and PHSRN (*i.e.* a synergistic sequence for RGD moiety in FN) peptides. They demonstrated that the co-presentation at equal concentrations enhanced fibroblast adhesion compared to single presentation (*i.e.* RGD or PHSRN). Moreover, they pointed out that cells could adhere onto surfaces bearing adhesive peptides buried at a distance of 23 nm from the interface [194].

Migration

The migration of cell occurs towards a region showing higher adhesiveness [156]. It is called haptotaxis when the migration results from a gradient of immobilized ECM proteins [22]. Moreover, a low level density of RGD peptides presented in a clustered manner is necessary for migration and also promotes secretion of matrix molecules [85]. For example, Mahashwari *et al.* studied fibroblasts onto surfaces showing different densities of clustered or not clustered RGD peptides to study the influence of YG**RGD** on migration. First, they showed that the migration speed increased with the RGD density. Then they interestingly showed that clusters of RGD increased migration speed compared to surface without clusters but the same average density of RGD. Moreover, increasing the density and having clusters of RGD had a positive effect on the formation of well-formed stress fibers [195]. Arnold *et al.* showed that the spacing between the ligands influenced the migration as well as the polarization of the osteoblasts. They produced surfaces coated with gold nanopaticles in a hexagonal patterns on which were immobilized c(**RGD**fK) moieties. Their spacing ranged from 50 to 80 nm with an non-adhesive background of PEG. For a spacing of 50 nm between the RGD features, cells were well-spread while for 80 nm they were elongated. When facing a gradient of nanoparticles grafted with the RGD derivatives, cells polarized in the direction of the gradient with an angle of 0 to 30° when the spacing of nanoparticles is comprised between 60 and 70 nm [196].

Proliferation and differentiation

The proliferation and differentiation of cells also depend on the chemical and biochemical agents displayed to them. Indeed, to retain MSCs multipotency, cell adhesions must allow cell proliferation while still being small enough to repress the differentiation machinery to take place [160].

The surface chemistry influences the differentiation of cells [2]. Indeed, the

chemical functions displayed to the MSCs influence their phenotypes propably due to the sequestration of the signaling molecules [166]. For instance, CH3 can maintain MSC phenotype while NH2 and SH promote osteogenesis [171]. Lan *et al.* showed that SAM surfaces showing different end-groups and coated with FN induced different degrees of proliferation and differentiation for myoblasts as a function of the nature of the end-group. COOH and NH2 surfaces supported well proliferation compared to CH3 and OH while a limited differentiation occurred on OH. Actually, COOH and NH2 surfaces allowed for the binding of two integrins compared to OH and CH3 [197].

The cell proliferation increased with the adhesiveness of the surface [156] but the density of RGD peptides can also influence the fate of differentiation of cells [85]. For instance, Rowley *et al.* modified alginates containing different mannuronic acid and guluronic acid ratios with RGD. They deduced that a particular combination of RGD density and monomer ratio was needed to induce efficient differentiation. A lower RGD density of 1 fmol/cm^2 promoted adhesion and spreading while a higher rate of proliferation was reached for a density of 30 fmol/cm^2. The intermediate density of 10 fmol/cm^2 induced fusion of myoblasts. They thus showed that the density of RGD ligands pushed myoblasts either in the proliferation or in the differentiation path [84]. Another example is given by Kilian *et al.* who used SAMs grafted by G**RGD**SC (a linear RGD peptide) or **RGD**fC (a cyclic peptide with a higher integrin affinity) at different densities and with an OEG background to study the differentiation of MSCs. They measured alkaline phosphatase expression (*i.e.* a marker for osteogenesis) and showed that linear RGD peptide did not induce a high alkaline phosphatase expression compared to the cyclic RGD peptide and the control surface coated with FN. However, surfaces grafted with a high density of linear peptide tended to induce a higher differentiation expression in the skeletal-muscle lineage compared to other surfaces; in contrast, surfaces grafted with the linear peptide at low density tended to promote neurogenesis. Cell on cyclic RGD-modified surface displayed a higher number of stress fibers compared to linear RGD [198].

Using nanocues [22, 161, 166] and a nanoscale periodicity can influence differentiation too [160]. Indeed, a controlled biochemical nanodisorder is important to induce osteogenic differentiation [160]. Cheng *et al.* produced surfaces covered by nanodots grafted with RGD peptides and distributed in a non-adhesive background. These RGD surfaces allowed the spreading of cells.

The nanopatterned surfaces (dots of 150 nm with an interdistance of 350 nm and dots of 80 nm with an interdistance of 110 nm) allowed the formation of FAs at the periphery of cells whereas on homogeneous surfaces, FAs were formed around the nuclei and at the periphery of cells. Nanopatterned surfaces led to a loss of stemness compared to homogeneous surfaces (Figure 2.35) [199]. On their side, Wang *et al.* produced surfaces showing RGD microdomains with a lateral size of 35 or 65 μm able to isolate a single cell. Inside these domains, the RGD moieties showed an interdistance of 46 or 95 nm. The cell spread in the same way regardless of the spacing of RGD peptides. The smaller spacing led to a stronger cytoskeleton and intracellular tension even when the spreading area of cells was the same. The condition providing the higher intracellular tension promoted osteogenesis [200]. Another experiment done by Wang *et al.* used arrays of RGD ligands with an interdistance varying from 37 to 124 nm. With an increasing spacing, the number of adherent cells and the spreading area of cells decreased while the circularity of cells increased. Both osteogenic and adipogenic markers increased with spacing even though the increase is not significant for a spacing higher than 70 nm. When the induction of both osteogenic and adipogenic lineages was done, the osteogenic lineage was favored. The spacing thus may need to be tuned to obtain different differentiation pathways [201].

Other factors can influence the differentiation of cells. For instance, Lee *et al.* showed that combining cell shape with matrix molecules specific to a cell lineage helped to differentiate cells into the targeted lineage even though cell spreading seemed to be a stronger factor for differentiation [158]. For example, Ren *et al.* immobilized BMP-2 and FN on poly(OEGMA-r-HEMA) brushes and demonstrated that these coatings induced adhesion and a higher differentiation (*i.e.* alkaline phosphatase activity) compared to the bare pristine substrate [87]. On their side, Zouani *et al.* grafted BMP-2 growth factor on a matrix mimicking *in vivo* microenvironment and showed that this factor is essential for osteoblast maturation. Moreover, cells seeded on the PET surface grafted with RGD and BMP-2 showed a greater volume than the ones seeded on PET grafted with BMP-2 alone [88].

Finally, the degradation of the substrate surface can influence stem cell phenotype [166]. Actually, this happens *in vivo* with degradation of ECM molecules [166].

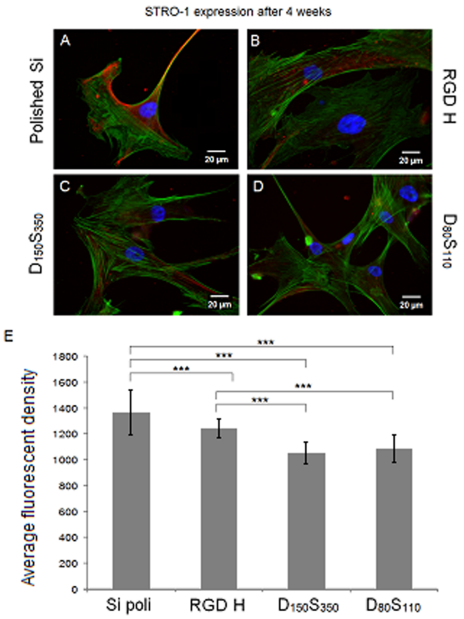

Figure 2.35: Commitment of human MSCs after 4 weeks in culture on (A,B) control surfaces (*i.e.* a bare silicon substrate (A) and a homogeneous surface grafted with RGD (B)) and (C,D) nanopatterned surfaces (*i.e.* dots of grafted RGD of 150 nm with an interdistance of 350 nm (C) and dots of grafted RGD of 80 nm with an interdistance of 110 nm (D)). STRO-1 (stemness marker) stained in red, F-actin stained in green and cell nucleus in blue. (E) Amount of STRO-1 measured on the different surfaces. The lost of stemness is visible for nanopatterned surfaces.*** represents a p-value of less than 0.05. Image extracted from reference [199].

2.5.3.4 Mechanical cues

Mechanical sensing mechanism of the surface

Stem cells respond to mechanical forces [155]. Actually, cells sense the stiffness of the surface via FAs, through which the forces are transmitted [168]: the cytoskeletal tension is proportional to the elastic modulus of the substrate [155,168]. The force exerted on the filaments produced by the cell can be maintained in the direction of the force tension. This results in the "orientation selection" [161]. This last observation can be seen in the research done by Monge *et al.* who designed stiffness patterns varying in their size (2-100 μm), their shape (circle or lines) and their spacing (5-100 μm) and tested them against myoblasts. Myoblasts grew on stiffer features for circular patterns. For linear patterns,

the adhesion of myoblasts depended on the dimensions and the interdistance between the stiff and soft lines. While some soft lines were overlapped by cells when the interdistance between the stiffer lines was low, some were not because of their larger dimensions. The cell alignment along the lines was thus also influenced [202]. Moreover, less spreading was seen on soft surfaces [22]. It is worth noting that cell might even remember the previous exposition to a particular mechanical environment [203].

Cell spreading, migration and proliferation

The stiffness of the substrate regulates cell functions [168] such as cell motility, cell spreading and proliferation [165]. Migration occurs along a gradient of matrix rigidity (durotaxis) or a gradient of mechanical forces (mechanotaxis) [22]. Proliferation can be modulated as a function of the substrate rigidity. For example, Vazquez *et al.* developed crosslinked PEM films with rigidity varying with the amount of crosslinkable segments. They showed that C2C12 myoblasts were influenced by this change of rigidity: the spreading and proliferation were larger on more rigid surfaces [204].

Differentiation

The stiffness also influences the commitment of MSCs: soft matrix induces neurogenesis, stiff matrix myogenesis and rigid matrix osteogenesis [22, 161, 165]. Indeed, the cytoskeletal organization and thus the differentiation is influenced by the substrate stiffness [2, 166]. The size of adhesive nanofibers controls FA formation and also induces a curvature of the membrane at the adhesion site [161]. Migliorini *et al.* compared the elasticity of patterned (Squared pillars of 250 nm-width with an increasing height of 35, 100, and 360 nm and period of 500 nm) and unpatterned surfaces of PDMS. They deduced that when the elasticity was lowered under 400 kPa, the differentiation into the neural lineage increased [205]. Thus the elasticity of the substrate plays a key role in the differentiation to the neural lineage.

2.5.4 Description of SCAPs

Five human dental stem or progenitor cells have been isolated and characterized till now. Among these cells lie the stem cells of the apical papilla (SCAPs). These cells have MSC-like characteristics such as self-renewal and multilineage

differentiation potential [206]. SCAPs are at the origin of primary odontoblasts responsible of the formation of root dentin but can commit to three cell lineages: osteo/odontogenic, adipogenic and neurogenic. SCAPs are less prone to adipogenesis in comparison with MSCs extracted from bone marrow but appear more potent for neurogenesis compared to bone marrow MSCs. This is probably due to their neural crest origin [206, 207]. Indeed, SCAPs express neurogenic markers without neurogenic stimulation [206].

2.6 Surfaces with dual purposes

Some researchers have already explored the possibility to combine different properties towards bacterial and mammalian cells. Here, we focus on the description of such surfaces that combine chemical, bioactive and topographical functionalities to control the development of both mammalian and bacterial cells.

One example of the use of killing agents is done by the work performed by Ferraris *et al.*. They embedded silver ions into the titanium oxide rough surfaces. These ions were progressively released confering an antibacterial activity against *S. aureus* while being biocompatible for human osteosarcoma cells. However, some cytotoxicity have been outlined [208].

The topographical modifications tested mainly include modifications of nanoroughness. Daw *et al.* evidenced the existence of a potential ideal roughness (with R_a roughness comprised between 140 and 172 nm) which prevented the colonization of the surface by *Porphyromonas gingivalis* while allowing the adhesion and proliferation of bone marrow stromal cells [209]. On their side, Svensson *et al.* also used nanostructured surfaces (with a R_a roughness of 26 nm) to discriminate the behaviors of bacteria (*S. epidermidis*) and cells (monocytes/macrophages). The amount of *S. epidermidis* was decreased on nanostructured surfaces and their viability was impaired compared to smooth surfaces. On the contrary, monocytes/macrophages did not show any specific behaviors on the nanostructured surfaces [210].

The biochemical modifications discriminating the bacterial and cell behaviors are based on the modifications of polymer coatings or on the patterning of biocompatible polymers. For example, Chua *et al.* formed PEMs of hyaluronic acid and naturally antimicrobial chitosan grafted with RGD peptides. These coatings retained antimicrobial activity against *S. aureus* while allowing the

adhesion and proliferation of osteoblasts [211]. On their side, Muszanska *et al.* used non-adhesive brushes of triblock copolymer pluronic F-127 grafted with AMPs and RGD peptides to reduce biofilm formation by *S. aureus*, *S. epidermidis* and *P. aeruginosa* and to allow the growth of fibroblasts [212]. Moreover, varying the nature of peptides or molecules immobilized on the surfaces may have diverse effects. For example, He *et al.* showed that the immobilization of adhesive RGD peptides has no apparent effect on the adhesion of *E. coli* and *S. aureus*. On the contrary, immobilized collagen promoted *S. aureus* adhesion. Fibroblast adhesion, on its side was promoted by both immobilized molecules. The choice of the adhesive ligand thus impacted the adhesion of bacteria and mammalian cells [213]. The concentration of biomolecules is also important for the behaviors of cells and bacteria. Dexter *et al.* notably coated FN in different concentrations on culture plates. The fibroblasts did not show any difference for adhesion. However, the adhesion of *S. epidermidis* after 4 hours, decreased with FN concentration increasing [214]. Finally, inducing periodicity of a non-adhesive polymer also leads to contrasts between bacterial and mammalian cell behaviors. In their study, Wang *et al.* designed patterns composed of submicrometer non-adhesive microgels with interspacing ranging from 0.5 to 3 μm, deposited on glass surface. They tested the adhesion of *S. aureus* on these surfaces and observed that an interspacing equal or smaller to the bacterial size induced the repression of adhesion. On the contrary, the spreading area of osteoblast-like cells was similar to the ones adhered on unpatterned surfaces when microgels were spaced by 1.5 μm or more. So there exists an optimal interspacing for cell spreading and bacterial adhesion inhibition [215].

This state of the art highlights the fact that the adhesion and the development of bacterial and mammalian cells can be individually controlled by varying the topography, stiffness and biochemistry of the material surface. Moreover, the patterning of these properties at the micro- or nanoscale also enables to control the bacterial and mammalian cell behaviors. However, surfaces fulfilling the dual goal of controlling both bacterial and mammalian cells at the same time are not yet fully developed. Nowadays, the fabrication of such surfaces is still a challenge and finds its interest for biomedical applications.

Chapter 3

Synthesis of functional polymer brushes

3.1 Introduction

As the goal of this PhD thesis was the elaboration of biofunctionalized surfaces for the control of bacteria and mammalian cell behaviors, we needed to choose the appropriate platform to display bioactive molecules specific to these two types of cells. Besides this primary consideration, the platform used needed to be included into a nanopattern. We therefore sought the different approaches to produce chemical nanopatterns [24, 47, 51, 216] in order to select the appropriate technique for our project. Among those techniques lie the micro-contact printing, nanoimprint lithography, photolithography, electron beam lithography, supramolecular nanostamping, Langmuir-Blogett deposition and dip-pen nanolithography. We chose nanoimprint lithography for its resolution at the nanometer scale, its wide variety of possible molecules used for backfilling the exposed surfaces, its tunable pattern and its fabrication speed [216].

Among the various molecules that can be grafted in the nanopattern, copolymer brushes are an interesting option. Indeed, the polymerization of copolymer brushes bearing functional groups is useful to prepare multifunctional platforms allowing the further grafting of different bioactive molecules. Polymer brushes are frequently used to modify biomaterial surfaces because they show a great variety of mechanical and chemical properties which depend on their nature

and structure [20] and can be further chemically modified through various post-polymerization treatments [40, 43]. Moreover, the amount of bioactive molecules that can be grafted per surface unit on the brushes is higher than the one allowed on SAMs due to the greater number of functional groups on their backbone chain [39].

Here, the grafting from technique was selected to synthesize polymer brushes and prepare multifunctional platforms. Indeed, this approach presents several advantages compared to the grafting to or adsorption techniques. First, The covalent grafting of polymer chains onto the substrate is necessary to prevent its detachment and thus a decrease of surface functionality. Moreover, the polymerization of the brush from the surface provides a higher grafting density of polymer chains and thus a higher concentration of functional groups per surface unit [26, 27, 45]. Furthermore, the variety of monomers that can be used in the grafting from technique allows for a large diversity of functional group that can be further modified after polymerization [29]. These brushes are also easily patterned as is exampled by Yu et *et al.* who used ATRP technique to polymerize PNIPAAm on nanopatterned lines of a SAM of ATRP initiator [78].

In this study, we defined several criteria to select the nature of polymer brushes suited for the design of chemical nanopatterns. We wanted biocompatible and anti-fouling brushes that provide a support for further grafting with bioactive compounds. These two characteristics were necessary to, first, ensure the viability of cells on our nanopatterns but also to enhance specific interactions of bacteria and cells with the biomolecules displayed. Salwiczek *et al.* mentioned some low-fouling polymer brushes of different nature such as polyacrylamide, dextran, poly(N-sulfobetaine-methacrylamide), poly(N-hydroxypropylmethacrylamide) and PEG-based polymers [20]. Among these examples, the brushes based on OEG derivatives have been the most studied. Indeed, these brushes are non-toxic, non-immunogenic, non-antigenic, anti-fouling, chemically inert and show great biocompatibility [22, 45, 134]. Due to these properties, Cheng *et al.* used them for the preparation of an anti-fouling background alternating with areas which displayed bioactive molecules to MSCs [217]. Glinel *et al.* also used OEG monomer derivatives to synthesize brushes as a non-adhesive layer allowing the interaction of bacteria with grafted magainin I antimicrobial peptide only [64]. The chemically inert character of these brushes is increased with their packing density as well as the polymer brush thickness [134, 218]. The second criterium we focused on was the

reactive groups present on the monomers used. In this context, monomers derived from ethylene glycol and bearing functional groups such as carboxyl, hydroxyl or amine are of particular interest for the grafting of biomolecules. Indeed, brushes synthesized from these monomers show lateral chains ended by these groups which can be advantageously used to graft antimicrobial or adhesive molecules used in the biomaterial field. For instance, Glinel *et al.* developed copolymer brushes of di(ethylene glycol) methyl ether methacrylate (MEO_2MA) and hydroxyl-terminated oligo(ethylene glycol) ether methacrylate (HOEGMA) whose pendent hydroxyl groups were grafted by antimicrobial peptides to produce bactericidal coatings [64]. Laloyaux *et al.* also synthesized thermoresponsive brushes based on MEO_2MA, HOEGMA and HEMA which were further grafted by an antimicrobial peptide to produce polymer brushes showing bactericidal or anti-fouling properties, depending on the temperature. Indeed, it was shown that the surface properties of these brushes switched from cell-repellent to bactericidal with the temperature due to the intrinsic thermoresponsive behavior of the copolymer chains [219]. Another example was provided by Bozukova *et al.* who modified a poly(2-hydroxyethyl methacrylate-co-methyl methacrylate) hydrogel with oligoethylene glycol methyl ether acrylate to confer anti-fouling properties to the surface [220]. Tugulu *et al.* also showed that P(HEMA) and P(HOEGMA) brushes, grafted with a mammalian cell adhesive (RGD) peptide, immobilized human umbilical vascular endothelial cells on the surface; their objective was to study the feasibility of promoting endothelialization of blood-contacting biomaterials [190]. These different examples show that PEG-based brushes can be used to provide both anti-fouling or bioactive properties, depending on the post-functionalization performed on their reactive pendent groups.

In this PhD thesis, we prepared four different hydrophilic polymer brushes based on OEG derived monomers and/or methacrylic acid: P(HEMA) (Figure 3.1a), P(MAA) (Figure 3.1b), P(HOEGMA) (Figure 3.1c) and poly(2-hydroxylethyl methacrylate-*co*-methacrylic acid) P(HEMA-*co*-MAA) (Figure 3.2). These brushes show either hydroxyl or/and carboxyl functions that can be used subsequently to graft bioactive moieties or substances. P(HEMA) and P(HOEGMA) have a methacrylate backbone and a lateral oligo(ethylene glycol) chain providing anti-fouling properties. The difference between these two brushes is the length of the lateral chains which consist of one ethylene glycol unit for HEMA monomers and oligo(ethylene glycol) composed of around

six units for HOEGMA monomers. Both brushes bear hydroxyl groups at the end of the lateral chains allowing their further biofuntionalization. Compared to P(HEMA) and P(HOEGMA) brushes, P(MAA) has also a methacrylate backbone but bears lateral carboxylic acid groups. Having both HEMA and MAA monomers in the same backbone would allow to graph different bioactive molecules on the respective carboxylic and hydroxyl groups.

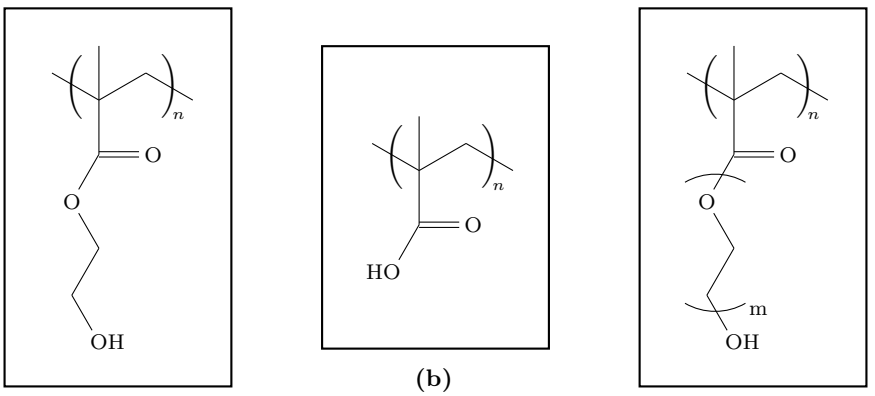

Figure 3.1: Chemical structures of (a) P(HEMA), (b) P(MAA) and (c) P(HOEGMA) chains.

Having well-defined polymer brushes showing homogeneous composition along polymerization time as well as the same length after a given polymerization time is essential to obtain specific properties such as anti-fouling characteristics. Living polymerization is often used to fulfill these objectives [29] and to reach multifunctional polymer brushes. Among the different living polymerization approaches, ATRP is very popular as it offers numerous advantages such as controlling the kinetics of the brush growth, use of common solvents and ambient growth conditions [131]. We thus chose the surface-initiated atom transfer radical polymerization (Si-ATRP) technique to perform the synthesis of the brushes based on the macromolecules described in Figures 3.1 and 3.2 despite the potential difficulties encountered with carboxylic acid residue. Indeed, even if this chemical group can complex with the catalyst of ATRP rendering it useless [221, 222], Tugulu *et al.* succeeded in polymerizing from the surface sodium methacrylate at an optimum pH of 9 [223]. Following its example, Laloyaux *et al.* succeeded in copolymerizing from the surface MEO_2MA bearing

an ethylene glycol side chain of two units and MAA by setting up the pH to 9 [224]. The ATRP approach was thus selected to produce polymer brushes during this PhD project in order to obtain P(HEMA), P(MAA), P(HEMA-*co*-MAA) and P(HOEGMA). First, an ATRP initiator was grafted on the surface using gas phase silanation to form a self-assembled monolayer. Then, the ATRP polymerization was initiated thanks to this SAM of ATRP initiator (Figure 3.3).

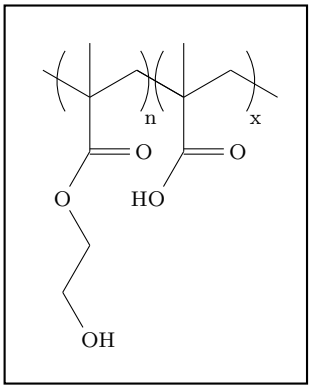

Figure 3.2: Chemical structure of random P(HEMA-*co*-MAA) copolymer.

In a first approach, we have systematically investigated the kinetics of growth as well as the composition of the different brushes (expressed in monomer ratio) allowing us to select the brushes that will be used to prepare the multifunctional patterned platforms for cell studies.

Figure 3.3: Silanation and ATRP polymerization steps for the formation of an homogeneous brush layer on silicon substrate.

3.2 Materials and methods

3.2.1 Materials

Single-side-polished (100) silicon wafers were purchased from TOPSIL. (3-(chlorodimethylsilyl)propyl 2-bromo-2-methylpropanoate) ATRP initiator was synthesized as described previously [225]. 2-hydroxylethyl methacrylate (HEMA) (97 %) and hydroxyl-terminated oligo(ethylene glycol) ether methacrylate (HOEGMA), copper(II) chloride (99.999 %) ($Cu(II)Cl_2$), 2,2'-Bipyridyl (bipy) and sodium hydroxide (97 %) (NaOH) were obtained from Sigma-Aldrich. Methacrylic acid (MAA) and copper(I) chloride (99 %) (Cu(I)Cl) were provided by Acros. Absolute ethanol (99 %) and absolute methanol (99.8 %) were bought from VWR. Milli-Q grade (resistivity of 18.2 mΩ) was produced by a Milli-Q® Reference system of Merck Millipore. All three monomers were used without purification.

3.2.2 Synthesis of polymer brushes

3.2.2.1 Grafting of ATRP silane

Silicon wafers were cut into 1x1cm^2 then cleaned by immersion in a freshly prepared piranha mixture (H_2O_2(35%):H_2SO_4(98%) (1:1 v/v)) for 20 minutes then rinsed extensively with Milli-Q water. An additional UV/ozone cleaning of 10 minutes was done right after piranha cleaning with UVO-Cleaner 42-220 from Jelight Company Inc. The cleaned samples were then placed on a teflon sample holder in a schlenk reactor placed in an oil bath heated at 80°C. The schlenk tube was then degassed to remove water and oxygen (argon (Ar) filling and vacuum cycles: 5 minutes of Ar, 10 minutes of vacuum, 30 minutes of Ar and 1.5 hours of vacuum), refilled with Ar. 15 μL of ATRP silane initiator (Figure 3.4) was then injected in the tube. The reaction was carried out for 2 hours. At the end of the reaction, the wafers were removed from the tube, washed with methanol then dried with a stream of N_2.

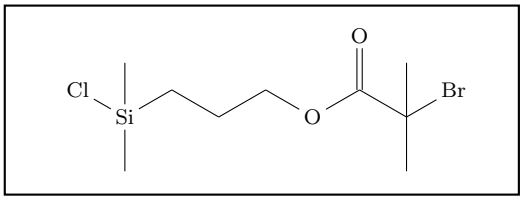

Figure 3.4: Chemical structure of ATRP silane grafted on silicon wafers.

3.2.2.2 Si-ATRP polymerization of P(HEMA), P(MAA) and P(HEMA-*co*-MAA)

The polymerization protocol was adapted from a previous procedure [224]. The monomers (190 mmol) (HEMA and/or MAA) were dissolved in a ethanol/Milli-Q water mixture (62.5:37.5 v:v) implemented or not with the mole number of NaOH corresponding to the mole number of MAA monomer, for a total volume of 16 mL. Then bipy (5 mmol) and Cu(II)Cl_2 (0.08 mmol) were added to the mixture and the pH was adjusted to 9 with 0.1 M NaOH or 0.1 M HCl solutions. This mixture was stirred and degassed thanks to a needle injecting Ar for 45 minutes in a schlenk tube sealed with a rubber septum. Cu(I)Cl (1.6 mmol) was then quickly added to the mixture and the polymerization solution was further degassed for 45 minutes. Meanwhile sealed schlenks containing each a 1x1 cm^2 silicon samples grafted with the ATRP initiator were degassed (3 vacuum/Ar cycles). The polymerization mixture was then quickly syringed and injected in each sealed schlenks which were maintained under argon atmosphere during the polymerization. After various polymerization times at room temperature, the samples were removed from the schlenks, washed with water then methanol and dried with a stream of N_2. The thickness of the brush was measured by ellipsometry.

3.2.2.3 Si-ATRP polymerization of P(HOEGMA)

The procedure was adapted from [226]. The monomer (95 mmol) (HOEGMA) was dissolved in 44 mL of a water/methanol mixture (50:50 v:v). Then bipy (5 mmol) and Cu(II)Cl_2 (0.16 mmol) were added to the mixture. This mixture was stirred and degassed thanks to a needle injecting Ar for 45 minutes in a schlenk tube sealed with a rubber septum. Cu(I)Cl (1.6 mmol) was then quickly added to the mixture and the polymerization solution was further degassed

for 45 minutes. Meanwhile sealed schlenks containing each a 1x1 cm^2 silicon samples grafted with the ATRP initiator were degassed (3 vacuum/Ar cycles). The polymerization mixture was then quickly syringed and injected in each sealed schlenks which were maintained under argon atmosphere during the polymerization. After various polymerization times at room temperature, the samples were removed from the schlenks, washed with water then methanol and dried with a stream of N_2. The thickness of the brush was measured by ellipsometry.

3.2.3 Ellipsometry measurements

Ellipsometric measurements were carried out with a single-wavelength ellipsometer (Jobin Yvon) with an incidence angle of 70°. The model consists of two layers: silicon substrate covered by a polymer brush. The indices for silicon were taken as n=3.882 and k=0.019 [227] while the refractive indexes were fitted to 1.48, 1.49 and 1.45 for P(HEMA), P(MAA) and P(HOEGMA) respectively. The average of five measurements was taken for each sample.

3.2.4 FTIR analysis

FTIR absorbance spectra of the dry homopolymer and copolymer brushes were recorded in transmission mode with a continuum microscope (AFK0401015), through the silicon substrate. 1056 scans were collected with a resolution of 8 cm^{-1} for each spectrum.

Briefly, the compositions of the copolymer brushes were determined according to the method used by Laloyaux *et al.* [224]. The molar composition of the brush is obtained by the formula:

$$\frac{n_{HEMA}}{(n_{HEMA} + n_{MAA})} = \left(1 + \frac{n_{MAA}}{n_{HEMA}}\right)^{-1} \tag{3.1}$$

With n_{MAA} and n_{HEMA} the number of MAA and HEMA moles, respectively, incorporated into the brush. The ratio between MAA and HEMA units incorporated into the copolymer brush is computed according to the following equation:

$$\frac{n_{MAA}}{n_{HEMA}} = \frac{A_{1554}}{A_{1725}} \frac{a_{HEMA}}{a_{MAA}} \frac{\overline{V}_{HEMA}}{\overline{V}_{MAA}} \tag{3.2}$$

With A_{1554} and A_{1725} the absorbance of the polymer brush at 1554 and 1725

cm^{-1}, respectively, a_{HEMA} and a_{MAA} is the specific parameters determined for P(HEMA) and P(MAA) brushes, respectively and $\overline{V}_{HEMA}$ and $\overline{V}_{MAA}$ the molar volume of the monomers. These molar volumes were evaluated from Van Krevelen's relationships [228]:

$$\overline{V}_{HEMA} = 106.4\ cm^3 mol^{-1} \tag{3.3}$$

and

$$\overline{V}_{MAA} = 62.6\ cm^3 mol^{-1} \tag{3.4}$$

The specific parameters a_{HEMA} and a_{MAA} were evaluated via the equation:

$$A = \epsilon ch = ah \tag{3.5}$$

relating the absorbance (A) to the brush thickness (h), the extinction coefficient (ϵ) and the molar concentration (c) of monomer units. Brush Polymerization on double-polished face silicon sample allowed computing the characteristic peak areas with an IGOR PRO routine decomposing the different peaks of the FTIR spectrum. This IGOR PRO routine first computes the baseline between wavelengths of 1269 and 1920 cm^{-1} and this computed baseline is subsequently subtracted from the spectrum to obtain only the characteristic peaks of the polymer brushes to be fitted. If we took an extended wavelength range, it was not possible to fit the baseline properly. Then the routine computes the peak area (A) based on set amplitude, position, width and shape of the peak (based on Voight components). The thickness of the polymer brush was measured by ellipsometry on a single-polished face silicon wafer and doubled to obtain the genuine thickness of the brush on the double-face silicon sample (h). From these measurements on homopolymer brushes, the value of a was computed.

3.3 Results and discussion

3.3.1 Growth of polymer brushes

The variation of the thickness of P(MAA) brush as a function of the polymerization time, displayed in Figure 3.5, shows that the growth of this brush was controlled for the first 40 min of polymerization since a linear increase of the thickness was observed with the time. Then the thickness reached a plateau at

a thickness of 283 ± 9 nm.

The polymerization kinetics of HEMA-based brush was rather slow (Figure 3.5) and a thickness of 63 nm ± 1 nm was reached after a polymerization time of 60 min.

Using HEMA and MAA, we were able to synthesize P(HEMA-*co*-MAA) copolymer brushes from a 30:70 mol/mol mixture of MAA and HEMA monomers (Figure 3.5). The used conditions allowed to control the growth of the brush during the first 30 minutes. The brush thickness measured by ellipsometry after 30 minutes of polymerization was around 46 nm ± 2 nm (Figure 3.5).

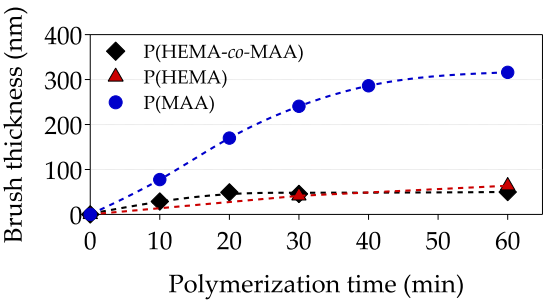

Figure 3.5: Thickness of P(HEMA), P(MAA) and P(HEMA-*co*-MAA) brushes versus polymerization time.

We also tried to prepare poly(hydroxyl-terminated oligo(ethylene glycol) ether methacrylate-*co*-methacrylic acid) (P(HOEGMA-co-MAA)) brushes using many different pH conditions. However, it was not possible to control properly the growth of these brushes due to very different polymerization kinetics between both monomers. The polymerization of HOEGMA, at neutral pH, was then monitored (Figure 3.6). The slow kinetics of this brush allowed a fine control over its thickness but required a long polymerization time: 3 hours were indeed necessary to obtain a thickness of 30 nm.

The very fast growth of P(MAA) brushes arises from multiple factors. First, the kinetics of ATRP polymerization can be influenced by the solvent used to dissolve the monomer. Indeed, water accelerates the polymerization reaction as shown by the study done by Huang *et al.* and already explained in section 2.1.2 [39]. The reason for this difference of growth kinetics results from the dissociation of the catalyst in presence of water [221, 222, 229]. However, adding halide salt in the reaction mixture might help suppressing the catalyst hydrolysis as demonstrated by Tsarevsky *et al.* for the polymerization of HEMA in solution

with water and methanol [229].

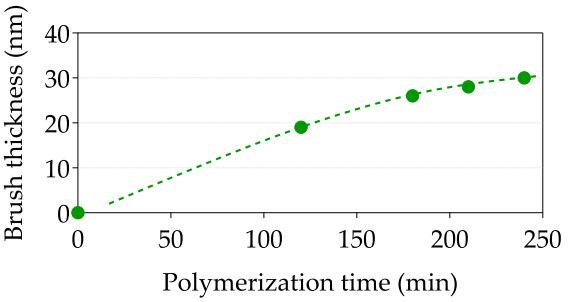

Figure 3.6: Thickness of P(HOEGMA) brush versus polymerization time.

Second, the pH of the polymerization solution influences the protonation of the MAA monomer thus influencing the polymerization kinetics. In basic condition in water, the MAA is partially deprotonated and the optimum polymerization pH lies between 8 and 9 [33, 230]. Actually, the optimum pH mentioned for MAA results from a balance between different mechanisms. At a lower pH, the bipy ligand is protonated and consequently unable to complex the catalyst [230]. At a higher pH, the monomer units incorporated into the brush are charged under carboxylate form. These charged groups distributed along the polymer backbone tend to repel the free monomers in solution. As a consequence, the polymerization rate is strongly decreased [230, 231]. Moreover, a deprotonated monomer can deactivate the catalyst by complexation [221, 222, 229]. To prevent complexation of MAA with the catalyst, Sankhe *et al.* added sodium chloride salt in the reaction medium. However, they mentioned that two conditions must be fulfilled to successfully control the P(MAA) growth: the salt must not compete with the catalyst to bind the ligand and the salt must compete effectively with the catalyst to bind to the deprotonated monomer [222]. Additionally, Tugulu *et al.* noticed that increasing the pH up to 10 hydrolyzed the siloxane groups used to anchor the brush to the surface resulting in a decrease of the film thickness [223].

To circumvent the problem of the monomer complexation with the catalyst, some researchers experimented the polymerization of protected monomers. For instance, Karanam *et al.* successfully used tBMA in solution to synthesize diblock copolymer of MMA and tBMA by ATRP [37]. Matyjaszewski *et al.* synthesized n-butyl acrylate based-brushes in solution but did not deprotect

them [232]. Gromadzki *et al.* synthesized copolymers containing tBMA then removed the tert-butyl group by hydrolysis to get P(MAA) brushes [233]. The main problem with this method is the harsh conditions used to remove the protective group which could cleave as well the siloxane links which ensure the anchoring of the polymer chains onto the substrate. [234–236].

3.3.2 Composition of polymer brushes

The study of the composition of the copolymer brushes was important to understand the ratio of monomers incorporated in the polymer chains but also their distribution into the brushes. First, we recorded the signal emitted from the homopolymer brushes in order to identify the characteristic peaks of the P(HEMA) and P(MAA) brushes. We fitted them with an IGOR PRO routine to extract information needed to compute the values of the specific parameters identified as a_{MAA} and a_{HEMA}. Finally, the peaks from the P(HEMA-*co*-MAA) brush were identified and used to compute the composition of the copolymer brush along with the previously computed parameters for homopolymer brushes.

The preliminary observation of the FTIR spectra of the homopolymer brushes allowed us to determine the characteristic peaks of the monomer units. Figure 3.7 shows that the main peak for HEMA unit was centered at 1725 cm^{-1}. It corresponds to the asymmetrical stretching of the carbonyl group of HEMA unit. Prior to FTIR analysis, P(MAA) and P(HEMA-*co*-MAA) copolymer brushes were immersed in NaOH solution (pH 9.8) for 10 minutes to deprotonate the carboxylic group of MAA units. Indeed, as can be seen in Figure 3.8, the peak centered at 1682 cm^{-1}, due to the presence of hydrogen bonds between carboxylic acid groups, decreased and the peak centered at 1554 cm^{-1}, associated with the asymmetrical stretching of the deprotonated carbonyl group of MAA, increased after immersion in basic solution. As expected, the peak centered at 1682 cm^{-1} decreased while the peak centered at 1554 cm^{-1} increased when the carboxylic acid groups get deprotonated.

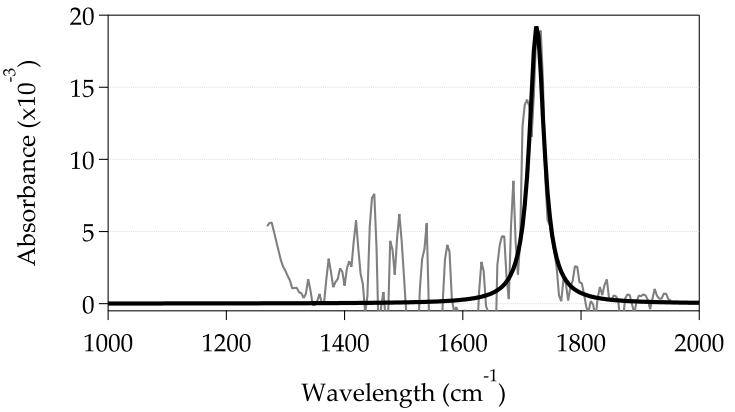

Figure 3.7: FTIR spectrum of a P(HEMA) brush of 56 nm thickness showing a characteristic peak centered at 1725 cm^{-1}. The grey line is the spectrum corrected by the baseline; the continuous thick dark line is the fit of the component peak.

Thanks to the spectra of both homopolymer brushes, P(MAA) and P(HEMA), it was possible to perform the peak assignment in the spectrum of the copolymer brush (Figure 3.9). The molar composition of this brush can be computed from the measurements of the surface areas of the peaks centered at 1554 and 1725 cm^{-1}, corresponding to MAA and HEMA units, respectively. Using equation 3.5, we obtained a value of 0.0078 and 0.02 for a_{HEMA} and a_{MAA}, respectively. The value obtained for a_{MAA} slightly differed from the one measured by Laloyaux *et al.* [224] who obtained a value of 0.03. This difference can be explained by the difficulty to fit the FTIR curves obtained due to the noise caused by the small intensity of the peaks compared to the signal of the background.

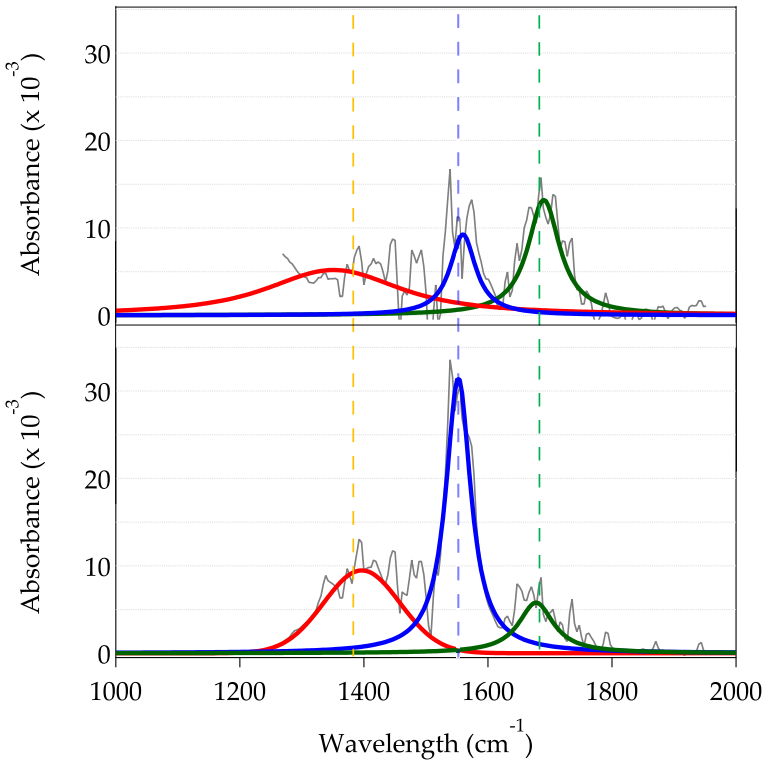

Figure 3.8: FTIR spectra of a P(MAA) brush of 74 nm thickness before (bottom) and after (top) immersion in a basic solution (pH 9.8). The grey lines are the spectra corrected by the baseline; the colored lines are the fits of the component peaks. The peak centered at 1682 cm^{-1} decreased while the peak centered at 1554 cm^{-1} increased after treatment in basic solution; this is due to the deprotonation of the carboxylic groups. The red component peak corresponds to another peak of the asymetric stretching of the carbonyl group at high pH [224].

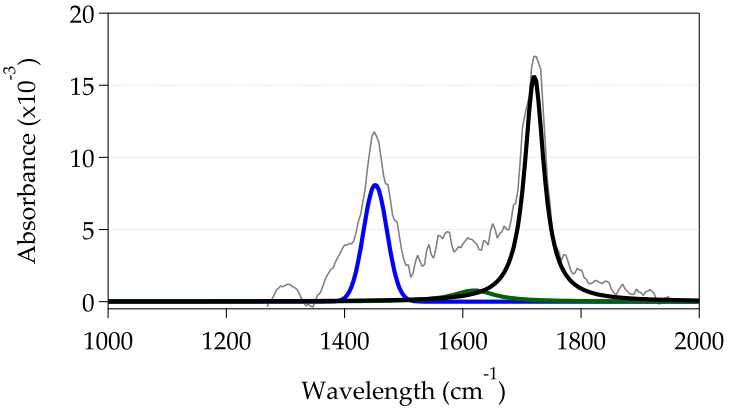

Figure 3.9: FTIR spectrum of a P(HEMA-*co*-MAA) brush of 46 nm thickness after 20 minutes polymerization showing the two main characteristic peaks centered at 1725 cm^{-1} and 1554 cm^{-1}. The component lines do not exactly sum to the signal because it was not possible to perfectly correct the baseline.

Finally, with all the computed parameters, the molar composition of the copolymer brushes obtained after 20 and 120 minutes of growth were determined from equation 3.1. Initially, the expected composition of the copolymer brush P(HEMA-*co*-MAA) starting from a blend of 30:70 mol/mol of MAA and HEMA was hypothesized close to the composition of the poly(di(ethylene glycol) methyl ether methacrylate-*co*-methacrylic acid) (P(MEO_2MA-*co*-MAA)) obtained by Laloyaux et al. [224], because of the close nature of MEO_2MA and HEMA, and should show a content of MAA around 20 %. This theoretical hypothesis was not confirmed since the FTIR analysis of the P(HEMA-*co*-MAA) brushes obtained showed a content of MAA of 34 % and 20 % after a polymerization time of 20 and 120 minutes, respectively (Figure 3.10). Therefore the composition of the copolymer brush varied as a function of the polymerization time.

These results indicate that the copolymer brush was composed of both monomer units but that its composition varied with the polymerization time. As the polymerization of MAA was faster than the one of HEMA, we hypothesized that the part of the brush closest to the surface contained a higher amount of MAA compared to HEMA. With polymerization time increasing, the amount of HEMA in the brush increased leading to a lower total amount of MAA in the brush.

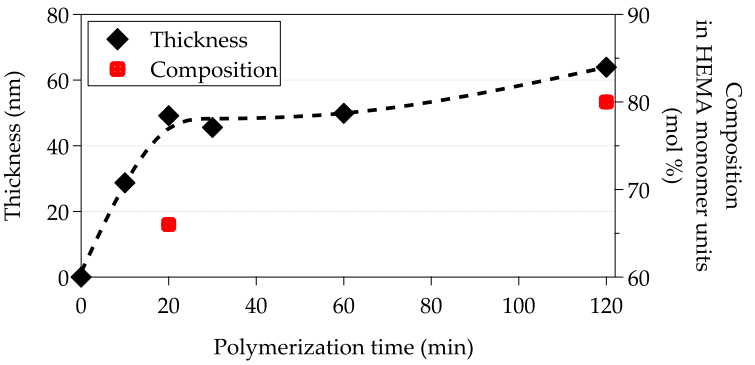

Figure 3.10: Thickness and composition of P(HEMA-*co*-MAA) brushes versus the polymerization time.

.

3.4 Conclusion

We were able to synthesize P(HEMA), P(MAA), P(HEMA-*co*-MAA) and P(HOEGMA) brushes. However, the composition of the copolymer brush was not precisely defined and varied with time. Therefore, the brush selected for the next experiment steps was the P(HOEGMA) brush. The hydroxyl groups along the backbone of this brush will allow the grafting of bioactive molecules targeting bacteria and mammalian stem cells.

Chapter 4

Elaboration of nanopatterned surfaces

4.1 Introduction

The elaboration and characterization of nanopatterned surfaces presenting bioactive molecules at the nanometer scale was one of the goals of this PhD thesis in order to control the cellular behavior. We chose to fabricate patterns designed at the nanometer scale because the natural ECM is also structured at the nanometer scale [1, 156, 166]. For example, *ex vivo* bones are composed of nanogrooves which consist in collagen type I fibrils with a width of 68 nm, a depth of 3-5 nm and an interfibrillar spacing depth of 35 nm [159]. The desired effects of the surface towards a targeted biological entity are influenced by the dimensions and design of the patterns [199], *i.e.* the spacing between active moieties interacting with the biological entity [156, 237], the spacer length pulling apart the bioactive moiety from the grafted surface [6, 77, 191, 237] as well as the orientation [6, 77, 105, 237], the architecture and sequence [81, 85] of the bioactive moiety.

In this PhD thesis, we chose to pattern bioactive polymer brushes at the nanometer scale. They are different possible approaches to prepare such surfaces. μCP and NIL [47] techniques, which are based on the use of a mold applied to the surface, are frequently used to prepare patterned polymer brushes. Some techniques such as photolithography [47] and EBL [22], are based on the

selective exposure to light or electron of precise spots of a surface. Finally, other techniques such as DPN and nanograting [48] allow the direct formation of the pattern on the surface. In this PhD thesis, the NIL technique was chosen because it allows the easy production of large patterned surfaces with a nanometer scale resolution and it is a rapid technique compared to other lithography techniques [22, 48].

We focused on the elaboration of nanopatterned surfaces composed of polymer brushes grafted with different peptides or with a given mixture of peptides. The synthesis of the polymer brushes was already described in Chapter 3 while their biofunctionalization is presented in this Chapter. Two types of nanopatterned surfaces were elaborated: chemical and topographical nanopatterns. The fabrication of chemical nanopatterns (Figure 4.1-path a) starts with the nanoimprinting of an annealed spin-coated PMMA film deposited onto a silicon substrate. Then the bottom parts of the thus formed PMMA mask are descummed by performing an oxygen plasma treatment. The exposed silicon parts are then silanized with a Si-ATRP silane, *i.e.* a silane bearing an initiator of ATRP polymerization. The PMMA mask is then removed and the newly exposed silicon surface is silanized with a PEG silane. The Si-ATRP silane, grafted onto the surface, is subsequently used to grow P(HOEGMA) brush by ATRP. Finally, peptides are grafted onto the hydroxyl pendent moieties of the polymer brush through a bioconjugation approach.

For the fabrication of topographical nanopatterns (Figure 4.1-path b), a reactive-ion etching is performed just after the descum step to etch the silicon oxide (Figure 4.1, step 2.b). Then the PMMA mask is removed and the whole available silicon surface is silanized by Si-ATRP silane. The other steps are performed as for chemical nanopatterns.

This chapter aims at describing the biofunctionalization of the P(HOEGMA) brushes as well as the final characteristics of the nanopatterns. First, the biofunctionalization of homogeneous P(HOEGMA) brushes with bioadhesive and antimicrobial peptides was qualitatively and quantitatively assessed. We deduced from these experiments the grafting degree as well as the peptide density grafted on the non-patterned polymer brushes. The nanopatterned surfaces were then elaborated using the processes explained above (Figure 4.1). Moreover these surfaces were characterized after each elaboration step to ensure the preservation of the lateral dimensions of the pattern.

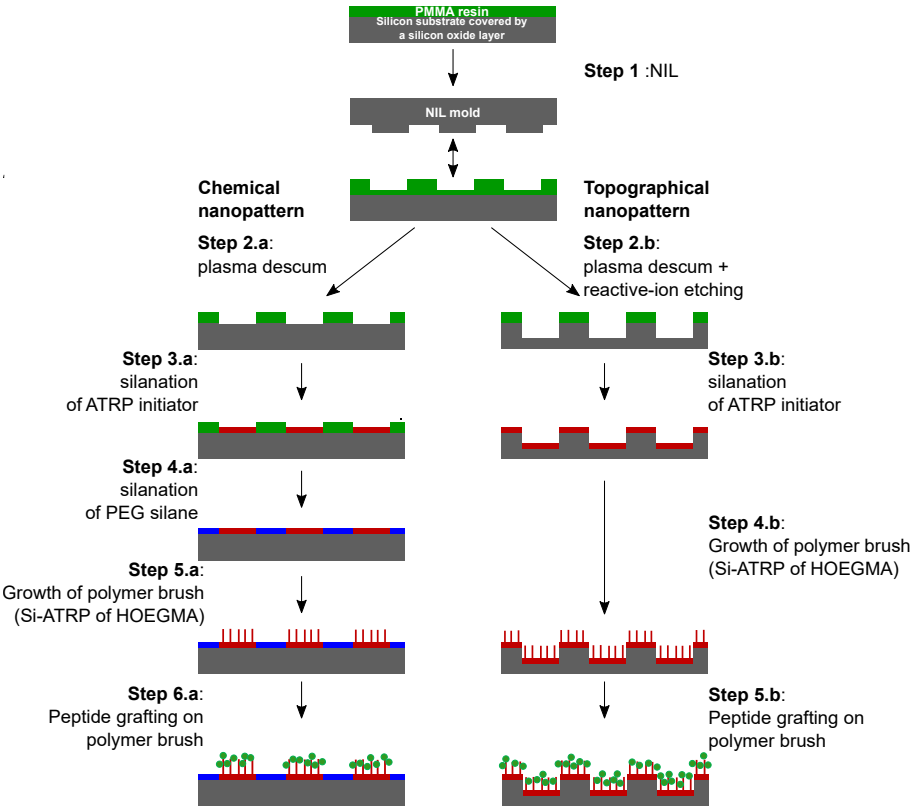

Figure 4.1: Elaboration of chemical (path a) and topographical patterns (path b) and their biofunctionalization.

4.2 Materials and methods

4.2.1 Materials

Single-side-polished (100) silicon wafers were purchased from TOPSIL. PMMA (M=130000 g/mol) was purchased from Agilent Technologies. Hydroxyl-terminated oligo(ethylene glycol) ether methacrylate (HOEGMA) (used without purification), copper(II) chloride (99.999 %) (Cu(II)Cl), 2,2'-Bipyridyl (bipy), sodium phosphate monobasic monohydrate ($\geq$ 99.5 %) ($NaH_2PO_4.H_2O$), sodium phosphate dibasic ($\geq$ 99.5 %) (Na_2HPO_4) and sodium chloride (99 %+) (NaCl) were purchased from Sigma-Aldrich. Copper(I) chloride (99 %) (Cu(I)Cl), 2-amino-2-(hydroxy-methyl)-1,3-propanediol (99.8 %) (Tris) were obtained from Acros.

Absolute methanol (99.8 %) was purchased from VWR. 2-[Methoxy(polyethyleneoxy)propyl]trichlorosilane (95 %)(PEG silane) and 1H,1H,2H,2H-perfluorodecyltrichlorosilane were supplied by ABCR. Triethylamine (99 %) was purchased from Fisher Scientific. 4-Maleimidophenyl isocyanate (PMPI) (Figure 4.2) was purchased from Apolo Scientific. Six different peptides (purity > 95 %) obtained from Genecust and bearing an additional C- or N-terminal cysteine residue, were used to modify the polymer brushes (Figure 4.3): A RGD peptide (with the sequence KRGDSPC and called RGD-C in this manuscript) and its fluorescent derivative bearing a N-terminal fluorescein isothiocyanate (FITC) moiety (FITC-RGD-C); an antibacterial magainin I peptide (MAG-C) and its derivative bearing a N-terminal biotin moiety (Biotin-MAG-C); and an antibacterial modified LL37 peptide (C-LL37) and its derivative bearing a N-terminal biotin moiety (Biotin-LL37-C). Dylight 488 conjugated streptavidin (FITC-strep) and Dylight 405 conjugated streptavidin (Blue-strep) were purchased from Thermo Scientific Pierce Protein Biology. Milli-Q grade water (resistivity of 18.2 mΩ) was produced by a Milli-Q® Reference system of Merck Millipore.

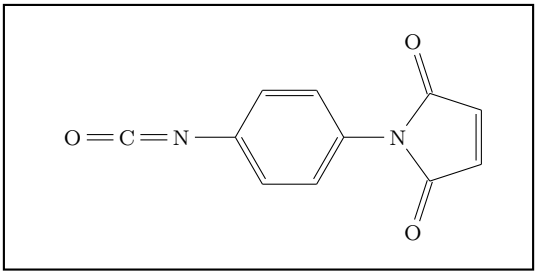

Figure 4.2: Chemical structure of the PMPI linker.

4.2.2 NIL mold description

The size of the NIL silicon molds used were of 1x1 cm^2. They were produced by AMO GmbH. The first mold presents a period of 250 nm. Its dimensions are 78 nm for the width of the protruding line and 172 nm for the width of the pit. The height of the lines is 200 nm. The second mold presents a period of 400 nm. Its dimensions are 200 nm for the width of the protruding line and 200 nm for the width of the pit. The height of the line is 200 nm. Both types of molds were coated with 1H,1H,2H,2H-perfluorodecyltrichlorosilane by gas phase silanation to prevent the adhesion between the mold and the nanoimprinted

surface, during the NIL process.

(a)	KRGDSPC
(b)	FITC - KRGDSPC
(c)	GIGKFLHSAGKFGKAFVGEIMKSC
(d)	Biotin — GIGKFLHSAGKFGKAFVGEIMKSC
(e)	CLLGDFFRKSKEKIGKEFKRIVQRIKDFLRNLVPRTES
(f)	Biotin - LLGDFFRKSKEKIGKEFKRIVQRIKDFLRNLVPRTESC

Figure 4.3: Sequences of (a) RGD-C, (b) FITC-RGD-C, (c) MAG-C, (d) Biotin-MAG-C, (e) C-LL37 and (f) Biotin-LL37-C which are derivatives of KRGDSP, magainin I and LL37 peptides.

4.2.3 Nanopattern elaboration

The elaboration of (bio)chemical and topographical nanopatterns is briefly represented in Figure 4.1. The step 1, 2.a and 2.b were carried out in a cleanroom. Two types of silicon surfaces were used. The first one allowed the fabrication of chemical nanopatterns and consisted in a silicon layer covered by an oxide layer of 1.5 nm. The second one allowed the fabrication of topographical nanopatterns and consisted in a silicon layer covered by an oxide layer of 200 nm. Silicon surfaces (1.2x1.2 cm^2) were first cleaned by immersion in freshly prepared piranha (H_2O_2(35%):H_2SO_4(98%) (1:1 v/v)) during 20 minutes then rinsed extensively with Milli-Q water. The cleaned surfaces were then covered by a spin-coated PMMA layer. For this, 0.1 mL of a PMMA solution (4% w:w) filtered through a 0.45 μm membrane, was deposited onto the surface. The spin coating was performed with a Laurell WS-650 spin coater. Different spin coating conditions described in the Table 4.1, were used depending on the film thickness targeted. The targeted thicknesses were computed based on the dimensions of the 250 or 400 molds used during the nanoimprint. During the NIL, the compressed PMMA constituting the spin-coated film was pushed inside the pits of the molds and filled them. In order not to crush the nanopatterned mold onto the underlying silicon substrate, a minimum film thickness needs to be deposited during the spin-coating process. Therefore, a thickness of 155-160 nm and 125-135 nm are necessary for the 250 and the 400 molds, respectively.

Table 4.1: Spin-coating parameters used to prepare PMMA films.

Molds	Acceleration (rpm/s)	Speed (rpm)	Spin-coating time (s)	Thickness[a] (nm)
250	2500	2700	60	155-160
400	3000	6000	60	125-135

[a]Measured by ellipsometry.

The spin coated PMMA film was finally annealed for 5 minutes at 170°C. The final thickness of PMMA film was measured by ellipsometry. The nanoimprint lithography (NIL) (Figure 4.1-step 1) was then performed with an Obducat NIL-3M, on a PMMA spin-coated film, according to the conditions described in Table 4.2. Briefly, a silicon mold was placed onto the PMMA film and the whole system was fixed in the nanoimprinter. Then, the temperature was increased up to 170°C and the NIL was performed by applying a pressure of 60 bars on the mold for 180 seconds. Finally, the pressure was released and the temperature was cooled down to 70°C before removing manually the mold from the imprinted surface.

Table 4.2: Conditions used for NIL on PMMA films (see Figure 4.1-step 1).

Step	Temperature (°C)	Pressure (bar)	Time (s)
1	170	0	180
2	170	60	180
3	70	0	0

The imprinted surfaces were then used differently depending on whether we wanted to elaborate chemical or topographical nanopatterns.

4.2.3.1 Chemical nanopattern

To produce chemical nanopatterns (Figure 4.4) four steps are necessary (Figure 4.1-steps 2.a-5.a).

Figure 4.4: Chemical nanopattern.

First, an oxygen plasma descum (Figure 4.1-step 2.a) with parameters described in Table 4.3 was applied with an Electrotech ET340 to remove the residual PMMA layer in the bottom parts of the imprinted film. A spin-coated PMMA film was used as a reference to ensure the thickness of PMMA removed in the same conditions.

Table 4.3: Parameters used during the plasma descum to clean the bottom parts of the PMMA mask obtained after NIL (see Figure 4.1-step 2.a and 2.b).

Temperature (°C)	Pressure (mT)	Power (W)	Flow O_2	Peak to peak	Vdc Bias
30	15	1	50	176	53

LCP/TCP	APC	Time (s)	Descummed thickness[a] (nm)
113/25	61	220	50

[a]This thickness was measured by ellipsometry on a reference spin-coated PMMA film before and after the descum process.

The descum step was followed by the silanation of ATRP initiator silane (Figure 4.1-step 3.a) according to the gas phase process described in Chapter 3 (section 3.2.2). The PMMA mask was subsequently dissolved by immersing the sample in acetone for at least 1 minute at 55°C. Then the wafer was sonicated in acetone for 10 seconds, rinsed with absolute methanol and finally dried with a stream of nitrogen. The exposed surface was silanized with PEG silane (Figure 4.1-step 4.a). This second silanation was performed overnight in a glovebox. For this reaction, the samples were immersed in toluene prior to add 0.2 ml of PEG silane and 0.1 ml of triethylamine. Two cleaned silicon samples were added with the patterned sample, in the same beaker, to get reference samples for the determination of the thickness of the PEG monolayer. At the end of the reaction, the surfaces were rinsed with toluene, sonicated for 20 seconds in methanol, rinsed with methanol and dried with a stream of nitrogen. The next step (Figure 4.1-step 5.a) consisted in the growth of P(HOEGMA) brush on the regions covered by the initiator ATRP. For this Si-ATRP of HOEGMA was performed according to the process described in Chapter 3 (section 3.2.2).

4.2.3.2 Topographical nanopattern

To produce topographical nanopatterns (Figure 4.5) three additional steps are necessary (Figure 4.1-steps 2.b-4.b).

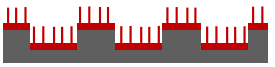

Figure 4.5: Topographical nanopattern.

To elaborate such patterns, we used silicon wafers covered with a 200 nm-thick silicon oxide layer (provided by UCL Winfab cleanrooms). After the NIL step, an oxygen plasma descum, performed with an Electrotech ET340, followed immediately by an reactive-ion etching process, also performed with the Electrotech ET340, (Figure 4.1-step 2.b) were applied to remove the residual PMMA layer in the open regions and to etch the silicon oxide, respectively. The conditions used for these two steps are described in Table 4.3 and 4.4. A PMMA film spin-coated onto a silicon wafer was used as a reference to check the thickness of PMMA removed during the descum and a reference thermally oxidized sample was used to measure the thickness of silicon oxide etched.

The etching step was followed by silanation of Si-ATRP initiator silane and growth of P(HOEGMA) brush by Si-ATRP polymerization (Figure 4.1-steps 3.b-4.b) according to the protocols described in Chapter 3 (section 3.2.2). The polymerization time was 4 hours in order to reach a brush thickness of about 30 nm (see Figure 3.6) (Chapter 3 section 3.3.1).

Table 4.4: Parameters for reactive-ion etching to etch the silicon substrate (see Figure 4.1-step 2.b).

Temperature (°C)	Pressure (mT)	Power (W)	Flow SF_6	Flow CHF_3	Peak to peak	Vdc Bias
30	30	60	50	500	1047	345

LCP/TCP	APC	Time (s)	Etched thickness[a] (nm)
114/24	17	90	50

[a]This thickness was computed from the silicon oxide thickness measured by ellipsometry on a control silicon oxide surface before and after the etching process.

4.2.4 Polymer brush biofunctionalization

4.2.4.1 General description of the biofunctionalized patterns

Following the fabrication of nanopatterned surfaces, the polymer brushes were grafted with different peptides to provide them bioactivity towards mammalian cells and/or bacteria (Figure 4.1-step 6.a or 5.b). We elaborated four different nanopatterns showing RGD-C and/or antimicrobial peptides with various topographies (Figure 4.6).

(a) Biochemical nanopattern showing RGD-C peptide.

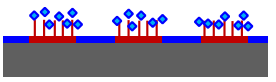

(b) Biochemical nanopattern showing antimicrobial peptide.

(c) Biochemical nanopattern showing both RGD-C and antimicrobial peptides.

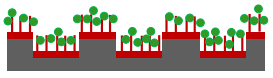

(d) Topographical nanopattern showing RGD-C peptide.

Figure 4.6: Biochemical and topographical nanopatterns elaborated for later assays with bacteria and mammalian cells.

4.2.4.2 Peptide grafting on P(HOEGMA) brush.

The peptide grafting on the P(HOEGMA) brush consists in a two-step process inspired from reference [64]: a heterolinker, bearing both isocyanate and maleimide moieties, was first tethered on the pendent hydroxyl groups of the P(HOEGMA) brush via the isocyanate group then a peptide molecule was grafted on the linker according to a click reaction through the maleimide group. Click reactions are irreversible reactions commonly used as a bioconjugation technique to immobilize a biomolecule on a given chemical structure [238]. So a reaction can be considered as a click reaction if its proceeds with a high yield, produces products stable under physiological conditions, generates inoffensive byproducts, is tolerant to a wide variety of functional groups and can be performed with simple reaction conditions (insensitive to oxygen and water and using benign or easily removed solvents) [42, 239].

Grafting of PMPI linkers on the hydroxyl groups of P(HOEGMA) brush.

The reaction is depicted in Figure 4.7. A 6 mM solution of PMPI was prepared in freshly distilled tetrahydrofuran (THF), under argon atmosphere to prevent hydrolysis of the isocyanate groups. After 30 minutes stirring at 30° C, the solution was syringed and rapidly injected in prior degassed schlenks containing 1x1 cm^2 surfaces modified with P(HOEGMA) brush. The volume injected in each schlenk tubes was 2 mL. After a reaction time of 6 hours at room temperature, the samples were sonicated in freshly distilled THF and rinsed once with THF before drying with a stream of nitrogen.

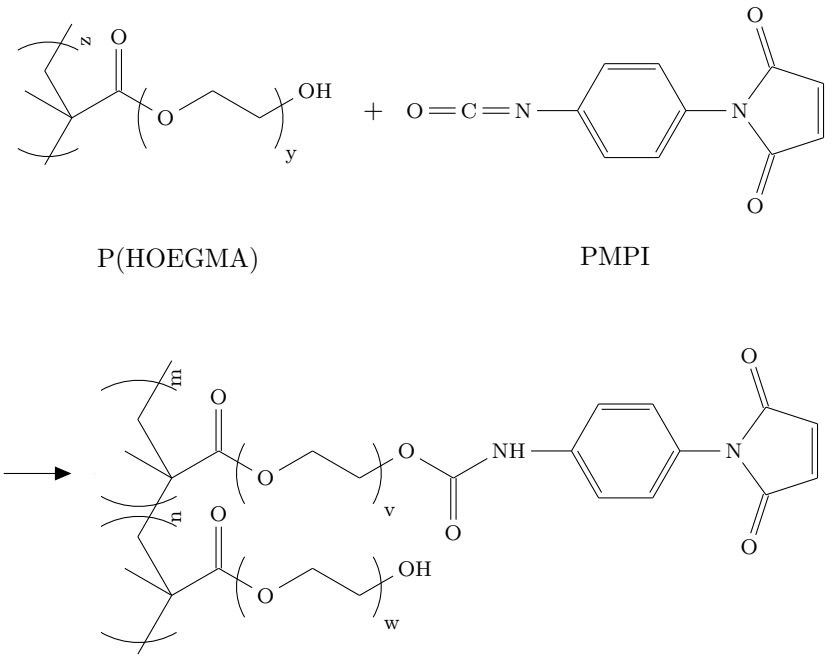

Figure 4.7: Reaction between the isocyanate moiety of PMPI and one hydroxyl pendent group of the P(HOEGMA) polymer chain.

Grafting of cysteine-ended peptides on the maleimide groups of PMPI linkers.

The grafting of the peptide molecules on the PMPI-modified brushes is depicted in Figure 4.8. The PMPI modified polymer brushes were immersed in a 280 μM solution of peptide prepared in filtered Tris buffer (100 mM, pH 7.05). After a reaction time of 2 hours and 30 minutes at room temperature, the surfaces

were sonicated 5 minutes in filtered Tris buffer then rinsed extensively with filtered Milli-Q water before drying with a stream of nitrogen. When peptides labeled with a fluorescent moiety were used, the grafting reaction was performed in the dark to avoid any denaturation of the dye. The grafting solutions comprised pure peptide solutions of RGD-C, MAG-C and C-LL37 or mixtures of C-LL37/RGD-C with different molar ratios varying from 10/90 to 90/100. The same concentrations and molar ratios were used to graft biotinylated or FITC-tagged peptides.

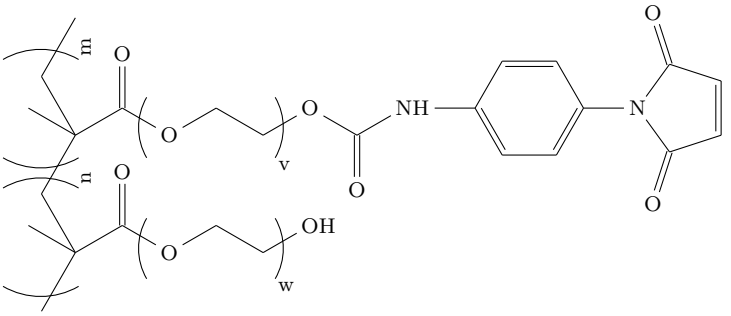

P(HOEGMA) grafted with the PMPI linker

+ SH − peptide

cysteine-terminated peptide

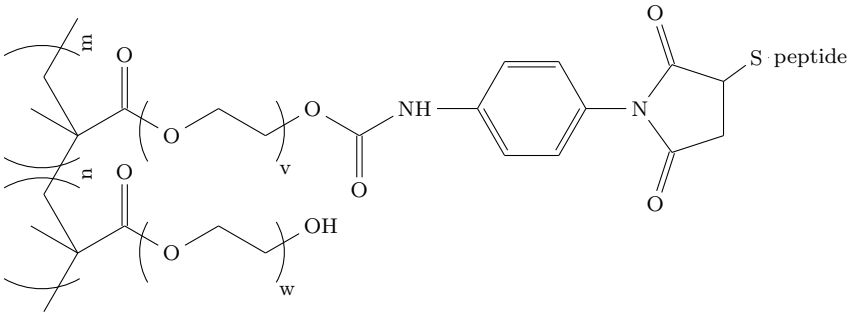

P(HOEGMA) grafted with the peptide

Figure 4.8: Grafting of a cysteine-terminated peptide on a maleimide group of a modified P(HOEGMA) polymer chain.

4.2.5 Characterization of nanopatterned surfaces

4.2.5.1 Detection of peptide grafting by fluorescence microscopy

The surfaces modified with a fluorescent dye were imaged with an Olympus epifluorescence IX71 microscope equipped with a blue filter U-MNUA2 (excitation 360-370 nm and emission 420-460 nm) and a green filter U-MWIBA3 (excitation 460-495 nm and emission 510-550 nm). The UV light is provided by an X-cite module, series 120PCQ from Lumen Dynamics. The observation of FITC-RGD-C peptide was direct since it is intrinsically fluorescent. To reveal the grafting of a peptide bearing a biotin group at their N-terminal end, we used an indirect method which consisted in the complexation of streptavidin, bearing a fluorescent marker, to the biotin (Figure 4.9). The grafting was revealed by performing a 20 minute immersion of surfaces grafted with Biotin-MAG-C or Biotin-LL37-C in 1 mL of 10 mM filtered PBS buffer mixed with 40 μL of FITC-strep or Blue-strep, respectively. The complexation was performed in the dark to avoid any denaturation of the dyes.

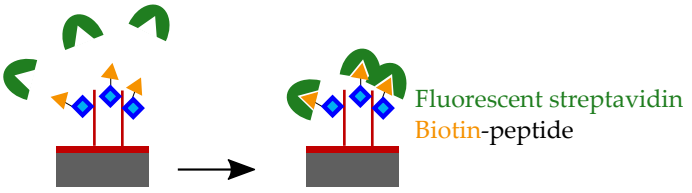

Figure 4.9: Complexation of biotin-peptides with streptavidin macromolecules bearing a fluorescent marker.

To qualitatively asses the fluorescence of the surfaces, a deliberate scratch was made to reach the fluorescence background linked to the measurement. The presence of FITC-RGD-C peptide was evidenced through the imaging via the green channel. The grafting of Biotin-MAG-C and Biotin-LL37-C on the P(HOEGMA) brushes were revealed by the complexation with streptavidin molecules labelled with Dylight 488 and Dylight 405, respectively. When mixtures of Biotin-LL37-C and FITC-RGD-C were grafted on the surfaces, the presence of FITC-RGD-C or Biotin-LL37-C was revealed by recording the green fluorescence and blue fluorescence, respectively. We also ensured that the recorded fluorescence was coming from covalently grafted peptides by imaging non-modified P(HOEGMA) brushes incubated with labeled streptavidins or fluorescent peptides then thoroughly rinsed.

The average fluorescence intensity was computed for the different tested surfaces according to the procedure described in reference [64]. Briefly, the fluorescent surface was deliberately scratched to determine the fluorescence of the background. Then the average fluorescence intensity of the rest of the image was evaluated after graying the image and computing the histogram of grey values. The fluorescence of surfaces modified with polymer brushes then incubated with fluorescent peptides or streptavidins was also measured to evaluate the contribution of the non-specific adsorption of these molecules onto the surface.

The fluorescence intensities are presented as mean values ± standard deviation (SD). Statistical analyses were performed using one-way analysis of variance (ANOVA) (IGOR PRO, wavemetrics) followed by post hoc Tukey (HSD) test with a significance level set at alpha = 0.05. Differences were considered significant for a p-value < 0.05.

4.2.5.2 Chemical characterization of modified brushes by XPS

XPS measurements were performed to determine the amount of peptide grafted onto the polymer brushes. The analyses were performed on a SSX 100/206 photoelectron spectrometer from Surface Science Instruments (USA) equipped with a monochromatized micro focused Al Xray source (powered at 20 mA and 10 kV). Samples were fixed onto the aluminium conductive carousel with double sided adhesive tape. The pressure in the analysis chamber was around 10 Pa. The angle between the surface normal and the axis of the analyzer lens was 55°. The analyzed area was approximately 1.4 mm^2 and the pass energy was set at 150 eV. In these conditions, the full width at half maximum (FWHM) of the Au 4f peak of a clean gold standard sample was about 1.6 eV. A flood gun set à 8 eV 7/2 and a Ni grid placed 3 mm above the sample surface were used for charge stabilization. The C(C,H) component of the C1s peak of carbon has been fixed to 284.8 eV to set the binding energy scale. Data treatment was performed with the CasaXPS program (Casa Software Ltd,UK); some spectra were decomposed with the least squares fitting routine provided by the software with a Gaussian/Lorentzian (85/15) product function and after subtraction of a non-linear baseline [240].

4.2.5.3 Computation of grafting ratio using XPS

Molar fractions were calculated using peak areas normalized on the basis of acquisition parameters and sensitivity factors provided by the manufacturer. The grafting ratio (*i.e.* the number of HOEGMA monomers units grafted with the peptide) can be computed from the atomic concentration of C1s and N1s. The percentage of nitrogen and carbon can be related to the number of HOEGMA and HOEGMA grafted with a peptide (HOEGMA-peptide) units:

$$\frac{\%N_{tot}}{\%C_{tot}} = \frac{N_{HOEGMA-peptide} n_{HOEGMA-peptide}}{C_{HOEGMA} n_{HOEGMA} + C_{HOEGMA-peptide} n_{HOEGMA-peptide}} \quad (4.1)$$

With $\%N_{tot}$ and $\%C_{tot}$ the total atomic concentrations of carbon and nitrogen measured by XPS; C_{HOEGMA}, $C_{HOEGMA-peptide}$ and $N_{HOEGMA-peptide}$ the number of carbons in non-grafted HOEGMA unit, the number of carbons in peptide-grafted HOEGMA unit and the number of nitrogen in a peptide-grafted HOEGMA unit, respectively; n_{HOEGMA} and $n_{HOEGMA-peptide}$ are the number of non-grafted HOEGMA and peptide-grafted HOEGMA units, respectively. Considering that

$$n_{HOEGMA} = n_{tot}(1 - x) \quad (4.2)$$

and

$$n_{HOEGMA-peptide} = n_{tot} x \quad (4.3)$$

By replacing these expressions in equation 4.1 with n_{tot} being the total number of monomer units and x the ratio of number of monomer units grafted with the peptide to the total number of monomer units (a.k.a. the grafting degree), we obtain:

$$x = \frac{\frac{\%N_{tot}}{\%C_{tot}} C_{HOEGMA}}{\frac{\%N_{tot}}{\%C_{tot}}(C_{HOEGMA} - C_{HOEGMA-peptide}) + N_{HOEGMA-peptide}} \quad (4.4)$$

4.2.5.4 Characterization of brush thickness by ellipsometry

The ellipsometry technique was used to determine the thicknesses of the different control surfaces produced during the elaboration of the patterned surfaces. First, the thickness of the spin-coated PMMA film was measured by a Sentech SE850 ellipsometer at an incidence angle of 70° and with a wavelength range from 300 nm to 900 nm. The model used consists in a silicon layer covered in a predetermined oxide layer of 1.5 nm or 200 nm, depending on the substrate

used, and a polymer film with a refractive index n of 1.48. To control the thickness of PMMA film removed, the spin-coated PMMA film surface was partially covered during the descum process then the thickness difference was computed from the thicknesses of covered and non-covered surface with the Sentech ellipsometer. Second, the silicon oxide thickness etched during the etching process was verified by the same Sentech SE850 ellipsometer using a model which consists in a silicon substrate covered by an oxide layer in air. Again, the thickness of oxide etched was computed by measuring the difference of thickness between a covered and non-covered surface exposed to the etching process.

We used a spectroscopic ellipsometer Uvisel from Horiba-Jobin-Yvon at an incidence angle of 70° and in a wavelength range from 400 to 850 nm to characterize the surfaces after SI-ATRP polymerization and biofunctionalization of the polymer brushes.The model used consists of a silicon substrate covered by a predetermined oxide layer of 1.5 nm and a polymer film with a refractive index value modeled by a Cauchy layer. The thickness of PEG silane monolayer and P(HOEGMA) brush before and after biofunctionalization were measured thanks to reference samples.

4.2.5.5 Determination of the peptide density using ellipsometry

The thickness variation measured for the P(HOEGMA) brush before and after the peptide grafting was used to compute the grafting density of peptide according to the following equation derived from [241]:

$$D_{pep} = \frac{Ep10^{-3}P_{pep}}{V_{pep}10^{-12}} \tag{4.5}$$

With D_{pep} the surface density of peptide (peptides/μm^2), Ep the thickness difference measured for the polymer brush after and before grafting of the peptide (nm), P_{pep} the fraction of peptide used in the grafting solution and V_{pep} the molecular volume of the grafted peptide and the linker (Å^3/peptide molecule). The molecular volume of the linker, computed thanks to the tool provided by the Molinspiration website [242], is 177 Å^3. The volume of the different peptide molecules grafted on the surfaces were computed thanks to the Peptide Property calculator provided by [243]. The molecular volume computed for MAG-C peptide, C-LL37 and RGD-C are 3041 Å^3, 5561 Å^3 and 922 Å^3, respectively. The final volumes of the peptides grafted on the linker were

computed by adding the outputted values for the linker and a given peptide.

It is worth noting that for a set of samples, the ellipsometry measurements were performed at the same time, after each fabrication step, to avoid the potential influence of the external conditions such as the room temperature and humidity, on the measured thickness.

4.2.5.6 Scanning electron microscopy (SEM)

The mold used to perform NIL were characterized by SEM using a JEOL 7600F scanning electron microscope. Five images were recorded to determine the means and SD of the lateral dimensions of the features of the silicon mold. Two magnifications were used (6000 and 100000) and the tension was of 15 kV.

4.2.5.7 Atomic force microscopy (AFM)

The AFM was used at different stages of the nanopattern elaboration process to characterize the surfaces. First, the nanoimprinted PMMA films (Figure 4.1-step 1) were characterized in contact mode with a SNL-10 Ultrasharp probe of 0.12 N/m force constant, 40 μm width, 0.6 μm thickness and 205 μm length with a Bruker Multimode Nanoscope V to ensure the geometrical characteristics of the silicon mold were retained during the NIL process. Second, the thickness of silicon oxide removed after the etching process was assessed with a Bruker Multimode Nanoscope VIII in tapping mode using a PPP-NCHR probe of 42 N/m force constant, 30 μm width, 4 μm thickness, 125 μm length and 330 kHz resonance frequency. Finally, the nanopatterns grafted or not with polymer brushes were characterized in tapping mode with a Nanoscope VIII using a PPP-NCHR probe. The images were treated with Gwyddion 2.47 software. All images were treated with the "Align rows" with "Median" method available on Gwyddion, then the minimum value of the image was shift to zero and finally, the data color was manually selected.

4.3 Results and discussion

4.3.1 Evidences for the grafting of the peptides onto polymer brushes

The grafting of three different peptide derivatives (RGD-C, MAG-C and C-LL37) as well as the grafting of the mixture of two peptides (RGD-C and C-LL37) were studied. These peptides were chosen due to their bactericidal behavior (magainin I and LL37 [23, 97]) or their specific interaction with mammalian cell integrin receptors (RGD derivatives [85]). Glinel *et al.* demonstrated the bactericidal behavior of MAG-C grafted on poly(di(ethylene glycol) methyl ether methacrylate-*co*-hydroxyl-terminated oligo(ethylene glycol) ether methacrylate) (P(MEO_2MA-*co*-HOEGMA)) brushes towards two gram-positive bacteria: *L. ivanovii* and *Bacillus cereus* [64]. Humblot *et al.* also confirmed the bactericidal behavior of magainin I grafted on mixed SAM of 11-mercaptoundecanoïc acid and 6-mercaptohexanol towards three gram-positive bacteria: *L. ivanovii*, *Enterococcus faecalis* and *S. aureus* [148]. It has been shown that the MAG-C peptide has to be grafted from its C-terminal end to ensure the bactericidal activity [64]. The antimicrobial properties of LL37 human antimicrobial peptide are also known [97] and were confirmed against gram-negative *E. coli* by Gabriel *et al.*. Indeed, the peptide was active while grafted on a surface via a PEG spacer from its N-terminal end [105].

The density of the polymer brush might affect the number of grafted peptide molecules. Indeed, when the number of polymer chains tethered per surface unit increases, the number of functional groups (present in the polymer chain) also increases. In the case of our surfaces, we used a dense SAM of ATRP initiator to grow our brushes. The number P(HOEGMA) chains thus reachs its maximum value. The density of polymer chains can be roughly evaluated based on the result obtained previously by Jonas *et al.* [244]. Indeed, they explained that the grafted area per chain for P(MEO_2MA) is 3 nm^2. Since HOEGMA has a molar mass of about twice the one of MEO_2MA and that the PEG side-chain of HOEGMA is three times bigger than the one of MEO_2MA, we assume that the grafted area per chain for P(HOEGMA) is comprised between 6 and 9 nm^2.

It is moreover worth noting that the grafting procedure of PMPI onto the P(HOEGMA) brush was performed in THF which is a good solvent for both the brush and the linker. The grafting procedure of the peptides was performed

in Tris buffer which is a good solvent for the brush and the peptides. Since a good solvents were used for both steps, it is assumed that the grafting of the peptides was performed in the best conditions.

4.3.1.1 Fluorescence imaging of P(HOEGMA) grafted brushes

The proper grafting of the peptides onto P(HOEGMA) brush was checked. For this, homogeneous reference surfaces modified with P(HOEGMA) brush were used as grafting platforms. Fluorescence microscopy was first chosen as a qualitative technique to evidence the grafting of the peptides. The fluorescent markers used to reveal the presence of the peptide onto the surfaces show specific excitation and emission wavelengths represented in Figure 4.10.

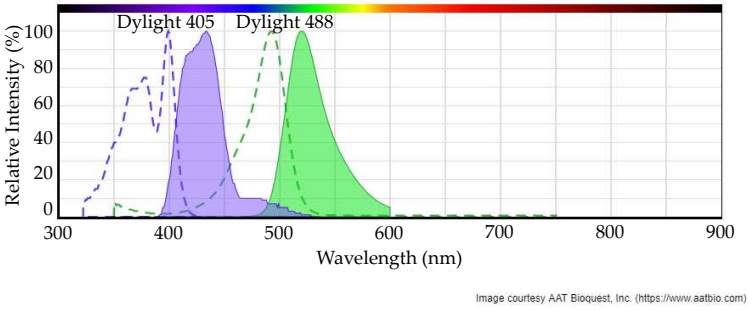

Figure 4.10: Fluorescence spectra of fluorescent markers Dylight 405 (purple) and Dylight 488 (green). The dashed lines represent the excitation spectra and the solid lines represent the emission spectra. Graph extracted from reference [245].

Grafting of Biotin-MAG-C onto P(HOEGMA) brush.
To evidence the grafting of the magainin peptide by fluorescence microscopy, a Biotin-MAG-C peptide bearing a biotin group on its N-terminal end was grafted on a P(HOEGMA) brush. The grafting was then revealed by the complexation of biotin with a fluorescent streptavidin (FITC-strep) (Figure 4.11a). Two controls were carried out to confirm the successful grafting of Biotin-MAG-C peptide: incubation of the FITC-strep or Biotin-MAG-C (followed by incubation with FITC-strep) were performed on non-modified P(HOEGMA) brushes. The Figures 4.11b and 4.11c show clearly that no significant amount of Biotin-MAG-C (followed by FITC-strep) or FITC-strep adhered on the non-modified P(HOEGMA) brush. This is due to the intrinsic non-adhesive properties of this

brush. In contrast, the adsorption of FITC-strep is clearly seen on P(HOEGMA) brush grafted with Biotin-MAG-C (Figure 4.11a).

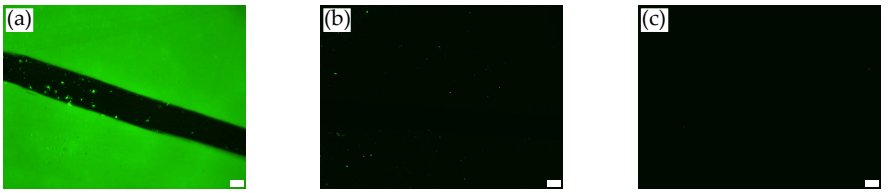

Figure 4.11: Fluorescence microscopy images of (a) P(HOEGMA) brush grafted with Biotin-MAG-C then incubated with FITC-strep; non-modified P(HOEGMA) brush incubated first with Biotin-MAG-C then FITC-strep (b); non-modified P(HOEGMA) brush incubated with FITC-strep (c). Fluorescence is significantly detected on the surface only when the Biotin-MAG-C is covalently grafted on the brush then put in contact with FITC-strep. Deliberate scratches were made to reach the fluorescence backgrounds. The white bars represent 20 μm.

The comparison of the fluorescence intensity recorded for the brush grafted with Biotin-MAG-C then complexed with FTIC-strep (Figure 4.11a) and the non-grafted brush simply incubated with Biotin-MAG-C then FITC-strep (Figure 4.11b), clearly confirmed the much higher content of Biotin-MAG-C in the grafted brush (Figure 4.12).

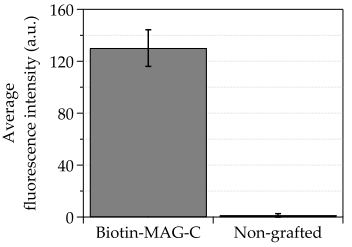

Figure 4.12: Relative fluorescence intensities measured for a Biotin-MAG-C-grafted brush incubated with FITC-strep and a non-modified brush incubated first with Biotin-MAG-C then FITC-strep.

Grafting of FITC-RGD-C or Biotin-LL37-C onto P(HOEGMA) brush.

Since the FITC-RGD-C peptide is intrinsically fluorescent, the grafted surfaces were observed directly after peptide grafting from the green channel. As expected

for the brush grafted with FITC-RGD-C, the fluorescence signal was clearly visible in the green channel (Figure 4.13a). The measurement of the non-specific adsorption of the tagged peptide on the non-modified P(HOEGMA) brush was also performed: no adsorption of FITC-RGD-C was detected in this test (Figure 4.13b). These measurements evidenced that the FITC-RGD-C peptide was grafted homogeneously on the surfaces.

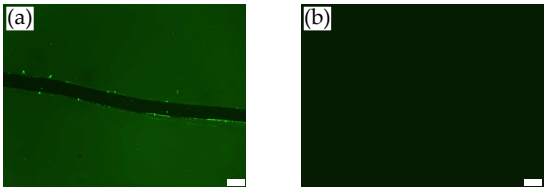

Figure 4.13: Fluorescence microscopy images of P(HOEGMA) brush (a) grafted with FITC-RGD-C and (b) non-modified P(HOEGMA) incubated with FITC-RGD. These images show that the FITC-RGD-C peptide was grafted on the P(HOEGMA) brush and did not adsorb on the non-modified P(HOEGMA) brush. Deliberate scratches were made to reach the fluorescence backgrounds. The white bars represent 50 μm.

The presence of Biotin-LL37-C peptide grafted onto the brush was indirectly evidenced by using a fluorescent streptavidin (Blue-strep) observed in microscopy from the blue channel. The grafted Biotin-LL37-C complexed with Blue-strep was visible in the blue channel, as expected (Figure 4.14a). However, two controls were carried out to ensure the effective grafting of Biotin-LL37-C onto the brush. First, non-modified P(HOEGMA) brushes incubated with Biotin-LL37-C then Blue-strep, did not show any fluorescence. This evidenced the absence of non-specific adsorption of Biotin-LL37-C peptide on the non-grafted brush (Figure 4.14b). Second, no adsorption of Blue-strep was seen onto the non-grafted brush (Figure 4.14c). Overall, these measurements evidenced that Biotin-LL37-C peptide was successively grafted homogeneously on the PMPI-modified brush.

Figure 4.14: Fluorescence microscopy images of (a) P(HOEGMA) brush grafted with Biotin-LL37-C then incubated with Blue-strep; non-modified P(HOEGMA) brush incubated first with Biotin-LL37-C then Blue-strep (b); non-modified P(HOEGMA) brush incubated with Blue-strep (c). Fluorescence is significantly detected on the surface only when the Biotin-LL37-C is covalently grafted on the brush then put in contact with Blue-strep. Deliberate scratches were made to reach the fluorescence backgrounds. The white bars represent 50 μm.

Since Biotin-LL37-C and FITC-RGD were later grafted on the same brush, using different mixtures, it was also necessary to control the fluorescence signals emitted in the blue and green channels for both FITC-RGD-C and Biotin-LL37-C (complexed with Blue-strep), respectively, in order to check any emission overlapping. Indeed, having distinct signals for both peptides allows to ensure their simultaneous successful grafting on the same polymer brush. We thus observed the image obtained from the blue channel for FITC-RGD-C grafted on the P(HOEGMA) brush. No fluorescence was detected confirming that FITC only emits signal in the green channel (Figure 4.15).

Figure 4.15: Fluorescence microscopy image of P(HOEGMA) brush grafted with FITC-RGD-C recorded from the blue channel. This image shows that the FITC-RGD-C peptide did not emit any signal in the blue channel. A deliberate scratch was made to reach the fluorescence background. The white bar represents 50 μm.

We then observed the image obtained from the green channel for Biotin-LL37-C (complexed with Blue-strep) grafted on the P(HOEGMA) brush. We observed a slight fluorescent signal (Figure 4.16). This is due to the emission

spectrum of the Dylight 405 which does not fit perfectly with the filters available on the fluorescence microscope that we used.

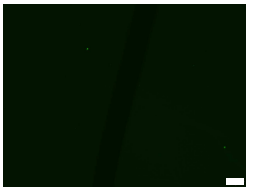

Figure 4.16: Fluorescence microscopy image of P(HOEGMA) brush grafted with Biotin-LL37-C then incubated with Blue-strep recorded from the green channel. This image shows that the Biotin-LL37-C peptide emitted a slight signal in the green channel. A deliberate scratch was made to reach the fluorescence background. The white bar represents 50 μm.

Moreover, it was also necessary to control the non-specific adsorption of blue-strep on the FITC-RGD-C grafted P(HOEGMA) brush. As expected, the FITC-RGD-C grafted peptide was seen in the green channel (Figure 4.17a) while no signal was recorded from the blue channel (Figure 4.17b). Thus, there was no non-specific adsorption of blue-strep on this brush.

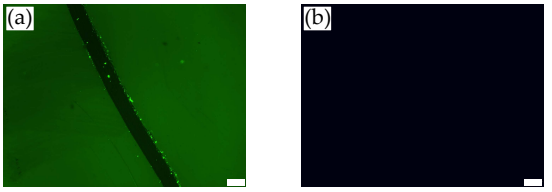

Figure 4.17: Fluorescence microscopy images of P(HOEGMA) brush grafted with FITC-RGD-C then incubated with Blue-strep recorded from (a) green and (b) blue channels. No adsorption of Blue-strep on the grafted brush was detected. Deliberate scratches were made to reach the fluorescence backgrounds. The white bars represent 50 μm.

The fluorescence intensities recorded for P(HOEGMA) brushes grafted either by FITC-RGD-C or Biotin-LL37-C (then complexed with Blue-strep) as well as the FITC-RGD-C grafted P(HOEGMA) brush incubated with Blue-strep were recorded from the green and blue channels (Figure 4.18). First, the green channel (Figure 4.18a) showed signals for FITC-RGD-C grafted brushes incubated or not with blue-strep which were larger than for brushes grafted with Biotin-LL37-C (then complexed with Blue-strep). This means that the FITC-

RGD-C peptide was grafted on the P(HOEGMA) brush and the Blue-strep, complexed with Biotin-LL37-C, emitted only a slight fluorescent signal in the green channel. Second, the blue channel (Figure 4.18b) showed no signal for the FITC-RGD-C grafted brush incubated or not with Blue-strep. This means that no Blue-strep was adsorbed on the brush. Finally, the Biotin-LL37-C peptide complexed with Blue-strep emitted a signal in the blue channel. This allowed to conclude that the grafting of the Biotin-LL37-C peptide was effective on the P(HOEGMA) brush. These observations confirmed the conclusions obtained with the fluorescence images (Figures 4.13-4.17).

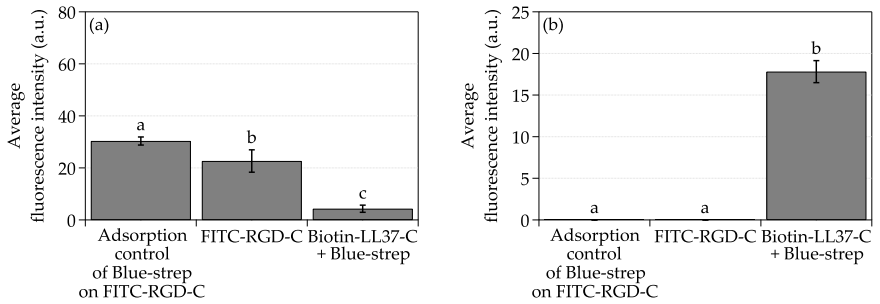

Figure 4.18: Relative fluorescence intensities recorded in the (a) green and (b) blue channels for P(HOEGMA) brushes grafted with FITC-RGD-C then incubated or not with blue-strep or grafted with Biotin-LL37-C then complexed with Blue-strep. The graphs show that both peptides were successfully grafted on the brushes. Additionally, the Blue-strep showed fluorescence mainly in the blue channel but also a little bit in the green channel. Bars with different letters indicate significant difference, p-value < 0.05.

Grafting of Biotin-LL37-C/FITC-RGD-C mixtures onto P(HOEGMA) brush.

Grafting both C-LL37 and RGD-C peptides onto the same polymer brush is interesting to produce surfaces interacting specifically with bacteria and mammalian cells. To optimize the composition of such brushes, different mixtures of Biotin-LL37-C peptide and a FITC-RGD-C peptide were grafted on P(HOEGMA) brushes (Figure 4.19). Again, the presence of Biotin-LL37-C peptide in the brush was indirectly evidenced by using a fluorescent streptavidin (Blue-strep) whereas the fluorescent FITC-RGD-C was directly detected on the surface. Different compositions of peptide solutions were tested to graft both FITC-RGD-C and Biotin-LL37-C peptides at the same time onto

the P(HOEGMA) brush: (Biotin-LL37-C/FITC-RGD-C) (30:70), (50:50) and (70:30). For each samples produced, the fluorescence signals recorded from green and blue channels were both clearly visible.

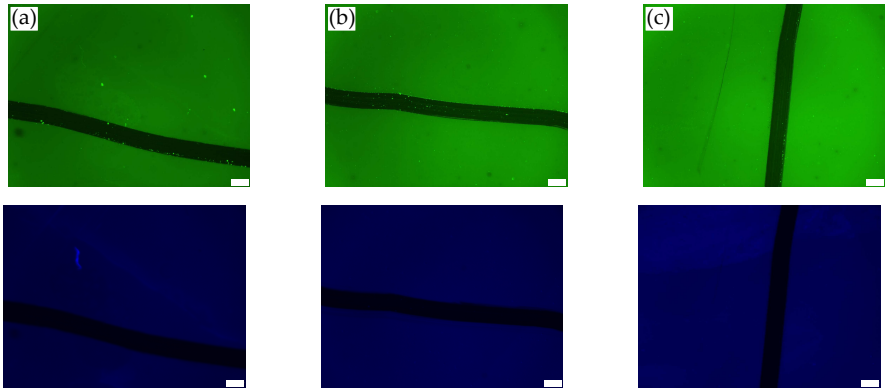

Figure 4.19: Fluorescence microscopy images (green channel on top, blue channel at the bottom) of P(HOEGMA) brushes grafted with Biotin-LL37-C/FITC-RGD-C (30:70) (a), (50:50) (b) and (70:30) (c) then incubated with Blue-strep. These images show that Biotin-LL37-C and FITC-RGD-C were both successfully grafted on the P(HOEGMA) brush. Deliberate scratches were made to reach the fluorescence backgrounds. The white bars represent 50 μm.

The measurements of the relative fluorescence intensities recorded from both channels for brushes grafted with different proportions of Biotin-LL37-C/FITC-RGD-C, after incubation in Blue-strep, are shown in Figure 4.20. The relative green fluorescent intensities (Figure 4.20a) showed that the brushes bearing both peptides had an increased intensity compared to pure FITC-RGD-C or Biotin-LL37-C (complexed with Blue-strep). Indeed, there was an overlap of the fluorescence signal emitted by both dyes, as explained above. Actually, the signal was significantly higher on surfaces grafted with the mixtures of peptides compared to the surfaces grafted with the pure FITC-RGD-C peptide. The measurements of the blue fluorescence intensities (Figure 4.20b) showed that the higher signal was emitted for the brush bearing only the Biotin-LL37-C peptide complexed with Blue-strep, as expected. Moreover, it is possible to deduce that the amount of Biotin-LL37-C grafted from the mixtures was smaller than the one from the pure peptide solution since the fluorescence intensities measured from the blue channel, for the surfaces bearing both peptides were lower than the ones recorded for the surfaces grafted with the Biotin-LL37-C only. However,

no significant difference was found between surfaces grafted with the different peptide mixtures. Overall, the relative fluorescence intensities recorded from both channels indicated that both peptides were sucessfully grafted on the brushes.

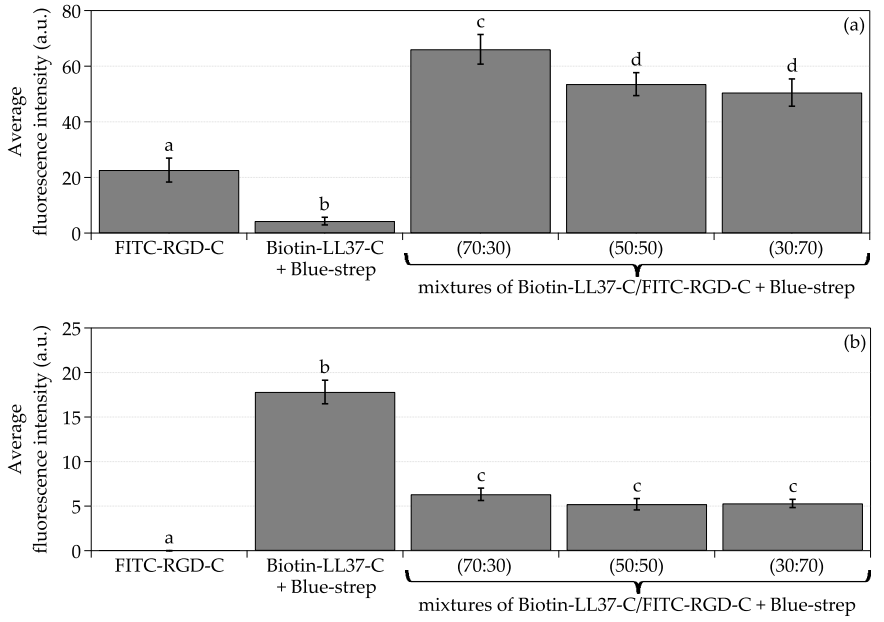

Figure 4.20: The relative green fluorescence intensity measured for (a) P(HOEGMA) brushes grafted with different mixtures of Biotin-LL37-C/FITC-RGD-C then incubated with Blue-strep, showed interaction between the different fluorochromes whereas the relative blue fluorescence intensity (b) P(HOEGMA) brushes grafted with different mixtures of Biotin-LL37-C/FITC-RGD-C, showed a net decrease of the fluorescence with the decrease of the Biotin-LL37-C content added in the grafting solution. Bars with different letters indicate significant difference, p-value < 0.05.

4.3.1.2 XPS and ellipsometry characterizations of P(HOEGMA) grafted brushes

XPS was used to quantify the percentage of grafting onto P(HOEGMA) brushes. However, it is important to stress that this technique probe only the first 10 nm of the polymer layer and not its whole thickness. Ellipsometry was used to further control the grafting density of the peptides.

Grafting of MAG-C onto P(HOEGMA) brush.
XPS measurements were performed to quantify the amount of MAG-C grafted onto the surface of P(HOEGMA) brush (Figures 4.21, 4.22 and 4.23). The comparison of the XPS spectra of the polymer brush measured before and after the peptide grafting revealed the presence of a N1s peak after grafting of the peptide confirming its presence on the P(HOEGMA) brush (Figure 4.21). The computed grafting degree was of 1.62 % of monomer units (according to equation 4.4). Similar experiments were performed by Glinel *et al.* who immobilized magainin onto P(MEO_2MA-*co*-HOEGMA) brushes on the hydroxyl pendent groups of HOEGMA. They obtained a grafting degree of 5 % [64]. A possible reason for the lower grafting obtained on our brush, compared to P(MEO_2MA-*co*-HOEGMA), is the lower accessibility of the hydroxyl groups present in the P(HOEGMA) brush due to the steric hindrance resulting for the longer lateral PEG chains. However, it has to be noticed that the XPS technique probed only the top surface of the polymer brush. Therefore the real grafting degree of the brush is maybe much higher.

C1s spextra displayed in Figures 4.22 and 4.23 also show that the percentage of carbon single bonded to another carbon increased. On the contrary, the percentage of carbon single bonded to oxygen decreased after the grafting of the peptide. This is due to the presence of MAG-C whose composition increases the number of single bonds of carbon to carbon while the amount of single bonds of carbon to oxygen is not increased. It is worth noting that after grafting the peaks of carbons single bonded to oxygen or nitrogen overlap. The third peak corresponds to an ester group before grafting and to ester and amide groups after grafting. The percentage linked to this peak did not vary with the grafting of MAG-C. Actually, the presence of MAG-C whose composition increases the number of amide bonds while the amount of ester bond did not vary, lead to this overall stable percentage. We can also notice that the S2s peak detected after the MAG-C grafting was not clearly defined and thus could not be used for quantification.

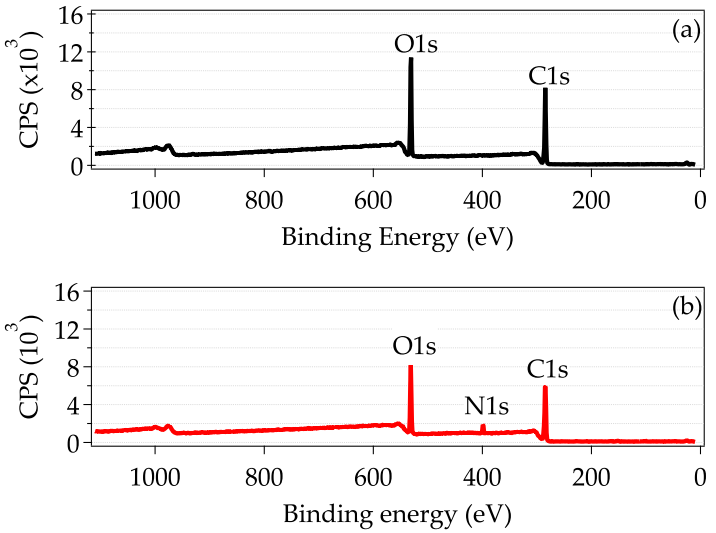

Figure 4.21: The comparison of XPS survey spectra measured for (a) P(HOEGMA) brush and (b) P(HOEGMA) brush grafted with MAG-C shows a N1s peak for the grafted brush which evidences the successful grafting of the peptide.

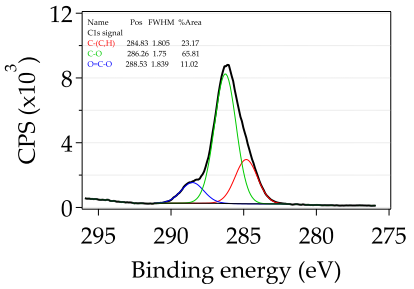

(a) C1s spectrum and its decomposition.

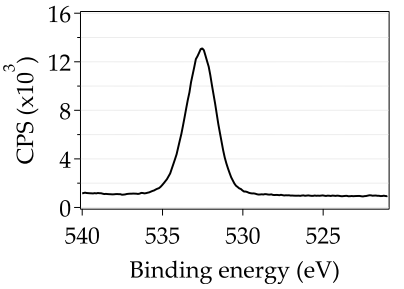

(b) O1s spectrum.

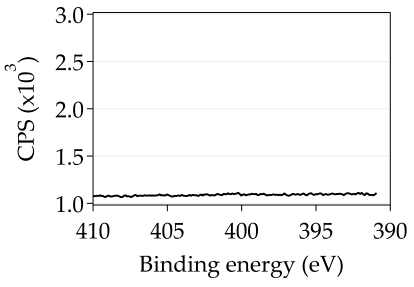

(c) N1s spectrum.

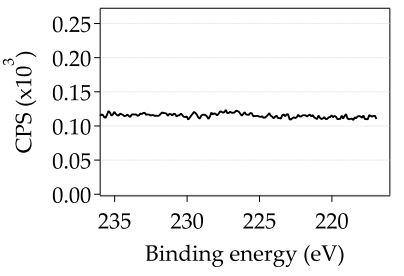

(d) S2s spectrum.

Figure 4.22: XPS spectra measured at high energy resolution in the C1s, O1s, N1s and S2s regions for a P(HOEGMA) brush. The color lines shown in (a) correspond to the decomposition of the C1s peak.

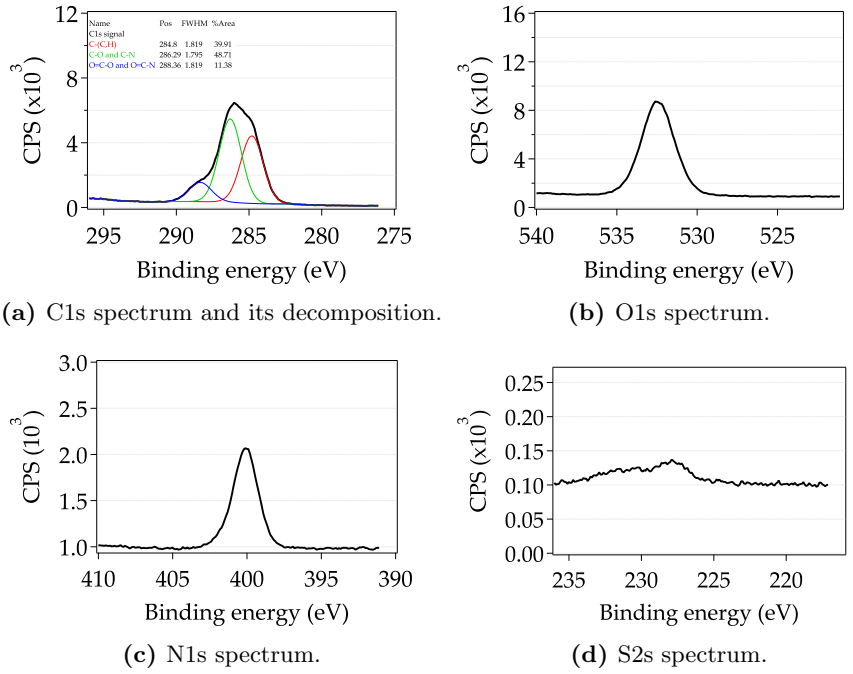

(a) C1s spectrum and its decomposition.

(b) O1s spectrum.

(c) N1s spectrum.

(d) S2s spectrum.

Figure 4.23: XPS spectra measured at high energy resolution in the C1s, O1s, N1s and S2s regions for a P(HOEGMA) brush grafted with MAG-C. The color lines shown in (a) correspond to the decomposition of the C1s peak.

The ellipsometry measurements showed a thickness difference between the grafted and non-grafted P(HOEGMA) brushes of 8.8 nm and the peptide density computed from equation 4.5 was $2.73 * 10^6$ peptides/μm^2. We can compare this value to the one computed from the results obtained in the article published by Humblot *et al.* [148]. In this study, magainin I was grafted onto a SAM layer and it was shown that the difference of the layer thickness measured before and after the grafting was 1.3 nm. Using equation 4.5 and the molecular volume of 2916 Å^3 computed for magainin I, by the Peptide Property calculator [243], we obtained a peptide density of $4.46 * 10^5$ peptides/μm^2 for these surfaces based on SAM. The peptide density obtained in our brushes is thus 6 times higher than the one obtained by Humblot *et al.*. This was expected since one polymer chain provides several anchoring possibilities for the peptide compared to a SAM which only gives one anchoring point per molecule. Using polymer brush thus allowed to increase the number of grafted peptide molecules per surface area.

Grafting of RGD-C or C-LL37 onto P(HOEGMA) brush.

XPS measurements were also performed to quantify the amount of RGD-C or C-LL37 molecules grafted on the P(HOEGMA) brush (Figures 4.24, 4.25, 4.26 and 4.27). These analyses showed systematically the presence of a N1s peak after grafting of the peptides confirming their successful grafting (Figure 4.24). The grafting degrees determined according to equation 4.4 were 12.85 % and 3.3 %, for the brushes grafted with RGD-C and C-LL37, respectively. As explained above, Glinel *et. al.* performed a similar experiment for the grafting of magainin and obtained a graftin degree of 5% [64]. The grafting degree obtained for C-LL37 is lower than the one obtained by Glinel *et al.*. As explained above, the lower accessibility of the hydroxyl groups used in our experiments may lead to steric hindrance allowing the grafting of a smaller amount of peptide. On the contrary, the larger peptide density obtained for RGD-C was expected since RGD-C has a smaller molecular volume than magainin and LL37 which facilitates its accessibility and consequently its grafting on the maleimide reactive groups.

C1s spectra displayed in Figures 4.25, 4.26 and 4.27 also show that the percentage of carbon single bonded to another carbon increased while the percentage of carbon single bonded to oxygen decreased. This is due to the presence of peptides whose composition increased the number of single bonds of carbon to carbon while the amount of single bonds of carbon to oxygen did not varied. Again, it is worth noting that after grafting, the peaks of carbons single bonded to oxygen or nitrogen overlap. The peak corresponding to ester and amide functionalities increased slightly after grafting. This means that the grafting of peptides counterbalanced for the lower ratio of ester functionalities and even increased the amount of amide functionalities such that the peak area increased. We can also notice that the S2s peak after peptide grafting was not clearly defined or even absent and thus could not be used for quantification.

To improve the determination of the grafting degree of the brush, the grafting of a C-RGD-F (CKRGDSPF(4-F)) peptide containing a fluor atom in its sequence was tested (Figure 4.28). Indeed, the use of heteroatoms in XPS is advantageous since it helps to tag molecules not bearing any discriminating groups. This helps to specifically quantify one molecule when co-grafting is performed. In our case, using an atom of fluor may help to quantify the grafting of the different peptides when co-grafted on the P(HOEGMA) brush. Unfortunately, the signal measured for the F1s peak was not large enough

compared to the background to perform quantification. Due to this limitation, the analysis of brushes co-grafted with C-LL37/RGD-C mixtures was not performed by XPS. Note that the signal of S2s could not be also used for quantification due to its poor intensity compared to the background.

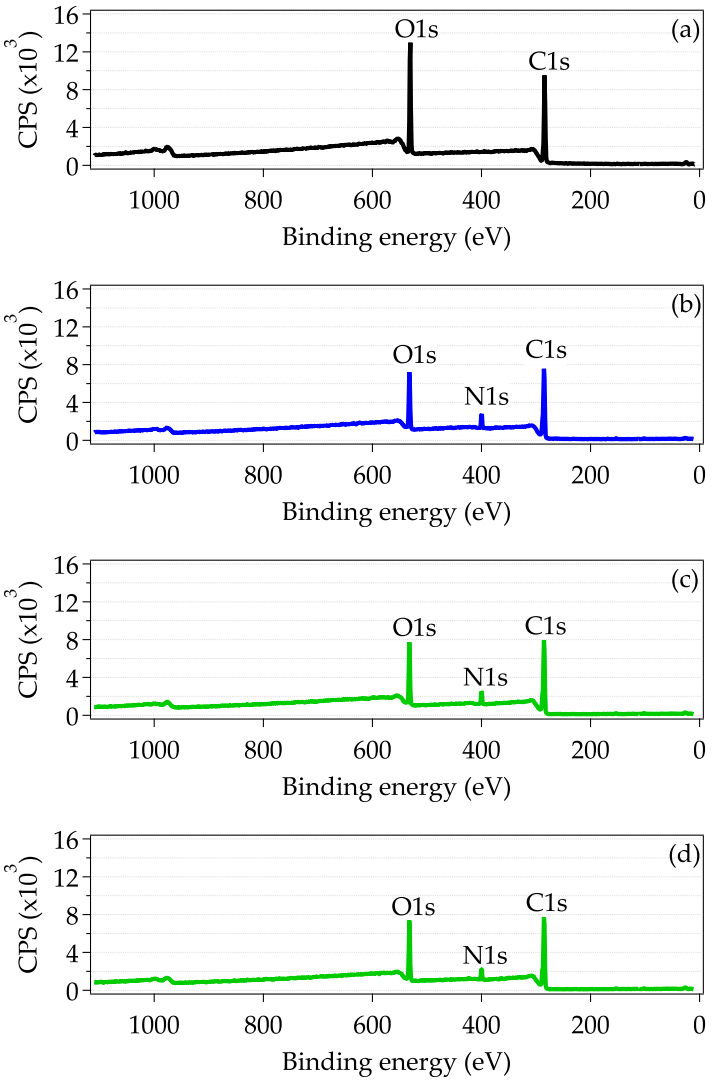

Figure 4.24: The comparison of XPS survey spectra measured for (a) P(HOEGMA) brush, (b) P(HOEGMA) brush grafted with C-LL37, (c) P(HOEGMA) brush grafted with RGD-C and (d) P(HOEGMA) brush grafted with C-RGD-F shows systematically a N1s peak for grafted brushes which evidences the successful grafting of the peptides.

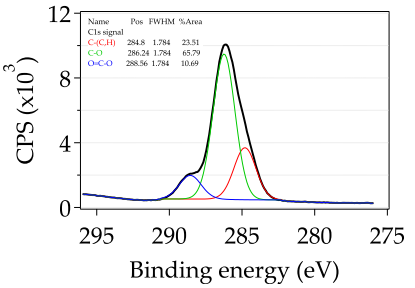

(a) C1s spectrum and its decomposition.

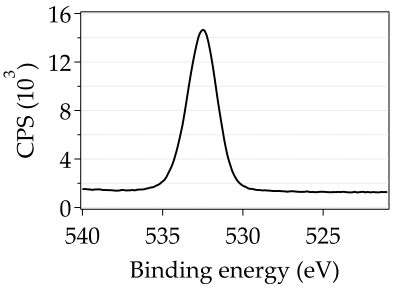

(b) O1s spectrum.

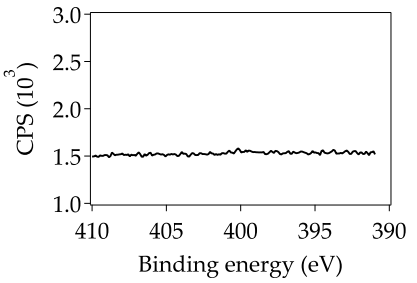

(c) N1s spectrum.

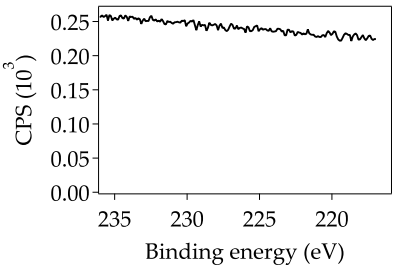

(d) S2s spectrum.

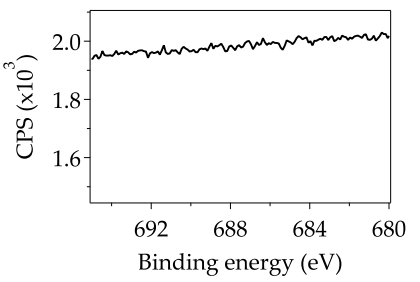

(e) F1s spectrum.

Figure 4.25: XPS spectra measured at high energy resolution in the C1s, O1s, N1s and S2s regions for a P(HOEGMA) brush. The color lines shown in (a) correspond to the decomposition of the C1s peak.

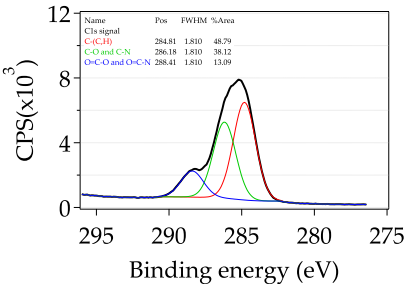

(a) C1s spectrum and its decomposition.

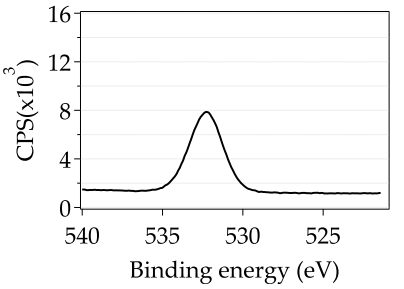

(b) O1s spectrum.

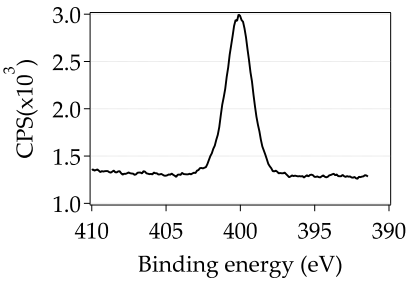

(c) N1s spectrum.

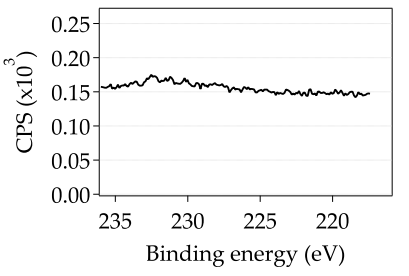

(d) S2s spectrum.

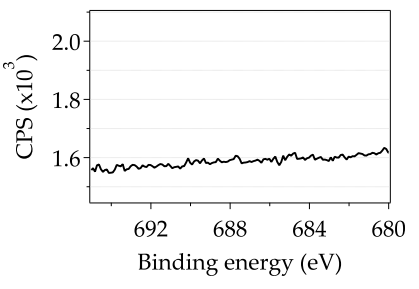

(e) F1s spectrum.

Figure 4.26: XPS spectra measured at high energy resolution in the C1s, O1s, N1s and S2s regions for a P(HOEGMA) brush grafted with C-LL37. The color lines shown in (a) correspond to the decomposition of the C1s peak.

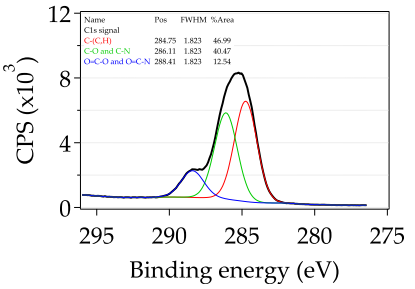

(a) C1s spectrum and its decomposition.

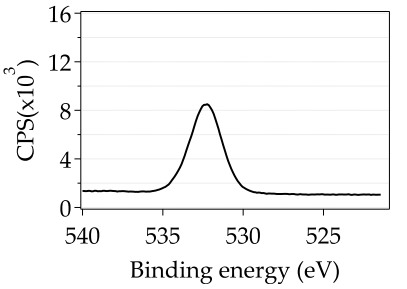

(b) O1s spectrum.

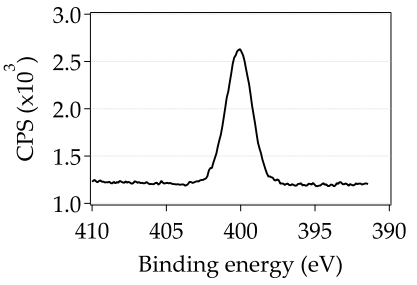

(c) N1s spectrum.

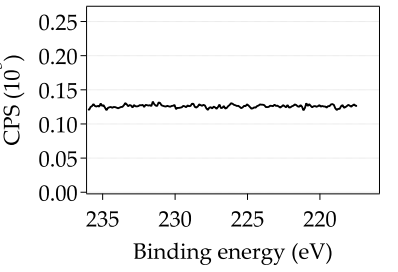

(d) S2s spectrum.

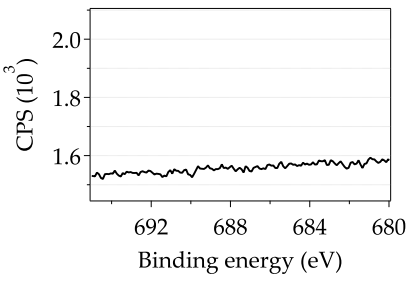

(e) F1s spectrum.

Figure 4.27: XPS spectra measured at high energy resolution in the C1s, O1s, N1s and S2s regions for a P(HOEGMA) brush grafted with RGD-C. The color lines shown in (a) correspond to the decomposition of the C1s peak.

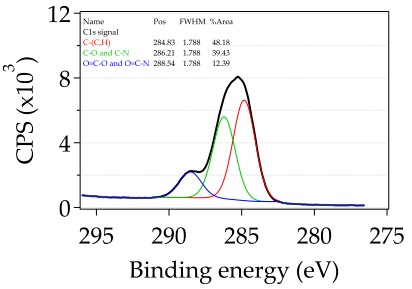

(a) C1s spectrum and its decomposition.

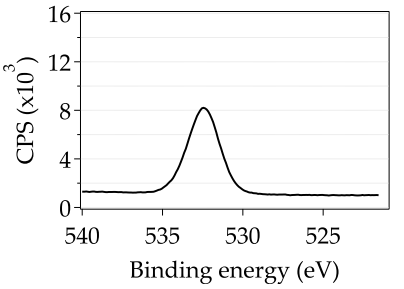

(b) O1s spectrum.

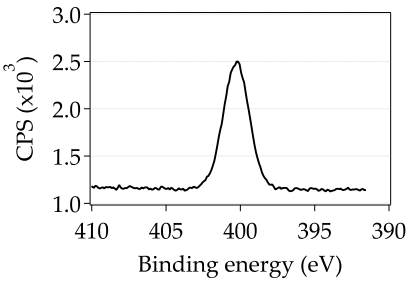

(c) N1s spectrum.

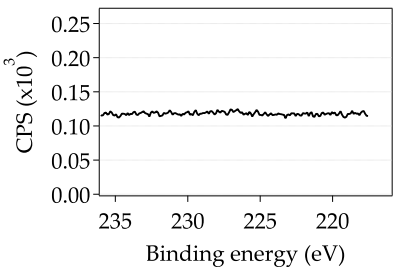

(d) S2s spectrum.

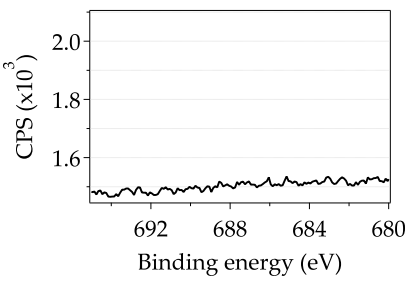

(e) F1s spectrum.

Figure 4.28: XPS spectra measured at high energy resolution in the C1s, O1s, N1s and S2s regions for a P(HOEGMA) brush grafted with C-RGD-F. The color lines shown in (a) correspond to the decomposition of the C1s peak.

The ellipsometry measurements showed a thickness difference between the brush grafted with RGD-C and non-grafted P(HOEGMA) brush of 8.25 nm giving rise to a peptide density (computed from equation 4.5) of $7.5 * 10^6$ peptides/μm^2. This is much higher than the threshold values obtained by Rowley *et al.* which claimed that 6.022 molecules/μm^2 was needed for the spreading and 60.22 molecules/μm^2 for proliferation of C2C12 myoblast cells [84].

In contrast, Weis *et al.* showed that 180.66 molecules/μm^2 needed to be used for differentiation of C2C12 myoblast cells [246]. These values may indicate ideal values of peptide density for adhesion, spreading and differentiation of this particular C2C12 cells but may not be the same for the SCAP cells used in our project. The research from Harris *et al.* is also interesting since they computed the density of peptides on P(MAA) brush grafted by GRGDS. They found values ranging from $4.82 * 10^5$ peptides/μm^2 to $49.98 * 10^6$ peptides/μm^2 depending on the initial thickness of the brush used. Moreover, they were able to show that a peptide density of $60 * 10^6$ peptides/μm^2 was the maxium density value allowing to improve the adhesion of fibroblasts cells [241]. We thus obtained a peptide density value of the same order of magnitude than the ones by Harris. This indicates that we have a sufficient amount of RGD-C peptide grafted onto the surface for the next steps of our experiments. Moreover, it seemed from the literature that the distance between RGD peptide molecules is more relevant to control the cell behavior than the total amount of peptide grafted onto the surface [1, 160, 167, 184, 191, 201].

In the case of the samples grafted with C-LL37, the ellipsometry measurements showed a thickness variation of 10.4 nm between the brush grafted with C-LL37 and the non-grafted P(HOEGMA) brush giving rise to peptide density (computed from equation 4.5) of $1.81 * 10^6$ peptides/μm^2. In the study of Gabriel *et al.*, they immobilized LL37 by its N-terminal end via a PEG spacer grafted on a SAM. They obtained a peptide density of $8.85 * 10^5$ peptides/μm^2 [105]. We thus obtained a grafting density twice larger. Once again, the polymer brush allowed a higher grafting density than the one obtained from SAM. It has to be noted that not only the surface density can affect the activity of antimicrobial peptide: a larger amount of peptide should induce a higher antimicrobial activity but this potential can fluctuate depending on parameters such as accessibility of the peptide towards the bacterial cell which depends on the length of the spacer used to immobilize the peptide onto the surface [237]. The peptide density of RGD-C was much higher than the one of C-LL37. This was probably due to the smaller molecular volume of RGD-C compared to C-LL37.

Grafting of C-LL37/RGD-C onto P(HOEGMA) brush.

The ellipsometry measurements performed on the mixed brushes (Figure 4.29) showed an increase of the brush thickness whatever the composition of the grafting solution. This result evidenced the grafting of peptide molecules. Furthermore, the increase of the brush thickness measured after peptide grafting

tended to increase for a higher amount of C-LL37 peptide in the grafting solution (Figure 4.29a). This was expected since the C-LL37 peptide has a larger molecular volume than RGD-C peptide. Finally, we observed a linear variation of the thickness difference as a function of the content of RGD-C peptide added in the grafting solution. This indicated that the final composition of the grafted brush was proportional to the composition of the grafting solution. For a given peptide, we thus assumed a linear increase of its surface density as a function of its percentage in the grafting solution (Figure 4.29b). To trace such a curve of the variation of the surface density of each peptide as a function of the composition of the grafting solution, we considered the peptide densities determined from the thickness difference in Figure 4.29a for the brushes grafted with 100% RGD-C and 100% C-LL37.

According to the linear variation of the thickness difference measured after and before peptide grafting as a function of the composition of the grafting solution, we assumed a linear variation of the density of each peptide (D_{pep}) with the composition of the grafting solution. Therefore, we computed a linear variation of the density of each peptide between 0, which is the density obtained for a non-grafted brush, and x, which is the density measured for a brush modified with only one type of peptide, (Figure 4.29b). This resulted in the equation:

$$D_{pep} = \frac{(10.249 - 0.016833 P_{RGD-C}) 10^{-3} P_{pep}}{V_{pep} 10^{-12}} \tag{4.6}$$

With P_{RGD-C} the molar percentage of RGD-C peptide in the grafting solution varying from 0 to 100. P_{pep} the fraction of peptide used in the grafting solution and V_{pep} the molecular volume of the grafted peptide and the linker ($Å^3$/peptide molecule).

The grafting solution chosen to prepare brushes grafted with both RGD-C and C-LL37 peptides, is the one with (50:50) (mol:mol) percentage and will be used for further experiments with bacteria and mammalian cells. This corresponds to peptide densities of $4.279 * 10^6$ peptides/μm^2 and $8.197 * 10^5$ peptides/μm^2 for RGD-C and C-LL37, respectively. These values can be compared to published studies described above and based on surfaces bearing only one type of peptide. For RGD-C, the value of the density that we obtained was much higher than the one obtained for SAMs [84, 246] and comparable to the one obtained on the polymer brush by Harris *et al.* [241]. For C-LL37, we reached values similar to the one obtained by Gabriel *et al.* for SAMs [105].

The (50:50) composition of the grafting solution allowed for the grafting of a large amount of both peptides which have thus more chance to retain their functionality.

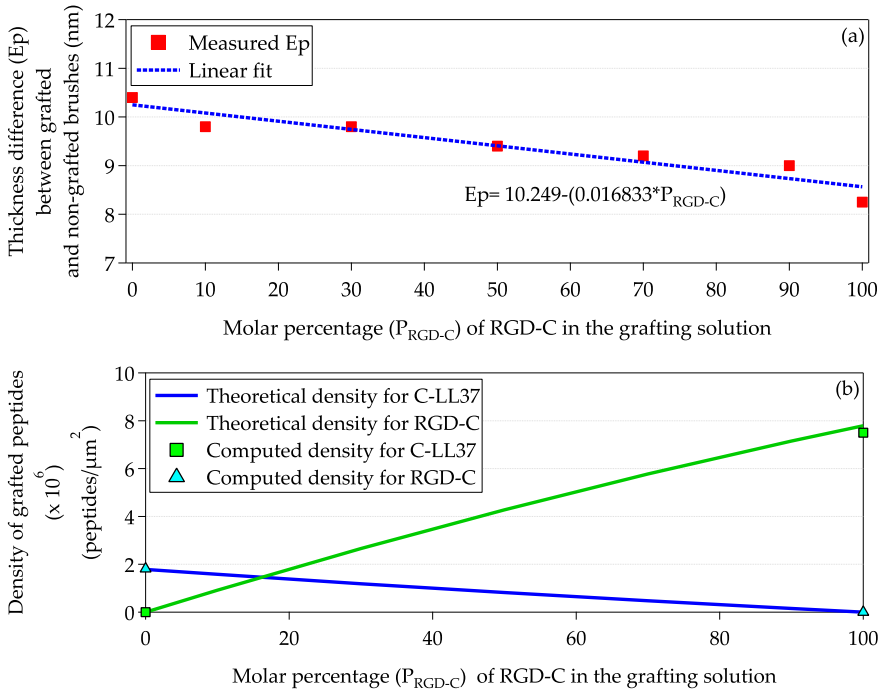

Figure 4.29: (a) Difference of brush thickness (E_p) between the grafted and non-grafted P(HOEGMA) brushes for different peptide mixtures of C-LL37 and RGD-C. The dashed line represents the linear fit obtained. (b) The densities in peptide C-LL37 (blue) and RGD-C (green) expected for brushes grafted with various compositions of both peptides. The values computed from the experimental data were close to the computed density. The density of a given peptide is expected to increase linearly with its content in the grafting solution.

4.3.2 Nanopatterned surface characterization

We characterized the nanopatterned surfaces after each modification steps as shown in Figure 4.1 to assess their overall regularity. To do that, we first characterized by SEM the lateral dimensions of the molds used for NIL. We also characterized the transfer of the pattern onto the PMMA film by AFM. Then we ensured by AFM that the dimensions found for the PMMA patterned mask were kept during the whole elaboration process.

The SEM analysis of the NIL molds (Figure 4.30) was performed using two different magnifications. The smaller one (*i.e.* magnification 6000x) helped to ensure that no major defects were present on the mold surface and that the lines were properly shaped (Figure 4.30a). In addition, images were recorded at a higher magnification of 100000x in order to assess the geometrical characteristics of the molds at the nanometer scale (Figure 4.30b). Different silicon molds composed of protruding lines and named 250 and 400, were imaged. The theoretical characteristics of the 250 mold provided by the supplier are 78 nm-width protruding line with a pit of 172 nm while the dimensions for the 400 mold are 200 nm-width protruding line with a pit of 200 nm. The line width and the pit, measured by SEM for the mold 250, were 71 +/- 1 nm and 171 +/- 1 nm, respectively and 172 +/- 2 nm and 226 +/- 5 nm for the mold 400. These values are close to the dimensions provided by the supplier.

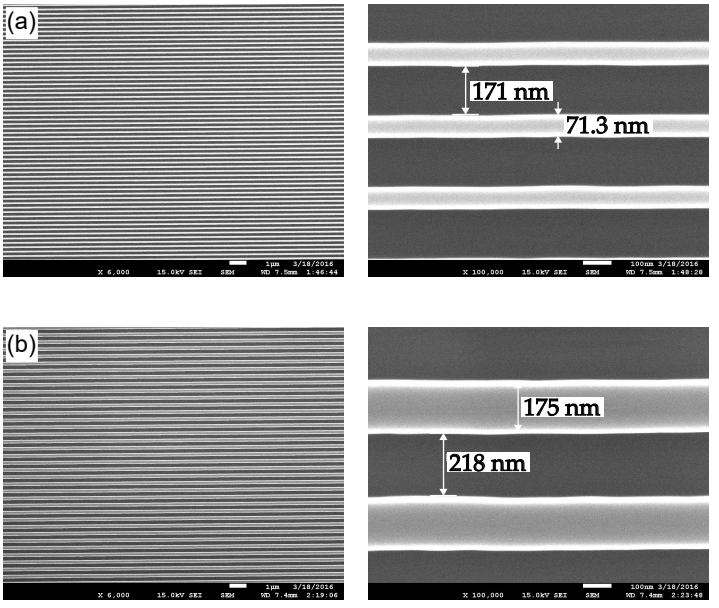

Figure 4.30: SEM images of (a) the 250 nanoimprint mold and (b) the 400 nanoimprint mold with two different magnifications. The white bars represent 1 μm and 100 nm for the magnifications 6000x and 10000x, respectively.

The PMMA patterns obtained after NIL were characterized by AFM in contact mode using an ultrasharp probe (Figures 4.31 and 4.32). As the imprint is the negative image of the mold, we expected to find protruding lines of 171 nm

with a pit of 71 nm for the 250 mold while it should be protruding lines of 226 nm with a pit of 172 nm for the 400 mold. The height of the lines should be 200 nm as it is the value provided by the manufacturer. The values obtained for the 250 mold were 150 +/- 4 nm for the width of the protruding line and 121 +/- 4 nm for the pit (Figure 4.31). The values obtained for the 400 mold were 255 +/- 3 nm for the width of the protruding line and 182 +/- 4 nm for the pit (Figure 4.32). These values were not exactly the same as the ones measured by SEM for the silicon molds. This could be due to the imprecision of the AFM measurements as the tip of the probe might enlarge the protruding lines while scanning. The heights of the protruding lines were around 120 nm and 220 nm for 250 and 400 PMMA nanopatterns, respectively. The value obtained for the 400 nanopattern was in agreement with the expected values given by the supplier while the value for the 250 nanopattern was smaller. Actually, the AFM probe was not able to reach the bottom of the 250 imprinted nanopattern pit. Overall, the NIL process went as expected showing a regular nanopattern of protrusions and pits.

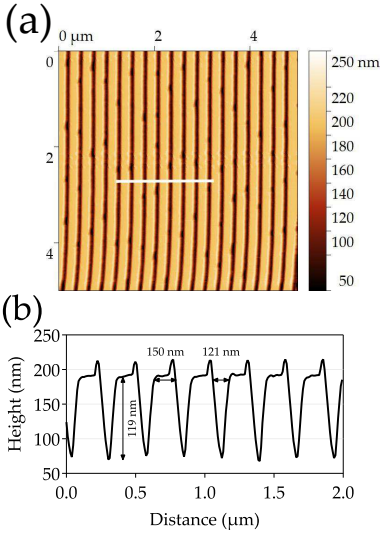

Figure 4.31: AFM analysis in contact mode of a 250 nanoimprinted PMMA surface: (a) topographical image and (b) line profile.

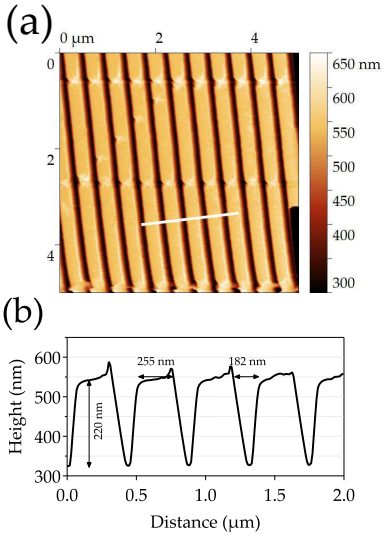

Figure 4.32: AFM analysis in contact mode of a 400 nanoimprinted PMMA surface: (a) topographical image and (b) line profile.

The nanopatterns were subsequently surface modified according to the

process explained in Figure 4.1. Here, we first analyze the elaboration of 250 and 400 chemical nanopatterns then we focus on the elaboration of 250 and 400 topographical nanopatterns.

The lateral dimensions as well as the thickness of the polymer brushes grown onto the chemically nanopatterned surfaces were characterized before (Figure 4.1 step 5.a) and after (Figure 4.1 step 6.a) grafting of the different peptides. The lateral dimensions of the brushes were measured at mid-height to balance for the non-ideal behavior of the confined brushes [244, 247]. The measured lateral dimensions of the 250 chemical nanopattern with non-grafted brush were 154 +/- 4 nm for the protruding lines and 120 +/- 3 nm for the pits (Figure 4.35). They were actually much larger than expected. This was probably due to the measurement imprecision because of the non-ideal behavior of the brushes. Some deformations of the PMMA mask occurring during the surface modification process may be the reason for some mask deformation during the different modification steps necessary for the formation of the pattern.

The thickness of the brushes before and after grafting of the peptides were measured by AFM using the height in the extracted line profile. The thickness increase was then deduced by subtracting the height of the brush measured before grafting from the one after grafting. The AFM measurements showed an increase of the brush thickness of 4 nm, 3 nm, 4.5 nm and 4.5 nm after the grafting of RGD-C, MAG-C, C-LL37 and C-LL37/RGD-C (50:50) peptides, respectively, as can be seen on the AFM line profiles (Figures 4.33, 4.34, 4.35, 4.36, 4.37 and 4.38, respectively). The ellipsometry measurements performed on homogeneous brushes show an increase of 8 nm, 8 nm, 9 nm and 9 nm, respectively. As expected, the grafting of the peptides or the peptide mixture induced an increase of the thickness of the nanopatterned brushes. However, the different thickness increments measured after grating by ellipsometry and AFM for homogeneous and patterned brushes, respectively, could be explained by the broadening of the width of the brush lines. Indeed, as explained above, the 250 chemical nanopatterns with non-grafted brushes consist of 154 +/- 4 nm protruding lines with pits of 120 +/- 3 nm. After RGD-C, MAG-C, C-LL37 and C-LL37/RGD-C (50:50) grafting, the widths of the protruding lines were 142 +/- 2 nm, 162 +/- 4 nm, 174 +/- 3 nm and 167 +/- 5 nm, respectively while the widths of the pits were 127 +/- 1 nm, 113 +/- 2 nm, 100 +/- 1 nm and 106 +/- 8 nm, respectively (Figures 4.34, 4.36, 4.37 and 4.38, respectively). Indeed, on homogeneous surfaces, the confined polymer chains could only expand

in the vertical direction while on nanopatterned surfaces, the chains were not confined and could also expand horizontally which resulted in a lower increase of thickness after peptide grafting.

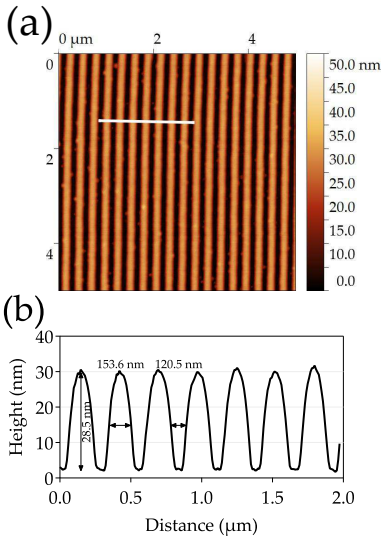

Figure 4.33: AFM analysis in tapping mode of a 250 chemical nanopattern with non-grafted brushes: (a) topographical image and (b) line profile.

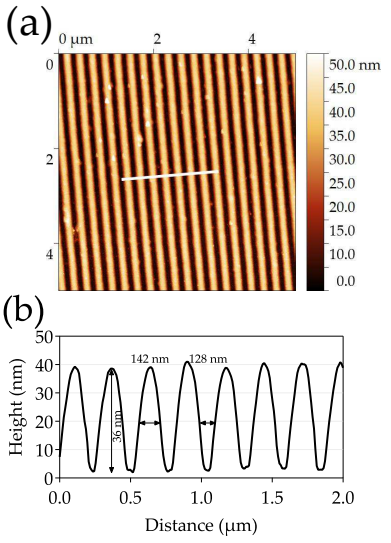

Figure 4.34: AFM analysis in tapping mode of a 250 chemical nanopattern grafted with RGD-C: (a) topographical image and (b) line profile.

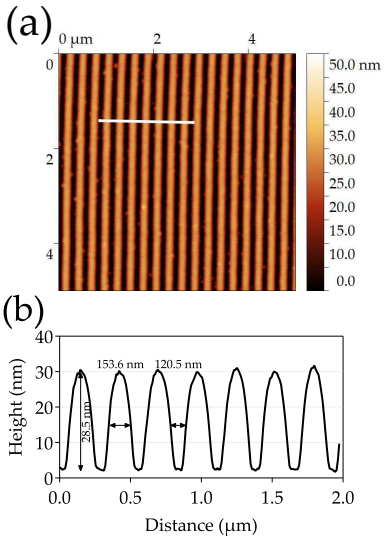

Figure 4.35: AFM analysis in tapping mode of a 250 chemical nanopattern with non-grafted brushes: (a) topographical image and (b) line profile.

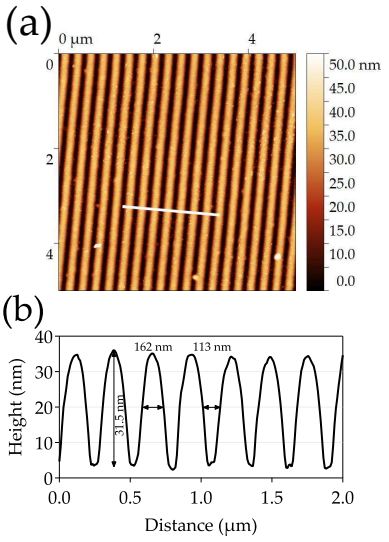

Figure 4.36: AFM analysis in tapping mode of a 250 chemical nanopattern grafted with MAG-C: (a) topographical image and (b) line profile.

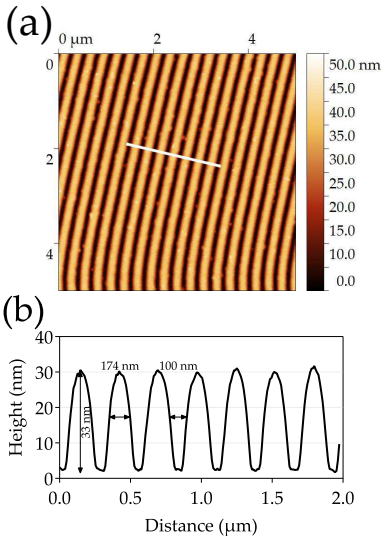

Figure 4.37: AFM analysis in tapping mode of a 250 chemical nanopattern grafted with C-LL37: (a) topographical image and (b) line profile.

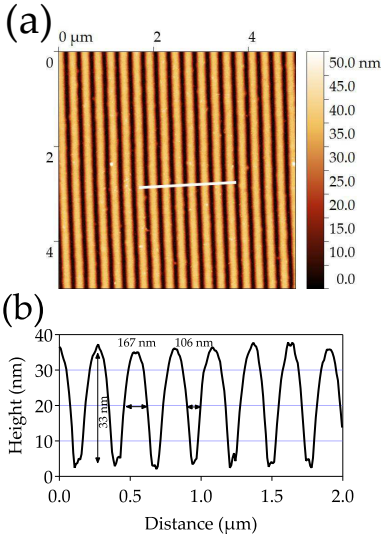

Figure 4.38: AFM analysis in tapping mode of a 250 chemical nanopattern grafted with C-LL37/RGD-C: (a) topographical image and (b) line profile.

The measured lateral dimensions of the 400 chemical nanopattern with non-grafted brush were 246 +/- 1 nm for the protruding lines and 188 +/- 1 nm for the pits (Figure 4.39). They were actually much larger than expected as previously observed for 250 chemical nanopattern with non-grafted brush. Moreover, the AFM measurements showed an increase of the brush thickness of 2 nm, 3 nm, 5.5 nm and 4 nm after the grafting of RGD-C, MAG-C, C-LL37 and C-LL37/RGD-C (50:50) peptides, respectively, as can be seen on the AFM line profiles (Figures 4.39, 4.40, 4.41, 4.42, 4.43 and 4.44, respectively). The ellipsometry measurements performed on homogeneous brushes showed an increase of 8 nm, 8 nm, 9 nm and 9 nm respectively. Indeed, as explained above, the 400 chemical nanopattern with non-grafted brushes consist of 246 +/- 1 nm protruding lines with pits of 188 +/- 1 nm. After RGD-C, MAG-C, C-LL37 and C-LL37/RGD-C (50:50) grafting the widths of the protruding lines were 258 +/- 1 nm, 263 +/- 2 nm, 266 +/- 5 nm and 265 +/- 5 nm, respectively while the widths of the pits were 178 +/- 4 nm, 179 +/- 3 nm, 174 +/- 7 nm and 175 +/- 1 nm, respectively (Figures 4.40, 4.42, 4.43 and 4.44, respectively). The same argument related to the non-confinement of the polymer chains given for the 250 chemical nanopattern grafted with a given peptide can be put forward to explain the lower increment of thickness observed after the grafting of the peptide compared to the homogeneous brushes and the broadening of the protruding lines.

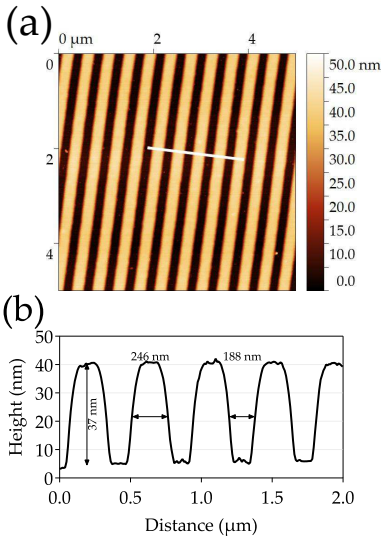

Figure 4.39: AFM analysis in tapping mode of a 400 chemical nanopattern with non-grafted brushes. (a) Topographical image and (b) Line profile.

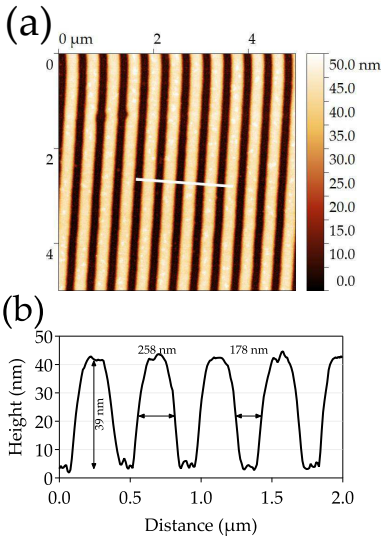

Figure 4.40: AFM analysis in tapping mode of a 400 chemical nanopattern grafted with RGD-C: (a) topographical image and (b) line profile.

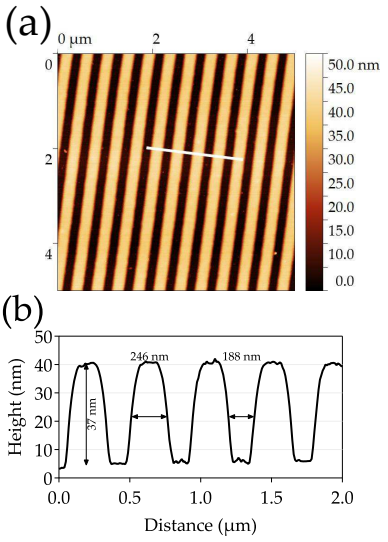

Figure 4.41: AFM analysis of the 400 chemical nanopattern with non-grafted brushes. (a) Topographical image and (b) Line profile.

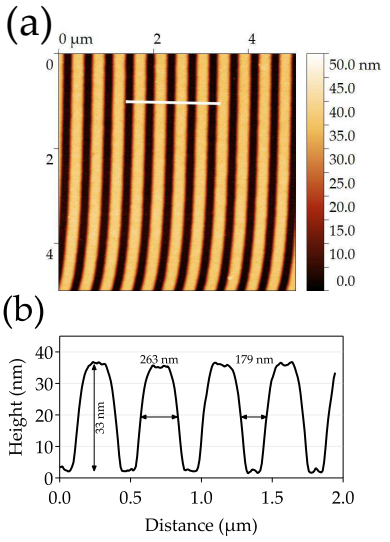

Figure 4.42: AFM analysis of the 400 chemical nanopattern grafted with MAG-C: (a) topographical image and (b) line profile.

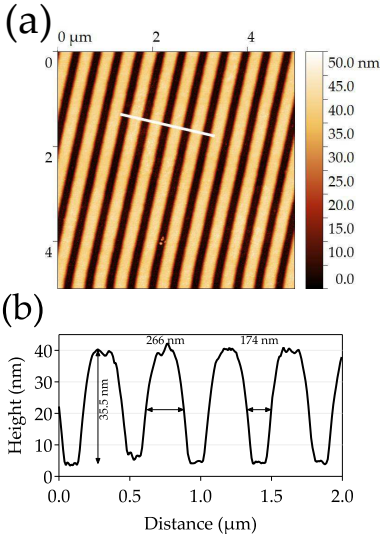

Figure 4.43: AFM analysis of the 400 chemical nanopattern grafted with C-LL37: (a) topographical image and (b) line profile.

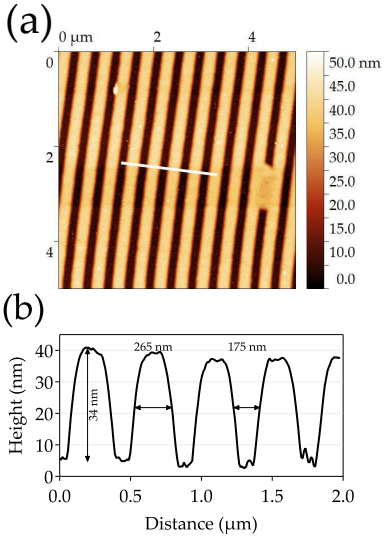

Figure 4.44: AFM analysis of the 400 chemical nanopattern grafted with C-LL37/RGD-C: (a) topographical image and (b) line profile.

The 250 and 400 topographically patterned surfaces were characterized after etching of the silicon oxide and before and after grafting of the polymer brushes. For the 250 topographical nanopatterns (Figures 4.45, 4.46 and 4.47), the height of the topography measured by AFM was of 53 nm which is in agreement with the measurement obtained by ellipsometry of 50 nm. This value corresponds to the silicon oxide thickness etched on the reference surface (Table 4.4). The lateral dimensions obtained after silicon oxide etching were 156 +/- 3 nm for the width of the protruding lines and 113 +/- 5 nm for the pits. These values match with the dimensions measured by AFM for the PMMA nanoimprinted films. When a P(HOEGMA) brush was grown on the topographical pattern, it was not possible anymore to fully scan the surface, notably the bottom parts of the pattern, due to the broadening of the lines observed.

For the 400 topographical nanopatterns (Figures 4.48, 4.49 and 4.50), the height of the topography measured by AFM was of 52 nm which is in agreement with the measurement obtained by ellipsometry of 49 nm. This value corresponds to the silicon oxide thickness etched on the reference surface (Table 4.4). The lateral dimensions obtained after silicon oxide etching were 188 +/- 11 nm for the width of the protruding lines and 250 +/- 8 nm for the pits. These values match with the dimensions measured by AFM for the PMMA nanoimprinted films. When a P(HOEGMA) brush was grown on the topographical pattern, it smoothed the topographical pattern due to the non-ideal behavior of the brush. The lateral dimensions of the brush was again larger compared to the topographical silicon oxide pattern.

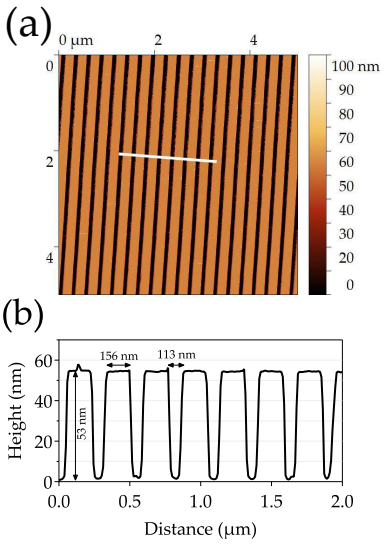

Figure 4.45: AFM analysis in tapping mode of the 250 etched topographical nanopattern without brushes: (a) topographical image and (b) line profile.

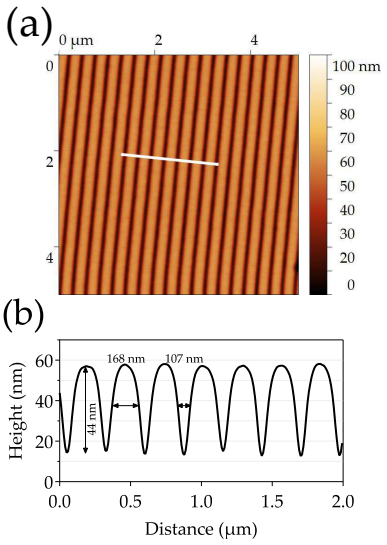

Figure 4.46: AFM analysis in tapping mode of the 250 topographical nanopattern with non-grafted brushes: (a) topographical image and (b) line profile.

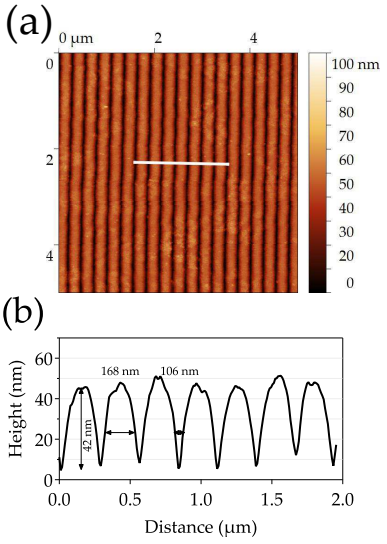

Figure 4.47: AFM analysis in tapping mode of the 250 topographical nanopattern grafted with RGD-C: (a) topographical image and (b) line profile.

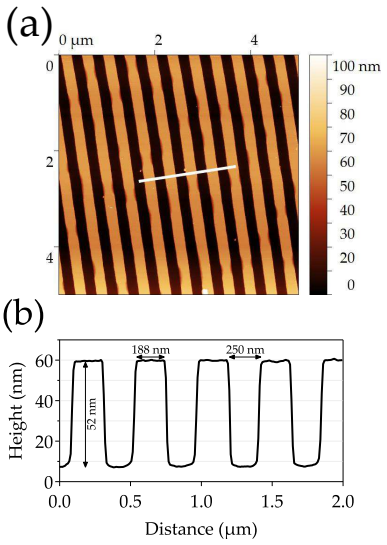

Figure 4.48: AFM analysis in tapping mode of the 400 etched topographical nanopattern without brushes: (a) topographical image and (b) line profile.

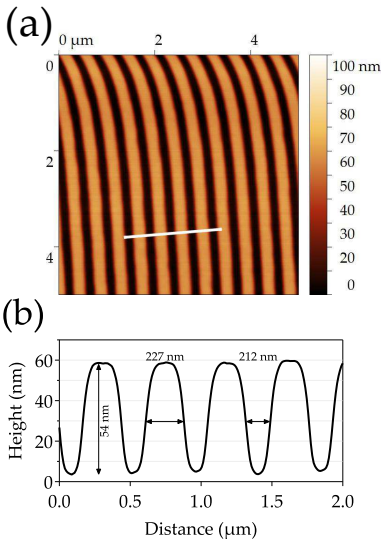

Figure 4.49: AFM analysis in tapping mode of the 400 topographical nanopattern with non-grafted brushes: (a) topographical image and (b) line profile.

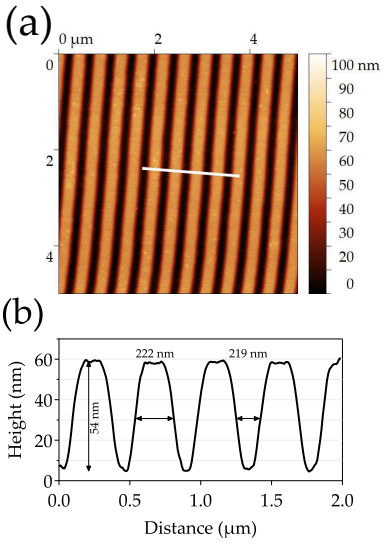

Figure 4.50: AFM analysis in tapping mode of the 400 topographical nanopattern grafted with RGD-C: (a) topographical image and (b) line profile.

4.4 Conclusion

In this chapter, we focused on the fabrication of nanopatterned surfaces showing biofunctionalized P(HOEGMA) brushes distributed in a non-adhesive background of PEG. We focused especially on the biofunctionalization process of P(HOEGMA) brush with RGD, magainin I and LL37 peptide derivatives. Then we characterized the nanopattern dimensions throughout the fabrication process.

We thus first developed the biofunctionalization of P(HOEGMA) brush by different peptides (RGD, magainin I and LL37 derivatives) using homogeneously grafted surfaces. For this, we combined fluorescent microscopy, XPS and ellipsometry. The use of fluorescence probes provided a qualitative proof of the grafting of FITC-RGD-C, Biotin-MAG-C and Biotin-LL37-C peptides. The XPS measurements allowed to quantitatively evaluate the grafting degree of the brushes in peptide molecules (*i.e.* RGD-C, MAG-C and C-LL37). The grafting degree varies from 1.62 % to 12.85 % as a function of the peptide used with a higher amount of monomer units grafted for the smaller RGD-C peptide grafted. The ellipsometry measurements helped to establish that about 10^6 peptide molecules were grafted per μm^2 when one type of peptide reacted with the brush. We were also able to estimate the peptide densities of RGD-C and C-LL37 while co-grafted on the polymer brush via ellipsometry measurements. We showed that the increment of thickness measured after peptide grafting varied linearly with the composition of the grafting mixture used to modify the brush. From this observation, we found that each co-grafted peptide density varied linearly with the amount of peptide incorporated into the grafting solution.

The dimensions of the nanopatterns were fully characterized and showed regular and well-defined biochemical and topographical features even though the lateral dimensions of the nanopatterns slightly differed from the initial dimensions of the silicon molds used to fabricate the patterns. Finally, the process developed to biofunctionalize the P(HOEGMA) brush was applied to graft peptides in order to produce biofunctionalized chemical and topographical nanopatterns. The grafting was assessed by the increase of the thickness of the patterned polymer brushes. A broadening of the lateral dimensions of the nanopatterns was also observed after grafting.

Overall, the chemical and topographical nanopatterns grafted with the different peptides possess the appropriate characteristics to be used for biological tests with bacteria and mammalian cells.

Chapter 5

Bacterial adhesion and viability on nanopatterned surfaces

5.1 Introduction

One goal of this PhD thesis was to elaborate nanopatterned surfaces allowing to kill bacteria and to control the behavior of mammalian cells. In this chapter, we focused on the effect of the nanopatterned surfaces on the bacterial behavior.

Among the strategies available to develop surfaces killing bacteria upon contact lie the surfaces showing high aspect ratio topography capable of mechanically piercing the bacterial membrane [17]. The immobilization of polycation polymers onto a surface also allows the disruption of the membrane due to the interactions between the positive charges of the polymer and the negatively charged bacterial membrane [71]. Finally, bioactive agents such as antimicrobial peptides can be grafted on surfaces [63].

This chapter focuses on the study of 250 or 400 chemical nanopatterns grafted with adhesive RGD-C, antimicrobial MAG-C and C-LL37 peptides and a C-LL37/RGD-C mixture (50:50) and 250 or 400 topographical nanopatterns grafted with RGD-C. The percentage of surface area covered by bacteria and the percentage of dead bacteria onto the surfaces were studied according to the nature of the peptide and the lateral dimensions of the chemical or topographical

nanopatterns.

The use of antimicrobial peptides was motivated by the antibiotic resistance commonly encountered in the medical domain [7, 68]. Antimicrobial peptides present many advantages such as a broad killing spectrum [20, 76, 98], low induced resistance [20, 76] and lower needed quantities compared to other killing reagents [20]. However, some of these peptides display some disadvantages such as local cytotoxicity [23, 76, 90] and potential susceptibility towards enzymatic degradation [212]. Among the large number of antimicrobial peptides available, we selected magainin I and LL37. Magainin I peptide was chosen because of its well-known antimicrobial activity even when immobilized onto a surface as explored by Glinel *et al.* [64] and Humblot *et al.* [148]. LL37 was chosen because of its human origin [97] and its non-toxic behavior towards mammalian cells at low concentration [98]. We also immobilized RGD peptide which is specific to mammalian cell adhesion [85] but nevertheless needs to be tested in the presence of bacteria to assess the potential interactions taking place. Generally speaking, immobilizing bioactive peptides on surfaces present advantages. Rai *et al.* showed that gold nanoparticles grafted with antimicrobial cecropin-melittin peptide can be reused five times without loss of their antimicrobial activity. Indeed some immobilized peptides retain their killing activivity for a long time [248]. However, Bagheri *et al.* also pointed out that immobilized peptides retained their specific activity spectrum but their activity can be reduced [249].

The strain of bacteria we chose for our experiment is *E. coli*. It is frequently used as a model of gram-negative bacterium. Moreover, magainin I and LL37 peptides are known to be active against *E. coli* in solution. For example, Maria-Neto *et al.* showed that a concentration of 0.075 mg/mL of magainin I was required to prevent the growth of *E. coli* [250]. On their side, Turner *et al.* found a concentration of 0.0076 mg/mL of LL37 was able to prevent the growth of *E. coli* in solution [251].

In this chapter, we pursued three objectives. First, we aimed at testing the antimicrobial properties of MAG-C and C-LL37 towards *E. coli* in solution. Then, the study of bacterial adhesion and viability were performed on various control and patterned surfaces, *i.e.* homogeneous, 250 and 400 chemical nanopatterns grafted with RGD-C, MAG-C, C-LL37 and C-LL37/RGD-C and 250 and 400 topographical nanopatterns grafted with RGD-C. The homogeneous surfaces are control surfaces consisting in non-patterned P(HOEGMA) brushes grafted with peptides.

5.2 Materials and methods

5.2.1 Materials

Luria Bertani Broth with agar (Lennox) (LB agar), Luria Bertani Broth (Lennox) (LB broth), Ampicillin sodium salt, sodium chloride (99%+) (NaCl), ammonium chloride (NH_4Cl) (>99.5%), sodium phosphate monobasic (99%) (KH_2PO_4), sodium phosphate dibasic (≥99.5%) (Na_2HPO_4), were purchased from Sigma-Aldrich. Milli-Q grade water (resistivity of 18.2 mΩ) was produced by a Milli-Q® Reference system of Merck Millipore and autoclaved by Systec Horizontal Benchtop Autoclave DB-23. MAG-C and C-LL37 are derivatives of magainin I and LL37 which possess a cysteine residue at their C-terminal and N-terminal ends, respectively. These peptides were synthesized by Genecust with a purity > 95 %. LIVE/DEAD® BacLight™ Bacterial Viability Kit, for microscopy, was purchased from ThermoFisher Scientific.

5.2.2 Medium and buffer preparation

Ampicillin solution of 100 μg/ml. 10 mg of ampicillin were added in 10 mL autoclaved water. This solution was diluted 10 times, filtered and stored at -20°C. The final solution was unfreezed before use.

Preparation of agar plates. 7 g of LB Broth with agar was dissolved in 200 mL of water. The solution was autoclaved and 200 μL of ampicillin solution (100 μg/ml) was added when the solution cooled down but was not yet a gel. 30 mL of the agar solution was poured in a 10 cm diameter and 15 mm height petri dish. Once the solution became a gel, the petri dishes were stored for one month max. at 4°C.

LB Broth medium. 4 g of LB Broth was dissolved in 200 mL of water. The solution was autoclaved and 200 μL of ampicillin solution (100 μg/ml) was added when the solution cooled down. The medium were stored at room temperature until use.

0.15 M NaCl solution. 2.19 g of NaCl was dissolved in 250 mL of water. The solution was autoclaved then the pH was adjusted to 7.25 right before use. The solution was stored at 4°C for one night before use.

Buffer solution. 0.0625 g of NaCl, 0.375 g of KH_2PO_4 and 0.723 g of Na_2HPO_4 were added in 500 ml of water. The pH was adjusted to 7.25 and the solution autoclaved. The buffer solution was stored for one night at 4°C.

5.2.3 *E. coli* cultures and harvesting

MG1655 *E. coli* strain was spread with a sterile inoculation loop onto an agar plate then incubated for 24h at 37°C (Figure 5.1a). Some colonies were taken out from the agar surface and seeded in 20 mL of LB Broth medium. This preculture referred to as "overnight culture" was performed overnight at 37°C in a 50 mL falcon tube (Figure 5.1b). Then, 5 mL of the overnight culture was collected and poured into 20 mL of fresh LB Broth medium in a 50 mL falcon tube. Bacteria were grown for 2 hours at 37°C (Figure 5.1c). Then a part of this fresh culture was collected in six 2 mL-eppendorf tubes. The bacteria were harvested by centrifugation for 3 minutes at 10 000 rpm. The pellets were subsequently resuspended in 2 mL of buffer solution. This rinsing step was repeated 3 times. Then buffer solution was added in the bacterial suspension to get a specific optical density (OD) (Figure 5.1d).

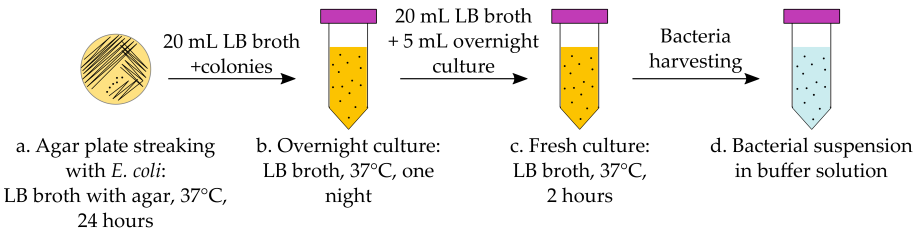

Figure 5.1: Methodology used to perform bacterial culture previous to tests on the surfaces.

5.2.4 Antimicrobial properties of MAG-C and C-LL37 peptides in solution

Freshly cultured bacteria were harvested, rinsed then dispersed in a buffer solution, as explained above, to get an OD around 0.4. Four peptide solutions with concentrations of 0, 0.01, 0.1 and 1 mg/mL were used to assess the antimicrobial properties of a given peptide. The peptide solutions used to investigate the antimicrobial properties of the peptides were prepared using a high concentrated solution of peptide of 2 mg/mL, buffer solution and harvested bacteria suspended in buffer solution for a final volume of 1 mL contained in an eppendorf tube. The concentration of bacteria was kept constant for each aliquot produced and corresponded to an OD of 0.2 (*i.e.* 10^8 CFUs/mL). Two peptides were tested for their antimicrobial properties: MAG-C and C-LL37.

The bacterial suspensions were left at room temperature for three hours without stirring. The viability of the bacteria was assessed by seeding 100 μL of 10^5 times diluted suspension on an agar plate which was subsequently incubated at 37°C overnight. The number of colonies grown on the agar plate were counted and the number of colony forming units (CFUs)/mL was computed. The agar plate tests were performed in duplicate for each conditions tested. Bacterial suspensions without peptide were used as a control. Moreover, a bacterial enumeration was systematically performed on the freshly prepared control suspension, before the 3h-incubation.

5.2.5 Surfaces used to perform bacterial adhesion tests

The surfaces tested for the adhesion and viability of bacteria are summarized in Table 5.1. Among these surfaces lie homogeneous brushes grafted with RGD-C, MAG-C, C-LL37 or C-LL37/RGD-C (50:50). These surfaces were used as control surfaces to compare the behavior of bacteria on non-patterned and patterned surfaces. The 250 or 400 chemical nanopatterns vary in their lateral dimensions as explained in Chapter 4 and consist of lines of P(HOEGMA) brushes grafted with RGD-C, MAG-C, C-LL37 or C-LL37/RGD-C (50:50), distributed in a non-adhesive background. The 250 or 400 topographical nanopatterns vary in their lateral dimensions, show pits of 50 nm and are covered with a P(HOEGMA) brush grafted with RGD-C.

Table 5.1: The surfaces presented in this table were used for the bacterial adhesion and viability tests. They are classified according to the nature of the grafted peptide and their structure.

		Peptide			
		RGD-C	MAG-C	C-LL37	C-LL37 /RGD-C
Surface structure	Homogenenous brushes			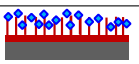	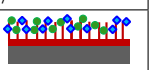
	250 chemical nanopatterns	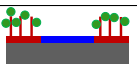	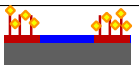	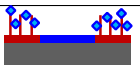	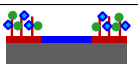
	400 chemical nanopatterns	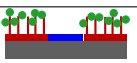		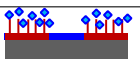	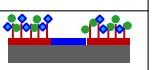
	250 topographical nanopatterns	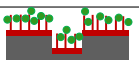	x	x	x
	400 topographical nanopatterns	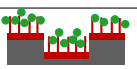	x	x	x

5.2.6 Bacterial adhesion on nanopatterned surfaces

Freshly cultured bacteria were harvested, rinsed then dispersed in a buffer solution, as explained above, to get an optical density between 0.22 and 0.24 (*i.e.* 10^8 CFUs/mL). The 0.5x1 cm^2 homogeneous and nanopatterned surfaces were rinsed with methanol then filtered Milli-Q water and dried with a stream of N_2 before being placed each in a 2x2 cm^2 well of a 25-well plate. 2 mL of bacterial suspension was added in each well. This adhesion step was performed without stirring at room temperature during three hours (Figure 5.2a). After that, all the samples were gently rinsed successively in three tubes filled with filtered 0.15 M NaCl solution to remove the non-adhered bacteria.

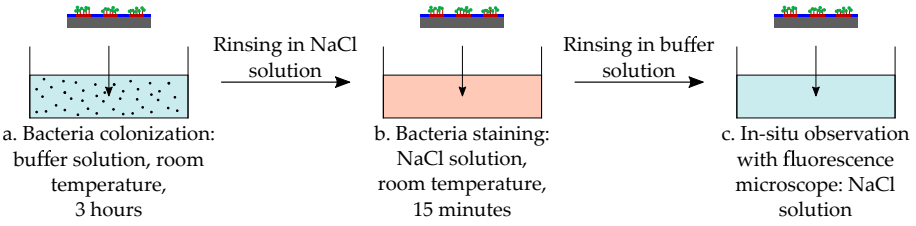

Figure 5.2: Methodology used to perform bacterial adhesion tests on the surfaces.

5.2.7 Fluorescence microscopy

The bacteria were stained with LIVE/DEAD® BacLight™ Bacterial Viability Kit according to the following protocol: 30 μL of LIVE/DEAD mixture (SYTO 9 dye, 1.67 mM/Propidium iodide, 18.3 mM) was added to 20 mL of filtered 0.15 M NaCl solution at neutral pH. The surfaces colonized by bacteria were immersed in this solution for 15 minutes in a container protected from the light (Figure 5.2b). After staining, the samples were rinsed once with fresh buffer solution (section 5.2.2) to remove the excess of dyes. The samples were placed upside down in Lab-Tek chambered covered glass (purchased from Thermo scientific) filled with filtered 0.15 M NaCl solution (Figure 5.2c). The bacteria adhered onto the surfaces were imaged with an Olympus inverted epifluorescence IX71 microscope equipped with a green filter U-MWIBA3 (excitation 460-495 nm and emission 510-550 nm) and a red filter U-MNIGA3 (excitation 540-550 nm and emission 575-625 nm). The UV light is provided by an X-cite module, series 120PCQ from Lumen Dynamics. For each surface, 9 images were taken at magnification 10X distributed on the whole sample surface. The images were analyzed with a custom made IGOR PRO routine allowing to count the numbers of green, red and orange pixels corresponding to lived and dead bacteria, respectively (Figure 5.3).

The percentage of surface area covered by bacteria was computed by measuring the ratio between the number of stained pixels and the total number of pixels in the recorded image (*i.e.* 1428288 pixels). These data are represented in a boxplot. The percentage of dead bacteria was estimated from the ratio of red and orange pixels to the total number of stained pixels. The percentages are presented as mean values ± standard error of the mean (sem). Statistical analyses were performed using one-way analysis of variance (ANOVA) (IGOR PRO,

Wavemetrics) followed by post hoc Tukey (HSD) test with a significance level set at alpha = 0.05. Differences were considered significant for a p-value < 0.05. The experiments were performed in triplicate with duplicate samples of each type of nanopatterned surfaces.

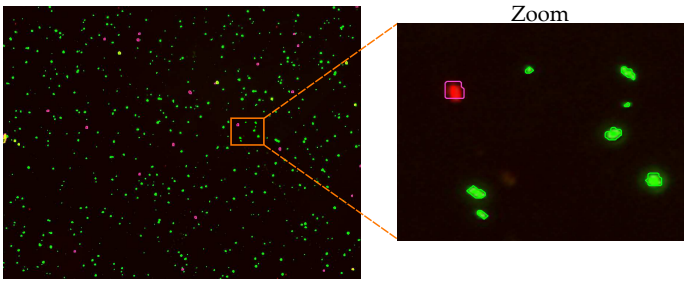

Figure 5.3: Fluorescence microscopy image of *E. coli* (stained with LIVE/DEAD kit) adhered on homogeneous brush grafted with C-LL37 (overlay images). The green, red and orange part of the bacteria are surrounded by green, pink and yellow lines which show the pixels counted as green, red and orange, respectively.

5.3 Results and discussion

We first ensured that MAG-C and C-LL37 showed bactericidal properties in solution towards *E. coli*. Then we analyzed the bacterial adhesion onto the nanopatterned and control surfaces qualitatively by fluorescence microscopy and quantitatively thanks to a homemade IGOR PRO routine explained above. Finally, the percentage of dead bacteria was computed to assess the bactericidal properties of the surfaces grafted with peptides.

5.3.1 Study of the bactericidal properties of the peptide derivatives in solution

The efficiency of the peptides in concentration varying from 0 to 1 mg/mL was assessed by the bacteria enumeration, initially seeded at 10^8 CFUs/mL, after 3h-incubation. The results obtained are presented in Table 5.2 and are expressed as colony forming units (CFUs/mL).

Table 5.2: Number of CFUs per mL for each condition tested. The results are displayed as mean ± SD. C_{pep} is the final concentration of the tested peptide in the solution.

			CFU/mL (x10^8)		% of killing
Peptide derivative	C_{pep}		Incubation time	Incubation time	
	(nmol/mL)	(mg/mL)	0 hour	3 hours	
None			1.29 ± 0.04	1.22 ± 0.22	
MAG-C	3.98	0.01	\	1.07 ± 0.11	12 ± 25
	39.8	0.1	\	1.12 ± 0.08	8 ± 23
	398	1	\	0.68 ± 0.08	44 ± 17
C-LL37	2.18	0.01	\	1.28 ± 0.03	0 ± 21
	21.8	0.1	\	0.59 ± 0.02	52 ± 10
	218	1	\	0 ± 0	100 ± 0

The enumeration of bacteria for the control solution (the one which does not contain any peptide) shows that there is no large decrease of CFU number before and after 3h-incubation. For MAG-C peptide, a decrease in the number of CFUs (of about 44 %) was observed for the concentration of 398 nmol/mL. The killing percentages obtained for 3.98 and 39.8 nmol/mL were not high enough to conclude about the efficiency of MAG-C against *E. coli* at these lower concentrations. The value of 398 nmol/mL was much higher than the minimal inhibitory concentration (MIC) (*i.e.* the concentration at which there is no bacterial growth in the medium chosen) found by Maria-Neto *et al.* for magainin I. Indeed, they found a MIC of 31.1 nmol/mL for a suspension of *E. coli* (5x10^5 CFU/mL in LB broth) incubated in the presence of the peptide for 2h at 37°C [250]. As can be seen, the concentration needed to impair bacterial growth was smaller than the one obtained to kill bacteria in our experiment. This may be due to several factors discussed later in this section: the metabolic state, the concentration of bacteria, the ionic strength, the medium used and the presence of C-terminal cysteine on the peptide chain. For C-LL37 peptide, a concentration of 21.8 nmol/mL already had a significant effect on the viability of bacteria (even if the SD is large) but a higher concentration of 218 nmol/mL led to the complete eradication of bacteria in the suspension in the conditions used. Turner *et al.* who studied the susceptibility of *E. coli* (2x$10^6 CFU/mL$) towards LL37 in 10 mM sodium phophate (100 mM NaCl and 1% v:v Trypticase

soy broth power) obtained a MIC value of 1.69 nmol/mL [251]. Cassin *et al.* compared the OD measurements performed at 600 nm before and after 18h-incubation of *E. coli* in Lysogeny broth. The MIC was set from the value of OD that did not vary in time after 18h with an initial OD value of 0.05. They deduced that the MIC of LL37 was of 8 nmol/mL [147]. The values found in the literature for LL37 and magainin I were smaller than the ones found in our experiment and may be due to the factors explained hereafter. Our experiment allowed to conclude that both peptides had an antimicrobial effect on *E.coli*. However, the concentrations at which this effect occurred were different between both peptides. C-LL37 showed a much higher bactericidal activity towards *E. coli* compared with MAG-C. Moreover, the effective concentrations that we obtained to affect *E. coli* viability are much higher than the ones reported in the literature. However, our results need to be taken with caution since we used a higher concentration of bacteria compared to the litterature and we did not test different dilutions to confirm the killing percentages measured.

The determination of the MIC values strongly depends on the conditions used for the test. There are some differences between our experiments and the previous studies performed by others that need to be taken into account when analyzing the data obtained as they may influence the results obtained. First, the medium used in our experiment was not a growth medium for bacteria. Consequently, we measured the killing activity against a non-growing bacteria. The metabolic activity may differ as the function of the medium used. Second, the concentration of bacteria used in our tests is much higher than the ones reported in other studies. We chose this concentration because it corresponds to the conditions used to perform tests on our nanopatterned surfaces (sections 5.3.2 and 5.3.3). This higher concentration may lead to a higher concentration of peptide required to kill bacteria. This is probably why the amount of peptide needed to kill bacteria is large in our experiment. Third, the ionic strength, the nutrient concentration and the bacteria type influence the bactericidal efficiency of the peptides [97]. Indeed, Turner *et al.* first performed a radial diffusion assay (in this technique, the agar gel seeded with bacteria is exposed to a solution of antimicrobial peptide) to test the antimicrobial properties of various peptides (e.g. LL37) against various bacterial strain among which lie *E. coli* strains. They showed that the bacterial strain as well as the salt (NaCl) concentration influenced the MIC value [251]. Moreover, the nature of the salts added in the medium can also influence the bactericidal properties of the peptides. For

instance, Ca^{2+} increased the MIC value of LL37 towards *E. coli* while Mg^{2+} has no effect [251]. Furthermore, Kandasami *et al.* simulated the insertion of magainin II in palmitoyloleoylphosphatidylcholine bilayer used as a model of bacterial membrane in presence of NaCl. They evidenced that the Na^{+} cation tightened the structure of the lipid bilayer which resulted in a lower insertion of the magainin peptide. [252]. Moreover, the microdilution assays (in this technique, the growing bacteria are incubated with the peptide) performed in three different media (*i.e.* MHB, refined MHB and modified 10 mM sodium phophate medium containing 100 mM NaCl and 1% v:v Trypticase soy broth powder) in the presence of *E. coli* ($2x10^6$ CFU/mL) incubated for 2 hours then seeded on agar plates and incubated for 24h at 37°C, showed that the medium used for the test influenced the MIC concentration. The richer medium (*i.e.* MHB), the refined medium (*i.e.* refined MHB) and the poorer medium (*i.e.* modified sodium phosphate solution) showed MIC values of 5.34-7.12 nmol/mL, 1.33-1.78 nmol/mL and 1.69 nmol/mL, respectively [251]. Finally, the supplementary cysteine added at the C-terminal and N-terminal of MAG-C and C-LL37 might also influence the folding of the peptides and thus influence their antimicrobial activity.

The difference of bactericidal properties between magainin I and LL37 can be due to their different structure. Indeed, the number of amino acids is smaller for magainin I peptide than for LL37 with 23 and 37 amino acids [95,97,98,253], respectively. These peptides have both an α-helix structure with hydrophobic residues on one side and hydrophilic residues on the other side [90, 91, 94] but differ by their net charge which is +4 and +6 for magainin I and LL37, respectively [97]. Their mechanism of action is the same as they are supposed to form toroidal pores in the bacterial membrane [76, 90, 91, 95] but magainin may also kill bacterial cells by other means than the formation of a toroidal pore [90].

The main difference between these two peptides thus relies on their total charge and their length which may therefore contribute to the difference in their antimicrobial efficiency.

5.3.2 Study of the surface colonization by bacteria

The bacterial adhesion was first observed qualitatively with fluorescence microscopy on a surface homogeneously covered by a non-grafted P(HOEGMA)

brush and on a surface homogeneously covered by a SAM of PEG to ensure the non-adhesiveness of the brush and the silane background, respectively. Then, we observed the bacterial adhesion on homogeneous brush, chemical and topographical nanopatterns grafted with RGD-C and on homogeneous brushes and chemical nanopatterns grafted with MAG-C, C-LL37 or C-LL37/RGD-C. Finally, the percentage area of each surface covered by bacteria was computed. We first compared the percentage of area covered by bacteria on samples showing the same structure but grafted with different peptides which allowed to conclude about the effect of the immobilized peptide. These comparisons were done for:

- homogeneous brushes grafted with RGD-C, MAC-C, C-LL37 and C-LL37/RGD-C
- 250 chemical nanopatterns grafted with RGD-C, MAC-C, C-LL37 and C-LL37/RGD-C
- 400 chemical nanopatterns grafted with RGD-C, MAC-C, C-LL37 and C-LL37/RGD-C

Then we compared the percentage of surface area covered by bacteria on surfaces showing the same immobilized peptide but differing by their structure which allowed to deduce the effect of the lateral dimensions of the nanopatterns. These comparisons were done for homogeneous brushes, 250 and 400 chemical nanopatterns grafted with RGD-C, MAG-C, C-LL37 and C-LL37/RGD-C. Eventually, we also compared chemical and topographical nanopatterns grafted with RGD-C.

The bacterial colonization was performed during three hours to explore the first steps of bacterial adhesion onto the surfaces and explored the initial effect of the surfaces on the bacteria viability.

5.3.2.1 Inspection of the surfaces colonized by bacteria

The images presented in this section are representative of the results observed for the different surfaces tested. However, it has to be noted that the coverage of the surface was not homogeneous. Indeed a higher number of adhered bacteria was sometimes observed on some parts of the surface.

The surface homogeneously covered by a non-grafted P(HOEGMA) brush and the surface homogeneously covered by a SAM of PEG were tested towards *E. coli* to assess their non-adhesiveness. Figure 5.4 confirms that no bacteria

adhered on both types of surfaces confirming the non-fouling characteristics of the P(HOEGMA) brush and the SAM of PEG.

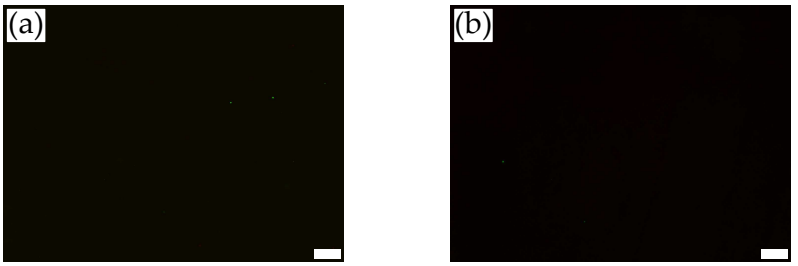

Figure 5.4: Fluorescence microscopy images of *E. coli* (stained with LIVE/DEAD kit) adhered on (a) homogeneous P(HOEGMA) brush and (b) homogeneous PEG layer (overlay images). The white bar represents 50 μm.

The adhesion of bacteria was then evaluated on homogeneous brush, chemical and topographical nanopatterns grafted with RGD-C. Figure 5.5 displays typical images recorded for these different surfaces. As can be seen on these images, the bacteria were able to adhere on all the surfaces grafted with RGD-C evidencing the adhesive properties of the RGD-C peptide towards *E. coli*. Moreover, whatever the RGD-C surface tested, only a few of red (*i.e.* dead) bacteria were seen which confirmed the non-toxic characteristics of these surfaces towards *E. coli*. Finally, no particular behavior was observed for bacteria on the biochemical and topographical nanopatterns compared to homogeneous surfaces which led to the conclusion that the lateral dimensions and the nanostructuration of the surface did not influence the collective behavior of bacteria. This contrasts with previous results obtained for *E. coli* and *L. lactis* adhered onto nanopatterns composed of PMMA brush lines distributed in a non-adhesive PEG background [254, 255]. Indeed, it was observed that these bacteria aligned along the nanopatterned lines after a growth time of about 2-4 hours. This difference in behavior of the bacteria can be explained by the chemical nature of the adhesive patterned lines. The PMMA polymer brush is strongly adhesive while the adhesiveness of the modified P(HOEGMA) brushes resulted only from the grafted peptide moieties.

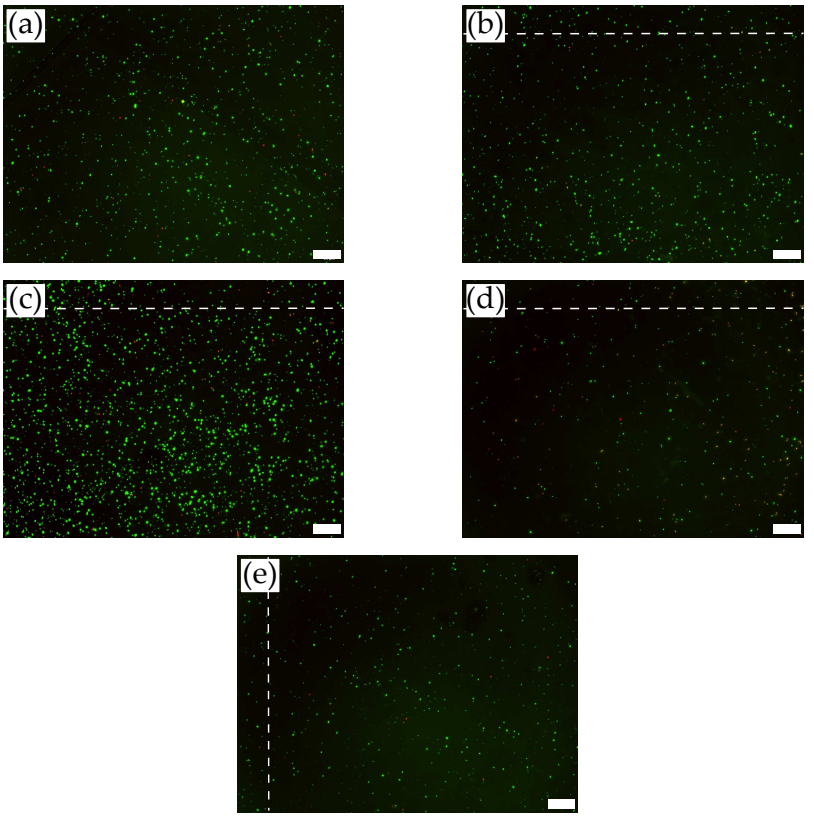

Figure 5.5: Fluorescence microscopy images of *E. coli* (stained with LIVE/DEAD kit) adhered on (a) homogeneous brush grafted with RGD-C, (b) 250 and (c) 400 chemical nanopatterns grafted with RGD-C, (d) 250 and (e) 400 topographical nanopatterns grafted with RGD-C (overlay images). The dashed lines represent the direction of the patterned lines. The white bars represent 50 μm.

The adhesion of bacteria was then tested on homogeneous brush and chemical nanopatterns grafted with MAG-C (Figure 5.6). The density of bacteria adhered on these surfaces seemed to be higher than the one observed in Figure 5.5. Only a few dead bacteria were seen on these surfaces. Again, no particular behavior was observed for bacteria on the biochemical nanopatterns grafted with MAG-C compared to homogeneous brush grafted with MAG-C.

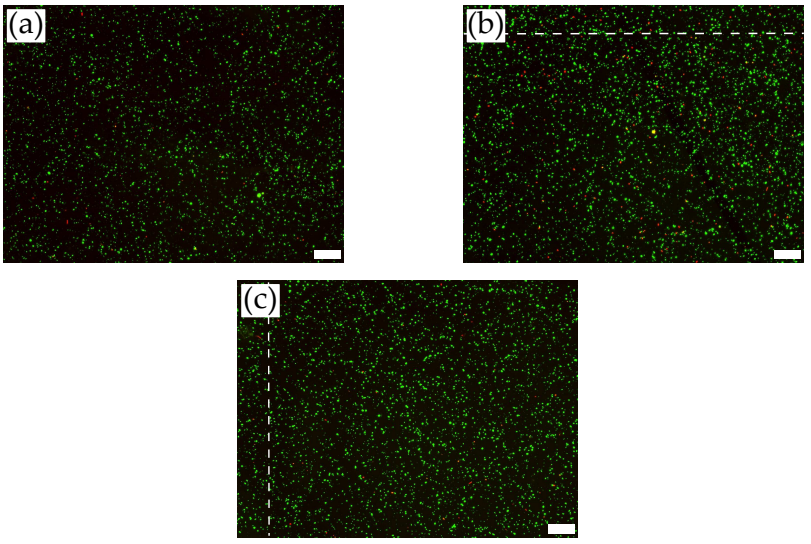

Figure 5.6: Fluorescence microscopy images of *E. coli* (stained with LIVE/DEAD kit) adhered on (a) homogeneous brush grafted with MAG-C, (b) 250 and (c) 400 chemical nanopatterns grafted with MAG-C (overlay images). The dashed lines represent the direction of the patterned lines. The white bars represent 50 μm.

The adhesion of bacteria was tested on homogeneous brush and chemical nanopatterns grafted with C-LL37 (Figure 5.7). The amount of adhered bacteria seemed smaller and the amount of dead bacteria seemed higher on these surfaces than on homogeneous brush, chemical and topographical nanopatterns grafted with RGD-C. There were still no effect of the biochemical nanopatterns on the distribution of bacteria.

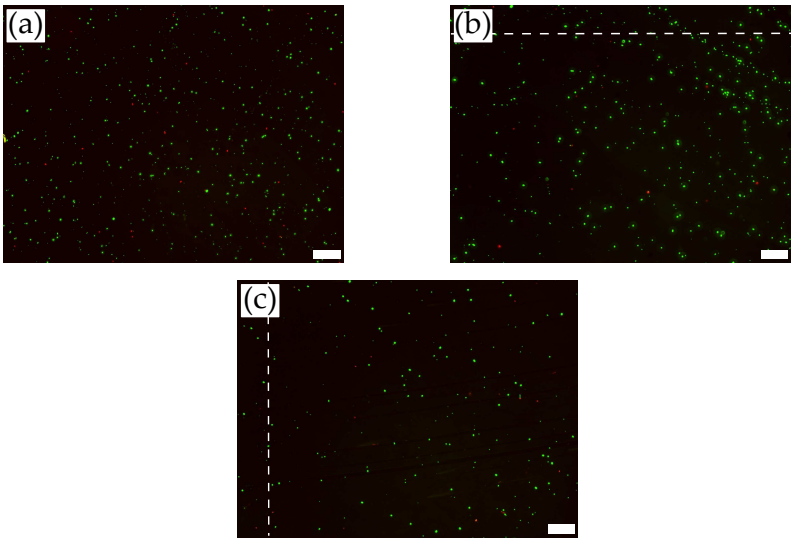

Figure 5.7: Fluorescence microscopy images of *E. coli* (stained with LIVE/DEAD kit) adhered on (a) homogeneous brush grafted with C-LL37, (b) 250 and (c) 400 chemical nanopatterns grafted with C-LL37 (overlay images). The dashed lines represent the direction of the patterned lines. The white bars represent 50 μm.

Finally, the adhesion of bacteria was tested on homogeneous brush and chemical nanopatterns grafted with C-LL37/RGD-C (Figure 5.8). Bacteria adhered on these surfaces and showed a higher amount of dead bacteria compared to homogeneous brush, chemical and topographical nanopatterns grafted with RGD-C. The mixture of peptide thus allowed to retain the bactericidal effect of the surfaces. As seen above, no effect of the biochemical patterns were observed on the behavior of bacteria compared to homogeneous surfaces.

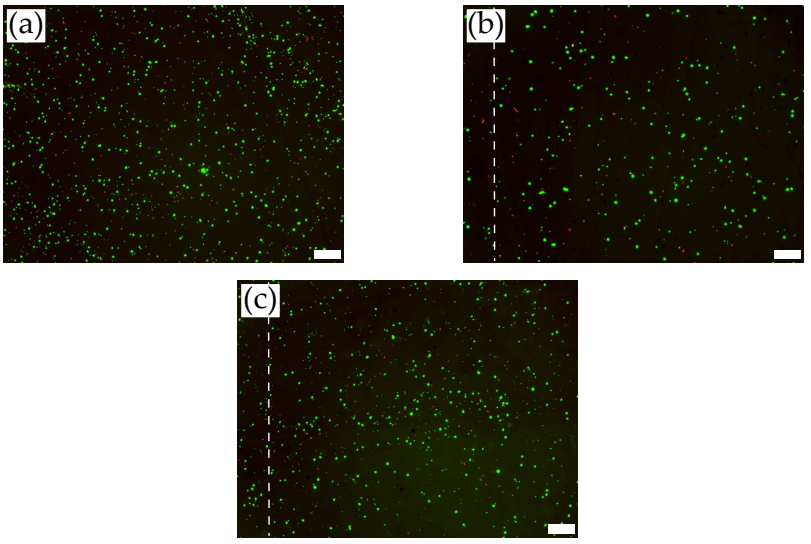

Figure 5.8: Fluorescence microscopy images of *E. coli* (stained with LIVE/DEAD kit) (a) homogeneous brush grafted with C-LL37/RGD-C, (b) 250 and (c) 400 chemical nanopatterns grafted with C-LL37/RGD-C (50:50) (overlay images). The dashed lines represent the direction of the patterned lines. The white bars represent 50 μm.

5.3.2.2 Quantitative analysis of the surface coverage

While analyzing the percentage of surface area covered by bacteria, we first focused on the effect of the nature of the peptide grafted on homogeneous surfaces. The Figure 5.9 shows that the surface area covered by bacteria was much higher for the homogeneous brush grafted with MAG-C and smaller for homogeneous brush grafted with C-LL37. The surfaces covered with RGD-C and C-LL37/RGD-C showed no statistical difference and showed intermediate values between MAG-C-grafted and C-LL37-grafted surfaces. Similar tendencies were observed by measuring the colonization percentages on nanopatterned surfaces grafted with the different peptides. However, the effect was less pronounced for 250 chemical nanopatterns (section 5.5 Figure 5.15).

Overall, the three peptides tested showed a bioadhesive effect towards bacteria. For a same type of surface, the MAG-C peptide induced a higher percentage of surface area covered by bacteria whereas it was the smallest for surfaces grafted with C-LL37. Surfaces grafted with RGD-C and C-LL37/RGD-C showed intermediate values for the surface area covered.

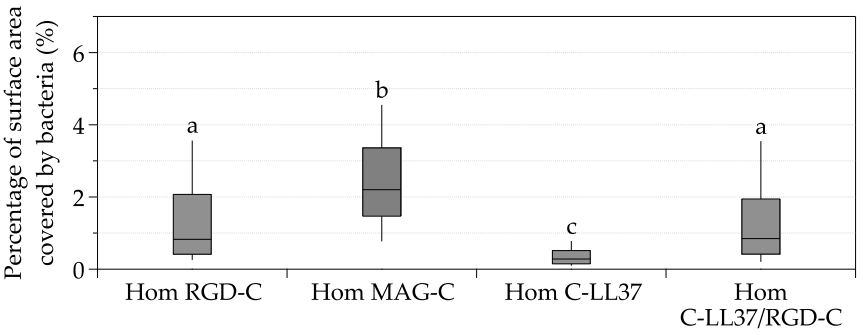

Figure 5.9: Comparison of the percentage of surface area covered by bacteria on homogeneous brushes grafted with RGD-C, MAG-C, C-LL37 and C-LL37/RGD-C (50:50). Bars with different letters indicate significant difference, p-value < 0.05.

We also studied systematically the effect of the dimensions of the patterns for a given grafted peptide on the percentage of surface area covered by bacteria. For example, Figure 5.10 shows that no difference was observed between the homogeneous brush and the chemical nanopatterns grafted with C-LL37/RGD-C. However, for the other surfaces tested, the lateral dimensions of the pattern influenced differently the percentage of surface area covered by bacteria depending on the peptide grafted on the brush (section 5.5 Figure 5.16). The percentage was higher for the 400 chemical nanopattern grafted with RGD-C compared to homogeneous brush and 250 chemical nanopattern grafted with RGD-C; the percentage was also higher for the 250 chemical nanopattern grafted with C-LL37 compared to homogeneous brush and 400 chemical nanopattern grafted with C-LL37. The other surfaces grafted with MAG-C did not show any difference in percentage of surface area regardless of the lateral dimensions used.

Thus, there was no defined trend regarding colonization by bacteria on the different surface structures.

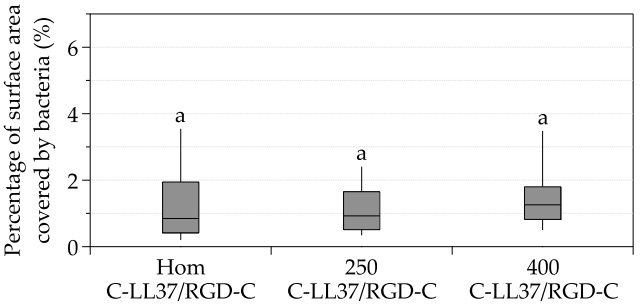

Figure 5.10: Comparison of the percentage of surface area covered by bacteria for homogeneous brush, 250 and 400 chemical nanopatterns grafted with C-LL37/RGD-C (50:50). Bars with different letters indicate significant difference, p-value < 0.05.

We also investigated the combined effect of both surface nanotopography and RGD-C peptide grafting on the percentage of surface area covered by bacteria. The Figure 5.11 shows that the topographical patterns tended to induce a decrease of the percentage of surface area covered by bacteria compared to the biochemical patterns and the homogeneous brush grafted with RGD-C.

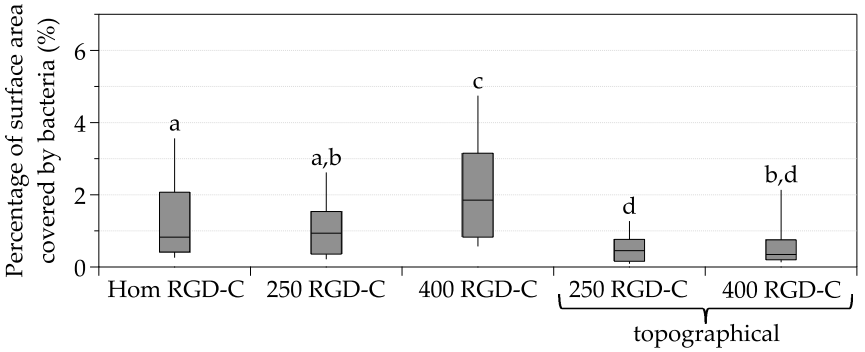

Figure 5.11: Percentage of surface area covered by bacteria for chemical and topographical nanopatterns grafted with RGD-C. Bars with different letters indicate significant difference, p-value < 0.05.

The colonization of peptide-grafted surfaces by bacteria resulted from specific or non-specific interactions between the peptide molecules and the bacterial membrane.

For RGD-C-grafted surfaces, the adhesion of *E. coli* can be attributed to

non-specific interactions between the bacterial surface and the RGD-C peptide. For example, Harris *et al.* compared the adhesion of *S. aureus* on titanium substrates coated with PEG or GCRGYG**RGD**SPG peptide immobilized on PEG. As the RGD peptide derivative did not promote the adhesion of bacteria, the RGD sequence can be considered as not specifically adhesive towards *S. aureus* [256]. He *et al.* compared the adhesion of *E. coli* and *S. aureus* on an antimicrobial PEM composed of dextran sulfate and chitosan grafted with G**RGD**SP peptide or collagen molecules. They showed that, while the RGD peptide derivative did not affect the adhesion of bacteria, the grafted collagen allowed a greater amount of *S. aureus* to adhere. This study also showed that the adhesion and proliferation of fibroblasts on all these surfaces was possible [257]. He *et al.* obtained similar results with *E. coli* and *S. aureus* by binding RGD peptide or collagen on immobilized dopamine. It is worth noting that the adhesion of fibroblasts was also successfully performed on these surfaces [213]. These two last studies evidenced that bacteria do not rely on the RGD recognition motif to bind on the surfaces [213, 257]. Shi *et al.* also showed that *S. aureus* and *S. epidermidis* adhesion was reduced on chitosan modified with RGD compared to the pristine substrate while cell activity was maintained [75]. Dexter *et al.* showed that by adapting surface concentration of fibronectin, is was possible to induce differential adhesion between bacteria (*i.e. S. epidermidis*) and mammalian cells (*i.e.* fibroblasts). The bacterial adhesion was lower with increasing fibronectin concentration while fibroblast adhesion was not influenced by fibronectin concentration [214]. Chua *et al.* and Shi *et al.* also demonstrated that surfaces modified with different polymers including chitosan and modified with RGD peptides can maintain antibacterial activity towards *S. aureus* and *S. epidermidis* while enhancing cell proliferation (*i.e.* osteoblasts) on the surfaces [75, 211].

In contrast, the antimicrobial peptides magainin I and LL37 are known to interact specifically with the bacterial wall to form toroidal pores which results in the lysis of the bacterial membrane [76]. A lower percentage of surface area covered by bacteria was observed for surfaces grafted with C-LL37 in our experiments compared to surfaces showing the same structure but bearing C-MAG or RGD-C. This is in agreement with the results obtained by Cassin *et al.* who evidenced that the immobilization of LL37 on the surface of PEMs reduced the colonization of *E. coli* compared to non-grafted PEMs surfaces [147]. On the contrary, a higher percentage of surface area covered by bacteria was observed

for MAG-C-grafted surfaces compared to surfaces showing the same structure but bearing RGD-C or C-LL37. Humblot *et al.* who immobilized magainin I on a mixed SAM of 11-mercaptoundecanoïc acid and 6-mercaptohexanol and tested bacterial adhesion on these surfaces, assumed that bacteria killed by magainin I peptide might later reinforce bacterial colonization due to the debris of bacterial material remaining on the surfaces [148]. Moreover, Pedrosa *et al.* compared the efficiency of magainin I and LL37 immobilized onto cotton used for wound dressing, againt *Klebsiella pneumoniae* and *S. aureus*. As obtained by us, they found out that surfaces modified with LL37 led to a lower number of adhered bacteria compared to the surfaces modified with magainin I. They claimed that this behavior was due to the difference in net charge between both peptides which is +6 and +4 for LL37 and magainin I, respectively. This difference might lead to a lower number of electrostatic interactions established with magainin I molecules compared to LL37 which decreased its antimicrobial effect towards *Klebsiella pneumoniae* and *S. aureus* [253].

We found that the surface nanotopography also decreased the bacterial colonization. The decrease in bacterial colonization observed onto topographical nanopatterns grafted with RGD-C compared to homogeneous brush grafted with RGD-C can be explained by the smaller size of the protruding lines compared to the size of bacteria. Indeed, Seddiki *et al.* showed that the contact area is of critical importance to prevent biofilm formation on the surface. Surfaces showing small contact points with bacteria are less prone to bacterial fouling [18]. For instance, it was observed that the adhesion of *E.coli* onto rough titanium surfaces was lower than on polished surfaces. This limited adhesion in presence of nanoroughness was attributed to the smaller number of cavities able to welcome bacteria whereas the remaining protruding parts of the surface provide a very limited contact area with bacteria [18]. Xu *et al.* also evidenced this phenomenon using surfaces decorated with submicrometer poly(urethane urea) pillars with a diameter smaller than the bacteria size (*i.e.* 400-560 nm). In these experiments, it was shown that the adhesion and biofilm formation of *S. epidermidis* and *S. aureus* were lower onto nanopillars compared to smooth polyurethane film [129]. Rizzelo *et al.* even showed that the nanostructuration of gold surface (with Ra roughness = 99.8 nm) induced modifications in the genome and proteome of the gram-negative bacteria *E. coli* leading to a change of their surface composition and preventing the expression of surface appendices playing an important role in the bacterial colonization process compared to flat

gold surfaces [123]. Moreover, even though nanostructured surfaces (with Ra roughness = 26 nm) induced a lower adhesion of *S. epidermidis* compared to flat surfaces, it did not seem to influence monocyte adhesion compared to a flat gold surface which is interesting since it is possible to influence the behavior of bacteria without imparting any triggering signal to the mammalian cell [210].

5.3.3 Study of bactericidal properties of the surfaces

The percentage of dead bacteria adhered onto homogeneous brushes, 250 and 400 nanopatterns grafted with the different peptides was systematically computed by image analysis in order to assess the effect of the nature and the spatial distribution of the peptide as well as the topography on the bacteria viability.

We first focused on the effect of the nature of the peptide on the percentage of dead bacteria. In a first approach, the influence of the nature of the peptide on bacteria viability was investigated using homogenous surfaces (Figure 5.12). It was observed that the percentage of dead bacteria varies from 34 % to 24 % for C-LL37 and C-LL37/RGD-C surfaces, respectively. In contrast, the surfaces grafted with RGD-C or MAG-C induced a lower percentage of dead bacteria of about 11 %. This result showed that MAG-C immobilized on P(HOEGMA) brush did not show bactericidal activity. Moreover, the surfaces grafted with RGD-C showed a small amount of dead bacteria probably due to the adhesion of dead bacteria coming from the bacterial suspension or due to bacteria dying after adhesion to the surfaces.

We then analyzed the data obtained for 250 and 400 chemical nanopatterns grafted with RGD-C, MAG-C, C-LL37 or C-LL37/RGD-C (50:50) to have an insight into the effect of the nature of the peptide for nanopatterned surfaces (section 5.5 Figure 5.17). The results on the 400 chemical nanopatterns support the ones on homogeneous brushes. However, on smaller 250 chemical nanopatterns, they were slightly different from the ones on homogeneous brushes. Indeed, the surface grafted with C-LL37/RGD-C showed the highest bactericidal activity followed by MAG-C, C-LL37 and finally RGD-C.

Altogether, these results evidenced that surfaces grafted with C-LL37 and C-LL37/RGD-C showed bactericidal properties towards *E. coli* while MAG-C effect was almost not present. Indeed, the percentages of dead bacteria on RGD-C were not significantly different from the ones on MAG-C surfaces.

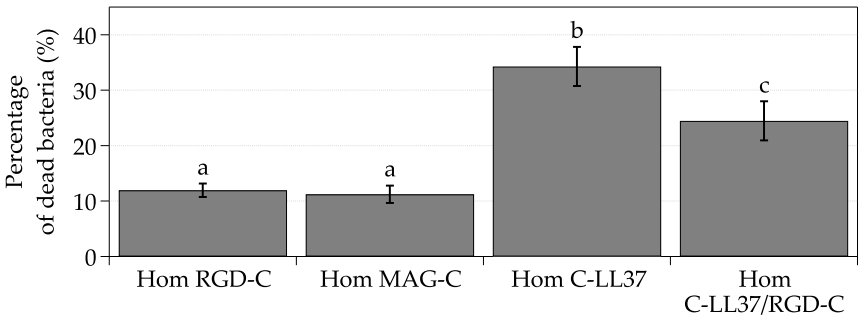

Figure 5.12: Comparison of the percentage of dead bacteria adhered onto homogeneous brushes grafted with RGD-C, MAG-C, C-LL37 and C-LL37/RGD-C (50:50). Bars with different letters indicate significant difference, p-value < 0.05.

We also studied systematically the effect of the dimensions of the nanopatterns for a given grafted peptide on the percentage of dead bacteria. The percentage of dead bacteria on the corresponding homogeneous surface was given for the comparison. The effect of the lateral dimensions on surfaces grafted with C-LL37 is shown in Figure 5.13. The percentage of dead bacteria was of 12 % and 16 % for 250 and 400 nanopatterns, respectively. This is rather small compared to homogeneous brush on which the percentage of dead bacteria was of 34 %. This suggests that the patterning of C-LL37 induced a strong decrease of its antimicrobial effect. These results were less pronounced on the surfaces grafted with the other peptides (section 5.5 Figure 5.18).

The comparison of the results obtained for chemical patterns with various lateral dimensions did not provide straightforward conclusions but allowed to hypothesize that the nanopatterning of the antimicrobial peptide decreased its antimicrobial effect. Indeed, the results obtained on homogeneous and nanopatterned surfaces grafted with antimicrobial C-LL37 clearly evidenced this tendency. Moreover, the grafting of a C-LL37/RGD mixture onto the surfaces, even though retaining antimicrobial efficiency, provided a lower bactericidal surface activity compared to pure C-LL37. This can be attributed to the lower number of C-LL37 molecules immobilized onto the surface in such configuration. Grafted MAG-C peptide, on its side, showed extremely low antimicrobial properties.

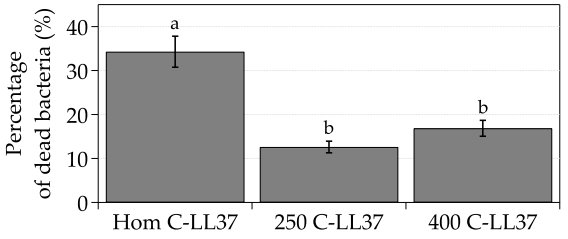

Figure 5.13: Comparison of the percentage of dead bacteria adhered onto homogeneous brush, 250 and 400 chemical nanopatterns grafted with C-LL37. Bars with different letters indicate significant difference, p-value < 0.05.

We then investigated the combined effect of both surface nanotopography and RGD-C peptide grafting on the percentage of dead bacteria. Figure 5.14 evidences that topographical nanopatterns grafted with RGD-C showed a higher number of dead bacteria compared to homogeneous brush and 250 and 400 chemical nanopatterns grafted with RGD-C.

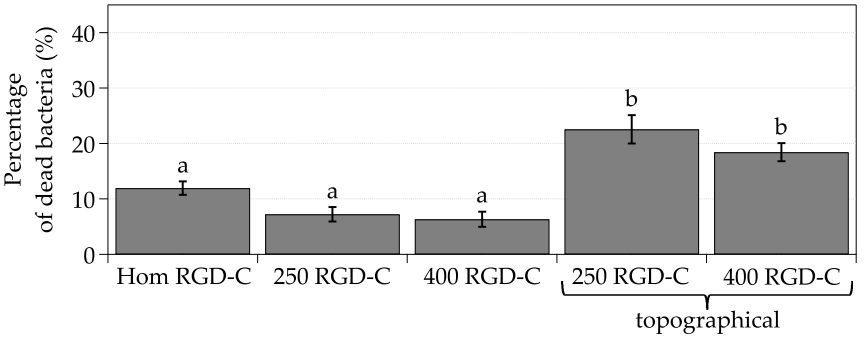

Figure 5.14: Percentage of dead bacteria adhered onto homogeneous brush, chemical and topographical nanopatterned surfaces displaying different dimensions. Bars with different letters indicate significant difference, p-value < 0.05.

The results obtained for MAG-C-modified surfaces in our experiments contradict the results obtained in previous studies reported by others. For example, Glinel *et al.*, who immersed silicon surfaces functionalized by P(MOE_2MA-*co*-HOEGMA) brushes with magainin I, in 10 mL bacterial suspension of *L. ivanovii* or *Bacillus cereus* (10^7 CFU/mL in distilled water) during 3 hours, demonstrated that immobilized magainin I was efficient against these bacteria [64]. Humblot

et al. also evidenced the antimicrobial properties of immobilized magainin I on a mixed SAM of 11-mercaptoundecanoïc acid and 6-mercaptohexanolagainst against three gram-positive bacteria (*i.e. L. ivanovii*, *Enterococcus faecalis* and *S. aureus*) (10^5 CFU/mL in Brain Heart infusion broth) by depositing 100μL of bacterial suspension on the samples during 3 hours [148]. Haynie *et al.* also confirmed that magainin 2 immobilized on a polyamide resin was able to kill *E. coli* (10^5 CFU/mL in LB or tryptic soy broth) and that its bactericidal action is based on interactions with outer membrane of bacterial cells [258].

On the contrary to MAG-C, the results obtained for C-LL37 confirmed its antimicrobial efficiency when grafted on a P(HOEGMA) brush. This supports the results obtained by Gabriel *et al.* who assessed the bactericidal activity of LL37 grafted by its N-terminal end on a tethered PEG spacer, against *E. coli* (100μL of bacterial suspension in 10mM phosphate buffer was deposited on the surface) [105]. However, the percentage of dead bacteria obtained in our experiments did not exceed 34 % which is quite low. This evidence that further studies need to be conducted to obtain truly antibacterial surfaces.

The bactericidal efficiency of MAG-C and C-LL37 grafted on P(HOEGMA) brushes is rather low compared to previous studies. However, the percentage of dead cells depends probably on the conditions used for the bacterial tests which are somehow different from the ones used in the previous studies. Some parameters have already been explained above (see section 5.3.1) for antimicrobial peptides in suspension but remain of interest for immobilized peptides: growth medium *vs.* not growth medium, the concentration of bacteria, the ionic strength of the medium, the nutrients present in the medium and the structure of MAG-C and C-LL37. Apart from these parameters, the spacer used to immobilize the peptide on the surface can also influence the antimicrobial efficiency of the peptide. For instance, Haynie *et al.* showed that the minimal bactericidal concentration was 50 folds higher, when the magainin 2 peptide was immobilized, compared to magainine 2 in solution but also evidenced that a spacer of two and six-carbon chain had no influence on the bactericidal capacity of the peptide towards *E. coli* and *S. aureus* [258]. Rai *et al.* also confirmed that the immobilization of cecropin-melittin increased its MIC but also showed that the spacer length (*i.e.* either cystamine or PEG in this study) as well as the number of immobilized peptides per surface unit influenced the MIC [248]. In addition, Bagheri *et al.* evidenced the importance of spacer length as well as the surface accessibility of the antimicrobial peptide, on the antibacterial activity of

the surfaces. Indeed, they immobilized KLAL model antimicrobial peptide and magainin-derived peptide on resin beads with polyethylene glycol spacers of different lengths and found that 75 units of ethylene oxide allow the peptide to exert its antimicrobial activity more efficiently than when 10 or 5 ethylene oxide units were used [249]. The use of a spacer thus lowered bactericidal activities of grafted MAG-C and C-LL37 compared to the ones measured in solution (see section 5.3.1). As the antimicrobial properties of MAG-C were already rather low in solution compared to C-LL37, it was not surprising to observe a similar difference while they were grafted onto the surfaces.

We also observed that topographical patterns were colonized by more dead bacteria compared to the homogeneous brush and chemical nanopatterns grafted with RGD-C. An explanation might be that the bacteria tried to adhere to the surface but faced a topography that is not favorable for their viability.

5.4 Conclusion

In this chapter, we studied the effect of the immobilization of three different peptides on P(HOEGMA) brush on the bacterial adhesion and antimicrobial activity. We first explored the antimicrobial activity of MAG-C and C-LL37 peptides in solution. While both peptides showed antimicrobial activity against *E. coli*, the bactericidal activity of C-LL37 was much higher than the one of MAG-C.

Then, we studied the percentage of surface area covered by bacteria and the percentage of dead bacteria on the surfaces grafted with RGD-C, MAG-C, C-LL37 and C-LL37/RGD-C. The nature of the peptide was first explored and showed to influence the results. Interestingly, while immobilized MAG-C induced the highest surface coverage, it also did not showed any significant bactericidal effect. The immobilized C-LL37 allowed the lowest surface area coverage and had a significant bactericidal effect. The results obtained for RGD-C peptide confirmed what was already reported in the literature *i.e.* bacteria do not adhere specifically on RGD-C peptide. The mixture of C-LL37/RGD-C showed adhesive and bactericidal properties. Then, the effect of the nanopatterning of the antimicrobial peptides was looked through and seemed to decrease the antimicrobial effect of the grafted brushes. This was attributed to the lower amount of peptide molecules per surface unit for the nanopatterned surfaces compared to the homogeneous ones. Finally, topographical nanopatterns allowed

a lower percentage of surface area covered by bacteria and higher amount of dead bacteria compared to chemical nanopatterns grafted with RGD-C. Therefore, the surface nanotopography seems to be an additional parameter to be considered to reduce the surface colonization by bacteria.

A higher antimicrobial activity was observed for the surfaces grafted with C-LL37 compared to MAG-C. Moreover, the percentage of surface area covered by bacteria was lower for the samples grafted with C-LL37 compared to MAG-C. These results support the ones obtained by Pedrosa *et al.* who showed that LL37 had a higher bacterial reduction percentage compared to magainin I [253]. The smaller surface area covered by bacteria measured for the C-LL37 surfaces compared to MAG-C surfaces and its higher antimicrobial efficiency explain the higher percentage of dead bacteria found on surfaces grafted with C-LL37.

According to these results, the samples selected for further use in experiments with cells were homogeneous surfaces grafted with RGD-C, C-LL37 and C-LL37/RGD-C, 400 chemical nanopatterns grafted with RGD-C, C-LL37 and C-LL37/RGD-C and 250 chemical and topographical nanopatterns grafted with RGD-C. We excluded the surfaces bearing MAG-C peptide because of their poor efficiency towards bacteria. We also removed 250 chemical nanopatterns grafted with C-LL37 and C-LL37/RGD-C because the bactericidal activity measured for these surfaces was not large enough. The topographical patterns were also selected to check the effect of the topography on mammalian cells.

5.5 Supporting Information

5.5.1 Surface colonization by bacteria

5.5.1.1 Effect of the nature of the peptide grafted on nanopatterns

The influence of the nature of the grafted peptide on surface colonization was also studied on nanopatterned surfaces. It was essentially seen the same tendencies that the ones observed for homogeneous surfaces. However, the variation in surface area covered by bacteria was less pronounced for the 250 chemical nanopatterns grafted with the different peptides (Figure 5.15a). Moreover, the surface area covered was much higher for the 250 nanopattern grafted with MAG-C and smaller for other surfaces.

On the contrary, the Figure 5.15b confirms that the surface area covered was much higher for the 400 nanopattern grafted with MAG-C and smaller for the surface grafted with C-LL37. The 400 nanopatterns grafted with RGD-C and C-LL37/RGD-C showed no statistical difference and showed intermediate values between surfaces grafted with MAG-C and C-LL37.

5.5.1.2 Effect of the lateral dimensions of the patterns

We also studied systematically the effect of the dimensions of the patterns for a given peptide on surface colonization.

The Figure 5.16a shows that among the RGD-C-grafted surfaces, the 400 chemical nanopattern grafted with RGD-C led to the highest percentage of surface area covered by bacteria. The values for the homogeneous brush and the 250 chemical nanopattern grafted with RGD-C were not significantly different.

The Figure 5.16b shows that no difference were observed between the homogeneous brush and the chemical nanopatterns grafted with MAG-C.

The Figure 5.16c shows that the highest percentage of surface area covered by bacteria was obtained for 250 chemical nanopattern grafted with C-LL37. In contrast, the percentages measured for homogeneous surface grafted with C-LL37 and 400 chemical nanopattern grafted with C-LL37 were not significantly different.

No significant trend was evidenced when studying the influence of the lateral dimensions of the grafted patterns on the surface area covered by bacteria.

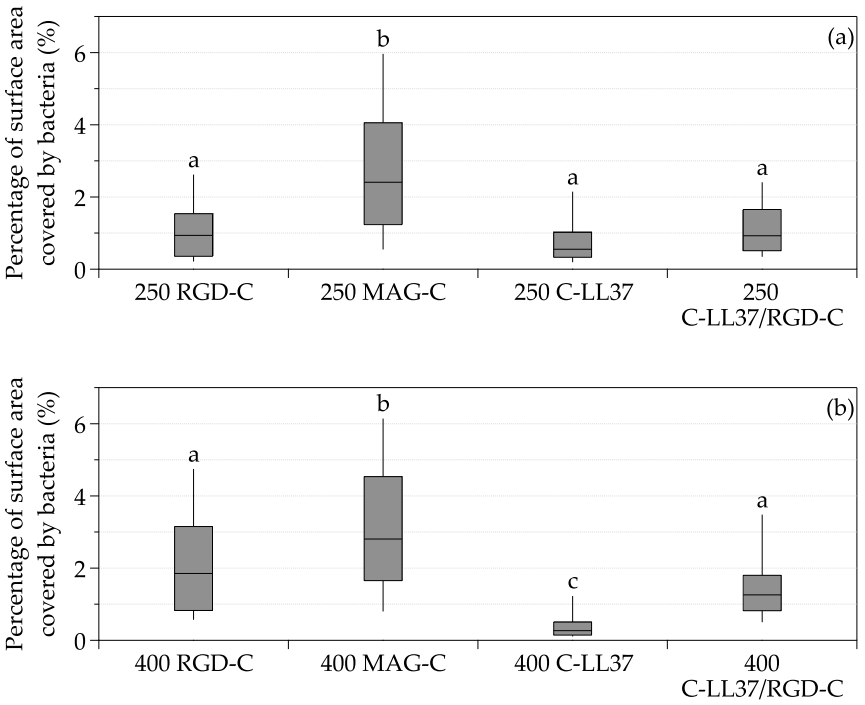

Figure 5.15: Comparison of the percentage of surface area covered by bacteria for different peptides and surface structures. The comparison is made between surfaces of the same design to study the effect of the nature of the peptide. Comparison of (a) 250 chemical nanopatterns grafted with RGD-C, MAG-C, C-LL37 and C-LL37/RGD-C (50:50) and (b) 400 chemical nanopatterns grafted with RGD-C, MAG-C, C-LL37 and C-LL37/RGD-C (50:50). Bars with different letters indicate significant difference, p-value < 0.05.

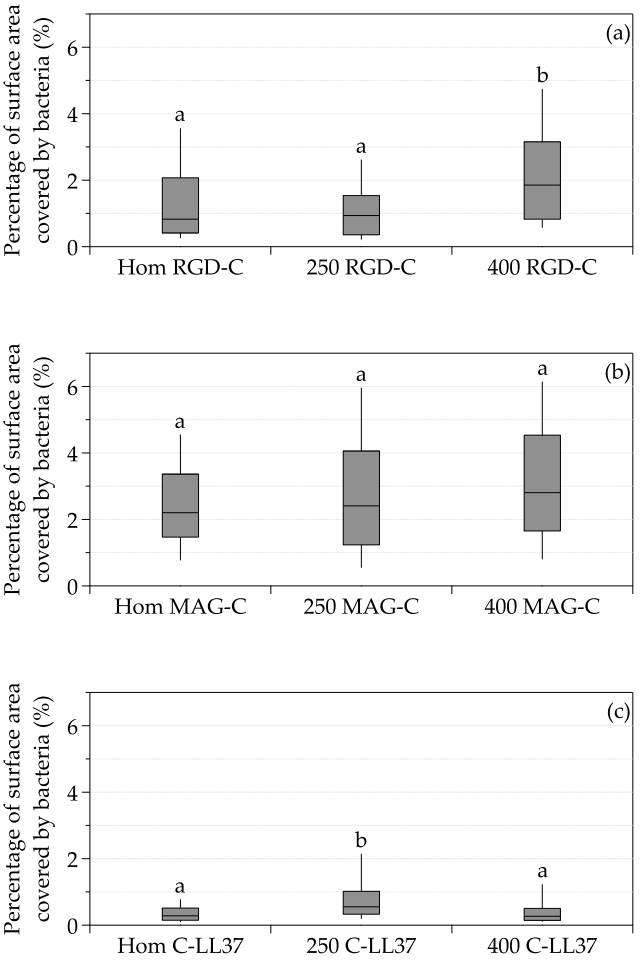

Figure 5.16: Comparison of the percentage of surface area covered by bacteria for different peptides and surface structures. The comparison is made between surfaces showing the same peptide or peptide mix but different patterns to study the effect of the design of the surfaces. Comparison between (a) homogeneous brush, 250 and 400 chemical nanopatterns grafted with RGD-C, (b) homogeneous brush, 250 and 400 chemical nanopatterns grafted with MAG-C and (c) homogeneous brush, 250 and 400 chemical nanopatterns grafted with C-LL37. Bars with different letters indicate significant difference, p-value < 0.05.

5.5.2 Study of bactericidal properties of the surfaces

5.5.2.1 Effect of the nature of the peptide grafted on nanopatterns

We focused on the effect of the nature of the peptide on the percentage of dead bacteria.

For the 250 chemical nanopatterns, the surface grafted with C-LL37/RGD-C showed the highest bactericidal activity with 26 % of dead bacteria. Then the percentages of dead bacteria were 16 %, 12 % and 7 % for MAG-C, C-LL37 and RGD-C, respectively.

For the 400 chemical nanopatterns, the results obtained support the ones measured for homogeneous surfaces. Indeed, the higher bactericidal effect were held by C-LL37 and C-LL37/RGD-C surfaces with percentage of dead bacteria around 16 %. The MAG-C and RGD-C surfaces did not show significant difference in the percentage of dead bacteria which was around 6 %.

5.5.2.2 Effect of the lateral dimensions of the patterns

We studied the effect of lateral dimensions for surfaces grafted with RGD-C (Figure 5.18a). The homogeneous brush grafted with RGD-C led to the presence of 12 % of dead bacteria while this percentage fell around 7 % for patterned surfaces. The number of dead bacteria was thus smaller on nanopatterned surfaces compared to homogeneous surfaces.

Then, we focused on bactericidal surfaces grafted with MAG-C (Figure 5.18b). The percentage of dead bacteria dropped to 6 % for 400 chemical nanopattern grafted with MAG-C while it remained between 11 and 16 % for the other surfaces grafted with MAG-C.

Finally, we studied the effect of the lateral dimensions of the nanopatterned surfaces grafted with C-LL37/RGD-C mixture (Figure 5.18c). The difference of dead bacteria was significantly different between 250 and 400 nanopatterns which showed percentages of 26% and 16%, respectively. However, no significant difference was seen between the 250 and 400 nanopatterns and homogeneous surfaces.

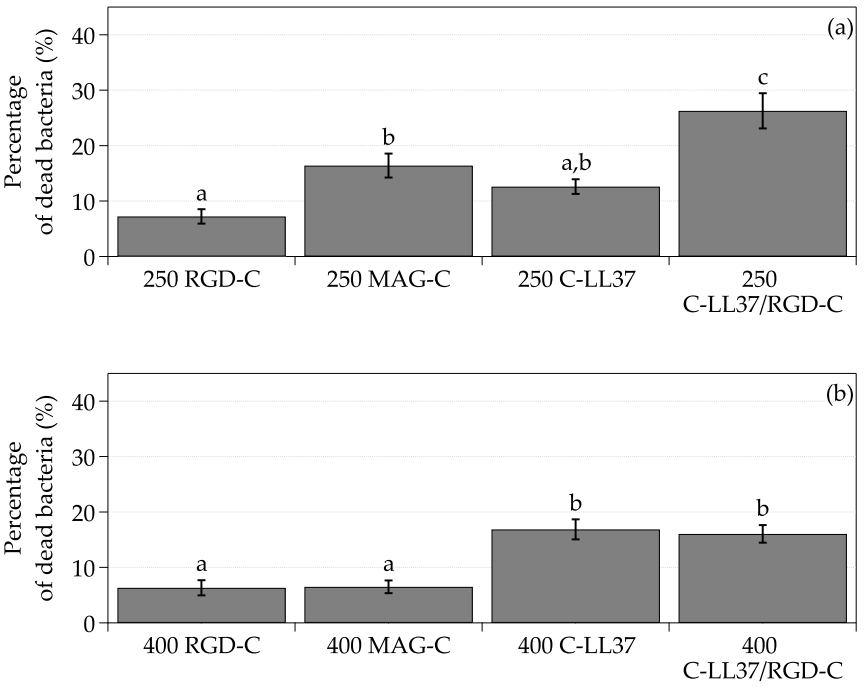

Figure 5.17: Comparison of the percentage of dead bacteria adhered onto surfaces grafted with different peptides and with different designs. Comparison of the percentage of dead bacteria adhered onto (a) homogeneous brushes, (b) 250 chemical nanopatterns and (c) 400 chemical nanopatterns grafted with RGD-C, MAG-C, C-LL37 and C-LL37/RGD-C (50:50). Bars with different letters indicate significant difference, p-value < 0.05.

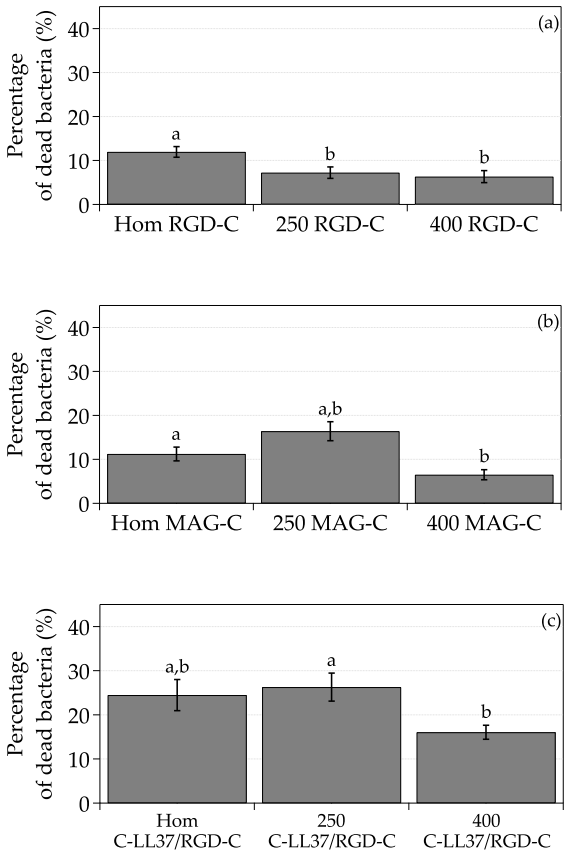

Figure 5.18: Comparison of the percentage of dead bacteria adhered onto surfaces grafted with different peptides and with different designs. Comparison of the percentage of dead bacteria adhered onto (a) homogeneous brush, 250 and 400 chemical nanopatterns grafted with RGD-C, (b) homogeneous brush, 250 and 400 chemical nanopatterns grafted with MAG-C and (c) homogeneous brush, 250 and 400 chemical nanopatterns grafted with C-LL37/RGD-C (50:50). Bars with different letters indicate significant difference, p-value < 0.05.

Chapter 6

Mammalian cell adhesion, proliferation and differentiation on nanopatterned surfaces

6.1 Introduction

In this chapter, we focused on the effect of the nanopatterned surfaces on the mammalian cell behaviors.

Different parameters of the surface can be used to influence the mammalian cell behaviors (*i.e.* adhesion, migration, proliferation and differentiation): the topography, the (bio)chemical composition and the stiffness. The most well-known phenomenon, related to the effect of the surface topography on cells, is called contact guidance. It consists in the response of a cell to anisotropic topographical features of the surface [22]. The biochemical molecules presented to cells can also influence their fate. Indeed, adhesion of a cell on a surface is principally mediated by the integrins [156]. The most well-known integrin binding motif is the RGD sequence [82]. The distribution and the density of this binding motif onto the surface is critical for the formation of mature FAs or to guide a stem cell to a particular lineage [1, 85, 161]. Other biomolecules such

as growth factors can be grafted on the surface to promote cell differentiation [158]. Finally, the mechanical forces exerted at the interface between a cell and a substrate also influence the cytoskeletal organization and thus the cell fate [155, 168].

This chapter focuses on the behavior of SCAPs on the following patterned surfaces: the 250 chemical nanopattern grafted with RGD-C or 400 chemical nanopatterns grafted with RGD-C, C-LL37 peptides and a C-LL37/RGD-C mixture (50:50) and 250 or 400 topographical nanopatterns grafted with RGD-C. The homogeneous surfaces grafted with RGD-C, C-LL37 and C-LL37/RGD-C were used as control surfaces. The RGD-C peptide was selected due to its specificity towards mammalian cell adhesion [85]. The antimicrobial peptide C-LL37 was selected due to its non-cytotoxicity towards mammalian cells and its bactericidal activity towards *E. coli* as demonstrated in Chapter 5.

The stem cells we chose for our experiments are dental human stem cells called SCAPs. These cells present MSC-like properties such as self-renewal and multilineage differentiation potential [206]. Indeed, they can commit to osteo/odontogenic, adipogenic and neurogenic lineages [206].

We investigated the cell behavior (*i.e.* proliferation and differentiation) and morphology (*i.e.* cell surface area, aspect ratio (AR), circularity, orientation compared to the pattern direction and the number and the distribution of FAs) on the selected surfaces. First, we studied the proliferation and morphology of cells on reference surfaces, *i.e.* glass surface and homogeneous brushes grafted with RGD-C, C-LL37 and a C-LL37/RGD-C mixture, and patterned surfaces. Second, we studied the differentiation of SCAPs on both reference and patterned surfaces, by immunofluorescence. Finally, we inspected the differentiation of SCAPs on reference and patterned surfaces, by performing a relative quantification of the markers expressed by cells.

6.2 Materials and methods

6.2.1 Materials

Minimum essential medium eagle (MEM eagle), fetal bovine serum (FBS), triton™ X-100 and monoclonal anti-vinculin antibody produced in mouse were purchased from Sigma-Aldrich. L-glutamine 200 mM (100 x), StemPro® Accutase® cell dissociation reagent, phosphate buffered saline (PBS) tablets,

goat anti-mouse IgG (H+L) secondary antibody, Alexa Fluor® 488 conjugate and rhodamine phalloidin were provided by ThermoFisher Scientific. Penicillin/streptomycin (PEST) was obtained from Life technologies. Paraformaldehyde (PFA) 4% was provided by Merck Millipore. Bovine serum albumin (BSA) was obtained from VWR. Pan-neurofilaments antibody (PanNF) was purchased from Covance, Belgium. VECTASHIELD® hardSet mounting medium containing DAPI was purchased from Labconsult. RNeasy micro kit (50) was obtained from Qiagen.

6.2.2 Surfaces used to perform tests with SCAPs

The surfaces tested for the proliferation of cells are summarized in Table 6.1. Among these surfaces lie homogeneous brushes grafted with RGD-C, C-LL37 or a C-LL37/RGD-C (50:50) mixture. These surfaces were used to compare the behavior of cells on non-patterned and patterned surfaces. The 250 or 400 chemical nanopatterns vary in their lateral dimensions as explained in Chapter 4 and consist of lines of P(HOEGMA) brushes grafted with different peptides and distributed in a non-adhesive background. Here, we used a 250 chemical nanopattern grafted with RGD-C and 400 chemical nanopatterns grafted with RGD-C, C-LL37 or C-LL37/RGD-C (50:50). The 250 or 400 topographical nanopatterns vary in their lateral dimensions, show a pit of 50 nm and are covered with a P(HOEGMA) brush grafted with RGD-C. Moreover, glass surfaces were used as control surfaces.

The surfaces tested for the differentiation of SCAPs via immunofluorescence were homogeneous brushes grafted with RGD-C, C-LL37 and C-LL37/RGD-C and 400 chemical nanopatterns grafted with RGD-C and C-LL37/RGD-C. An additional glass surface was used as a control surface. The surfaces tested for the differentiation of SCAPs in quantitative reverse transcription polymerase chain reaction (qRT-PCR) analysis were homogeneous brushes grafted with C-LL37 and C-LL37/RGD-C and the 400 chemical nanopattern grafted with C-LL37/RGD-C. Moreover, glass surfaces were used as control surfaces.

Table 6.1: The surfaces presented in this table were used to investigate the proliferation and the morphology of SCAPs. A subset of these surfaces were used for differentiation tests. They are classified according to the nature of the grafted peptide and their structure.

		Peptide		
		RGD-C	C-LL37	C-LL37 /RGD-C
Surface structure	Homogenenous brushes		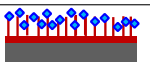	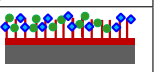
	250 chemical nanopatterns	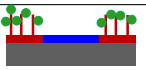	x	x
	400 chemical nanopatterns		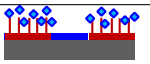	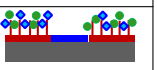
	250 topographical nanopatterns	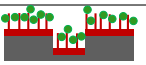	x	x
	400 topographical nanopatterns	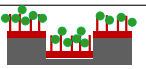	x	x

6.2.3 Cell culture

SCAPs were kindly provided by Prof. Anne des Rieux (SSS/LDRI, UCL). SCAPs were cultured at 37°C under 21% O_2 and 5% CO_2 atmosphere in a MEM eagle supplemented with 10% (v:v) FBS, 1% (v:v) L-glutamine and 1% (v:v) PEST. Before seeding the surfaces with cells, the samples were sterilized in 70% ethanol during 1 minute and left to dry in a laminar flow hood. Cells harvested between passages 1 to 10 were seeded at a density of 10^4 cells/cm^2 in MEM supplemented medium and the samples were left in the incubator for 18 hours before renewing the MEM supplemented medium. The samples were then left for an additional 30 hours to get a total proliferation time of 48 hours.

For immunofluorescence studies, the samples were then immersed in PFA

during 15 minutes at room temperature. For the adhesion and proliferation studies, some samples were removed from the incubator after 18 hours and the remaining samples were removed after 48 hours. For the differentiation studies, the samples were removed from the incubator after 48 hours.

For gene expression studies, the samples were removed from the medium after 48 hours and analyzed by RT-qPCR.

6.2.4 Immunostaining

The fixation of cells via PFA was performed for one night at 4°C, then the samples were rinsed with PBS buffer (pH 7.45) during 10 minutes at room temperature. Fixed cells were permeabilized with 0.1% triton in PBS buffer for 10 minutes at room temperature then blocked with 5% BSA in PBS Tween 0.05% for 1 hour at room temperature. Cells were then incubated with primary antibody anti-vinculin for proliferation studies and PanNF antibody for differentiation studies in 1% BSA PBS Tween 0.05% for 1 hour at 37°C. After washing with PBS Tween 0.05%, cells were stained with Alexa Fluor® 488 secondary antibody for vinculin or neurofilaments staining and with rhodamine phalloidin for actin in 1% BSA PBS Tween 0.05% during 1 hour at room temperature. During this step, the samples were protected from light to avoid the bleaching of the dyes. After a final wash in PBS Tween 0.05%, samples where mounted between microscope slides with VECTASHIELD® hardset containing DAPI which stains the nucleus in blue. The hardening was initiated 15 minutes at room temperature then the samples were placed at 4°C overnight.

6.2.5 Generation of negative controls by omitting the primary antibodies

The specificity of the secondary antibody bearing the Alexa Fluor® 488 marker needed to be assessed. Indeed, if the secondary antibody was bound to other parts of the cell, the analysis of vinculin and neurofilament stainings would not be possible. We thus tested the specific complexation of the secondary antibody on surfaces previously incubated or not with primary antibody. The secondary antibody did not adhere on the surface not previously tagged with the primary antibody. In contrast, the specific complexation between the primary and the secondary antibody was assessed. This thus confirmed the specificity of the secondary antibody towards the primary antibody.

6.2.6 Fluorescence microscopy

After staining, the samples were imaged with an Olympus epifluorescence IX71 microscope equipped with a blue filter U-MNUA2 (excitation 360-370 nm and emission 420-460 nm), a green filter U-MWIBA3 (excitation 460-495 nm and emission 510-550 nm) and a red filter U-MNIGA3 (excitation 540-550 nm and emission 575-625 nm). The UV light is provided by an X-cite module, series 120PCQ from Lumen Dynamics. Cells were imaged for vinculin or Pan-neurofilaments (green), actin (red) and nucleus (blue). For proliferation and differentiation studies, 18 images for each type of surfaces were taken at magnification 10X. For morphological studies, 50 individual cells were imaged for each type of surfaces at magnification 40X.

6.2.7 Image analysis

The quantification were carried out using imageJ software. The images were converted into an 8-bit file. For the proliferation studies, the number of cells was estimated by counting up the number of nuclei on the surfaces. First, the background was removed using a rolling ball radius of 10. After adjusting the threshold and using the process "fill holes" and "watershed" to split up sticking nuclei, the number of nuclei was counted with the "Analyze particles" tool with size set between 50 and 1000 pixels. Figure 6.1 shows the original image showing the nuclei stained with DAPI (Figure 6.1a) and the surrounded nuclei counted (Figure 6.1b). The nuclei are thus well selected. The cell proliferation percentages computed were relative to a glass control surface after 18 hours.

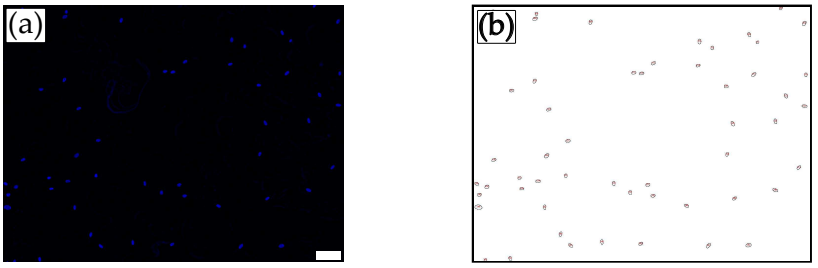

Figure 6.1: (a) Fluorescence microscopy image of cell nuclei stained with DAPI and (b) selected nuclei after image analysis, on a homogeneous brush grafted with RGD-C after a culture time of 18 hours. The white bar represents 100 μm.

For the analysis of cell surface area, circularity and AR as well as cell orientation according to the pattern, the threshold was manually adjusted and the cell outline was delimited with the wand tracing tool. The properties were measured with the "Measure" tool of imageJ software for each individual cell. Figure 6.2a shows the original image showing the actin filament stained with rhodamine phalloidin. Then, the cell actin was selected with the threshold (Figure 6.2b). Finally, the actin filaments of the targeted cell were properly extracted from the original image and the surface area and circularity computed (Figure 6.2c). In Figure 6.2d, the fitting ellipse allowing imageJ to compute the AR is shown and the cell angle according to the horizontal axis is computed. When the pattern is present, the angle is corrected in order to obtain the orientation of the cell according to the pattern direction.

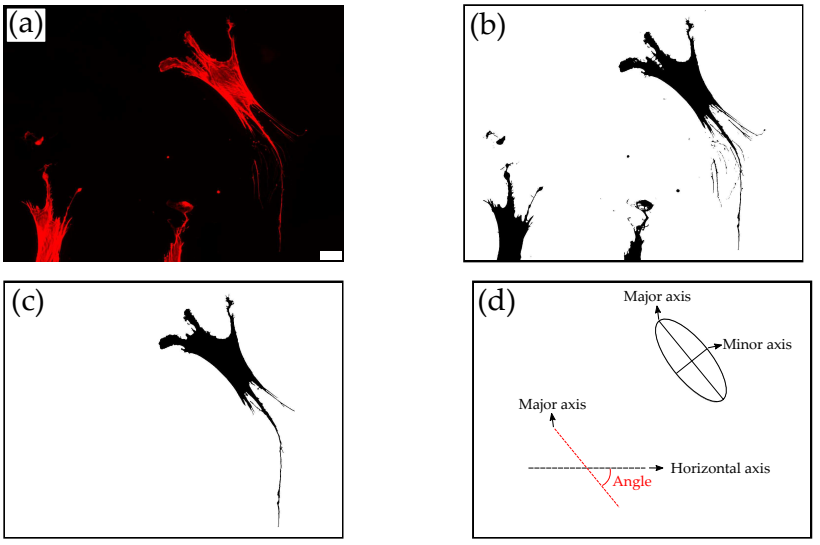

Figure 6.2: (a) Fluorescence microscopy image of cell actin stained with rhodamine phalloidin, (b) actin threshold selection, (c) selected actin for a targeted cell and (d) fitting ellipse and angle computation, on a homogeneous brush grafted with RGD-C after a culture time of 18 hours. The white bar represents 20 μm.

For the focal adhesion area, the background was removed using a rolling ball radius of 10. After adjusting the threshold, the "Analyze Particles" tool was used with particle size comprised between 30 and 1000 pixels to measure the surface area of focal adhesions located at the periphery of cells. The periphery

was selected manually. Figure 6.3 displays the original image showing the FAs stained with the primary antibody complexed by the fluorescent secondary antibody (Figure 6.3a) and the surrounded FAs counted (Figure 6.3b). The FAs are thus well selected at the periphery of the cell.

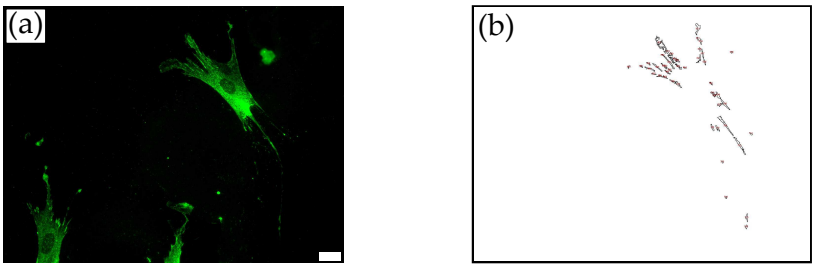

Figure 6.3: (a) Fluorescence microscopy image of cell vinculin stained with fluorescent antibody and (b) selected FAs, on a homogeneous brush grafted with RGD-C after a culture time of 18 hours. The white bar represents 20 μm.

For the differentiation studies, we established the number of green pixels (*i.e.* related to the stained neurofilaments) per cell as well as the corrected total fluorescence (CTF). First, the background was removed using a rolling radius of 10. After adjusting the threshold, the "Measure" tool was used to compute the surface area covered by green pixels. The number of cells was counted following the method described for proliferation studies. Then, the number of green pixels per cell was computed. The original image of neurofilaments stained in green is displayed in Figure 6.4a while the green pixels selected are displayed in Figure 6.4b. Thus, the green pixels could be selected properly. The corrected total fluorescence was computed according to the following equation:

$$CTF = IntDen - (Area * Mean) \tag{6.1}$$

with *IntDen* the integrated density for all the cells present on the image, *Area* the surface area corresponding to the total cells and *Mean* the background fluorescence value. The CTF per cell is obtained by dividing the value obtained by the number of cells on the image computed as explained above. To measure these parameters the following method was applied. First, the background was removed using a rolling radius of 10. After adjusting the threshold, the "Measure" tool was used to compute the *IntDen* of the surface and the surface area of cells. Then the mean grey value of the background was computed by

using the "Measure" tool of ImageJ software on a selected area without cell.

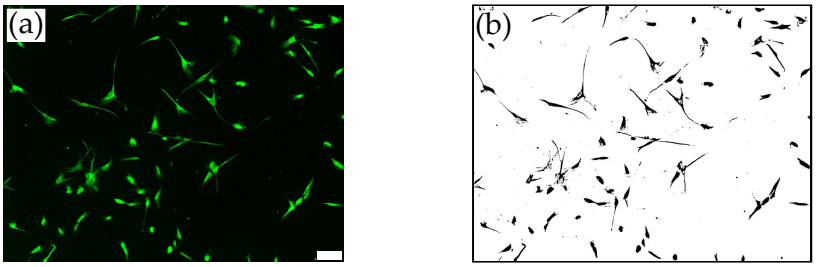

Figure 6.4: (a) Fluorescence microscopy image of cell neurofilaments stained with fluorescent antibody and (b) selected green pixels, on a homogeneous brush grafted with RGD-C after a culture time of 48 hours. The white bar represents 100 μm.

Numerical data are presented as mean values ± sem. Statistical analyses were performed using one-way analysis of variance (ANOVA) (IGOR PRO, wavemetrics) followed by post hoc Tukey (HSD) test with a significance level set at alpha = 0.05 for comparison of multiple means. T-tests were performed for each individual surface for values obtained at 18 hours and 48 hours, for the proliferation and morphology studies. T-tests were performed by comparing homogeneous brushed and 400 chemical nanopatterns grafted with RGD-C and C-LL37/RGD-C, for differentiation studies. Differences were considered significant for a p-value < 0.05. Each experiment was performed three times with duplicate samples for each condition.

6.2.8 qRT-PCR

For mRNA analysis, media was removed from the wells containing the surfaces with adhered cells and TriPure reagent (Roche, Basel, Switzerland) was added to each well at the end of the incubation period. The plates were then stored at -80°C for later assessment. Total RNA was extracted using the TriPure reagent according to the manufacturer's instructions. cDNA was synthesized using a reverse transcription kit (Promega corporation, Leiden, The Netherlands) from 1 μg of total RNA. qPCR was performed with a STEP one PLUS instrument and software (Applied Biosystems, Foster City, CA, USA) as previously described [259]. Data were normalized to the GAPDH mRNA expression. The markers analyzed were pan neurofilaments, for the neuronal differentiation, olig2 for

the oligodendrocyte lineage, GFAP for the astrocyte lineage, RunX2 for the osteogenic differentiation and ALPL for adipogenic differentiation.

Numerical data are presented as mean values ± sem. Statistical analyses were performed using one-way analysis of variance (ANOVA) (IGOR PRO, wavemetrics) followed by post hoc Tukey (HSD) test with a significance level set at alpha = 0.05 for comparison of multiple means. T-tests were performed by comparing the homogeneous brush and the 400 chemical nanopattern grafted with C-LL37/RGD-C. Differences were considered significant for a p-value < 0.05. Six samples of each type of surfaces were produced and results were pooled by pair before analysis with $\Delta\Delta$CT method. This experiment was performed twice for PanNF, RunX2 and ALPL and once for olig2 and GFAP.

6.3 Results and discussion

6.3.1 Analysis of cell proliferation and morphology

In this section, the SCAP proliferation was first observed qualitatively by fluorescence microscopy on a surface homogeneously covered by a non-grafted P(HOEGMA) brush and on a surface homogeneously covered by a SAM of PEG to ensure the non-adhesiveness of the non-grafted brush and the silane background used to prepare the patterns. In a second step, we focused on the quantitative analysis of the cell proliferation and morphological parameters (*i.e.* surface area, AR, circularity, orientation compared to the pattern direction, FA number and distribution) on the different surfaces after 18 and 48 hours of culture. Finally, for a given surface, we compared the values obtained for each parameters after 18 and 48 hours of culture. For each proliferation or morphological parameters studied, we focused on the following surface parameters to conclude about the effect of the surface characteristics on SCAP behavior:

- The effect of the nature of the grafted peptide by comparing homogeneous brushes grafted with RGD-C, C-LL37 and C-LL37/RGD-C.
- The effect of the patterning of the peptides by comparing 400 chemical nanopatterns grafted with RGD-C, C-LL37 and C-LL37/RGD-C.
- The effect of the lateral dimensions of the 250 and 400 chemical nanopatterns by comparing nanopatterns grafted with RGD-C. The effect of the

total area covered by RGD-C was compared between nanopatterned and homogeneous brushes grafted with RGD-C.

- The effect of both surface nanotopography and the grafting of RGD-C peptide.

6.3.1.1 Adhesion and proliferation of cells on various surfaces

Cell assays performed on SAM of PEG and non-grafted P(HOEGMA) brush to control the non-adhesiveness of these surfaces towards SCAPs.

Surfaces homogeneously covered by a SAM of PEG and surfaces homogeneously covered by a non-grafted P(HOEGMA) brush were tested against SCAPs to assess their non-adhesiveness. As can be seen in Figure 6.5a, the PEG surface allowed the adhesion of a very little number of cells that were not spread properly after 18 hours. However, after 48 hours, a very little number of spread cells could be seen on the surface (Figure 6.5b). Overall, the non-adhesiveness of the SAM of PEG could be confirmed.

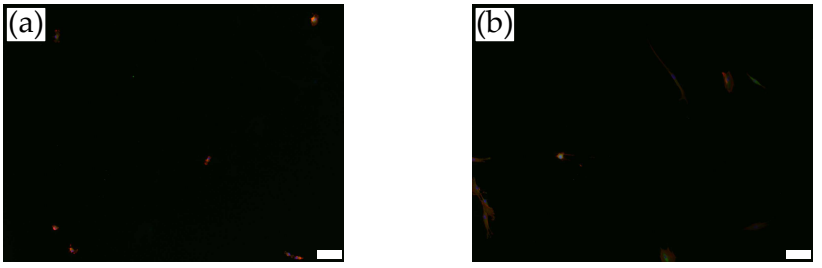

Figure 6.5: Fluorescence microscopy overlay images of SCAPs cultured onto a homogeneous SAM of PEG for (a) 18 and (b) 48 hours. The white bars represent 100 μm.

In Figure 6.6, only a few cells are seen on a homogeneous surface covered by a non-grafted P(HOEGMA) brush after 72 hours. Even though some cells adhered, they tended to form clusters and were not well spread. These adhered cells might have found a small defect on the surface thus allowing them to adhere. The non-adhesive behavior of P(HOEGMA) brush was thus confirmed.

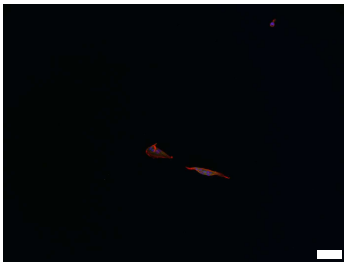

Figure 6.6: Fluorescence microscopy image of SCAPs on a homogeneous non-grafted P(HOEGMA) brush after 72 hours. The white bar represents 100 μm.

Proliferation of cells on homogeneous brushes grafted with different peptides.

The number of SCAPs on homogeneous brushes grafted with peptides increased with time, whatever the nature of the grafted peptide. This phenomenon is illustrated in Figure 6.7 for a homogeneous brush grafted with C-LL37/RGD-C. Moreover, the cells on homogeneous brushes grafted with different peptides showed a spread morphology with protrusions of different sizes extending from their edges as is illustrated in Figures 6.8 and 6.9 after 18 and 48 hours, respectively. The morphological characteristics of cells are detailed statistically in section 6.3.1.3.

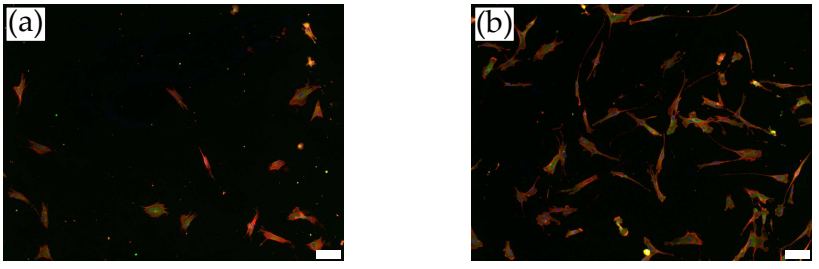

Figure 6.7: Fluorescence microscopy images of cells on homogeneous brushes grafted with C-LL37/RGD-C after a culture time of (a) 18 hours and (b) 48 hours. Nuclei are stained with DAPI (blue), actin filaments with rhodamine phalloidin (red) and vinculin with a secondary antibody complexed with a primary antibody (green). The white bars represent 100 μm.

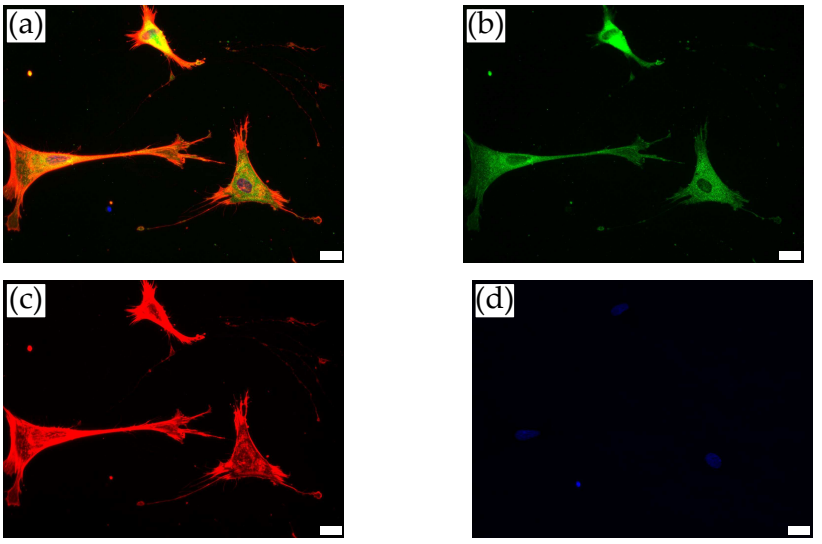

Figure 6.8: Fluorescence microscopy images of cells on a homogeneous brush grafted with C-LL37/RGD-C after 18 hours. The images are: (a) the overlay image, (b) the vinculin staining (green), (c) the actin staining (red) and (d) the nucleus staining (blue). The white bars represent 20 μm.

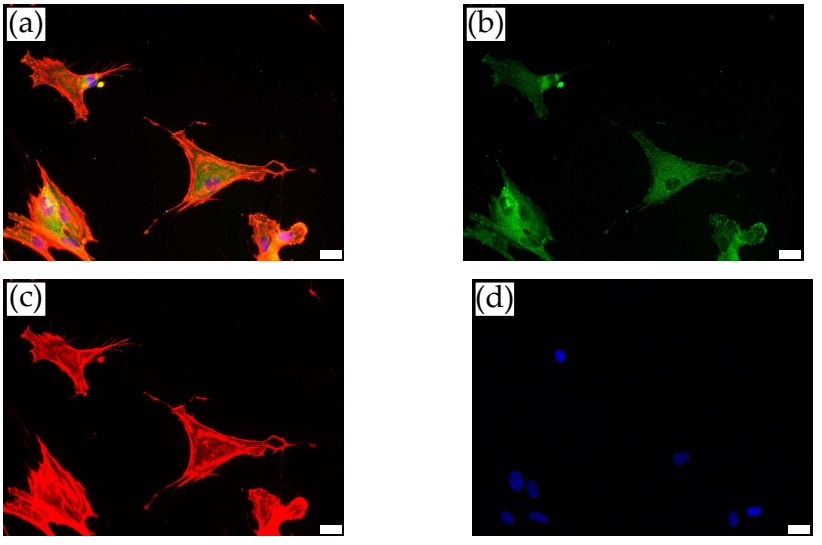

Figure 6.9: Fluorescence microscopy images of cells on a homogeneous brush grafted with C-LL37/RGD-C after 48 hours. The images are: (a) the overlay image, (b) the vinculin staining (green), (c) the actin staining (red) and (d) the nucleus staining (blue). The white bars represent 20 μm.

Proliferation of cells on chemical nanopatterns grafted with different peptides.

The number of SCAPs on chemical nanopatterns grafted with different peptides increased with time. However, the increase was less pronounced onto the 400 chemical nanopattern grafted with C-LL37/RGD-C compared to the other surfaces. The proliferation is illustrated in Figure 6.10 for a 400 chemical nanopattern grafted with C-LL37/RGD-C. Moreover, cells on chemical nanopatterns grafted with different peptides tended to align according to the direction of the pattern. They showed a more elongated morphology compared to homogeneous grafted brushes and had protrusions of different sizes extending from their edges as is illustrated in Figures 6.11 and 6.12 after 18 and 48 hours, respectively. The morphological characteristics of cells are detailed statistically in section 6.3.1.3.

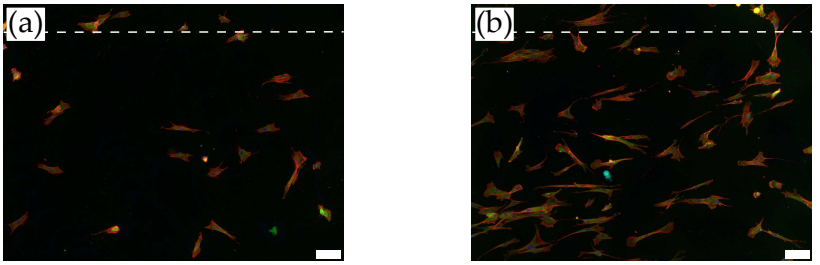

Figure 6.10: Fluorescence microscopy images of cells on 400 chemical nanopatterns grafted with C-LL37/RGD-C after a culture time of (a) 18 hours and (b) 48 hours. Nuclei are stained with DAPI (blue), actin filaments with rhodamine phalloidin (red) and vinculin with a secondary antibody complexed with a primary antibody (green). The dashed lines represent the direction of the patterned lines. The white bars represent 100 μm.

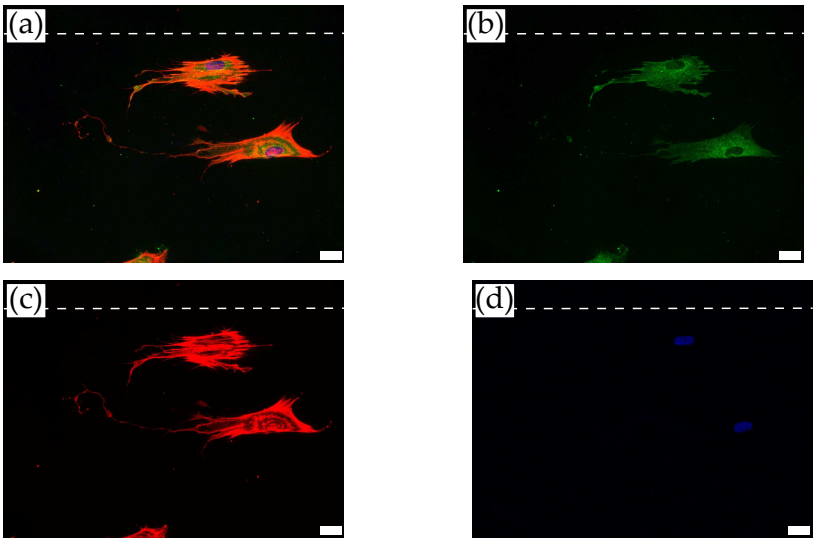

Figure 6.11: Fluorescence microscopy images of cells on a 400 chemical nanopattern grafted with C-LL37/RGD-C after 18 hours. The images are: (a) the overlay image, (b) the vinculin staining (green), (c) the actin staining (red) and (d) the nucleus staining (blue). The dashed lines represent the direction of the patterned lines. The white bars represent 20 μm.

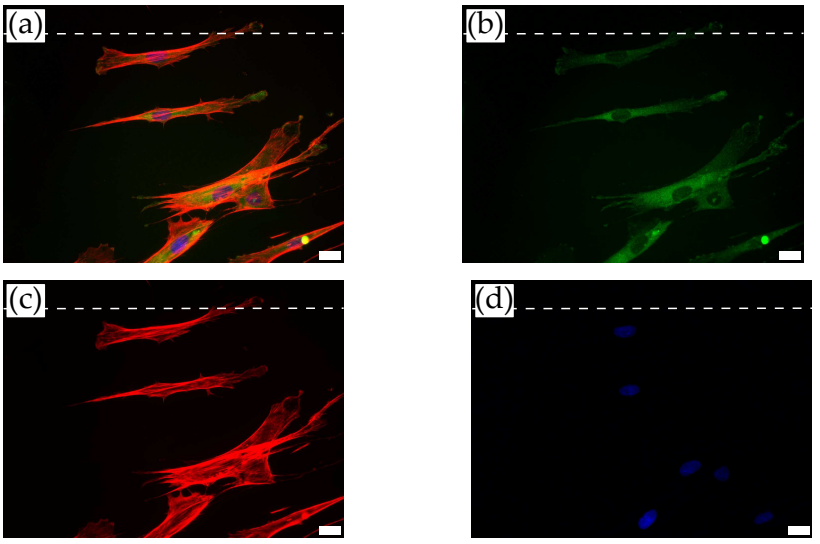

Figure 6.12: Fluorescence microscopy images of cells on a 400 chemical nanopattern grafted with C-LL37/RGD-C after 48 hours. The images are: (a) the overlay image, (b) the vinculin staining (green), (c) the actin staining (red) and (d) the nucleus staining (blue). The dashed lines represent the direction of the patterned lines. The white bars represent 20 μm.

Proliferation of cells on topographical nanopatterns.

The number of SCAPs on topographical nanopatterns grafted with different peptides increased with time. However, the increase was less pronounced onto the 400 topographical nanopattern grafted with RGD-C. The proliferation is illustrated in Figure 6.13 for a 400 topographical nanopattern grafted with RGD-C. Moreover, cells on topographical nanopatterns grafted with RGD-C tended to align according to the direction of the pattern. They showed a more elongated morphology compared to homogeneous brushes and had protrusions of different sizes extending from their edges as is illustrated in Figures 6.14 and 6.15 after 18 and 48 hours, respectively. The morphological characteristics of cells are detailed statistically in section 6.3.1.3.

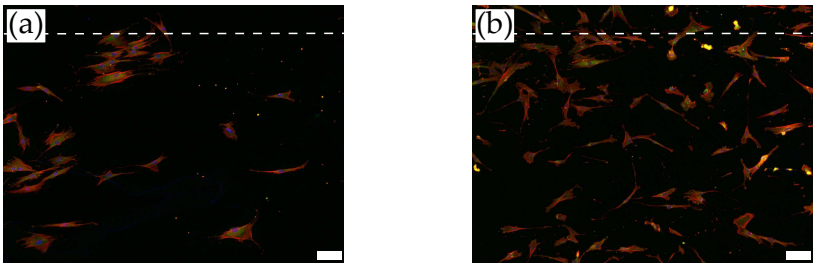

Figure 6.13: Fluorescence microscopy images of cells on 400 topographical nanopatterns grafted with RGD-C after a culture time of (a) 18 hours and (b) 48 hours. Nuclei are stained with DAPI (blue), actin filaments with rhodamine phalloidin (red) and vinculin with a secondary antibody complexed with a primary antibody (green). The dashed lines represent the direction of the patterned lines. The white bars represent 100 μm.

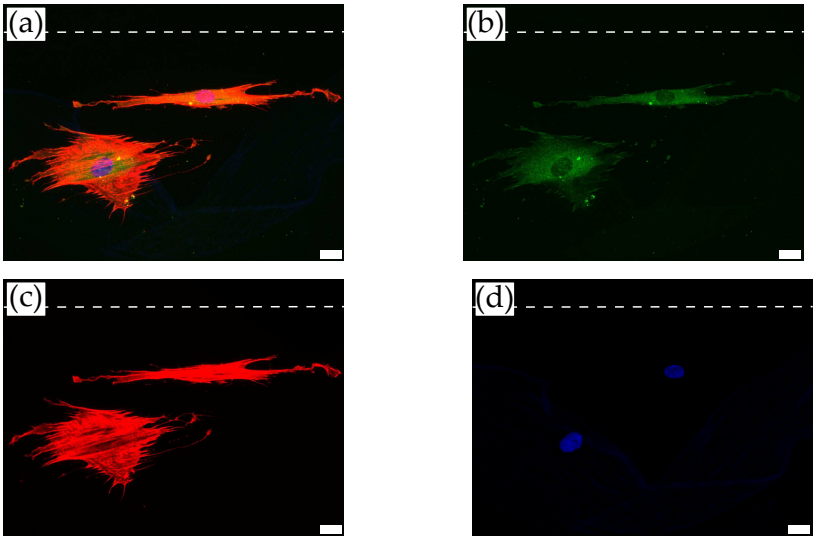

Figure 6.14: Fluorescence microscopy images of cells on a 400 topographical nanopattern grafted with RGD-C after 18 hours. The images are: (a) the overlay image, (b) the vinculin staining (green), (c) the actin staining (red) and (d) the nucleus staining (blue). The dashed lines represent the direction of the patterned lines. The white bars represent 20 μm.

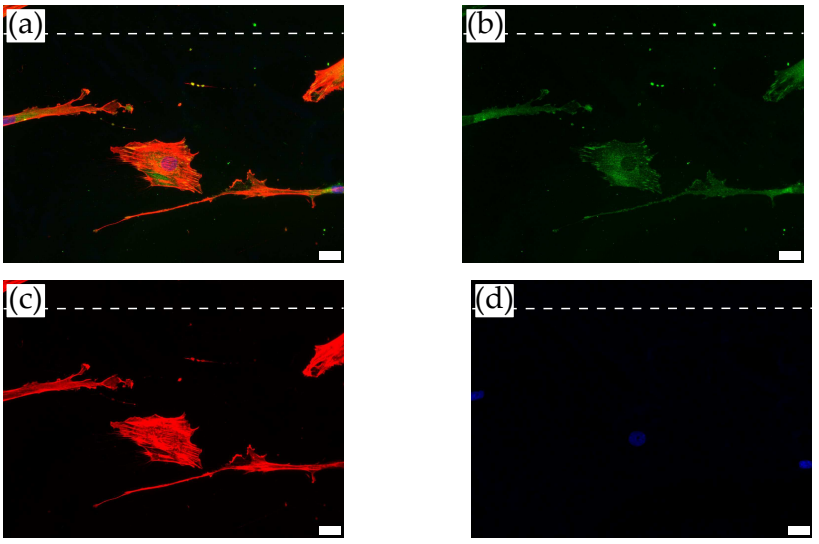

Figure 6.15: Fluorescence microscopy images of cells on a 400 topographical nanopattern grafted with RGD-C after 48 hours. The images are: (a) the overlay image, (b) the vinculin staining (green), (c) the actin staining (red) and (d) the nucleus staining (blue). The dashed lines represent the direction of the patterned lines. The white bars represent 20 μm.

6.3.1.2 Quantitative analysis of cell proliferation

We focused on the effect of the nature of the grafted peptide, the surface patterning, the dimensions of the pattern and the nanotopography on the proliferation of cells. For each condition, we systematically compared the values obtained after a culture time of 18 and 48 hours. Finally, we compared the values obtained on a given surface between 18 and 48 hours. All proliferation values were expressed in percentage relative to the glass surface after 18 hours.

First, we focused on the effect of the nature of the peptide using homogeneous brushes grafted with RGD-C, C-LL37 or C-LL37/RGD-C (section 6.5 Figure 6.35). The main interesting observation was that the percentage of proliferation was larger for the homogeneous brush grafted with RGD-C compared to the homogeneous brush grafted with C-LL37/RGD-C after 48 hours. Moreover the increase of proliferation on the surfaces grafted with the peptide mixture, between 18 and 48 hours was rather limited.

Second, we examined the patterning of the biofunctionalized brushes using 400 chemical nanopatterns grafted with RGD-C, C-LL37 or C-LL37/RGD-

C (Figure 6.16). After 18 hours (Figure 6.16a), the percentages were not statistically different between the different surfaces. After 48 hours (Figure 6.16b), the percentage were statistically higher for 400 chemical nanopatterns grafted with RGD-C and C-LL37 compared to 400 chemical nanopattern grafted with C-LL37/RGD-C. In addition, the proliferation on the glass surface was not significantly different from the other surfaces. When comparing the values between 18 and 48 hours for a given surface, only the proliferation on the 400 chemical nanopattern grafted with C-LL37/RGD-C was not statistically different meaning that there is no proliferation on this surface.

These observations confirmed that the RGD-C peptide was favorable for the proliferation of cells on both homogeneous and nanopatterned surfaces whereas the mixture of C-LL37/RGD-C hindered the proliferation on both homogeneous and nanopatterned surfaces. C-LL37 surfaces showed intermediate values of proliferation between RGD-C and C-LL37/RGD-C. The use of 400 chemical nanopatterns may accentuate this phenomenon compared to homogeneous surfaces since the amount of peptide molecules available on the surface is lower.

Third, we studied the effect of the lateral dimensions of the patterns by comparing the proliferation measured on 250, 400 and homogeneous brush, all grafted with RGD-C as well as glass surface used as a control. After 18 hours (Figure 6.17a), the proliferation was statistically higher on homogeneous brush compared to 250 chemical nanopattern. No other statistical difference was detected between the percentages of the different surfaces. After 48 hours (Figure 6.17b), no statistical difference was seen between the different surfaces. Finally, the percentage was statistically different for a given surface between 18 and 48 hours. So, the lateral dimensions of the nanopattern might influence the proliferation on the first few hours of proliferation after which the effect was smoothed.

Finally, the nanotopography effect was studied. After 18 hours, the topography did not influence differently the percentage of proliferation of cells compared to chemical nanopatterns and glass surface (Figure 6.18a). After 48 hours, the percentage was lower for topographical surfaces compared to the chemical nanopatterns showing the same lateral dimensions. The percentage measured for the glass surface did not show any difference with the ones of other surfaces (Figure 6.18b). Moreover, when comparing proliferation percentages after 18 and 48 hours, it appeared that the proliferation was significant for all the surfaces tested except the 400 topographical nanopattern grafted with RGD-C.

In this case, the proliferation was significantly affected by the topography.

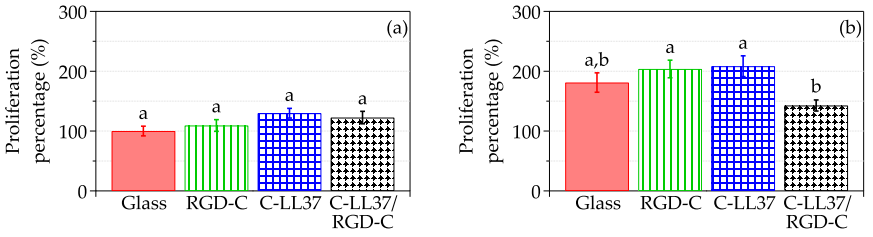

Figure 6.16: Comparison of cell proliferation on 400 chemical nanopatterns grafted with different peptides (a) after 18 and (b) 48 hours. Bars with different letters indicate significant difference, p-value < 0.05.

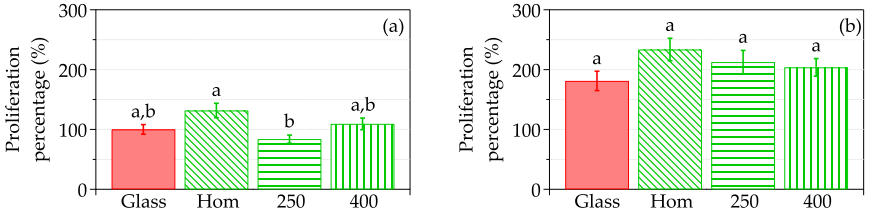

Figure 6.17: Comparison of cell proliferation on homogeneous, 250 and 400 chemical nanopatterns grafted with RGD-C (a) after 18 and (b) 48 hours. Bars with different letters indicate significant difference, p-value < 0.05.

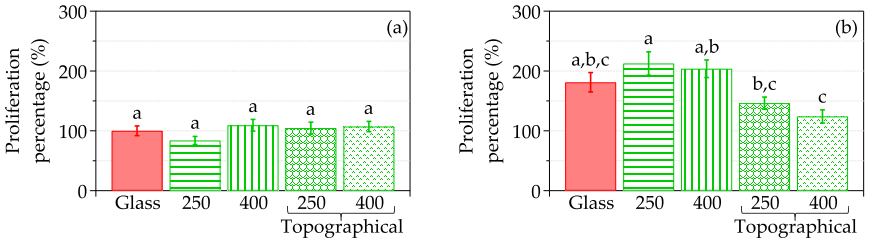

Figure 6.18: Comparison of cell proliferation on chemical and topographical patterns displaying different dimensions (*i.e.* 250 vs 400) (a) after 18 and (b) 48 hours. Bars with different letters indicate significant difference, p-value < 0.05.

6.3.1.3 Cell Morphology

For each cellular characteristic analyzed (*i.e.* cell surface area, aspect ratio, circularity, cell orientation compared to the pattern direction, FA number and distribution), we focused on the effect of the nature of the grafted peptide, the surface patterning, the dimensions of the pattern and the nanotopography. For each condition, we systematically compared the values obtained after a culture time of 18 and 48 hours. Finally, we compared the values obtained on a given surface between 18 and 48 hours.

Cell surface area

No significant difference was detected between the cell surface areas measured for a given time on all the tested surfaces (section 6.5 Figure 6.36a-b). Only the culture time influenced the cell surface area which decreased after 48 hours compared to 18 hours for a given surface.

Cellular AR

The AR of cells was computed with imageJ which calculates the ratio between the major and minor axis of the fitting ellipse of the object. When the AR increases, the cell is more elongated (Figure 6.2).

First, we focused on the effect of the nature of the peptide using homogeneous brushes grafted with RGD-C, C-LL37 or C-LL37/RGD-C (section 6.5 Figure 6.37). There were two interesting results: the AR of cells onto the homogeneous surfaces grafted with different peptides did not vary for a given culture time and the AR increased with culture time for homogeneous surfaces grafted with C-LL37.

Second, we examined the patterning of these biofunctionalized brushes using 400 chemical nanopatterns grafted with RGD-C, C-LL37 or C-LL37/RGD-C (Figure 6.19). After 18 hours (Figure 6.19a), the AR of cells grown on the 400 chemical nanopattern grafted with C-LL37 was smaller than the ones measured for the 400 chemical nanopattern grafted with RGD-C and the glass surface. No significant difference was detected between the cellular AR measured for the 400 chemical nanopattern grafted with C-LL37/RGD-C and the other surfaces. After 48 hours (Figure 6.19b), there was no more difference between the ARs measured for cells grown on the different surfaces. Moreover, only the cellular ARs measured for the 400 chemical nanopatterns grafted with C-LL37 and

C-LL37/RGD-C increased with the culture time.

We can thus conclude that the presence of the C-LL37 peptide only on the homogeneous and patterned surfaces induced an increase of the cellular AR with time. However, on the homogeneous brush grafted with C-LL37/RGD-C no increase in cellular AR with time was detected. It could be hypothesized that the presence of RGD-C peptide on the surface counterbalanced the effect of C-LL37 peptide. On the contrary, on the 400 chemical nanopattern grafted with C-LL37/RGD-C, the cellular AR increased with time. It is probable that the patterning counterbalanced the effect of the RGD-C peptide in this case.

Third, we studied the effect of the lateral dimensions of the patterns by comparing the cellular AR measured on 250, 400 and homogeneous brush, all grafted with RGD-C as well as glass surface used as a control. After 18 hours (Figure 6.20a), homogeneous brush grafted with RGD-C showed a smaller cellular AR compared to the glass surface and the 250 and 400 chemical nanopatterns grafted with RGD-C. After 48 hours (Figure 6.20b), the homogeneous brush showed again a smaller cellular AR compared to the nanopatterns. Moreover, the glass surface also showed a significantly smaller cellular AR compared to the 250 chemical nanopattern. When comparing ARs measured for a given surface between 18 and 48 hours, only the 250 chemical nanopattern induced an increase of cellular AR. We can thus say that the patterning the RGD-C peptide induced a higher cellular AR compared to homogeneous brush. Moreover, the smaller dimensions of the 250 nanopattern led to an increase of the cellular AR with time.

Finally, the nanotopography effect was studied and it did not provide any additional effects on the cellular AR when compared to chemical nanopatterns (section 6.5 Figure 6.38).

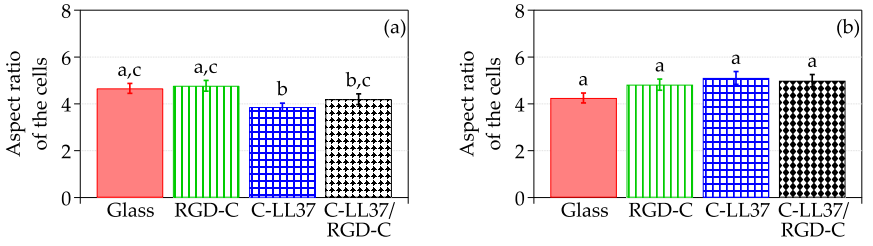

Figure 6.19: Comparison of cellular AR measured on 400 chemical nanopatterns grafted with different peptides (a) after 18 and (b) 48 hours. Bars with different letters indicate significant difference, p-value < 0.05.

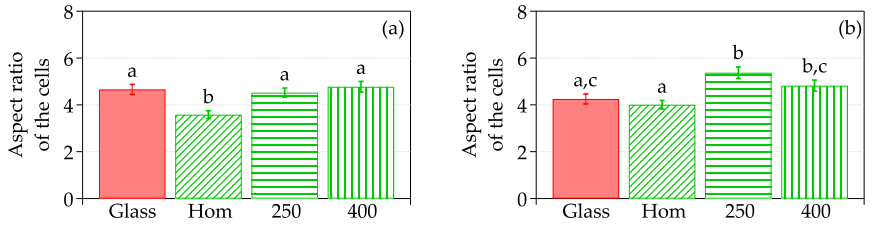

Figure 6.20: Comparison of cellular AR measured on homogeneous brush, 250 and 400 chemical nanopatterns grafted with RGD-C (a) after 18 and (b) 48 hours. Bars with different letters indicate significant difference, p-value < 0.05.

Cell circularity

The circularity is computed via ImageJ program. The formula used is:

$$Circularity = 4\pi \frac{cell\ surface\ area}{Perimeter^2} \tag{6.2}$$

When the circularity decreases, it means the cells are more elongated or form more protrusions. For a perfect circle, the obtained value is equal to 1.

First, we focused on the effect of the nature of the peptide using homogeneous brushes grafted with RGD-C, C-LL37 and C-LL37/RGD-C (section 6.5 Figure 6.39). No variation of the circularity was observed between the different surfaces tested after a given culture time. However, the circularity increased with time for all surfaces.

Second, we examined the patterning of these biofunctionalized brushes using 400 chemical nanopatterns grafted with RGD-C, C-LL37 or C-LL37/RGD-C (Figure 6.21). After 18 hours (Figure 6.21a), no difference was seen between the circularity measured for the different surfaces. After 48 hours (Figure 6.21b), the 400 chemical nanopattern grafted with RGD-C induced a smaller circularity than the 400 chemical nanopattern grafted with C-LL37/RGD-C and glass. The 400 chemical nanopattern grafted with C-LL37 did not show a circularity significantly different from the other surfaces. Moreover, the circularity systematically increased with time for a given surface.

Overall, this means that the patterning of the RGD-C peptide had a specific effect on cell circularity whereas it was not the case for other peptides.

Third, we studied the effect of the lateral dimensions of the patterns by comparing the circularity measured on 250, 400 and homogeneous brush, all grafted with RGD-C as well as glass surface used as a control (section 6.5

Figure 6.40). Overall, the circularity of cells was not influenced by the lateral dimensions of the patterns.

Finally, the nanotopography effect was studied. The most interesting observation was that the circularity increased with time for all surfaces (section 6.5 Figure 6.41).

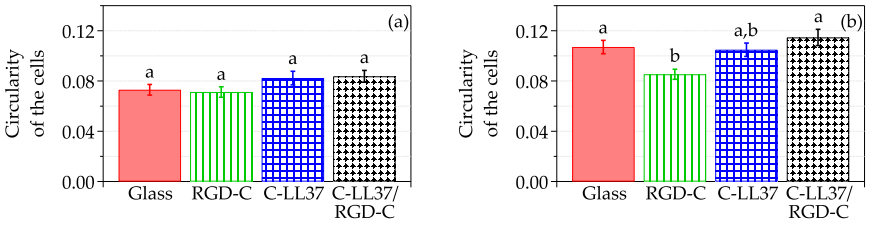

Figure 6.21: Comparison of cell circularity measured on 400 chemical nanopatterns grafted with different peptides (a) after 18 and (b) 48 hours. Bars with different letters indicate significant difference, p-value < 0.05.

Cell orientation compared to pattern direction

The cell did not orient in any particular direction on homogeneous surfaces and the glass surface after 18 and 48 hours (Figures 6.22, 6.25a-b). Thus, the homogeneous surfaces did not have any influence on cell orientation, as expected.

On 400 chemical nanopatterns grafted with RGD-C, C-LL37 and C-LL37/ RGD-C, cells tended to align along the pattern direction after 18 and 48 hours (Figure 6.23). After 18 hours, the number of aligned cells (angle between 0° and 36°) was higher on 400 chemical nanopatterns grafted with C-LL37 (78%) and RGD-C (70%) compared to 400 chemical nanopattern grafted with C-LL37/RGD-C (63%). After 48 hours, the number of aligned cells was still higher on 400 chemical nanopatterns grafted with RGD-C and C-LL37 (± 66%) compared to 400 chemical nanopattern grafted with C-LL37/RGD-C (62%) (Figure 6.25). This percentage decrease was due to the decrease of the number of cells oriented with an angle comprised between 0° and 18° according to the pattern direction; indeed this angle varied between 18 and 48 hours from 51% to 36% and from for 56% to 45% for 400 chemical nanopatterns grafted with RGD-C and C-LL37, respectively. To sum up, even though the 400 chemical nanopattern grafted with C-LL37/RGD-C showed a smaller number of aligned cells compared to the other patterns, this number did not vary with the culture

time. The nature of the grafted peptide thus played an important role in keeping the cell orientation in the pattern direction. The mixture of C-LL37/RGD-C allowed the greatest stability regarding orientation versus the culture time.

Then, we studied the effect of the lateral dimensions of 250 and 400 chemical nanopatterns grafted with RGD-C and compared the obtained results with a homogeneous brush grafted with RGD-C and a glass surface (Figures 6.23 and 6.25). On a 250 chemical nanopattern grafted with RGD-C, the alignment of cell was maintained for 48 hours (around 63% of aligned cells) while on 400 chemical nanopattern grafted with RGD-C, the percentage of aligned cells decreased slightly from 70% after 18 hours to 66% after 48 hours. Thus, both nanopatterns allow to maintain the alignment of the cells. However, this effect is slightly more pronounced on the 250 chemical nanopattern compared to the 400 chemical nanopattern.

Finally, the orientation of cells on 250 and 400 topographical nanopatterns was studied (Figures 6.24 and 6.25). After 18 hours, the percentage of aligned cells were 60% and 70% for 250 and 400 topographical nanopatterns, respectively. After 48 hours, they were 64% and 62% for 250 and 400 topographical nanopatterns, respectively. Cells on topographical nanopatterns thus showed a similar behavior than the ones observed on chemical nanopatterns. Therefore, these patterns played a similar role on the cell alignment process.

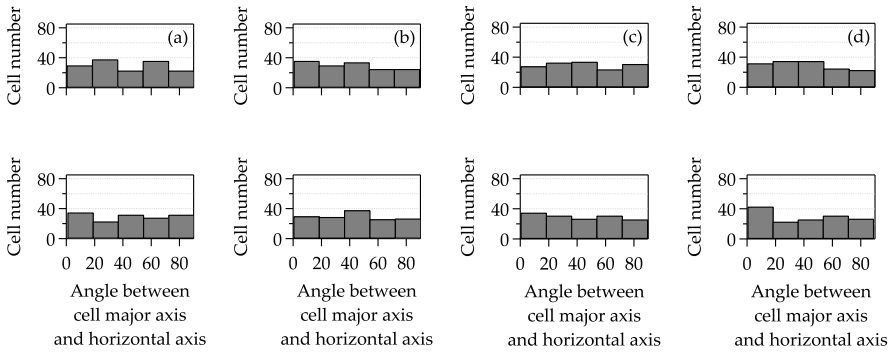

Figure 6.22: Comparison of cell orientation after 18 (top) and 48 hours (bottom) on (a) a glass surface and on homogeneous brushes grafted with (b) RGD-C, (c) C-LL37 and (d) C-LL37/RGD-C.

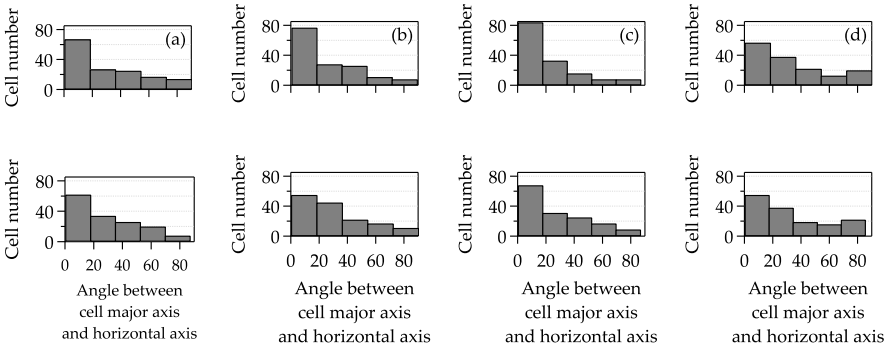

Figure 6.23: Comparison of cell orientation after 18 (top) and 48 hours (bottom) on (a) a 250 chemical nanopattern grafted with RGD-C and on 400 chemical nanopatterns grafted with (b) RGD-C, (c) C-LL37 and (d) C-LL37/RGD-C.

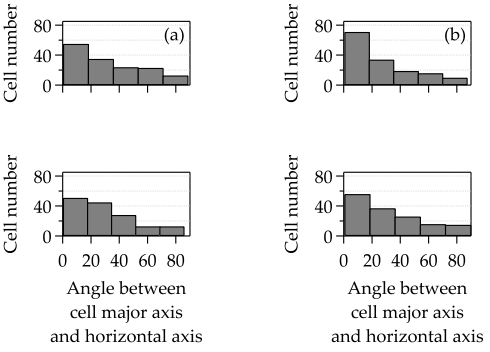

Figure 6.24: Comparison of cell orientation after 18 (top) and 48 hours (bottom) on (a) 250 and (b) 400 topographical nanopatterns grafted with RGD-C.

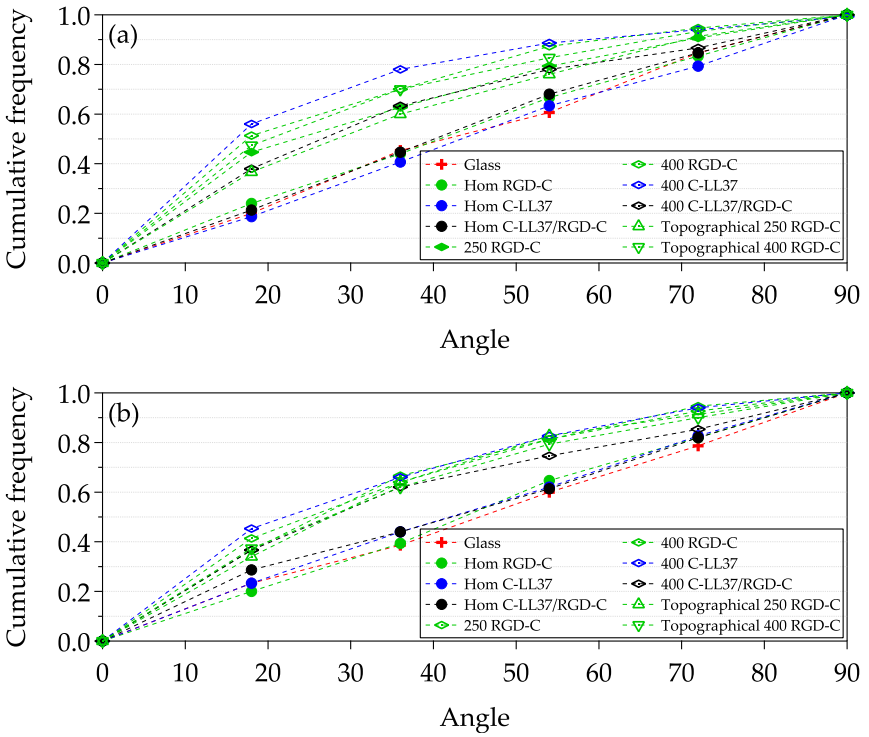

Figure 6.25: Comparison of cell orientation after (a) 18 and (b) 48 hours in cumulative frequency.

FA number per cell

In this section, the FAs analyzed have a size superior to 1.965 μm^2.

First, we focused on the effect of the nature of the peptide using homogeneous brushes grafted with RGD-C, C-LL37 or C-LL37/RGD-C (Figure 6.26). After 18 hours (Figure 6.26a), the number of FAs per cell was higher for homogeneous brush grafted with RGD-C compared to homogeneous brushes grafted with C-LL37 and C-LL37/RGD-C. The glass surface showed also a higher number of FAs compared to homogeneous brush grafted with C-LL37. After 48 hours (Figure 6.26b), the difference in number of FAs between the surfaces was smoothed but the number of FAs per cell was still higher for homogeneous brush grafted with RGD-C compared to C-LL37. Except for this difference, no significant feature was observed. Moreover, the number of FAs per cell did not vary with time for homogeneous brushes.

Second, we examined the patterning of these biofunctionalized brushes using

400 chemical nanopatterns grafted with RGD-C, C-LL37 or C-LL37/RGD-C (section 6.5 Figure 6.42). No difference was detected between the different surfaces. However, the number of FAs decreased with time for 400 chemical nanopatterns grafted with RGD-C and C-LL37.

So, the number of FAs per cell was influenced in the first few hours by the nature of the peptide and was higher for homogeneous surfaces grafted with RGD-C compared to the other peptides. However, such an effect of the peptide nature was not observed for patterned surfaces. So, it seemed that the patterning canceled the effect due to the nature of the peptide. Moreover, the number of FAs systematically decreased with the time on 400 chemical nanopatterns grafted only with RGD-C or C-LL37.

Third, we studied the effect of the lateral dimensions of the patterns by comparing the number of FAs measured on 250, 400 and homogeneous brush, all grafted with RGD-C as well as glass surface used as a control (Figure 6.27). After 18 and 48 hours, the number of FAs on the 250 chemical nanopattern grafted with RGD-C was smaller than on the homogeneous brush and the 400 chemical nanopattern grafted with RGD-C. After 18 hours, the number of FAs on the glass surface was smaller than the one on 400 chemical nanopattern. The number of FAs decreased with time on the 250 and 400 chemical nanopatterns. The dimensions of the nanopatterns influenced thus greatly the number of FAs per cell and patterning the RGD-C peptide might decrease the number of FAs per cell after 48 hours compared to homogeneous brush grafted with RGD-C.

Finally, the influence of the nanotopography on the FA number per cell was explored (section 6.5 Figure 6.43). It was seen that the topography influenced the number of FAs for the 250 topographical nanopattern: the number of FAs was indeed higher for topographical nanopatterns compared to chemical nanopatterns showing the same lateral dimensions.

These results are encouraging since they highlight the differences in FA formation of cells on the surfaces. However, it is worth noting that the FAs analyzed here have a size superior to 1.965 μm^2. This means that the number of FAs could be higher if the FAs of smaller size and the focal complexes were taken into account in the analysis for all surfaces.

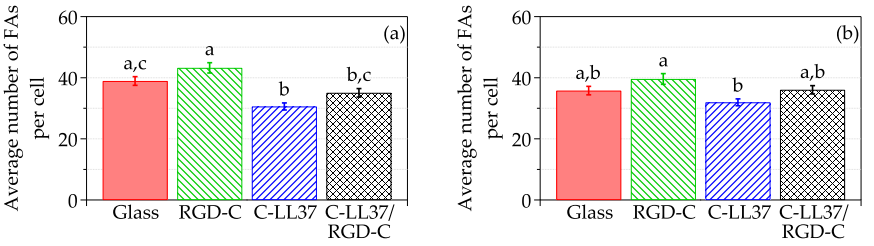

Figure 6.26: Comparison of FA number per cell measured on homogeneous brushes grafted with different peptides (a) after 18 and (b) 48 hours. Bars with different letters indicate significant difference, p-value < 0.05.

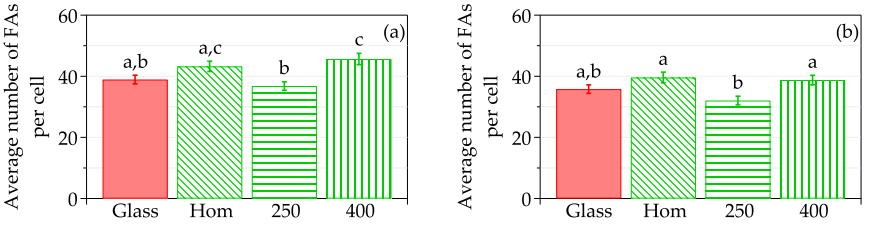

Figure 6.27: Comparison of FA number per cell measured on homogeneous brush, 250 and 400 chemical nanopatterns grafted with RGD-C (a) after 18 and (b) 48 hours. Bars with different letters indicate significant difference, p-value < 0.05.

FA distribution per size

The distribution of the size of FAs was systematically studied for the different surfaces. The variations observed between the different samples were quite small (Figure 6.28). However, one could notice a slight increase of smaller FAs at the expense of larger FAs for all surfaces with the time. This effect might be more pronounced for 250 chemical nanopattern and 250 topographical nanopattern grafted with RGD-C underlying the effect of the smaller lateral dimensions on FA distribution.

It is worth noting that the percentages obtained would probably differ if FAs smaller than 1.965 μm^2 were taken into account into the percentage estimations. Indeed, as the percentage of small FAs would increase, the percentage of super mature adhesions would have lesser importance.

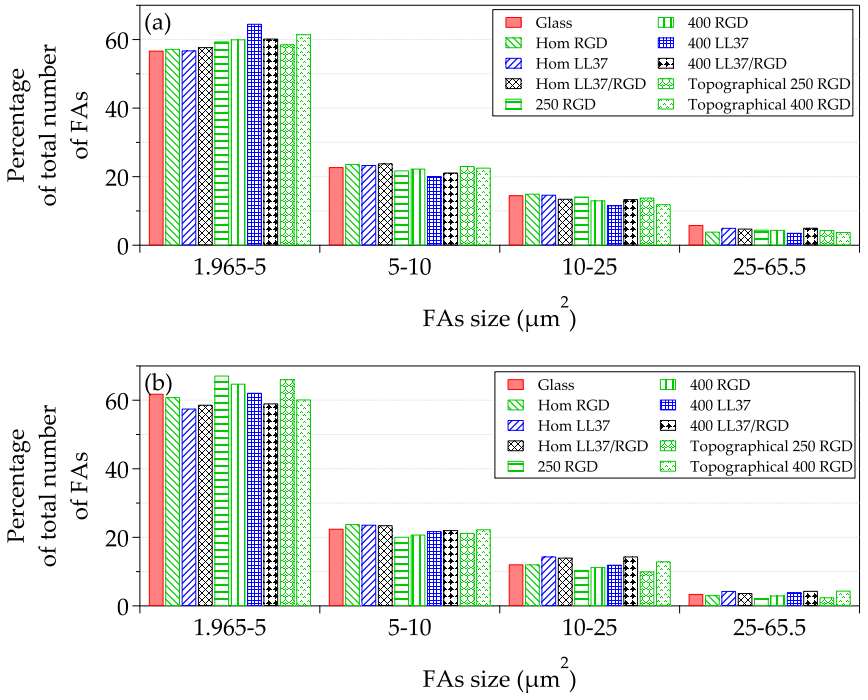

Figure 6.28: Comparison of FA distribution per size (expressed in percentage) after (a) 18 and (b) 48 hours for the different surfaces.

6.3.1.4 Discussion

We first focus on the effect of surfaces grafted with RGD-C on the cell proliferation and morphology. Then, we compare these behaviors to the ones observed for surfaces grafted with C-LL37/RGD-C and C-LL37 peptides. Finally, we focus on the effect of the nanotopography.

Effects of the surfaces grafted with RGD-C

The RGD peptide is an essential bioadhesive peptide for cell attachment to the surface. For this reason, we focus here only on surfaces grafted with RGD-C. In this context, it is also required to define the percentage of adhesive surface area. This percentage of adhesive surface area is computed by the ratio of the theoretical width of the lines grafted with RGD-C moieties to the theoretical width of the non-adhesive lines. The adhesive area are thus 31%, 50% and 100% for a 250 nanopattern, a 400 nanopattern and a homogeneous brush,

respectively.

- *Influence of the surface area grafted by RGD-C peptide on the adhesion and proliferation of cells.*

  The proliferation on homogeneous surfaces and nanopatterned surfaces grafted with RGD-C occurred at the same rate. However, the percentage of adhesive surface area on the nanopatterns influenced the initial amount of cells adhered on the surfaces (after 18 hours). Indeed, a smaller number of cells was measured for the surface showing a smaller percentage of adhesive surface area (250 chemical pattern grafted with RGD-C) compared to surfaces showing a larger percentage of adhesive surface area (400 chemical nanopattern and homogeneous brush grafted with RGD-C). These results are consistent with the results observed in the literature. Indeed, Gallant *et al.*, who fabricated surfaces with a gradient of immobilized RGD peptides, evaluated the effect of their density on smooth muscle cells. They first pointed out that the number of adhered cells increased with the RGD density. Then, they evidenced that the cell spreading was smaller on the regions with a high density of peptides whilst the AR was lower on the regions with a lower density of peptides. [185].

- *Influence of the surface patterning on the morphology and orientation of cells along the pattern direction.*

  The patterning of RGD-C peptide induced an increase of the cellular AR compared to homogeneous surfaces. This means that the cells were more elongated on nanopatterned surfaces. On the contrary, the cell circularity was not influenced by the patterning since no difference was observed between homogeneous and patterned surfaces. Thus the cells were more elongated but did not show any difference in their number of protrusions on patterns grafted with RGD-C compared to homogeneous brush grafted with RGD-C.

  Moreover, depending on the percentage of adhesive region on the surface, the cells could or could not strongly maintain their alignment along the pattern direction, with the culture time. For a smaller percentage of adhesive area (250 chemical pattern grafted with RGD-C), cells showed less adhesion spots and were maintained in their initial alignment while surfaces presenting a larger percentage of adhesive region (400 chemical

nanopattern grafted with RGD-C), a higher number of cells were aligned after 18 hours but tended to misalign with the culture time thanks to the higher number of adhesion spots. It is worth noting that 60-65% of cells were still aligned (angle comprised between 0° and 36°) along the pattern direction after 48 hours on both patterned surfaces.

We assume that the cell alignment and the increase of AR on RGD-C patterned surfaces compared to the homogeneous surface is due to an "orientation selection" mechanism [47, 161]. Even thought this phenomenon was highlighted for surfaces decorated with nanogrooves, we believe that it can also be applied to chemically nanopatterned surfaces. Indeed, as the filopodia at the edge of the cells sense the surface, they can form nascent adhesions with the RGD lines of the nanopatterns. The filopodia that are perpendicularly oriented compared to the patterned lines can only form small adhesion points (of 200 nm length maximum which corresponds to the width of the patterned bioactive lines) while the ones that are parallel to the patterned lines can form elongated adhesion complexes (with no restriction in length). As larger adhesive areas are able to sustain stronger contractile forces, they are favored and thus the cells elongate.

- *Influence of the surface patterning on the number of FAs.*

  The FA number per cell can also be related to the percentage of adhesive area. On the surface showing a smaller adhesive percentage, the number of FAs per cell was smaller. For a larger adhesive area percentage (400 and homogeneous surfaces), the number of FAs was similar. We thus hypothesized the existence of a threshold of adhesive area percentage needed for the formation of FAs: above a certain size of adhesive regions, the number of FAs did not increase; however, when the size of adhesive regions was too small, the number of FAs decreased.

Comparison of the effects of the surfaces grafted with RGD-C, C-LL37 and C-LL37/RGD-C

One of the objective of this thesis being on one side to control cell behavior through engineered surfaces but on the other side to hinder the bacterial colonization, we tested the cell growth on surfaces functionalized with C-LL37/RGD-C and C-LL37 peptide. We then compared the behaviors of cells on these surfaces with the ones grown on the surfaces bearing only RGD-C peptide.

- *Influence of the nature of the peptide on cell proliferation.*

  The first phenomenon we could point out was that using pure RGD-C or C-LL37 peptides led to a larger proliferation compared to using C-LL37/RGD-C peptides. On 400 chemical nanopattern grafted with C-LL37/RGD-C, the proliferation was not significant between 18 and 48 hours. This was due to the combination of the smaller bioactive area available for cell adhesion and the smaller proliferation rate induced by the co-presentation of C-LL37 and RGD-C.

- *Influence of the nature of the peptide and the surface patterning on the morphology and orientation of cells along the pattern direction.*

  The cellular AR and cell circularity did not vary between homogeneous brushes grafted with RGD-C, C-LL37 and C-LL37/RGD-C. Thus, having other peptides grafted on homogeneous surfaces did not influence the cell elongation nor the number of protrusions produced by cells. On patterned surfaces, however, the cellular AR on 400 chemical nanopattern grafted with RGD-C was higher than the one on C-LL37 pattern after 18 hours only. However, the cellular AR on 400 chemical nanopattern grafted with RGD-C was not different than the one on C-LL37/RGD-C. Moreover, the circularity of cells was smaller for 400 chemical nanopattern grafted with RGD-C compared to C-LL37/RGD-C surfaces after 48 hours. However, the circularity of cells for RGD-C patterns was not different compared to C-LL37 patterns. These observations highlight the fact that, after 48 hours and for cells showing the same AR, the cells growing on 400 chemical nanopattern grafted with RGD-C produced more protrusions than the cells adhered on C-LL37/RGD-C patterns.

  The initial cellular AR was influenced by the nature of the peptide. Combining the orientation selection phenomenon and the fact that the RGD-C peptide is specifically adhesive towards cell, the number of initially bound peptides should be larger on 400 chemical nanopattern grafted with RGD-C compared to the one grafted with C-LL37. Moreover, the specific interaction taking place with RGD-C peptide might not happen with C-LL37. The interaction with the surface might happen solely via cell secreted compounds adhering on the surface in the case of C-LL37. Thus the induction of elongated cells might happen faster on RGD-C patterns compared to C-LL37 patterns.

As shown for RGD-C-grafted surfaces, the cells aligned along the pattern direction. The presence of RGD-C or C-LL37 peptide on the patterned lines induced a high number of cells aligned after 18 hours. However, after 48 hours, the percentage of aligned cells decreased. On pattern with C-LL37/RGD-C mixture, the number of cells aligned was smaller after 18 hours compared to patterns grafted with C-LL37 and RGD-C but was kept constant at least until 48 hours. Here, it is noteworthy to outline that surfaces showing a higher proliferation also had a greater cell misalignment. It can thus be hypothesized that cells which were not proliferating were more durably anchored on the surfaces. This feature prevented their misalignment.

- *Influence of the nature of the peptide and the surface patterning on the number of FAs.*

  Using C-LL37 peptide instead of RGD-C also had an impact on the number of FAs per cell on homogeneous surfaces. The lowest number of FAs was noticed on C-LL37-grafted surfaces compared to RGD-C grafted surfaces. This phenomenon can be explained by the specificity of RGD-C peptide towards cell integrins.

Effects of the nanotopography

Topographical patterns were also explored to deduce the effect of nanotopography on cell behavior. Here, we focus on the difference found between 250 and 400 chemical and topographical nanopatterns grafted with RGD-C.

- The proliferation was greater on chemical nanopatterns compared to topographical nanopatterns. The topography might actually act as a physical barrier blocking cell proliferation.

- The topography had the same effect as the chemical nanopatterns on cellular AR and on circularity.

- The cells aligned along the direction of the patterned lines on both chemical and topographical patterns.

The question that arises from the two previous observations is: Is it the topography or the biochemical contrast which induces cell elongation and alignment? This question can be divided in three sub-questions that we will attempt to answer: Could the alignment of cells be mediated by topographical

contact guidance through filopodia? Could the alignment of cells be mediated by orientation selection? As the topographical nanopatterns are fully covered by RGD, why do the cells do not react as for homogeneous patterns?

Filopodia do not likely undergo topographical contact guidance since the threshold of height for this phenomenon is around 35 nm [160] which is exceeded for our topographical nanopatterns. Also, filopodia access easily the top part of the topographical pattern but it is not so clear whether or not filopodia attain the bottom of the pits from the topographical nanopatterns since their diameter range from 200 to 400 nm [260] and that the pit width is 200 nm or smaller. As a consequence, the orientation selection process seems more likely for the elongation and alignment of cells along the topographical nanopatterns.

- The topographical pattern with smaller lateral dimensions showed a higher number of FAs than for its biochemical nanopattern counterpart.

These conclusions helped us determine the surfaces that will be tested for cell differentiation. First, we chose the homogeneous surfaces grafted with different peptides to check the effect of the nature of the peptide on the cell differentiation without the effect of the cell alignment on the surface. We also used 400 chemical nanopatterns grafted with RGD-C and C-LL37/RGD-C to investigate the effect of the cell alignment on the differentiation process as well as the influence of cellular AR and circularity.

6.3.2 Analysis of cell differentiation

6.3.2.1 Inspection of cells stained for Pan-neurofilaments (green), actin (red) and nucleus (blue)

The cells were cultured on the surfaces for 48 hours before immunofluorescence staining (Figure 6.29). The neuronal differentiation was chosen over other differentiations since cells adhered on patterned surfaces showed elongated morphology with long protrusions. The immunofluorescence used labeled selectively Pan-neurofilaments (green) which outline the potential development of neurites [261]. Additionally, the actin filaments are stained in red and the nuclei are stained in blue. The staining for neurofilaments was then statistically analyzed to distinguish the effect of the surface nature and design on neuronal differentiation.

As observed before, the cells aligned along the nanopatterned lines on 400

chemical nanopatterns grafted with RGD-C and C-LL37/RGD-C but not on the homogeneous surfaces (Figure 6.29).

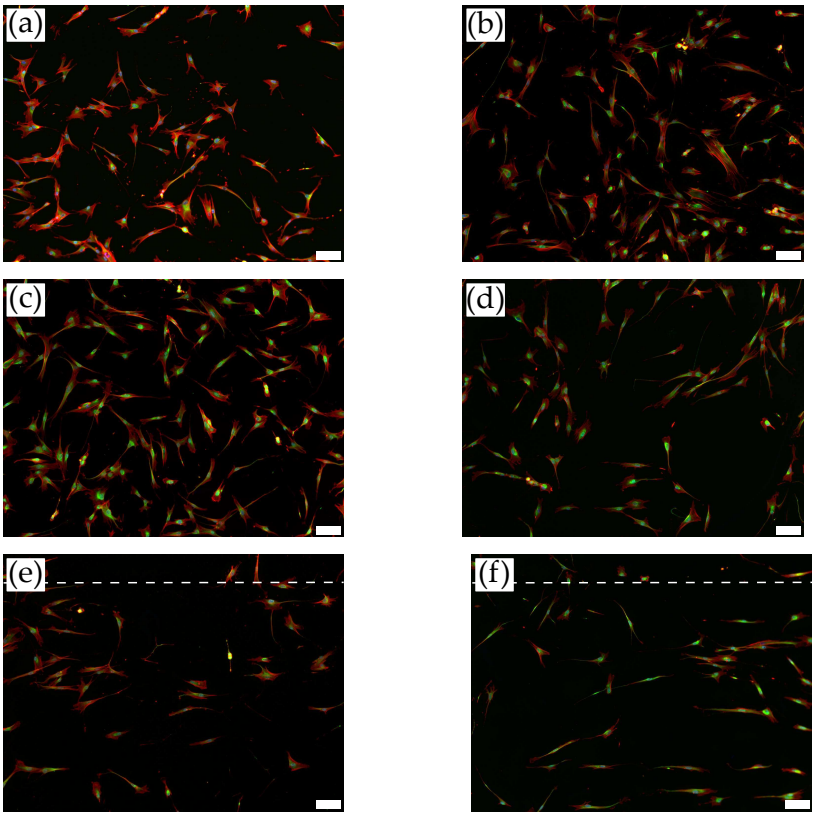

Figure 6.29: Fluorescence microscopy images of cells on (a) glass; homogeneous brushes grafted with (b) RGD-C, (c) C-LL37 and (d) C-LL37/RGD-C; 400 chemical nanopatterns grafted with (e) RGD-C and (f) C-LL37/RGD-C. Nuclei are stained with DAPI (blue), actin filaments with rhodamine phalloidin (red) and neurofilaments with a secondary antibody complexed with a primary antibody (green). The dashed lines represent the direction of the patterned lines. The white bars represent 100 μm.

6.3.2.2 Image analysis to access the cell fate

Number of green pixels per cell

The average number of green pixels per cell was calculated for homogeneous surfaces (Figure 6.30(a)) and 400 nanopatterns (Figure 6.30(b)). As can be seen for homogeneous surfaces, surfaces bearing the C-LL37 peptide alone showed

a higher number of green pixels per cell compared to the other homogeneous surfaces. The glass surface (*i.e.* control surface) also showed a higher number of green pixels compared to homogeneous brushes grafted with RGD-C and C-LL37/RGD-C. On 400 nanopatterned surfaces, however, the number of pixels did not differ between the different peptides.

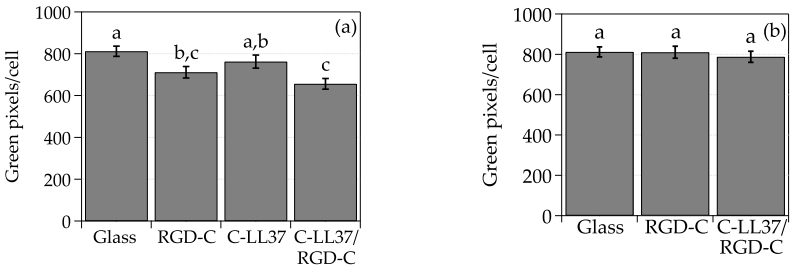

Figure 6.30: Analysis of the Pan-neurofilament staining (green) on various surfaces: (a) homogeneous and (b) 400 nanopatterned surfaces. Bars with different letters indicate significant difference, p-value < 0.05.

T-tests were also performed between homogeneous and 400 nanopatterned surfaces grafted with the same peptide. As a result, the values obtained for homogeneous brushes grafted with RGD-C and C-LL37/RGD-C were different from the ones measured for 400 chemical nanopatterns grafted with the same peptides. The increase of green pixels from homogeneous to 400 nanopatterns were 14 % and 20% for surfaces bearing RGD-C and C-LL37/RGD-C, respectively. The patterning of RGD-C and the mix C-LL37/RGD-C thus allowed to increase the average number of green pixels per cell and consequently the expression of Pan-neurofilaments.

CTF per cell

The CTF per cell was calculated for homogeneous surfaces (Figure 6.31(a)) and 400 nanopatterns (Figure 6.31(b)). No difference was seen between homogeneous surfaces and 400 nanopatterned surfaces.

T-tests were also performed between homogeneous and 400 nanopatterned surfaces grafted with the same peptide. As a result, the value measured for the homogeneous brush grafted with C-LL37/RGD-C was smaller than the one obtained for the 400 chemical nanopattern grafted with C-LL37/RGD-C. The CTF increased of 48% between these surfaces.

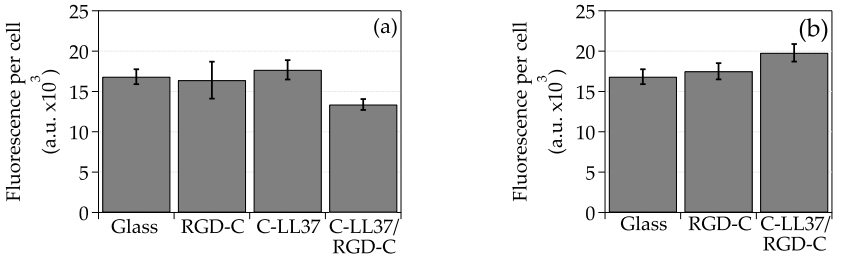

Figure 6.31: Analysis of CTF per cell for Pan-neurofilament staining (green) on various surfaces: (a) homogeneous and (b) 400 nanopatterned surfaces. No significant difference was found between the surfaces.

6.3.2.3 Impact of surface structure and peptide on SCAP gene expression

The PCR analysis was thus performed on cells grown on homogeneous brushes grafted with C-LL37 and C-LL37/RGD-C and on a 400 chemical nanopattern grafted with C-LL37/RGD-C due to the observation done in fluorescence. A glass surface was used as a control surface. SCAPs can undergo neuronal, osteogenic and adipogenic differentiation [261]. We thus focused on the neuronal differentiation but also tested genes for the osteogenic and adipogenic differentiations.

Neuronal differentiation

No significant difference was detected for the expression of neurofilaments between cells grown on homogeneous brushes grafted with C-LL37 and C-LL37/RGD-C and a 400 chemical nanopattern grafted with C-LL37/RGD-C (Figure 6.32). However, even if the difference was not statistically significant, it is worth noting that the mean value of NeuroF for the homogeneous brush grafted with C-LL37 was smaller than the ones measured for the homogeneous brush and the 400 chemical nanopattern grafted with C-LL37/RGD-C. Moreover, the neurofilaments were detected in a larger amount on glass surface compared to homogeneous brush grafted with C-LL37 and C-LL37/RGD-C.

A t-test was performed between the homogeneous brush and the 400 chemical nanopattern both grafted with C-LL37/RGD-C. It did no show any significant difference between these surfaces.

The differentiation in the oligodendrocyte and astrocyte lineages were also tested. As no expression of Olig2 and GFAP was detected, there was no

differentiation in these lineages.

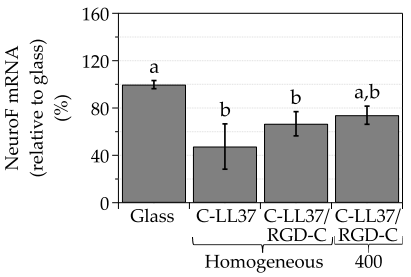

Figure 6.32: Expression of neuronal differentiation marker for neurofilaments for cells grown on homogeneous brushes grafted with C-LL37 and C-LL37/RGD-C and a 400 chemical nanopattern grafted with C-LL37/RGD-C relative to glass control surface. Bars with different letters indicate significant difference, p-value < 0.05.

Osteogenic differentiation

No significant difference was detected for the expression of RunX2 (osteogenic differentiation marker) by cells grown on homogeneous brushes grafted with C-LL37 and C-LL37/RGD, a 400 chemical nanopattern grafted with C-LL37/RGD and a glass surface (Figure 6.33).

A t-test was performed between the homogeneous brush and the 400 chemical nanopattern both grafted with C-LL37/RGD-C. It did no show any significant difference between the surfaces.

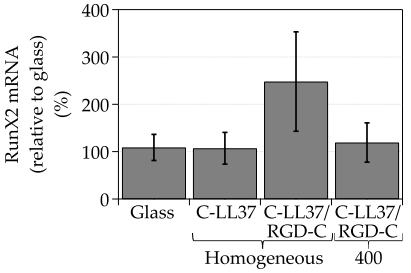

Figure 6.33: Expression of RunX2 (osteogenic differentiation marker) by cells grown on homogeneous brushes grafted with C-LL37 and C-LL37/RGD-C and a 400 chemical nanopattern grafted with C-LL37/RGD-C relative to glass control surface. No significant difference was found between the surfaces.

Adipogenic differentiation

No significant difference was detected for the expression of ALPL (adipogenic differentiation marker) by cells grown on homogeneous brushes grafted with C-LL37 and C-LL37/RGD-C, a 400 chemical nanopattern grafted with C-LL37/RGD-C and a glass surface (Figure 6.34).

A t-test was performed between the homogeneous brush and the 400 chemical nanopattern both grafted with C-LL37/RGD-C. It did no show any significant difference between the surfaces.

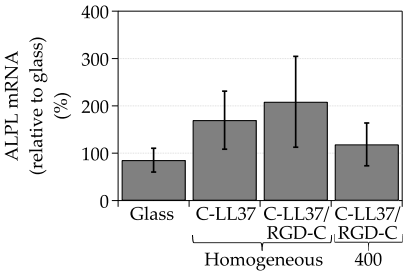

Figure 6.34: Expression of ALPL (adipogenic differentiation marker) by cells grown on homogeneous brushes grafted with C-LL37 and C-LL37/RGD-C and a 400 chemical nanopattern grafted with C-LL37/RGD-C relative to glass control surface. No significant difference was found between the surfaces.

6.3.2.4 Discussion

We first tested the neuronal differentiation by a specific immunostaining for neurodifferentiation (*i.e.* Pan-neurofilament) and could conclude that:

- C-LL37 peptide grafted alone might increase the number of neurofilaments expressed by cells compared to RGD-C or the mixture of C-LL37/RGD-C.
- We evidenced that the cells were more committed to the neural lineage on the patterned surfaces because the Pan-neurofilaments were expressed more extensively on 400 chemical nanopatterns grafted with RGD-C and C-LL37/RGD-C compared to homogeneous brushes grafted with RGD-C and C-LL37/RGD-C, respectively.
- This last effect is more pronounced for the cells grown on the homogeneous brush and the 400 chemical nanopattern grafted with C-LL37/RGD-C since differences in the number of stained pixels as well as in the CTF per cell were larger than the ones measured for cells grown on the homogeneous brush and the 400 chemical nanopattern grafted with RGD-C.

Interestingly, as outlined above for the proliferation studies, the cells on the 400 chemical nanopattern grafted with C-LL37/RGD-C showed no significant proliferation after 48 hours compared to the 400 chemical nanopattern grafted with RGD-C. This seems logical since proliferation has an inverse relationship to differentiation [12]. Moreover, the alignment of the cells was kept during 48 hours for 400 chemical nanopattern grafted with C-LL37/RGD-C while for 400 chemical nanopattern grafted with RGD-C, it varied over time. We hypothesized that the cells on 400 chemical nanopattern grafted with C-LL37/RGD-C were more permanently fixed than the ones on the 400 chemical nanopattern grafted with RGD-C. This was also confirmed by the decreasing number of FAs for 400 chemical nanopattern grafted with RGD-C compared to 400 chemical nanopattern grafted with C-LL37/RGD-C which stayed fixed over time. As for the higher number of protrusions produced on 400 chemical nanopattern grafted with RGD-C compared to the one on 400 chemical nanopattern grafted with C-LL37/RGD-C, we hypothesized that the cell can probe the surface in all the directions for the RGD-C pattern because of the higher number of RGD-C molecules grafted. This thus did not allow for the immediate commitment into the neural lineage.

The differences in proliferation, morphology and neurofilaments expression of cells onto 400 chemical nanopatterns grafted with RGD-C and C-LL37/RGD-C (explained above) were the results of the interactions of cells with the surfaces. In order to go even further, we have to consider the whole process occurring inside the cell. The adhesions formed on a surface allow the organization of the cytoskeletal elements (notably actin fibers). Since the cell adhesions depend on the surface displayed, the cytoskeleton assembly differs between the different surfaces tested and thus it triggers different transduction signals. As these signals regulated the response of cells to the sensed surface, the proliferation and morphology such as the cellular AR were different on the surfaces showing different peptides and structures. This explains why the 400 chemical nanopattern grafted with C-LL37/RGD-C was more appropriate for neuronal differentiation.

In sum, we analyzed the potential neuronal, osteogenic and adipogenic differentiations using different markers analyzed by PCR and concluded that:

- The higher differentiation potential in the neuronal lineage detected by immunostaining for cells cultured on 400 nanopattern grafted with C-LL37/RGD-C compared to homogeneous brush grafted with C-LL37/RGD-

C was not confirmed by PCR analysis.

- The presence of C-LL37 only on the surface tends to decrease the neuroF expression (even though it was not significant).
- No differentiation of cells in the oligodendrocyte and astrocyte lineages were detected by PCR.
- The expression of RunX2 marker related to osteogenic differentiation did not vary between the surfaces tested.
- The expression of ALPL marker related to adipogenic differentiation did not vary between the surfaces tested.

The lack of detection for the neuronal differentiation with PCR contrasted with the results obtained by immunofluorescence. However, the expressed ribonucleic acid (RNA) does not always reflect the amount of proteins present at the time of analysis in the image taken. Indeed, there may be a delay between the production of RNA and its traduction into the associated protein in the cell. The difference in expression of neurofilament-related proteins might thus not yet be detected by in fluorescence microscopy. Moreover, the immunofluorescence analysis is less precise since it is based on an image analysis. Additionally, it could be hypothesized that the differentiation in the neuronal lineage would be larger if cells could make contact with each others. Indeed, Shah *et al.* explained that cell-cell interactions are important to form neurons [170]. To obtained such cell-cell interactions on our surfaces, we should culture the cells for more than 48 hours.

There were no difference in osteogenic differentiation for the marker tested. We assumed that the differentiation in the neuronal lineage prevented the differentiation in the osteogenic lineage for cells adhered on the homogeneous brush and the 400 chemical nanopattern grafted with C-LL37/RGD-C. For the homogeneous brush grafted with C-LL37, the lack of differentiation in the osteogenic lineage might be due to the lack of specific anchorage of cells on the surface as the specific interaction taking place with RGD-C peptide certainly not occur with C-LL37. The interaction with the surface might happen solely via cell secreted compounds adhering on the surface. This layer might lack the required amount of adhesion ligands to form FAs able to sustain mechanical forces.

It is not surprising to not see a significant difference in the adipogenic marker for cells grown on the different surfaces tested. Indeed, ARs measured for cells on different surfaces (see section 6.3.1.3) revealed a elongated morphology even for homogeneous brushes which is far from the rounded morphology favoring adipogenic differentiation. The study from Lee *et al.* confirmed this result. Indeed, they compared the behavior of MSCs grown on a poly(acrylamide) gel showing micro-regions (1000 μm^2) grafted with fibronectin, laminin and/or collagen type I and on homogeneous poly(acrylamide) gels grafted with the same proteins. They showed that round confined cells on the patterned regions expressed adipogenesis markers while spread cells observed on homogeneous gels tended to show neurogenesis markers. They also showed that the use of different proteins on the same surface reinforced the differentiation in neurogenic or adipogenic lineage depending if they use homogeneous or patterned gels. In particular, any combination of proteins containing collagen promoted neurogenic differentiation [158].

6.4 Conclusion

In this chapter, we first studied the effect of the nature of the peptide (*i.e.* bioadhesive peptide RGD-C and antimicrobial peptide C-LL37) and its surface patterning on the proliferation and morphology of SCAPs.

We showed that the surface area of cells varied with the culture time but was not influenced by the lateral dimensions of the nanopatterns, the peptide grafted on the surfaces or the nanotopography.

We were able to show that a larger amount of RGD-C peptide induced a larger initial number of adhered cells and a larger number of FAs. The patterning of the RGD-C peptide allowed to align the cells along the patterned lines and increased the AR of the cells. The alignment of cell was more easily maintained on the smaller 250 chemical nanopattern grafted with RGD-C showing a smaller percentage of adhesive area.

Moreover, the surface grafted with a mixture of C-LL37/RGD-C decreased the rate of cellular proliferation, the AR value in the first few hours and the number of protrusions compared to surfaces grafted with RGD-C. The alignment of cells along the nanopatterned lines grafted with C-LL37/RGD-C was however more stable compared to the one observed on surfaces grafted with RGD-C and C-LL37 only. The number of FAs was also decreased compared to surfaces

grafted with RGD-C only.

Topographical nanopatterns, on their side, induced a decrease of cell proliferation compared to surfaces grafted with RGD-C. The other parameters, however, followed the same tendency than the one observed for chemical nanopatterns grafted with RGD-C.

After that, we focused on the differentiation of cells. It appeared that the neuronal differentiation was favored on homogeneous brush and 400 chemical nanopattern grafted with C-LL37/RGD-C. Fluorescence analysis even showed that peptide patterning led to a more pronounced neuronal differentiation. No variation of the osteogenic and adipogenic differentiation was detected between the different surfaces tested.

6.5 Supporting Information

6.5.1 Cell proliferation

In this section, we describe in detail the effect of the nature of the peptide using homogeneous brushes grafted with RGD-C, C-LL37 or C-LL37/RGD-C (Figure 6.35). After 18 hours (Figure 6.35a), the percentage was larger on homogeneous brushes grafted with C-LL37 and C-LL37/RGD-C compared to the glass surface. But no significant difference was detected between the percentage measured for the homogeneous brush grafted with RGD-C and the ones measured for other surfaces grafted with C-LL37 or the mixture or the glass surface. After 48 hours (Figure 6.35b), the proliferation was larger for the homogeneous brush grafted with RGD-C compared to the homogeneous brush grafted with C-LL37/RGD-C. No other significant difference was detected between the percentages measured for the different surfaces. The percentages were statistically different for a given surface between 18 and 48 hours. The lowest proliferation percentage was found on the homogeneous brush grafted with C-LL37/RGD-C.

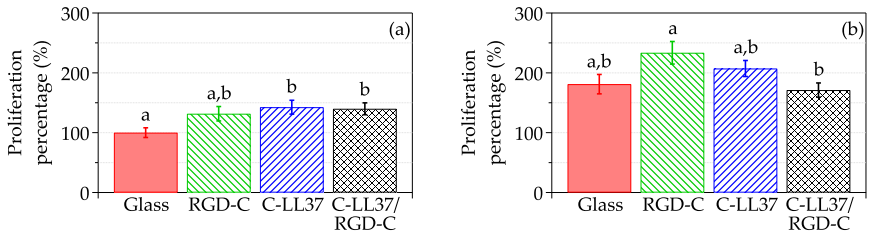

Figure 6.35: Comparison of cell proliferation on homogeneous brushes grafted with different peptides (a) after 18 and (b) 48 hours. Bars with different letters indicate significant difference, p-value < 0.05.

6.5.2 Cell surface area

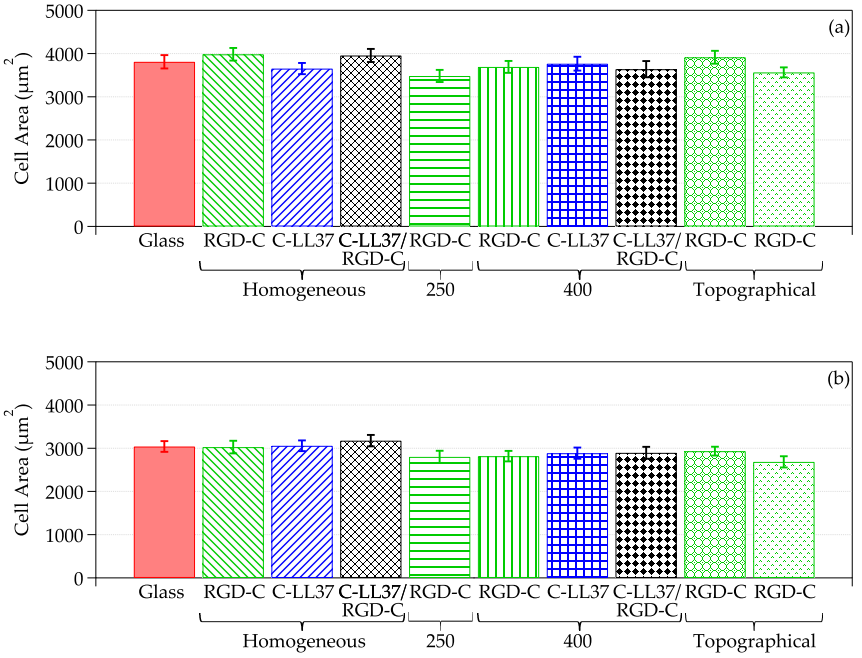

Figure 6.36: Cell surface area measured on different surfaces tested (a) after 18 and (b) 48 hours. No significant differences were detected.

6.5.3 Cellular AR

In this section, we describe in detail the effect of the nature of the peptide using homogeneous brushes grafted with RGD-C, C-LL37 or C-LL37/RGD-C (Figure 6.37). After 18 hours (Figure 6.37a), the AR values were smaller on homogeneous brushes grafted with RGD-C and C-LL37 compared to the glass control surface. No significant difference was detected between the cellular AR measured for homogeneous brush grafted with C-LL37/RGD-C and the other surfaces. After 48 hours (Figure 6.37b), there was no more difference between the ARs of cells measured on the different surfaces. The only cellular AR that increased significantly with the culture time was the one measured for the homogeneous brush grafted with C-LL37. For the other surfaces, no significant variation of AR was detected.

We also studied the effect of the nanotopography. After 18 hours, the glass

surface, the chemical and topographical nanopatterns did not show any difference in cellular ARs (Figure 6.38a). After 48 hours (Figure 6.38b), the cellular AR was smaller on glass surface compared to the 250 chemical nanopattern. No other significant difference was detected in the cellular ARs. When comparing ARs measured for a given surface between 18 and 48 hours, only the 250 chemical nanopattern induced an increase of cellular AR.

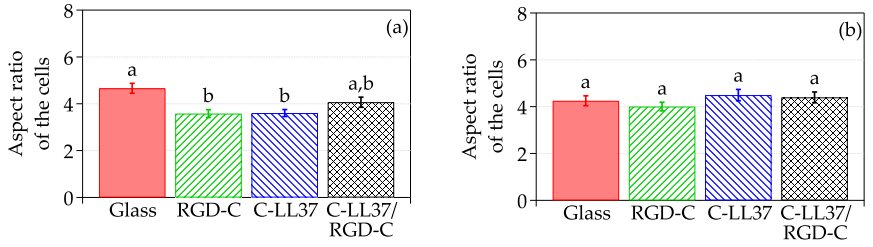

Figure 6.37: Comparison of cellular AR measured on homogeneous brushes grafted with different peptides (a) after 18 and (b) 48 hours. Bars with different letters indicate significant difference, p-value < 0.05.

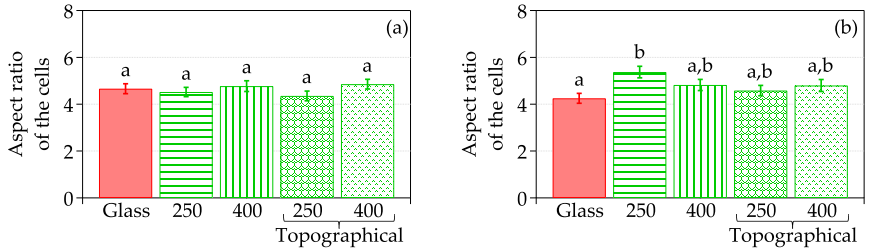

Figure 6.38: Comparison of cellular AR measured on chemical and topographical patterns displaying different dimensions (*i.e.* 250 vs 400) (a) after 18 and (b) 48 hours. Bars with different letters indicate significant difference, p-value < 0.05.

6.5.4 Cell circularity

In this section, we describe in detail the effect of the nature of the peptide using homogeneous brushes grafted with RGD-C, C-LL37 or C-LL37/RGD-C (Figure 6.39). No variation of the circularity was observed between the different surfaces tested on a given time. However, the circularity increased with time for all surfaces.

We also studied the effect of the lateral dimensions of 250 and 400 chemical nanopatterns grafted with RGD-C and compared with a homogeneous brush grafted with RGD-C and a glass surface (Figure 6.40). After 18 hours, no difference in circularity was seen between the different surfaces. After 48 hours, the glass surface showed a circularity significantly higher than the one obtained for the 400 chemical nanopattern. No other difference was detected. In addition, the circularity increased with time for a given surface.

Finally, the nanotopography effect was studied. After 18 hours (Figure 6.41a), the 250 chemical nanopattern showed a smaller value of cell circularity compared to 250 and 400 topographical nanopatterns. No difference of cell circularity was detected for the other surfaces. After 48 hours (Figure 6.41b), the circularity of the glass surface was higher than the one measured for the 400 chemical nanopattern. No other difference was detected between the circularity of cells measured for the different surfaces. The circularity increased with time for all surfaces.

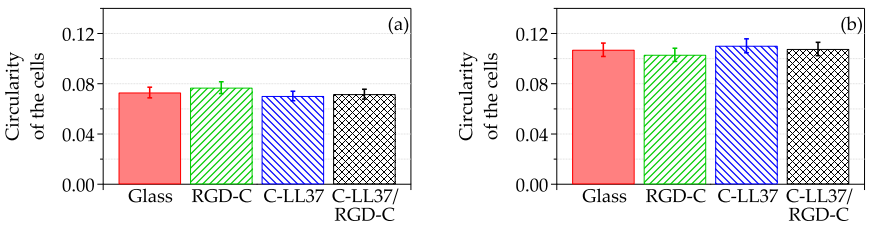

Figure 6.39: Comparison of cell circularity measured on homogeneous brushes grafted with different peptides (a) after 18 and (b) 48 hours. No significant differences were detected.

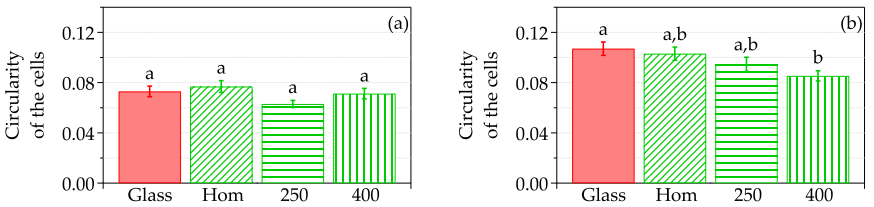

Figure 6.40: Comparison of cell circularity measured on homogeneous brush, 250 and 400 chemical nanopatterns grafted with RGD-C (a) after 18 and (b) 48 hours. Bars with different letters indicate significant difference, p-value < 0.05.

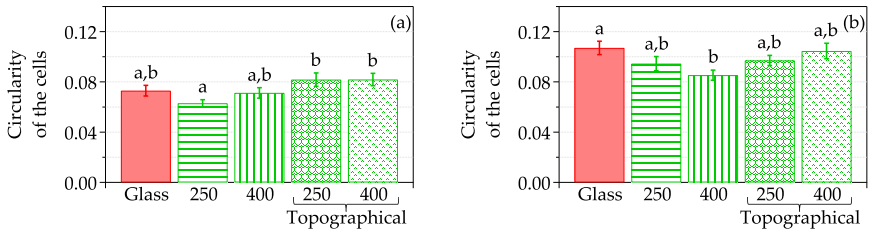

Figure 6.41: Comparison of cell circularity measured on chemical and topographical patterns displaying different dimensions (*i.e.* 250 vs 400) (a) after 18 and (b) 48 hours. Bars with different letters indicate significant difference, p-value < 0.05.

6.5.5 FA number per cell

We examined the influence of the peptide patterning on the FA number per cell. For this, cells cultured on 400 chemical nanopatterns grafted with RGD-C, C-LL37 or C-LL37/RGD-C (Figure 6.42) were analyzed. No difference was detected between the different surfaces. However, the number of FAs decreased with the culture time for 400 chemical nanopatterns grafted with RGD-C and C-LL37.

The influence of the nanotopography on the FA number per cell was also explored (Figure 6.43). After 18 and 48 hours, the number of FAs per cell for the 250 chemical nanopattern was smaller than for the 250 topographical nanopattern. This phenomenon was not seen when comparing 400 chemical and topographical nanopatterns. It is also worth noting that after 18 hours, the number of FAs was higher for 250 topographical nanopattern compared to 400 topographical nanopattern. Moreover, the number of FAs for the glass surface was smaller than the ones on 400 chemical and 250 topographical nanopatterns. The number of FAs per cell decreased with time for 250 chemical and topographical nanopatterns.

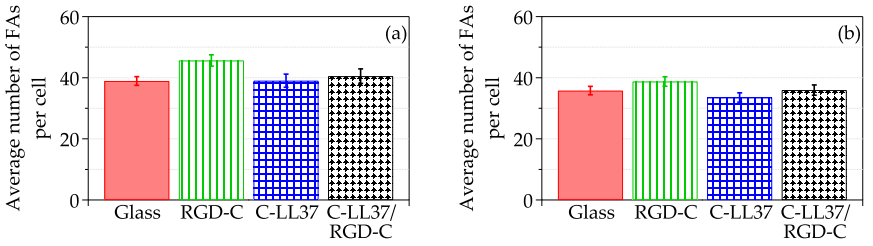

Figure 6.42: Comparison of FA number per cell measured on 400 chemical nanopatterns grafted with different peptides (a) after 18 and (b) 48 hours. No significant differences were detected.

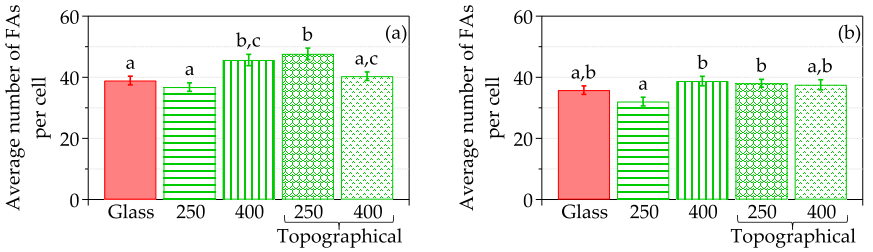

Figure 6.43: Comparison of FA number per cell measured on chemical and topographical patterns displaying different dimensions (*i.e.* 250 vs 400) (a) after 18 and (b) 48 hours. Bars with different letters indicate significant difference, p-value < 0.05.

Chapter 7

Conclusion and perspectives

The design of surfaces able to guide stem cells in a specific lineage while preventing the bacterial colonization is the dual goal to be attained in tissue engineering. To find new strategies to guide cells towards a specific behavior or to prevent bacterial colonization, some researches recently explored the effect of the surface topography, stiffness, biochemistry and the patterning of these surface cues [15, 17, 18]. The influence of micro- and nanotopographical features on bacterial colonization and stem cell development was notably reported. The influence of the surface biochemistry was also studied for both types of cells. However, only chemical patterning at the micrometer scale was considered so far for bacterial cells while the study for mammalian cells focused mainly on the ligand spacing effect.

In this context, we aimed at producing surfaces showing nanometer-sized areas grafted with bioactive molecules targeting specifically bacteria or mammalian stem cells in order to control the mammalian cell processes occurring during the cell culture while limiting the potential colonization of the surface by bacteria. The use of nanopatterned surfaces is interesting since the ECM present in the *in vivo* environment, is structured at the nanometer scale [1] and consequently the presentation of ligands reflects this pattern. To control the development of both bacterial and mammalian cells, we grafted antimicrobial (AMPs) and bioadhesive peptides on the nanopatterned surfaces. This allows to

meet the dual goal of providing antimicrobial surfaces while keeping cell friendly properties. The reason to use AMPs to confer antibacterial properties to the material surface instead of antibiotic molecules frequently used, is to avoid the potential emergence of multi-resisting bacteria. The use of adhesive ligand, on its side, is required to control the adhesion and the development of stem cells.

We systematically studied the influence of the nature and the structure of these biofunctional surfaces on *E. coli* proliferation and viability as well as on SCAP morphology, growth and differentiation.

Our first achievement was to successfully fabricate and characterize chemically nanopatterned surfaces showing both bactericidal and/or bioadhesive peptides. To this end, we first optimized the synthesis of hydrophilic polymer brushes showing functional groups on their side-chains which were later grafted by bioactive molecules. These brushes were polymerized by Si-ATRP to obtain dense layers of defined thickness and composition. They were chosen instead of SAMs because of the greater amount of functional groups present on their chains. We first investigated the kinetics of growth and the composition of four different hydrophilic polymer brushes by ellipsometry and FTIR, respectively: P(HEMA), P(MAA), P(HEMA-*co*-MAA) and P(HOEGMA). The polymerization of MAA was rather quick but not well-controlled due to the presence of carboxylic groups interfering with the polymerization catalyst. On the contrary, the polymerizations of HEMA and HOEGMA leading to brushes showing pendent hydroxyl groups, were well-controlled but quite slow. The synthesis of P(HEMA-*co*-MAA) copolymer was also explored in order to obtain a brush bearing both carboxylic and hydroxyl groups. However, the composition of this last brush could not be precisely defined and varied as a function of the polymerization time. Given these results, we selected the P(HOEGMA) brush as a hydrophilic functionnal platform to produce bioactive layers in a second step.

Then, we focused on the biofunctionalization of the P(HOEGMA) brush. For this, we studied the grafting of a cell-adhesive peptide (RGD-C) and two antimicrobial peptides (C-LL37 or MAG-C) bearing a cysteine residue (C) on one of their extremity. The idea was to obtain brushes showing bioactive properties towards stem cells and/or bactericidal properties. These peptides were grafted on the polymer brush via an heterolinker reacting first with hydroxyl pendent groups of the brush and then with the thiol group located in a cysteine residue at one extremity of the peptide. This grafting approach was used to ensure a

specific orientation of the peptide molecules immobilized onto the brush which facilitates their interaction with bacteria and mammalian cells. We were able to evidence the successful grafting of labelled peptides on the P(HOEGMA) brushes, by using fluorescence microscopy. Then we quantitatively assessed the grafting degree of P(HOEGMA) brushes grafted by performing quantitative XPS measurements. Finally, by using ellipsometry measurements performed before and after peptide grafting, we were able to determine the peptide density onto the surfaces. In the case of co-grafting, we proved that the composition of the grafted brushes was directly related to the composition of the peptide solution used for the grafting. Moreover, we showed that the peptide density on the different surfaces was about 10^6 peptides/μm^2 which is much larger than the density obtained on SAMs [105,148,246] but similar to the density obtained by Harris et al. on P(MAA) [241]

The last fabrication step to produce bioactive nanopatterned surfaces, was to pattern the brushes at the nanometer scale. For this, NIL technique was combined with Si-ATRP and peptide grafting. The AFM characterization of the nanopatterned surfaces evidenced their well-defined geometry. The produced patterns showed bioactive lines of 78 or 200 nm width distributed in a non-adhesive PEG background with a period of 250 and 400 nm, respectively. The nanopatterned lines were grafted with RGD-C, MAG-C, C-LL37 or C-LL37/RGD-C (50:50). Topographical nanopatterns covered with a P(HOEGMA) brush grafted with RGD-C and showing 50 nm-depth nanogrooves and flat surfaces homogeneously covered with P(HOEGMA) brushes grafted with the different peptides were also produced for the comparison.

Our second achievement was to prove that homogeneous and nanopatterned platforms grafted with antibacterial peptides can be used as antibacterial surfaces even though some improvements need to be carried out.

First, we studied the bactericidal activity of MAG-C and C-LL37 in solution. We showed that C-LL37 was more efficient against *E. coli* than MAG-C. Moreover, the MIC values we obtained were much larger than the ones reported in the litterature for MAG and LL37 [147,250,251]. However, these results need to be taken with caution since the conditions used to perform these tests were not optimized. Then, the bacterial colonization and the bactericidal activity were studied on biofunctionalized surfaces. When MAG-C was grafted on the surfaces, it did not retain its bactericidal activity and induced the highest bacterial coverage among the surfaces tested. This lack of bactericidal activity

of the polymer brush grafted with MAG-C was in contradiction with the results obtained previously by others and was attributed to the different nature and structure of the P(HOEGMA) brush used in this study compared to the other platforms used by the others [64, 148]. On the contrary, brushes grafted with C-LL37 retained bactericidal activity and induced a lower bacterial coverage. However, the percentage of bacterial viability measured on these surfaces was quite large compared to the ones reported in the litterature for SAMs grafted with LL37 [105]. On its side, polymer brush grafted with RGD-C peptide allowed bacteria to adhere non-specifically on the surface without killing them, as expected. This is in agreement with various studies previously reported (see reference [256] for instance). Finally, we were able to prove that the brushes grafted with a C-LL37/RGD-C (50:50) mixture retained bactericidal activity and adhesive properties of C-LL37 and RGD-C, respectively. This highlights the fact that antibacterial peptides can be co-grafted with a peptide targeting mammalian cell without reduction of the antibacterial properties of the surface. It is also worth noting that no specific arrangement of bacteria were noticed on nanopatterned surfaces. Altogether, these results are encouraging since they prove that we can produce surfaces retaining their bactericidal efficiency even when the bactericidal peptides are patterned and when they are co-grafted with a non-bactericidal peptide. However, the bactericidal activity obtained were quite low compared to previous studies showing the immobilization of antibacterial peptides onto various organic layers [64, 105, 148]. This was mainly attributed to the structure and the superhydrophilic nature of the P(HOEGMA) used to produce the bioactive platforms.

Considering the results obtained during the antibacterial tests, a set of surfaces (*i.e.* a 250 chemical nanopattern grafted with RGD-C, 400 chemical nanopatterns grafted with RGD-C, C-LL37 or C-LL37/RGD-C, 250 and 400 topographical nanopatterns grafted with RGD-C and homogneous brushes grafted with RGD-C, C-LL37 or C-LL37/RGD-C) was selected to investigate the SCAP behaviors.

Our third achievement was to assess that chemical nanopatterns affect stem cell behaviors.

To prove that, we seeded SCAPs on previously selected surfaces and let them grew for 18 or 48 hours. The mammalian cell morphology, proliferation and differentiation were systematically inspected as a function of the nature and the design of the surface to conclude about the effect of the surface char-

acteristics on stem cells. First, the proliferation was lowered on homogeneous and nanopatterned surfaces grafted with C-LL37/RGD-C as well as on both topographical nanopatterns compared to surfaces grafted with RGD-C. We assumed these results were due to the co-presentation of the peptides which is less selective than the presentation of the RGD-C peptide only and to the physical barrier caused by the nanotopography, respectively. Second, we were able to show that, while the chemical and topographical nanopatterning of the peptides allowed the alignment and elongation of SCAPs whatever the nature of the peptide, the nature of the peptide grafted induced a significant effect on the cellular morphology. Indeed, on chemical nanopatterns grafted with C-LL37/RGD-C, the cellular aspect ratio was smaller in the first few hours, the number of protrusions and the number of FAs were smaller and the alignment according to the nanopattern direction was more stable compared to chemical nanopatterns grafted with RGD-C only. We hypothesized that the alignment phenomenon was due to an "orientation selection" mechanism, even though this phenomenon was originally explained for nanotopographical surfaces. Moreover, the difference observed on surfaces grafted with different peptides are due to the non-specific characteristics of C-LL37 towards cells. Third, the total amount of RGD-C peptide available, varying with the lateral dimensions of the patterns, influenced the initial amount of cells adhered on the surfaces, the amount of FAs produced and also the alignment of cells along the pattern direction. Indeed, when the amount of peptide is smaller, such as for 250 chemical nanopatterns grafted with RGD-C compared to 400 chemical nanopatterns and homogeneous brushes grafted with RGD-C, the amount of adhered cells and the number of FAs decreased, while the alignment of cells was more easily preserved. Finally, it was observed that neuronal differentiation was favored on homogeneous and chemical nanopatterns grafted with C-LL37/RGD-C compared to homogeneous and nanopatterned brushes grafted with RGD-C. We attempted to link the proliferation and morphological features of cells to the neuronal differentiation. Indeed, cells showing the lower proliferation and an elongated morphology tended to orient in the neuronal lineage.

These results prove that the cell behaviors are influenced by the patterning of the bioactive peptides immobilized on the surface as well as their nature and the dimensions of the nanopatterned lines.

These results are encouraging to produce nanopatterns displaying bioactive molecules targeting specifically bacterial and mammalian cells. However, some

further researches need to be done to better understand the phenomenons revealed by our study and to improve the design of the bioactive surfaces.

First, the behavior of cells cultured onto biofunctionalized surfaces for longer time should be studied to eventually detect the expression of specific markers due to cell-cell interactions.

Second, the presentation of antimicrobial and adhesive peptides could be done on different lines (or other motif geometries) of patterned surfaces. This geometrical separation of both peptides on the same surface would allow to optimize the size and the geometry of the two different bioactive regions for a better control of the activity towards both cell types. To achieve this, it should be necessary to develop nanopatterned platforms showing different reactive chemical groups located at specific positions onto the surface. In a second step, the different chemical groups should react with two different (or more) bioactive compounds according to selective bioconjugation routes. However, the fabrication of such platforms remains quite complex.

Third, the systematic variation of the pattern geometry, meaning the shape, the size and the interdistance between the features, should be investigated to define the optimal pattern characteristics to trigger the behaviors of both bacteria and mammalian cells. In particular, it would be interesting to see under which percentage of adhesive area cells would not adhere and above which percentage of adhesive area, they would lose their alignment with the nanopattern direction. This would help us to understand more deeply the effect of the density and distribution of immobilized peptides on the cell adhesion as well as to study the orientation selection phenomenon taking place and leading to proliferation and/or differentiation of cells via the modification of transduction signals. These experiments could be performed by using NIL molds of various geometries to fabricate the patterns.

Fourth, other bioactive molecules such as growth factors or quorum sensing inhibitors could be grafted on the surfaces in order to guide cells towards a specific lineage while enhancing antimicrobial properties of the surfaces. These experiments would define the most efficient bioactive compounds that should be grafted on the surface to control the behavior of both mammalian and bacterial cells.

Fifth, in order to improve the efficiency of the grafted AMPs, other polymer brushes could be used as anchoring platform to see the effect of the nature and structure of the polymer layer on the surface bioactivity. It would be also

interesting to check if the decrease of antibacterial activity on our surfaces was due (or not) to the steric hindrance resulting from densely packed superhydrophilic polymer chains which could hinder the proper interaction between the antimicrobial peptide and the cellular membrane. For instance, copolymer brushes with side-chains of different lengths or grafted onto the surface with a lower density could be used to influence the overall packing density of the polymer chains.

Sixth, the nanopatterning of bioactive molecules should certainly be combined with other surface parameters. Indeed, the ECM in which cells live *in vivo*, presents a 3D architecture exhibiting both topographical and biochemical cues. Therefore, it would be interesting to see if any synergistic effects can occur by combining topographical and chemical patterning at the micro- and/or nanoscale.

Finally, in the future, the co-seeding of bacteria and stem cells in *in vitro* conditions should be considered to study simultaneously the effect of the surfaces on both cell types. However, this cannot be performed until some surfaces with optimized properties preventing efficiently bacterial colonization while promoting desired behaviors of cells are designed.

Bibliography

[1] K. von der Mark, J. Park, S. Bauer, and P. Schmuki. Nanoscale engineering of biomimetic surfaces: cues from the extracellular matrix. *Cell Tissue Res.*, 339(1):131–53, 2010.

[2] C. Zhao, A. Tan, G. Pastorin, and H. K. Ho. Nanomaterial scaffolds for stem cell proliferation and differentiation in tissue engineering. *Biotechnol. Adv.*, 31(5):654–68, 2013.

[3] J.N. Kearny. Clinical evaluation of skin substitutes. *Burns*, 27:545–551, 2001.

[4] Letizia Ventrelli, Leonardo Ricotti, Arianna Menciassi, Barbara Mazzolai, and Virgilio Mattoli. Nanoscaffolds for guided cardiac repair: The new therapeutic challenge of regenerative medicine. *Journal of Nanomaterials*, 2013:16, 2013.

[5] James D. Bryers. Medical biofilms. *Biotechnol. Bioeng.*, 100(1):1–18, 2008.

[6] F. Costa, I. F. Carvalho, R. C. Montelaro, P. Gomes, and M. C. Martins. Covalent immobilization of antimicrobial peptides (amps) onto biomaterial surfaces. *Acta Biomater.*, 7(4):1431–40, 2011.

[7] U. Römling and C. Balsalobre. Biofilm infections, their resilience to therapy and innovative treatment strategies. *J. Intern. Med.*, 272(6):541–561, 2012.

[8] Lydie Ploux, Arnaud Ponche, and Karine Anselme. Bacteria/material interfaces: Role of the material and cell wall properties. *J. Adhes. Sci. Technol.*, 24(13-14):2165–2201, 2010.

[9] Bruno M. C. Martins and James C. W. Locke. Microbial individuality: how single-cell heterogeneity enables population level strategies. *Curr. Opin. Microbiol.*, 24:104–112, 2015.

[10] Philip S. Stewart and Michael J. Franklin. Physiological heterogeneity in biofilms. *Nat. Rev. Microbiol.*, 6(3):199–210, 2008.

[11] C. Lee Ventola. The antibiotic resistance crisis: Part 1: Causes and threats. *Pharmacy and Therapeutics*, 40(4):277–283, 2015.

[12] Dennis E. Discher, David J. Mooney, and Peter W. Zandstra. Growth factors, matrices, and forces combine and control stem cells. *Science*, 324(5935):1673–1677, 2009.

[13] P. C. Dave P. Dingal and Dennis E. Discher. Combining insoluble and soluble factors to steer stem cell fate. *Nat. Mater.*, 13(6):532–537, 2014.

[14] Keith A. Blackwood, Nathalie Bock, Tim R. Dargaville, and Maria Ann Woodruff. Scaffolds for growth factor delivery as applied to bone tissue engineering. *International Journal of Polymer Science*, 2012:1–25, 2012.

[15] L. Bacakova, E. Filova, M. Parizek, T. Ruml, and V. Svorcik. Modulation of cell adhesion, proliferation and differentiation on materials designed for body implants. *Biotechnol. Adv.*, 29(6):739–67, 2011.

[16] Cloutier M., Mantovani D., and Rosei F. Antibacterial coatings: Challenges, perspectives, and opportunities. *Trends Biotechnol.*, 33(11):637–652, 2015.

[17] Jingxin Meng, Pengchao Zhang, and Shutao Wang. Recent progress in biointerfaces with controlled bacterial adhesion by using chemical and physical methods. *Chemistry – An Asian Journal*, pages n/a–n/a, 2014.

[18] O. Seddiki, C. Harnagea, L. Levesque, D. Mantovani, and F. Rosei. Evidence of antibacterial activity on titanium surfaces through nanotextures. *Appl. Surf. Sci.*, 308(0):275–284, 2014.

[19] Angus Hucknall, Srinath Rangarajan, and Ashutosh Chilkoti. In pursuit of zero: Polymer brushes that resist the adsorption of proteins. *Adv. Mater.*, 21(23):2441–2446, 2009.

[20] Mario Salwiczek, Yue Qu, James Gardiner, Richard A. Strugnell, Trevor Lithgow, Keith M. McLean, and Helmut Thissen. Emerging rules for effective antimicrobial coatings. *Trends Biotechnol.*, 32(2):82–90, 2014.

[21] N. Saha, C. Monge, V. Dulong, C. Picart, and K. Glinel. Influence of polyelectrolyte film stiffness on bacterial growth. *Biomacromolecules*, 14(2):520–8, 2013.

[22] Xiang Yao, Rong Peng, and Jiandong Ding. Cell–material interactions revealed via material techniques of surface patterning. *Adv. Mater.*, 25(37):5257–5286, 2013.

[23] Wataru Aoki and Mitsuyoshi Ueda. Characterization of antimicrobial peptides toward the development of novel antibiotics. *Pharmaceuticals*, 6(8):1055–1081, 2013.

[24] M. Elizabeth Welch and Christopher K. Ober. Responsive and patterned polymer brushes. *J. Polym. Sci., Part B: Polym. Phys.*, 51(20):1457–1472, 2013.

[25] B. Zhao and W. J. Brittain. Polymer brushes: surface-immobilized macromolecules. *Prog. Polym. Sci.*, 25(5):677–710, 2000.

[26] Myungwoong Kim, Samantha Schmitt, Jonathan Choi, John Krutty, and Padma Gopalan. From self-assembled monolayers to coatings: Advances in the synthesis and nanobio applications of polymer brushes. *Polymers*, 7(7):1346–1378, 2015.

[27] Jenny E. Raynor, Jeffrey R. Capadona, David M. Collard, Timothy A. Petrie, and Andrés J. García. Polymer brushes and self-assembled monolayers: Versatile platforms to control cell adhesion to biomaterials (review). *Biointerphases*, 4(2):FA3–FA16, 2009.

[28] Casey J. Galvin and Jan Genzer. Applications of surface-grafted macromolecules derived from post-polymerization modification reactions. *Prog. Polym. Sci.*, 37(7):871–906, 2012.

[29] Jian Qiu, Bernadette Charleux, and Krzysztof Matyjaszewski. Controlled/living radical polymerization in aqueous media: homogeneous and heterogeneous systems. *Prog. Polym. Sci.*, 26(10):2083–2134, 2001.

[30] Krzysztof Matyjaszewski and Jianhui Xia. Atom transfer radical polymerization. *Chem. Rev.*, 101(9):2921–2990, 2001.

[31] Wade A. Braunecker and Krzysztof Matyjaszewski. Controlled/living radical polymerization: Features, developments, and perspectives. *Prog. Polym. Sci.*, 32(1):93–146, 2007.

[32] Piotr Król and Paweł Chmielarz. Recent advances in atrp methods in relation to the synthesis of copolymer coating materials. *Prog. Org. Coat.*, 77(5):913–948, 2014.

[33] Krzysztof Matyjaszewski. Atom transfer radical polymerization: From mechanisms to applications. *Isr. J. Chem.*, 52(3/4):206–220, 2012.

[34] Timothy E. Patten and Krzysztof Matyjaszewski. Atom transfer radical polymerization and the synthesis of polymeric materials. *Adv. Mater.*, 10(12):901–915, 1998.

[35] Sreepadaraj Karanam, Han Goossens, Bert Klumperman, and Piet Lemstra. "controlled" synthesis and characterization of model methyl methacrylate/tert-butyl methacrylate triblock copolymers via atrp. *Macromolecules*, 36(9):3051–3060, 2003.

[36] Nan Cheng, Omar Azzaroni, Sergio Moya, and Wilhelm T. S. Huck. The effect of [cui]/[cuii] ratio on the kinetics and conformation of polyelectrolyte brushes by atom transfer radical polymerization. *Macromol. Rapid Commun.*, 27(19):1632–1636, 2006.

[37] Sreepadaraj Karanam, Goossens, Bert Klumperman, and Lemstra. "controlled" synthesis and characterization of high molecular weight methyl methacrylate/tert-butyl methacrylate diblock copolymers via atrp. *Macromolecules*, 36(22):8304–8311, 2003.

[38] Ajaya Kumar Nanda and Krzysztof Matyjaszewski. Effect of [bpy]/[cu(i)] ratio, solvent, counterion, and alkyl bromides on the activation rate constants in atom transfer radical polymerization. *Macromolecules*, 36(3):599–604, 2003.

[39] Wenxi Huang, Jong-Bum Kim, Merlin L. Bruening, and Gregory L. Baker. Functionalization of surfaces by water-accelerated atom-transfer radical

polymerization of hydroxyethyl methacrylate and subsequent derivatization. *Macromolecules*, 35(4):1175–1179, 2002.

[40] Greg T. Hermanson. *Bioconjugate techniques*. Academic Press, San Diego, 1 edition, 1996.

[41] Ian W. Hamley. Peg–peptide conjugates. *Biomacromolecules*, 15(5):1543–1559, 2014.

[42] Kemal Arda Günay, Patrick Theato, and Harm-Anton Klok. Standing on the shoulders of hermann staudinger: Post-polymerization modification from past to present. *J. Polym. Sci., Part A: Polym. Chem.*, 51(1):1–28, 2013.

[43] Marc A. Gauthier, Matthew I Gibson, and Ham-Anton Klok. Synthesis of functional polymers by post-polymerization modification. *Angew. Chem. Int. Ed.*, 48(1):48–58, 2009.

[44] Joy Romulus, John T. Henssler, and Marcus Weck. Postpolymerization modification of block copolymers. *Macromolecules*, 47(16):5437–5449, 2014.

[45] Qian Yu, Yanxia Zhang, Hongwei Wang, John Brash, and Hong Chen. Anti-fouling bioactive surfaces. *Acta Biomater.*, 7(4):1550–1557, 2011.

[46] J. M. Goddard and J. H. Hotchkiss. Polymer surface modification for the attachment of bioactive compounds. *Prog. Polym. Sci.*, 32(7):698–725, 2007.

[47] K. Anselme, P. Davidson, A. M. Popa, M. Giazzon, M. Liley, and L. Ploux. The interaction of cells and bacteria with surfaces structured at the nanometre scale. *Acta Biomater.*, 6(10):3824–46, 2010.

[48] Karen L. Christman, Vanessa D. Enriquez-Rios, and Heather D. Maynard. Nanopatterning proteins and peptides. *Soft Matter*, 2(11):928–939, 2006.

[49] V. N. Truskett and M. P. Watts. Trends in imprint lithography for biological applications. *Trends Biotechnol.*, 24(7):312–7, 2006.

[50] Paula M. Mendes, Chun L. Yeung, and Jon A. Preece. Bio-nanopatterning of surfaces. *Nanoscale Res. Lett.*, 2(8):373–384, 2007.

[51] Qian Yu, Linnea K. Ista, Renpeng Gu, Stefan Zauscher, and Gabriel P. Lopez. Nanopatterned polymer brushes: conformation, fabrication and applications. *Nanoscale*, 8:680–700, 2016.

[52] LJ. Arsov, M. Ramasubramanian, and Popov B.N. *Ellipsometry.* John Wiley & Sons, Inc., 2012.

[53] J.S. Gaffney, N.A. Marley, and D.E. Jones. *Fourier Transform Infrared (FTIR) Spectroscopy.* John Wiley & Sons, Inc., 2012.

[54] D.N. Leonarrd, G.W. Chandler, and S. Seraphin. *Scanning Electron Microscopy.* John Wiley & Sons, Inc., 2012.

[55] H. Hölscher, J. Falter, and A. Schirmeisen. *Atomic Force Microscopy and Spectroscopy.* John Wiley & Sons, Inc., 2012.

[56] David Alsteens, Audrey Beaussart, Sofiane El-Kirat-Chatel, Ruby May A. Sullan, and Yves F. Dufrêne. Atomic force microscopy: A new look at pathogens. *PLoS Pathog.*, 9(9):1–3, 2013.

[57] Philippe Herman, Sofiane El-Kirat-Chatel, Audrey Beaussart, Joan A. Geoghegan, Thomas Vanzieleghem, Timothy J. Foster, Pascal Hols, Jacques Mahillon, and Yves F. Dufrêne. Forces driving the attachment of staphylococcus epidermidis to fibrinogen-coated surfaces. *Langmuir*, 29(42):13018–13022, 2013.

[58] Audrey Beaussart, Sofiane El-Kirat-Chatel, Philippe Herman, David Alsteens, Jacques Mahillon, Pascal Hols, and Yves F Dufrêne. Single-cell force spectroscopy of probiotic bacteria. *Biophys. J.*, 104(9):1886–1892, 2013.

[59] David Alsteens, Audrey Beaussart, Sylvie Derclaye, Sofiane El-Kirat-Chatel, Hye Rim Park, Peter N. Lipke, and Yves F. Dufrêne. Single-cell force spectroscopy of als-mediated fungal adhesion. *Anal. Methods*, 5:3657–3662, 2013.

[60] Audrey Beaussart, Philippe Herman, Sofiane El Kirat Chatel, Peter N. Lipke, Sona Kucharikova, Patrick Van Dijck, and Yves F. Dufrene. Single-cell force spectroscopy of the medically important staphylococcus epidermidis-candida albicans interaction. *Nanoscale*, 2013.

[61] J.J. Weimer. *X-ray photoelectron spectroscopy.* John Wiley & Sons, Inc., 2012.

[62] O.D. Lavrentovich. *Confocal Fluorescence Microscopy.* John Wiley & Sons, Inc., 2012.

[63] John-Bruce D. Green, Timothy Fulghum, and Mark A. Nordhaus. A review of immobilized antimicrobial agents and methods for testing. *Biointerphases*, 6(4):MR13–MR28, 2011.

[64] Karine Glinel, Alain M. Jonas, Thierry Jouenne, Jérôme Leprince, Ludovic Galas, and Wilhelm T. S. Huck. Antibacterial and antifouling polymer brushes incorporating antimicrobial peptide. *Bioconjugate Chem.*, 20(1):71–77, 2009.

[65] Joanna Ziemska, Aleksandra Rajnisz, and Jolanta Solecka. New perspectives on antibacterial drug research. *Central European Journal of Biology*, 8(10):943–957, 2013.

[66] I. Armentano, C. R. Arciola, E. Fortunati, D. Ferrari, S. Mattioli, C. F. Amoroso, J. Rizzo, J. M. Kenny, M. Imbriani, and L. Visai. The interaction of bacteria with engineered nanostructured polymeric materials: a review. *ScientificWorldJournal*, 2014:410423, 2014.

[67] Indrani Banerjee, Ravindra C. Pangule, and Ravi S. Kane. Antifouling coatings: Recent developments in the design of surfaces that prevent fouling by proteins, bacteria, and marine organisms. *Adv. Mater.*, 23(6):690–718, 2011.

[68] Davide Campoccia, Lucio Montanaro, and Carla Renata Arciola. A review of the biomaterials technologies for infection-resistant surfaces. *Biomaterials*, 34(34):8533–8554, 2013.

[69] W. C. Schofield and J. P. Badyal. A substrate-independent approach for bactericidal surfaces. *ACS Appl. Mater. Interfaces*, 1(12):2763–7, 2009.

[70] Chun-Jen Huang, Yen-Sheng Chen, and Yung Chang. Counterion-activated nanoactuator: Reversibly switchable killing/releasing bacteria on polycation brushes. *ACS Appl. Mater. Interfaces*, 7:2415–2423, 2015.

[71] Jenny A. Lichter, Krystyn J. Van Vliet, and Michael F. Rubner. Design of antibacterial surfaces and interfaces: Polyelectrolyte multilayers as a multifunctional platform. *Macromolecules*, 42(22):8573–8586, 2009.

[72] M. Pollini, F. Paladini, M. Catalano, A. Taurino, A. Licciulli, A. Maffezzoli, and A. Sannino. Antibacterial coatings on haemodialysis catheters by photochemical deposition of silver nanoparticles. *J. Mater. Sci.: Mater. Med.*, 22(9):2005–2012, 2011.

[73] Hao Cheng, Yong Li, Kaifu Huo, Biao Gao, and Wei Xiong. Long-lasting in vivo and in vitro antibacterial ability of nanostructured titania coating incorporated with silver nanoparticles. *Journal of Biomedical Materials Research Part A*, 102(10):3488–3499, 2014.

[74] Olaya Rendueles, Jeffrey B. Kaplan, and Jean-Marc Ghigo. Antibiofilm polysaccharides. *Environ. Microbiol.*, 15(2):334–346, 2013.

[75] Zhilong Shi, K. G. Neoh, E. T. Kang, Chyekhoon Poh, and W. Wang. Bacterial adhesion and osteoblast function on titanium with surface-grafted chitosan and immobilized rgd peptide. *Journal of Biomedical Materials Research Part A*, 86A(4):865–872, 2008.

[76] K. Glinel, P. Thebault, V. Humblot, C. M. Pradier, and T. Jouenne. Antibacterial surfaces developed from bio-inspired approaches. *Acta Biomater.*, 8(5):1670–84, 2012.

[77] Diana Alves and Maria Olívia Pereira. Mini-review: Antimicrobial peptides and enzymes as promising candidates to functionalize biomaterial surfaces. *Biofouling*, 30(4):483–499, 2014.

[78] Q. Yu, L. K. Ista, and G. P. Lopez. Nanopatterned antimicrobial enzymatic surfaces combining biocidal and fouling release properties. *Nanoscale*, 6(9):4750–7, 2014.

[79] Michigan State University Board of Trustees. Antimicrobial resistance learning site. *https://amrls.cvm.msu.edu/microbiology/bacterial-resistance-strategies*, consulted on 01/09/2017.

[80] W. Kohnen. Development of a long-lasting ventricular catheter impregnated with a combination of antibiotics. *Biomaterials*, 24(26):4865–4869, 2003.

[81] Erkki Ruoslahti. Rgd and other recognition sequences for integrins. *Annual Review of Cell and Developmental Biology Developmental Biology*, 12(1):697, 1996.

[82] Yoshikazu Takada, Xiaojing Ye, and Scott Simon. The integrins. *Genome Biol.*, 8, 2007.

[83] Y. Lei, M. Remy, C. Labrugere, and M. C. Durrieu. Peptide immobilization on polyethylene terephthalate surfaces to study specific endothelial cell adhesion, spreading and migration. *J Mater Sci Mater Med*, 23(11):2761–72, 2012.

[84] Jon A. Rowley and David J. Mooney. Alginate type and rgd density control myoblast phenotype. *J. Biomed. Mater. Res.*, 60(2):217–223, 2002.

[85] Ulrich Hersel, Claudia Dahmen, and Horst Kessler. Rgd modified polymers: biomaterials for stimulated cell adhesion and beyond. *Biomaterials*, 24(24):4385–4415, 2003.

[86] Maria B. Rahmany and Mark Van Dyke. Biomimetic approaches to modulate cellular adhesion in biomaterials: A review. *Acta Biomater.*, 9(3):5431–5437, 2013.

[87] Xiaoshuai Ren, Yuanzi Wu, Yan Cheng, Hongwei Ma, and Shicheng Wei. Fibronectin and bone morphogenetic protein-2-decorated poly(oegma-r-hema) brushes promote osseointegration of titanium surfaces. *Langmuir*, 27(19):12069–12073, 2011.

[88] Omar F. Zouani, Lila Rami, Yifeng Lei, and Marie-Christine Durrieu. Insights into the osteoblast precursor differentiation towards mature osteoblasts induced by continuous bmp-2 signaling. *Biology Open*, 2013.

[89] Yunfei Wang, Peifeng Liu, Yourong Duan, Xia Yin, Qi Wang, Xiaofei Liu, Xinran Wang, Jinhua Zhou, Wenwen Wang, Lihua Qiu, and Wen Di. Specific cell targeting with aprpg conjugated peg–plga nanoparticles for treating ovarian cancer. *Biomaterials*, 35(3):983–992, 2014.

[90] Leonard T. Nguyen, Evan F. Haney, and Hans J. Vogel. The expanding scope of antimicrobial peptide structures and their modes of action. *Trends Biotechnol.*, 29(9):464–472, 2011.

[91] K. A. Brogden. Antimicrobial peptides: pore formers or metabolic inhibitors in bacteria? *Nat. Rev. Microbiol.*, 3(3):238–50, 2005.

[92] Nobuaki Ozeki, Poonam Jethanandani, Hiroshi Nakamura, Barry L. Ziober, and Randall H. Kramer. Modulation of satellite cell adhesion and motility following bmp2-induced differentiation to osteoblast lineage. *Biochem. Biophys. Res. Commun.*, 353(1):54–59, 2007.

[93] K. Lim, R. R. Chua, R. Saravanan, A. Basu, B. Mishra, P. A. Tambyah, B. Ho, and S. S. Leong. Immobilization studies of an engineered arginine-tryptophan-rich peptide on a silicone surface with antimicrobial and antibiofilm activity. *ACS Appl. Mater. Interfaces*, 5(13):6412–22, 2013.

[94] Andreas Peschel and Hans-Georg Sahl. The co-evolution of host cationic antimicrobial peptides and microbial resistance. *Nat. Rev. Microbiol.*, 4(7):529–536, 2006.

[95] Jéssica M. Nascimento, Octávio L. Franco, Maria D. L. Oliveira, and César A. S. Andrade. Evaluation of magainin i interactions with lipid membranes: An optical and electrochemical study. *Chem. Phys. Lipids*, 165(5):537–544, 2012.

[96] S D Hauschka and I R Konigsberg. The influence of collagen on the development of muscle clones. *Proceedings of the National Academy of Sciences*, 55(1):119–126, 1966.

[97] Ulrich H. N. Dürr, U. S. Sudheendra, and Ayyalusamy Ramamoorthy. Ll-37, the only human member of the cathelicidin family of antimicrobial peptides. *Biochimica et Biophysica Acta (BBA) - Biomembranes*, 1758(9):1408–1425, 2006.

[98] Dieter Vandamme, Bart Landuyt, Walter Luyten, and Liliane Schoofs. A comprehensive summary of ll-37, the factotum human cathelicidin peptide. *Cell. Immunol.*, 280(1):22–35, 2012.

[99] Kem A. Sochacki, Kenneth J. Barns, Robert Bucki, and James C. Weisshaar. Real-time attack on single escherichia coli cells by the human antimicrobial peptide ll-37. *Proc. Natl. Acad. Sci. U.S.A.*, 108(16):6347–6348, 2011.

[100] Chang-Chun Lee, Yen Sun, Shuo Qian, and Huey W Huang. Transmembrane pores formed by human antimicrobial peptide ll-37. *Biophys. J.*, 100(7):1688–1696, 2011.

[101] M. Sobczak, C. Debek, E. Oledzka, and R. Kozlowski. Polymeric systems of antimicrobial peptides–strategies and potential applications. *Molecules*, 18(11):14122–37, 2013.

[102] Peng-Yuan Wang, Helmut Thissen, and Wei-Bor Tsai. The roles of rgd and grooved topography in the adhesion, morphology, and differentiation of c2c12 skeletal myoblasts. *Biotechnol. Bioeng.*, 109(8):2104–2115, 2012.

[103] Q. Wang, E. Uzunoglu, Y. Wu, and M. Libera. Self-assembled poly(ethylene glycol)-co-acrylic acid microgels to inhibit bacterial colonization of synthetic surfaces. *ACS Appl. Mater. Interfaces*, 4(5):2498–506, 2012.

[104] Mojtaba Bagheri, Michael Beyermann, and Margitta Dathe. Mode of action of cationic antimicrobial peptides defines the tethering position and the efficacy of biocidal surfaces. *Bioconjugate Chem.*, 23(1):66–74, 2012.

[105] Matthias Gabriel, Kamran Nazmi, Enno C. Veerman, Arie V. Nieuw Amerongen, and Andrej Zentner. Preparation of ll-37-grafted titanium surfaces with bactericidal activity. *Bioconjugate Chem.*, 17(2):548–550, 2006.

[106] Ting Cao, Anfeng Wang, Xuemei Liang, Haiying Tang, Gregory W. Auner, Steven O. Salley, and K. Y. Simon Ng. Investigation of spacer length effect on immobilized escherichia coli pili-antibody molecular recognition by afm. *Biotechnol. Bioeng.*, 98(6):1109–1122, 2007.

[107] Marwan Abdallah, Corinne Benoliel, Djamel Drider, Pascal Dhulster, and Nour-Eddine Chihib. Biofilm formation and persistence on abiotic surfaces in the context of food and medical environments. *Arch. Microbiol.*, 196(7):453–472, 2014.

[108] Ece Karatan and Paula Watnick. Signals, regulatory networks, and materials that build and break bacterial biofilms. *Microbiol. Mol. Biol. Rev.*, 73(2):310–347, 2009.

[109] Huan Gu and Dacheng Ren. Materials and surface engineering to control bacterial adhesion and biofilm formation: A review of recent advances. *Frontiers of Chemical Science and Engineering*, 8(1):20–33, 2014.

[110] Loris Rizzello, Roberto Cingolani, and Pier Paolo Pompa. Nanotechnology tools for antibacterial materials. *Nanomedicine*, 8(5):807–821, 2013.

[111] Rodney M. Donlan and J. William Costerton. Biofilms: Survival mechanisms of clinically relevant microorganisms. *Clin. Microbiol. Rev.*, 15(2):167–193, 2002.

[112] Christophe Beloin, Agnès Roux, and Jean-Marc Ghigo. Escherichia coli biofilms. *Curr. Top. Microbiol. Immunol.*, 322:249–289, 2008.

[113] Roberto Kolter and E. Peter Greenberg. Microbial sciences: The superficial life of microbes. *Nature*, 441(7091):300–302, 2006.

[114] Katsutoshi Hori and Shinya Matsumoto. Bacterial adhesion: From mechanism to control. *Biochem. Eng. J.*, 48(3):424–434, 2010.

[115] Alexandre Persat, Carey D Nadell, Minyoung Kevin Kim, Francois Ingremeau, Albert Siryaporn, Knut Drescher, Ned S Wingreen, Bonnie L Bassler, Zemer Gitai, and Howard A Stone. The mechanical world of bacteria. *Cell*, 161(5):988–997, 2015.

[116] Malte Hermansson. The dlvo theory in microbial adhesion. *Colloids Surf., B*, 14(1):105–119, 1999.

[117] Shen Jie-Pan and Chou Chia-Fu. Morphological plasticity of bacteria–open questions. *Biomicrofluidics*, 10(3):1–17, 2016.

[118] Shuyu Hou, Huan Gu, Cassandra Smith, and Dacheng Ren. Microtopographic patterns affect escherichia coli biofilm formation on poly(dimethylsiloxane) surfaces. *Langmuir*, 27(6):2686–2691, 2011.

[119] Shuyu Hou, Erik A. Burton, Karen A. Simon, Dustin Blodgett, Yan-Yeung Luk, and Dacheng Ren. Inhibition of escherichia coli biofilm formation by self-assembled monolayers of functional alkanethiols on gold. *Appl. Environ. Microbiol.*, 73(13):4300–4307, 2007.

[120] R. L. Taylor, J. Verran, G. C. Lees, and A. J. P. Ward. The influence of substratum topography on bacterial adhesion to polymethyl methacrylate. *J. Mater. Sci.: Mater. Med.*, 9:17–22, 1998.

[121] Ajay Vikram Singh, Varun Vyas, Rajendra Patil, Vimal Sharma, Pasquale Emanuele Scopelliti, Gero Bongiorno, Alessandro Podestà, Cristina Lenardi, Wasudev Namdev Gade, and Paolo Milani. Quantitative characterization of the influence of the nanoscale morphology of nanostructured surfaces on bacterial adhesion and biofilm formation. *PLoS One*, 6(9):1–12, 2011.

[122] L. C. Hsu, J. Fang, D. A. Borca-Tasciuc, R. W. Worobo, and C. I. Moraru. Effect of micro- and nanoscale topography on the adhesion of bacterial cells to solid surfaces. *Appl. Environ. Microbiol.*, 79(8):2703–12, 2013.

[123] Loris Rizzello, Barbara Sorce, Stefania Sabella, Giuseppe Vecchio, Antonio Galeone, Virgilio Brunetti, Roberto Cingolani, and Pier Paolo Pompa. Impact of nanoscale topography on genomics and proteomics of adherent bacteria. *ACS Nano*, 5(3):1865–1876, 2011.

[124] P. Decuzzi and M. Ferrari. Modulating cellular adhesion through nanotopography. *Biomaterials*, 31(1):173–9, 2010.

[125] Guimel M. Kappell, James P. Grover, and Thomas H. Chrzanowski. Micro-scale surface-patterning influences biofilm formation. *Electron. J. Biotechnol.*, 12(3), 2009.

[126] A. I. Hochbaum and J. Aizenberg. Bacteria pattern spontaneously on periodic nanostructure arrays. *Nano Lett.*, 10(9):3717–21, 2010.

[127] C. Díaz, A. Miñán, P. L. Schilardi, and M. Fernández Lorenzo de Mele. Synergistic antimicrobial effect against early biofilm formation: micropatterned surface plus antibiotic treatment. *Int. J. Antimicrob. Agents*, 40(3):221–226, 2012.

[128] C. Diaz, P. L. Schilardi, R. C. Salvarezza, and F. Lorenzo de Mele. Nano microscale order affects the early stages of biofilm formation. *Langmuir*, 23(22):11206–11210, 2007.

[129] L. C. Xu and C. A. Siedlecki. Submicron-textured biomaterial surface reduces staphylococcal bacterial adhesion and biofilm formation. *Acta Biomater.*, 8(1):72–81, 2012.

[130] Carolina Díaz, María Cecilia Cortizo, Patricia Laura Schilardi, Sandra Gabriela Gómez de Saravia, and Mónica Alicia Fernández Lorenzo de Mele. Influence of the nano-micro structure of the surface on bacterial adhesion. *Mater. Res.*, 10:11–14, 2007.

[131] H. Ma, J. Hyun, P. Stiller, and A. Chilkoti. "non-fouling" oligo(ethylene glycol)- functionalized polymer brushes synthesized by surface-initiated atom transfer radical polymerization. *Adv. Mater.*, 16(4):338–341, 2004.

[132] T. Merian and J. M. Goddard. Advances in nonfouling materials: perspectives for the food industry. *J. Agric. Food. Chem.*, 60(12):2943–57, 2012.

[133] J. Hasan, R. J. Crawford, and E. P. Ivanova. Antibacterial surfaces: the quest for a new generation of biomaterials. *Trends Biotechnol.*, 31(5):295–304, 2013.

[134] Sascha Herrwerth, Wolfgang Eck, Sven Reinhardt, and Michael Grunze. Factors that determine the protein resistance of oligoether self-assembled monolayers - internal hydrophilicity, terminal hydrophilicity, and lateral packing density. *J. Am. Chem. Soc.*, 125(31):9359–9366, 2003.

[135] Linnea K. Ista, Hongyou Fan, Oswald Baca, and Gabriel P. López. Attachment of bacteria to model solid surfaces: oligo(ethylene glycol) surfaces inhibit bacterial attachment. *FEMS Microbiol. Lett.*, 142(1):59–63, 1996.

[136] Stefano Tugulu and Harm-Anton Klok. Stability and nonfouling properties of poly(poly(ethylene glycol) methacrylate) brushes under cell culture conditions. *Biomacromolecules*, 9(3):906–912, 2008.

[137] Peter Krsko, Jeffrey B. Kaplan, and Matthew Libera. Spatially controlled bacterial adhesion using surface-patterned poly(ethylene glycol) hydrogels. *Acta Biomater.*, 5(2):589–596, 2009.

[138] B. Pidhatika, J. Moller, E. M. Benetti, R. Konradi, E. Rakhmatullina, A. Muhlebach, R. Zimmermann, C. Werner, V. Vogel, and M. Textor. The

role of the interplay between polymer architecture and bacterial surface properties on the microbial adhesion to polyoxazoline-based ultrathin films. *Biomaterials*, 31(36):9462–72, 2010.

[139] Bidhari Pidhatika, Mathias Rodenstein, Yin Chen, Ekaterina Rakhmatullina, Andreas Mühlebach, Canet Acikgöz, Marcus Textor, and Rupert Konradi. Comparative stability studies of poly(2-methyl-2-oxazoline) and poly(ethylene glycol) brush coatings. *Biointerphases*, 7(1):1, 2012.

[140] Chang-Hyung Choi, Ji-Hye Lee, Taek-Sung Hwang, Chang-Soo Lee, Yun-Gon Kim, Yung-Hun Yang, and Kang Moo Huh. Preparation of bacteria microarray using selective patterning of polyelectrolyte multilayer and poly(ethylene glycol)-poly(lactide) diblock copolymer. *Macromol. Res.*, 18(3):254–259, Mar 2010.

[141] Ieong Wong, Xianting Ding, Chunsheng Wu, and Chih-Ming Ho. Accurate and effective live bacteria microarray patterning on thick polycationic polymer layers co-patterned with hmds. *RSC Adv.*, 2:7673–7676, 2012.

[142] Q. Yu, J. Cho, P. Shivapooja, L. K. Ista, and G. P. Lopez. Nanopatterned smart polymer surfaces for controlled attachment, killing, and release of bacteria. *ACS Appl. Mater. Interfaces*, 5(19):9295–304, 2013.

[143] Jenny A. Lichter, M. Todd Thompson, Maricela Delgadillo, Takehiro Nishikawa, Michael F. Rubner, and Krystyn J. Van Vliet. Substrata mechanical stiffness can regulate adhesion of viable bacteria. *Biomacromolecules*, 9(6):1571–1578, 2008. PMID: 18452330.

[144] Sergey Pogodin, Jafar Hasan, Vladimir A Baulin, Hayden K Webb, Vi Khanh Truong, The Hong Phong Nguyen, Veselin Boshkovikj, Christopher J Fluke, Gregory S Watson, Jolanta A Watson, Russell J Crawford, and Elena P Ivanova. Biophysical model of bacterial cell interactions with nanopatterned cicada wing surfaces. *Biophys. J.*, 104(4):835–840, 2013.

[145] Elena P. Ivanova, Jafar Hasan, Hayden K. Webb, Gediminas Gervinskas, Saulius Juodkazis, Vi Khanh Truong, Alex H. F. Wu, Robert N. Lamb, Vladimir A. Baulin, Gregory S. Watson, Jolanta A. Watson, David E. Mainwaring, and Russell J. Crawford. Bactericidal activity of black silicon. *Nat. Commun.*, 4, 2013.

[146] Thomas Blin, Viswas Purohit, Jérôme Leprince, Thierry Jouenne, and Karine Glinel. Bactericidal microparticles decorated by an antimicrobial peptide for the easy disinfection of sensitive aqueous solutions. *Biomacromolecules*, 12(4):1259–1264, 2011.

[147] Margaret E. Cassin, Andrew J. Ford, Sophia M. Orbach, Scott E. Saverot, and Padmavathy Rajagopalan. The design of antimicrobial ll37-modified collagen-hyaluronic acid detachable multilayers. *Acta Biomater.*, 40:119–129, 2016.

[148] Vincent Humblot, Jean-Fabrice Yala, Pascal Thebault, Kada Boukerma, Arnaud Héquet, Jean-Marc Berjeaud, and Claire-Marie Pradier. The antibacterial activity of magainin i immobilized onto mixed thiols self-assembled monolayers. *Biomaterials*, 30(21):3503–3512, 2009.

[149] Jessie Peyre, Vincent Humblot, Christophe Méthivier, Jean-Marc Berjeaud, and Claire-Marie Pradier. Co-grafting of antiadhesive and antimicrobial agents onto uv-micropatterned copper surfaces. *Colloids Surf., B*, 2015.

[150] Gang Cheng, Hong Xue, Zheng Zhang, Shengfu Chen, and Shaoyi Jiang. A switchable biocompatible polymer surface with self-sterilizing and non-fouling capabilities. *Angew. Chem. Int. Ed.*, 47(46):8831–8834, 2008.

[151] Job Ubbink and Prisca Schär-Zammaretti. Colloidal properties and specific interactions of bacterial surfaces. *Curr. Opin. Colloid Interface Sci.*, 12(4–5):263–270, 2007.

[152] Leslie A. Pratt and Roberto Kolter. Genetic analysis of escherichia coli biofilm formation: roles of flagella, motility, chemotaxis and type i pili. *Mol. Microbiol.*, 30(2):285–293, 1998.

[153] Rob Van Houdt and Chris W. Michiels. Role of bacterial cell surface structures in escherichia coli biofilm formation. *Res. Microbiol.*, 156(5):626–633, 2005.

[154] Mathai Mammen, Seok-Ki Choi, and George M. Whitesides. Polyvalent interactions in biological systems: Implications for design and use of multivalent ligands and inhibitors. *Angew. Chem. Int. Ed.*, 37(20):2754–2794, 1998.

[155] Yubing Sun, Christopher S. Chen, and Jianping Fu. Forcing stem cells to behave: A biophysical perspective of the cellular microenvironment. *Annu. Rev. Biophys.*, 41(1):519–542, 2012.

[156] NathanJ Sniadecki, RaviA Desai, SamiAlom Ruiz, and ChristopherS Chen. Nanotechnology for cell–substrate interactions. *Ann. Biomed. Eng.*, 34(1):59–74, 2006.

[157] Ajay Vikram Singh, Rajendra Patil, Dipalee K. Thombre, and W. N. Gade. Micro-nanopatterning as tool to study the role of physicochemical properties on cell–surface interactions. *Journal of Biomedical Materials Research Part A*, 101(10):3019–3032, 2013.

[158] Junmin Lee, Amr A. Abdeen, Douglas Zhang, and Kristopher A. Kilian. Directing stem cell fate on hydrogel substrates by controlling cell geometry, matrix mechanics and adhesion ligand composition. *Biomaterials*, 34(33):8140–8148, 2013.

[159] E. Lamers, te J. Riet, M. Domanski, R. Luttge, C. G. Figdro, J.G.E. Gardeniers, X.F. Walboomers, and J.A. Jansen. Dynamic cell adhesion and migration on nanoscale grooved substrates. *Eur. Cell. Mater.*, 23:182–194, 2012.

[160] Matthew J. Dalby, Nikolaj Gadegaard, and Richard O. C. Oreffo. Harnessing nanotopography and integrin-matrix interactions to influence stem cell fate. *Nat. Mater.*, 13(6):558–569, 2014.

[161] Stefania Di Cio and J.E. Gautrot. Cell sensing of physical properties at the nanoscale: Mechanisms and control of cell adhesion and phenotype. *Acta Biomater.*, 30:26–48, 2016.

[162] Makato Nagano, Daisuke Hoshino, Naohiko Koshikawa, Toshifumi Akizawa, and Motoharu Seiki. Turnover of focal adhesions and cancer cell migration. *International Journal of Cell Biology*, 2012, 2012.

[163] Alberto Elosegui-Artola, Elsa Bazellières, Michael D. Allen, Ion Andreu, Roger Oria, Raimon Sunyer, Jennifer J. Gomm, John F. Marshall, J. Louise Jones, Xavier Trepat, and Pere Roca-Cusachs. Rigidity sensing and adaptation through regulation of integrin types. *Nat. Mater.*, 13(6):631–637, 2014.

[164] Margaret L. Gardel, Ian C. Schneider, Yvonne Aratyn-Schaus, and Clare M. Waterman. Mechanical integration of actin and adhesion dynamics in cell migration. *Annu. Rev. Cell Dev. Biol.*, 26(1):315–333, 2010.

[165] Jose R. Garcia and Andres J. Garcia. Cellular mechanotransduction: Sensing rigidity. *Nat. Mater.*, 13(6):539–540, 2014.

[166] William L. Murphy, Todd C. McDevitt, and Adam J. Engler. Materials as stem cell regulators. *Nat. Mater.*, 13(6):547–557, 2014.

[167] Paula M. Mendes. Cellular nanotechnology: making biological interfaces smarter. *Chem. Soc. Rev.*, 42(24):9207–9218, 2013.

[168] Xueli Liu and Shutao Wang. Three-dimensional nano-biointerface as a new platform for guiding cell fate. *Chem. Soc. Rev.*, 43(8):2385–2401, 2014.

[169] Kristopher A. Kilian, Branimir Bugarija, Bruce T. Lahn, and Milan Mrksich. Geometric cues for directing the differentiation of mesenchymal stem cells. *Proceedings of the National Academy of Sciences*, 107(11):4872–4877, 2010.

[170] Shreyas Shah, Aniruddh Solanki, and Ki-Bum Lee. Nanotechnology-based approaches for guiding neural regeneration. *Acc. Chem. Res.*, 49(1):17–26, 2016.

[171] Hassan Rashidi, Jing Yang, and Kevin M. Shakesheff. Surface engineering of synthetic polymer materials for tissue engineering and regenerative medicine applications. *Biomater. Sci.*, 2(10):1318–1331, 2014.

[172] HoJun Jeon, Carl G. Simon, and GeunHyung Kim. A mini-review: Cell response to microscale, nanoscale, and hierarchical patterning of surface structure. *Journal of Biomedical Materials Research Part B: Applied Biomaterials*, 102(7):1580–1594, 2014.

[173] Florent Badique, Dimitar R. Stamov, Patricia M. Davidson, Matthieu Veuillet, Günter Reiter, Jean-Noël Freund, Clemens M. Franz, and Karine Anselme. Directing nuclear deformation on micropillared surfaces by substrate geometry and cytoskeleton organization. *Biomaterials*, 34(12):2991–3001, 2013.

[174] Hervé Guillou, Adeline Depraz-Depland, Emmanuelle Planus, Benoit Vianay, Jacques Chaussy, Alexei Grichine, Corinne Albigès-Rizo, and Marc R. Block. Lamellipodia nucleation by filopodia depends on integrin occupancy and downstream rac1 signaling. *Exp. Cell. Res.*, 314(3):478–488, 2008.

[175] M. J. Dalby, S. Childs, M. O. Riehle, H. J. H. Johnstone, S. Affrossman, and A. S. G. Curtis. Fibroblast reaction to island topography: changes in cytoskeleton and morphology with time. *Biomaterials*, 24(6):927–935, 2003.

[176] Xiongtu Zhou, Jian Shi, Jie Hu, and Yong Chen. Cells cultured on microgrooves with or without surface coating: Correlation between cell alignment, spreading and local membrane deformation. *Materials Science and Engineering: C*, 33(2):855–863, 2013.

[177] Kilsoo Jeon, Hyun-Jik Oh, Hyejin Lim, Jung-Hyun Kim, Duk Hyun Lee, Eung-Ryoung Lee, Bae Ho Park, and Ssang-Goo Cho. Self-renewal of embryonic stem cells through culture on nanopattern polydimethylsiloxane substrate. *Biomaterials*, 33(21):5206–5220, 2012.

[178] Daekyeong Bae, Sung-Hwan Moon, Bo Gi Park, Soon-Jung Park, Taekhee Jung, Jung Suk Kim, Kyu Back Lee, and Hyung-Min Chung. Nanotopographical control for maintaining undifferentiated human embryonic stem cell colonies in feeder free conditions. *Biomaterials*, 35(3):916–928, 2014.

[179] T. L. Downing, J. Soto, C. Morez, T. Houssin, A. Fritz, F. Yuan, J. Chu, S. Patel, D. V. Schaffer, and S. Li. Biophysical regulation of epigenetic state and cell reprogramming. *Nat. Mater.*, 12(12):1154–62, 2013.

[180] Joseph L. Charest, Andrés J. García, and William P. King. Myoblast alignment and differentiation on cell culture substrates with microscale topography and model chemistries. *Biomaterials*, 28(13):2202–2210, 2007.

[181] O. F. Zouani, C. Chanseau, B. Brouillaud, R. Bareille, F. Deliane, M. P. Foulc, A. Mehdi, and M. C. Durrieu. Altered nanofeature size dictates stem cell differentiation. *J. Cell Sci.*, 125(Pt 5):1217–24, 2012.

[182] Marco Arnold, Elisabetta Ada Cavalcanti-Adam, Roman Glass, Jacques Blümmel, Wolfgang Eck, Martin Kantlehner, Horst Kessler, and Joachim P.

Spatz. Activation of integrin function by nanopatterned adhesive interfaces. *ChemPhysChem*, 5(3):383–388, 2004.

[183] Elisabetta A. Cavalcanti-Adam, Alexandre Micoulet, Jacques Blümmel, Jörg Auernheimer, Horst Kessler, and Joachim P. Spatz. Lateral spacing of integrin ligands influences cell spreading and focal adhesion assembly. *Eur. J. Cell Biol.*, 85(3–4):219–224, 2006.

[184] E. A. Cavalcanti-Adam, T. Volberg, A. Micoulet, H. Kessler, B. Geiger, and J. P. Spatz. Cell spreading and focal adhesion dynamics are regulated by spacing of integrin ligands. *Biophys. J.*, 92(8):2964–74, 2007.

[185] N. D Gallant, K. A Lavery, E. J Amis, and M. L Becker. Universal gradient substrates for click biofunctionalization. *Adv. Mater.*, 19(7):965–969, 2007.

[186] Dirk Lehnert, Bernhard Wehrle-Haller, Christian David, Ulrich Weiland, Christoph Ballestrem, Beat A. Imhof, and Martin Bastmeyer. Cell behaviour on micropatterned substrata: limits of extracellular matrix geometry for spreading and adhesion. *J. Cell Sci.*, 117(1):41–52, 2004.

[187] Sviatlana Kalinina, Hartmut Gliemann, Mónica López-García, Andre Petershans, Jörg Auernheimer, Thomas Schimmel, Michael Bruns, Alexandra Schambony, Horst Kessler, and Doris Wedlich. Isothiocyanate-functionalized rgd peptides for tailoring cell-adhesive surface patterns. *Biomaterials*, 29(20):3004–3013, 2008.

[188] C. A. Hoesli, A. Garnier, P. M. Juneau, P. Chevallier, C. Duchesne, and G. Laroche. A fluorophore-tagged rgd peptide to control endothelial cell adhesion to micropatterned surfaces. *Biomaterials*, 35(3):879–90, 2014.

[189] Nathan D. Gallant, Kristin E. Michael, and Andrés J. García. Cell adhesion strengthening: Contributions of adhesive area, integrin binding, and focal adhesion assembly. *Mol. Biol. Cell*, 16(9):4329–4340, 2005.

[190] Stefano Tugulu, Paolo Silacci, Nikolaos Stergiopulos, and Harm-Anton Klok. Rgd-functionalized polymer brushes as substrates for the integrin specific adhesion of human umbilical vein endothelial cells. *Biomaterials*, 28(16):2536–2546, 2007.

[191] Diego Pallarola, Alexander Bochen, Heike Boehm, Florian Rechenmacher, Tariq R. Sobahi, Joachim P. Spatz, and Horst Kessler. Interface immobilization chemistry of crgd-based peptides regulates integrin mediated cell adhesion. *Adv. Funct. Mater.*, 24(7):943–956, 2014.

[192] Melba Navarro, Edmondo M. Benetti, Szczepan Zapotoczny, Josep A. Planell, and G. Julius Vancso. Buried, covalently attached rgd peptide motifs in poly(methacrylic acid) brush layers: The effect of brush structure on cell adhesion. *Langmuir*, 24(19):10996–11002, 2008.

[193] Chen Zhang, Sogol Hekmatfer, and Nancy W. Karuri. A comparative study of polyethylene glycol hydrogels derivatized with the rgd peptide and the cell-binding domain of fibronectin. *Journal of Biomedical Materials Research Part A*, 102(1):170–179, 2014.

[194] Solenne Desseaux and Harm-Anton Klok. Fibroblast adhesion on ecm-derived peptide modified poly(2-hydroxyethyl methacrylate) brushes: Ligand co-presentation and 3d-localization. *Biomaterials*, 44:24–35, 2015.

[195] G. Maheshwari, G. Brown, D.A. Lauffenburger, A. Wells, and L.G. Griffith. Cell adhesion and motility depend on nanoscale rgd clustering. *J. Cell Sci.*, 113(10):1677–1686, 2000.

[196] Marco Arnold, Vera C. Hirschfeld-Warneken, Theobald Lohmüller, Patrick Heil, Jacques Blümmel, Elisabetta A. Cavalcanti-Adam, Mónica López-García, Paul Walther, Horst Kessler, Benjamin Geiger, and Joachim P. Spatz. Induction of cell polarization and migration by a gradient of nanoscale variations in adhesive ligand spacing. *Nano Lett.*, 8(7):2063–2069, 2008.

[197] Michael A. Lan, Charles A. Gersbach, Kristin E. Michael, Benjamin G. Keselowsky, and Andrés J. García. Myoblast proliferation and differentiation on fibronectin-coated self assembled monolayers presenting different surface chemistries. *Biomaterials*, 26(22):4523–4531, 2005.

[198] Kristopher A. Kilian and Milan Mrksich. Directing stem cell fate by controlling the affinity and density of ligand–receptor interactions at the biomaterials interface. *Angew. Chem. Int. Ed.*, 51(20):4891–4895, 2012.

[199] Zhe A. Cheng, Omar F. Zouani, Karine Glinel, Alain M. Jonas, and Marie-Christine Durrieu. Bioactive chemical nanopatterns impact human mesenchymal stem cell fate. *Nano Lett.*, 13(8):3923–3929, 2013.

[200] X. Wang, S. Li, C. Yan, P. Liu, and J. Ding. Fabrication of rgd micro/nanopattern and corresponding study of stem cell differentiation. *Nano Lett.*, 15(3):1457–67, 2015.

[201] Xuan Wang, Ce Yan, Kai Ye, Yao He, Zhenhua Li, and Jiandong Ding. Effect of rgd nanospacing on differentiation of stem cells. *Biomaterials*, 34(12):2865–2874, 2013.

[202] Claire Monge, Naresh Saha, Thomas Boudou, Cuauhtemoc Pózos-Vásquez, Virginie Dulong, Karine Glinel, and Catherine Picart. Rigidity-patterned polyelectrolyte films to control myoblast cell adhesion and spatial organization. *Adv. Funct. Mater.*, 23(27):3432–3442, 2013.

[203] Jeroen Eyckmans and Christopher S. Chen. Stem cell differentiation: Sticky mechanical memory. *Nat. Mater.*, 13(6):542–543, 2014.

[204] Cuauhtémoc Pozos Vázquez, Thomas Boudou, Virginie Dulong, Claire Nicolas, Catherine Picart, and Karine Glinel. Variation of polyelectrolyte film stiffness by photo-cross-linking: A new way to control cell adhesion. *Langmuir*, 25(6):3556–3563, 2009.

[205] Elisa Migliorini, Jelena Ban, Gianluca Grenci, Laura Andolfi, Alessandro Pozzato, Massimo Tormen, Vincent Torre, and Marco Lazzarino. Nanomechanics controls neuronal precursors adhesion and differentiation. *Biotechnol. Bioeng.*, 110(8):2301–2310, 2013.

[206] Gt-J. Huang, S. Gronthos, and S. Shi. Mesenchymal stem cells derived from dental tissues vs. those from other sources: Their biology and role in regenerative medicine. *J. Dent. Res.*, 88(9):792–806, 2009.

[207] Wataru Sonoyama, Yi Liu, Takayoshi Yamaza, Rocky S. Tuan, Songlin Wang, Songtao Shi, and George T. J. Huang. Characterization of apical papilla and its residing stem cells from human immature permanent teeth –a pilot study. *J. Endod.*, 34(2):166–171, 2008.

[208] S. Ferraris, A. Venturello, M. Miola, A. Cochis, L. Rimondini, and S. Spriano. Antibacterial and bioactive nanostructured titanium surfaces for bone integration. *Appl. Surf. Sci.*, 311(0):279–291, 2014.

[209] Abdulaziz E Daw, Hizbullah AA Kazi, John S Colombo, Wendy G Rowe, David W Williams, Rachel J Waddington, David W Thomas, and Ryan Moseley. Differential cellular and microbial responses to nano-/micron-scale titanium surface roughness induced by hydrogen peroxide treatment. *J. Biomater. Appl.*, 28(1):144–160, 2013.

[210] S. Svensson, M. Forsberg, M. Hulander, F. Vazirisani, A. Palmquist, J. Lausmaa, P. Thomsen, and M. Trobos. Role of nanostructured gold surfaces on monocyte activation and staphylococcus epidermidis biofilm formation. *Int J Nanomedicine*, 9:775–94, 2014.

[211] Poh-Hui Chua, Koon-Gee Neoh, En-Tang Kang, and Wilson Wang. Surface functionalization of titanium with hyaluronic acid/chitosan polyelectrolyte multilayers and rgd for promoting osteoblast functions and inhibiting bacterial adhesion. *Biomaterials*, 29(10):1412–1421, 2008.

[212] Agnieszka K. Muszanska, Edward T. J. Rochford, Agnieszka Gruszka, Andreas A. Bastian, Henk J. Busscher, Willem Norde, Henny C. van der Mei, and Andreas Herrmann. Antiadhesive polymer brush coating functionalized with antimicrobial and rgd peptides to reduce biofilm formation and enhance tissue integration. *Biomacromolecules*, 15(6):2019–2026, 2014.

[213] Tao He, Z. L. Shi, Ning Fang, K. G. Neoh, E. T. Kang, and Vincent Chan. The effect of adhesive ligands on bacterial and fibroblast adhesions to surfaces. *Biomaterials*, 30(3):317–326, 2009.

[214] Sarah J. Dexter, Richard G. Pearson, Martyn C. Davies, Miguel Cámara, and Kevin M. Shakesheff. A comparison of the adhesion of mammalian cells and staphylococcus epidermidis on fibronectin-modified polymer surfaces. *J. Biomed. Mater. Res.*, 56(2):222–227, 2001.

[215] Yi Wang, Guruprakash Subbiahdoss, Jan Swartjes, Henny C. van der Mei, Henk J. Busscher, and Matthew Libera. Length-scale mediated differential adhesion of mammalian cells and microbes. *Adv. Funct. Mater.*, 21(20):3916–3923, 2011.

[216] Nikos Kehagias. Nanofabrication: Nanoimprint lithography. *http://www.unizar.es/nanolito/pdf/ponencias_jaca/Nanofabrication_NIL.pdf*, consulted on 05/02/2017.

[217] Gang Cheng, Hong Xue, Guozhu Li, and Shaoyi Jiang. Integrated antimicrobial and nonfouling hydrogels to inhibit the growth of planktonic bacterial cells and keep the surface clean. *Langmuir*, 26(13):10425–10428, 2010.

[218] Emanuele Ostuni, Robert G. Chapman, R. Erik Holmlin, Shuichi Takayama, and George M. Whitesides. A survey of structure−property relationships of surfaces that resist the adsorption of protein. *Langmuir*, 17(18):5605–5620, 2001.

[219] C. Chollet, C. Chanseau, B. Brouillaud, and M. C. Durrieu. Rgd peptides grafting onto poly(ethylene terephthalate) with well controlled densities. *Biomol. Eng.*, 24(5):477–82, 2007.

[220] Dimitriya Bozukova, Christophe Pagnoulle, Marie-Claire De Pauw-Gillet, Nadia Ruth, Robert Jérôme, and Christine Jérôme. Imparting antifouling properties of poly(2-hydroxyethyl methacrylate) hydrogels by grafting poly(oligoethylene glycol methyl ether acrylate). *Langmuir*, 24(13):6649–6658, 2008.

[221] Amit Y. Sankhe, Scott M. Husson, and S. Michael Kilbey. Effect of catalyst deactivation on polymerization of electrolytes by surface-confined atom transfer radical polymerization in aqueous solutions. *Macromolecules*, 39(4):1376–1383, 2006.

[222] Amit Y. Sankhe, Scott M. Husson, and S. Michael Kilbey. Direct polymerization of surface-tethered polyelectrolyte layers in aqueous solution via surface-confined atom transfer radical polymerization. *J. Polym. Sci., Part A: Polym. Chem.*, 45(4):566–575, 2007.

[223] Stefano Tugulu, Raphaël Barbey, Marc Harms, Marc Fricke, Dirk Volkmer, Antonella Rossi, and Harm-Anton Klok. Synthesis of poly(methacrylic acid) brushes via surface-initiated atom transfer radical polymerization of sodium methacrylate and their use as substrates for the mineralization of calcium carbonate. *Macromolecules*, 40(2):168–177, 2007.

[224] Xavier Laloyaux, Bertrand Mathy, Bernard Nysten, and Alain M. Jonas. Bidimensional response maps of adaptive thermo- and ph-responsive polymer brushes. *Macromolecules*, 43(18):7744–7751, 2010.

[225] Marc Husseman, Eva E. Malmström, Molly McNamara, Mathew Mate, David Mecerreyes, Didier G. Benoit, James L. Hedrick, Paul Mansky, E. Huang, Thomas P. Russell, and Craig J. Hawker. Controlled synthesis of polymer brushes by "living" free radical polymerization techniques. *Macromolecules*, 32(5):1424–1431, 1999.

[226] Alain M. Jonas, Karine Glinel, Ron Oren, Bernard Nysten, and Wilhelm T. S. Huck. Thermo-responsive polymer brushes with tunable collapse temperatures in the physiological range. *Macromolecules*, 40(13):4403–4405, 2007.

[227] Edward D.. Palik. *Handbook of optical constants of solids*. Academic press, Orlando (Fla.), 1 edition, 1985-1991.

[228] D. Van Krevelen. *Properties of Polymers: Correlations with Chemical Structure*. Elsevier, Amsterdam, 1 edition, 1972.

[229] Nicolay V. Tsarevsky, Tomislav Pintauer, and Krzysztof Matyjaszewski. Deactivation efficiency and degree of control over polymerization in atrp in protic solvents. *Macromolecules*, 37(26):9768–9778, 2004.

[230] E. J. Ashford, V. Naldi, R. O'Dell, N. C. Billingham, and S. P. Armes. First example of the atom transfer radical polymerisation of an acidic monomer: direct synthesis of methacrylic acid copolymers in aqueous media. *Chem. Commun.*, 0(14):1285–1286, 1999.

[231] Parul Jain, Jinhua Dai, Gregory L. Baker, and Merlin L. Bruening. Rapid synthesis of functional polymer brushes by surface-initiated atom transfer radical polymerization of an acidic monomer. *Macromolecules*, 41(22):8413–8417, 2008.

[232] Krzysztof Matyjaszewski, Yoshiki Nakagawa, and Christina B. Jasieczek. Polymerization of n-butyl acrylate by atom transfer radical polymerization. remarkable effect of ethylene carbonate and other solvents. *Macromolecules*, 31(5):1535–1541, 1998.

[233] Daniel Gromadzki, Petr Štěpánek, and Ričardas Makuška. Synthesis of densely grafted copolymers with tert-butyl methacrylate/2-(dimethylamino ethyl) methacrylate side chains as precursors for brush polyelectrolytes and polyampholytes. *Mater. Chem. Phys.*, 137(3):709–715, 2013.

[234] Hideharu Mori and Axel H. E. Müller. New polymeric architectures with (meth)acrylic acid segments. *Prog. Polym. Sci.*, 28(10):1403–1439, 2003.

[235] Kelly A. Davis and Krzysztof Matyjaszewski. Atom transfer radical polymerization of tert-butyl acrylate and preparation of block copolymers. *Macromolecules*, 33(11):4039–4047, 2000.

[236] Su Lu, Qu-Li Fan, Shao-Yong Liu, Soo-Jin Chua, and Wei Huang. Synthesis of conjugated-acidic block copolymers by atom transfer radical polymerization. *Macromolecules*, 35(27):9875–9881, 2002.

[237] Sagheer A. Onaizi and Susanna S. J. Leong. Tethering antimicrobial peptides: Current status and potential challenges. *Biotechnol. Adv.*, 29(1):67–74, 2011.

[238] Christopher Barner-Kowollik and Andrew J. Inglis. Has click chemistry lead to a paradigm shift in polymer material design? *Macromol. Chem. Phys.*, 210(12):987–992, 2009.

[239] Hartmuth C. Kolb, M. G. Finn, and K. Barry Sharpless. Click chemistry: Diverse chemical function from a few good reactions. *Angew. Chem. Int. Ed.*, 40(11):2004–2021, 2001.

[240] Shirley D. A. High-resolution x-ray photoemission spectrum of the valence bands of gold. *Phys. Rev. B*, 5(7):4709–4714, 1972.

[241] Bradley P. Harris, Jaishankar K. Kutty, Edward W. Fritz, Charles K. Webb, Karen J. L. Burg, and Andrew T. Metters. Photopatterned polymer brushes promoting cell adhesion gradients. *Langmuir*, 22(10):4467–4471, 2006.

[242] Nova ulica. Calculation of molecular properties and bioactivity score. *www.molinspiration.com/cgi-bin/properties*, consulted on 07/14/2016.

[243] IL 60201 Adam Chazan Center for Biotechnology Northwestern University Evanston. Peptide property calculator. *http://biotools.nubic.northwestern.edu/proteincalc.html*, consulted on 07/14/2016.

[244] Alain M. Jonas, Zhijun Hu, Karine Glinel, and Wilhelm T. S. Huck. Chain entropy and wetting energy control the shape of nanopatterned polymer brushes. *Macromolecules*, 41(19):6859–6863, 2008.

[245] AAT Bioquest. Spectrum viewer. *https://www.aatbio.com/spectrum/?request=WyJEeUxpZ2h0XzQ4OCIsMSwxXSw=*, consulted on 07/11/2017.

[246] Simone Weis, Ted T. Lee, Aránzazu del Campo, and Andrés J. García. Dynamic cell-adhesive microenvironments and their effect on myogenic differentiation. *Acta Biomater.*, 9(9):8059–8066, 2013.

[247] Alain M. Jonas, Zhijun Hu, Karine Glinel, and Wilhelm T. S. Huck. Effect of nanoconfinement on the collapse transition of responsive polymer brushes. *Nano Lett.*, 8(11):3819–3824, 2008.

[248] Akhilesh Rai, Sandra Pinto, Marta B. Evangelista, Helena Gil, Silvar Kallip, Mario G. S. Ferreira, and Lino Ferreira. High-density antimicrobial peptide coating with broad activity and low cytotoxicity against human cells. *Acta Biomater.*, 33:64–77, 2016.

[249] Mojtaba Bagheri, Michael Beyermann, and Margitta Dathe. Immobilization reduces the activity of surface-bound cationic antimicrobial peptides with no influence upon the activity spectrum. *Antimicrob. Agents Chemother.*, 53(3):1132–1141, 2009.

[250] Simone Maria-Neto, Elizabete de Souza Cândido, Diana Ribas Rodrigues, Daniel Amaro de Sousa, Ezequiel Marcelino da Silva, Lidia Maria Pepe de Moraes, Anselmo de Jesus Otero-Gonzalez, Beatriz Simas Magalhães, Simoni Campos Dias, and Octávio Luiz Franco. Deciphering the magainin resistance process of escherichia coli strains in light of the cytosolic proteome. *Antimicrob. Agents Chemother.*, 56(4):1714–1724, 2012.

[251] Jeffrey Turner, Yoon Cho, Nhu-Nguyen Dinh, Alan J. Waring, and Robert I. Lehrer. Activities of ll-37, a cathelin-associated antimicrobial peptide of human neutrophils. *Antimicrob. Agents Chemother.*, 42(9):2206–2214, 1998.

[252] Senthil K. Kandasamy and Ronald G. Larson. Effect of salt on the interactions of antimicrobial peptides with zwitterionic lipid bilayers. *Biochimica et Biophysica Acta (BBA) - Biomembranes*, 1758(9):1274–1284, 2006.

[253] Marta Pedrosa, Cláudia Mouro, Frederico Nogueira, Joana Vaz, and Isabel Gouveia. Comparison of the antibacterial activity of modified-cotton with magainin i and ll-37 with potential as wound-dressings. *J. Appl. Polym. Sci.*, 131(21):n/a–n/a, 2014.

[254] Aurélie Merckx. Surfaces nanopatternées pour le contrôle de la croissance bactérienne. Master's thesis, Université catholique de Louvain, 2012.

[255] Catherine Philippart. Elaboration de surfaces macromoléculaires nanopatternées pour l'étude de l'adhésion de bactéries gram positif. Master's thesis, Université catholique de Louvain, 2013.

[256] L. G. Harris, S. Tosatti, M. Wieland, M. Textor, and R. G. Richards. Staphylococcus aureus adhesion to titanium oxide surfaces coated with non-functionalized and peptide-functionalized poly(l-lysine)-grafted-poly(ethylene glycol) copolymers. *Biomaterials*, 25(18):4135–4148, 2004.

[257] He Tao, Zhang Ying, C. K. Lai Alvin, and Chan Vincent. Engineering bio-adhesive functions in an antimicrobial polymer multilayer. *Biomed. Mater.*, 10(1):015015, 2015.

[258] Sharon L. Haynie, Grace A. Crum, and Bruce A. Doele. Antimicrobial activities of amphiphilic peptides covalently bonded to a water-insoluble resin. *Antimicrob. Agents Chemother.*, 39(2):301–307, 1995.

[259] M Alhouayek, J Masquelier, PD Cani, DM Lambert, and GG Muccioli. Implication of the anti-inflammatory bioactive lipid prostaglandin d2-glycerol ester in the control of macrophage activation and inflammation by abhd6. *Proc. Natl. Acad. Sci. U.S.A.*, 110(43):17558–17563, 2013.

[260] Antonio Jacinto and Lewis Wolpert. Filopodia. *Curr. Biol.*, 11(16):R634, 2001.

[261] Julie Vanacker, Aiswarya Viswanath, Pauline De Berdt, Amandine Everard, Patrice D. Cani, Caroline Bouzin, Olivier Feron, Anibal Diogenes,

Julian G. Leprince, and Anne des Rieux. Hypoxia modulates the differentiation potential of stem cells of the apical papilla. *J. Endod.*, 40(9):1410–1418, 2014.